Hannes Weber

Ausbreitung hochfrequenter Wellen in fluktuierenden Plasmen

Universität Ulm | 89069 Ulm | Germany

Masterarbeit zum Thema

Ausbreitung hochfrequenter Wellen in fluktuierenden Plasmen

vorgelegt von:

Hannes Weber
hannes.weber@uni-ulm.de

Gutachter:

PD Dr. Emanuele Poli
apl. Prof. Dr. Matthias Freyberger

IPP-Betreuer:

Dr. Omar Maj

2013

Max-Planck-Institut für Plasmaphysik | 85748 Garching | Germany

Kurzfassung

Herkömmliche Simulationen hochfrequenter Wellen in Tokamak-Plasmen können den Einfluss von kurzskaligen Elektronendichteschwankungen nicht korrekt beschreiben und produzieren außerdem keine akkuraten Ergebnisse, wenn Reflektometriefälle mit spitzen Eintrittswinkeln untersucht werden. In dieser Masterarbeit wird ein neuer Code (WKBeam) entwickelt, der auf einer Phasenraumbeschreibung der Wellen aufbaut. Mathematisches Fundament sind Wigner-Weyl-Symbole. Grundlegende Hintergründe werden besprochen und an die Problemstellung der Mikrowellen in Fusionsplasmen angepasst. Als Ergebnis wird die wellenkinetische Gleichung formuliert. Ein numerisches Lösungsschema für diese Gleichung wird dargestellt und implementiert. Es wird anhand von vereinfachten Modellen gezeigt, dass die Ergebnisse des Codes gegen korrekte Resultate konvergieren. Zum Schluss wird die Simulation für Heizungs- und Reflektometriefälle in den Tokamaks ASDEX Upgrade und ITER verwendet.

Abstract

State of the art high frequency wave simulations in tokamak plasmas are not able to describe the effect of short scale electron density fluctuations on the beam propagation and have accuracy problems when employed under reflectometry conditions with steep injection angles. Within the framework of this master thesis, a new code (WKBeam), based on a phase space description of the beam obtained from Wigner-Weyl symbol calculus, is developed. The basic theoretical background is reviewed and adapted to the purposes of microwaves in tokamak plasmas, with the wave kinetic equation as a result. A numerical scheme solving this equation is presented and implemented. Convergence of the new code to correct results is shown for benchmarks with various simplified models. Finally, it is employed for heating and reflectometry applications in the tokamaks ASDEX Upgrade and ITER.

Acknowledgement

Contents

Contents

1

Introduction

In times of climate change, worries about the safety of fission power plants, and an increasing power demand, it would be extremely beneficial to have a save and reliable energy source. One future option under investigation is nuclear fusion. Historically, people understood in the 1920s that the huge amount of energy the sun emits is produced by nuclear fusion processes and in the 1950s, a rough estimate done by E. Teller and E. Konopinsky showed that in principle it would be possible to exploit fusion power also on earth, envisaging a fusion power plant [1]. It was recognized soon that this is an ambitious goal and even if during the last 50 years huge technical progress was achieved, still some obstacles are left. An introduction to contemporary approaches and problems for nuclear fusion can be found in [2]. As a fuel, a mixture of deuterium and tritium is considered. This is advantageous because the fusion reaction of deuterium and tritium into Helium is not based on weak interactions unlike the proton-proton chains taking place in the sun and hence provides a large cross section which is a welcome property for a fusion power plant.

Therefore, the reaction

$$D + T \rightarrow {}^4He + n + 17.6\,MeV \tag{1.1}$$

is planned to be exploited. In general, since the nuclear forces act on very short distances, there is the problem that the deuterium and tritium nuclei must be brought close together to react. This requires to overcome or tunnel through their Coulomb barrier. It turns out that a temperature of $10\,keV$ is needed to provide the required energy. In order to confine the fuel, one promising concept is the tokamak. In this device, a plasma is confined with a magnetic field. The confinement is based on Lorentz force. It constrains the charged plasma particles to helical trajectories around the magnetic field lines. The circular motion in the plane perpendicular to the field lines is called gyration. A particle mainly following the field lines within the tokamak chamber cannot escape[1]. The magnetic field lines for the tokamak ASDEX Upgrade (AUG) are shown in figure 1.1. On the left, the toroidal plasma chamber can be seen. On the right, only a cut through the torus is shown. This plane is referred to as poloidal plane. The direction perpendicular to such a plane is called toroidal direction. The magnetic field lines do not point purely in the toroidal direction, but they are twisted so that the they span surfaces, referred to as magnetic surfaces and shown on the left in figure 1.1. This is the plasma configuration considered in the applications discussed later in this thesis.

Through the fusion reaction (1.1), α-particles with a kinetic energy of $E_\alpha = 3.5\,MeV$ are produced. They are charged and thus confined by the magnetic field. Their high energy allows a heating of the plasma. For a commercial power plant, energy losses must be minimized so that the α-particle heating compensates them and basically no external heating is required. In present-day tokamak experiments, external heating is needed to obtain the targeted plasma parameters. Moreover, even in a reactor, methods are required to drive part of the current flowing in a tokamak. One such method is based on the injection of electromagnetic waves resonating with the gyration of the electrons around the magnetic field lines. Their angular frequency in cgs-units is therefore in the range

$$\Omega = \frac{eB}{cm_e}, \tag{1.2}$$

---

[1]Collisional and turbulence transport, however, can lead to a loss of particles and energy. These losses, together with the requirement of operational stability, lead to the temperature requirement of $10\,keV$ mentioned above.
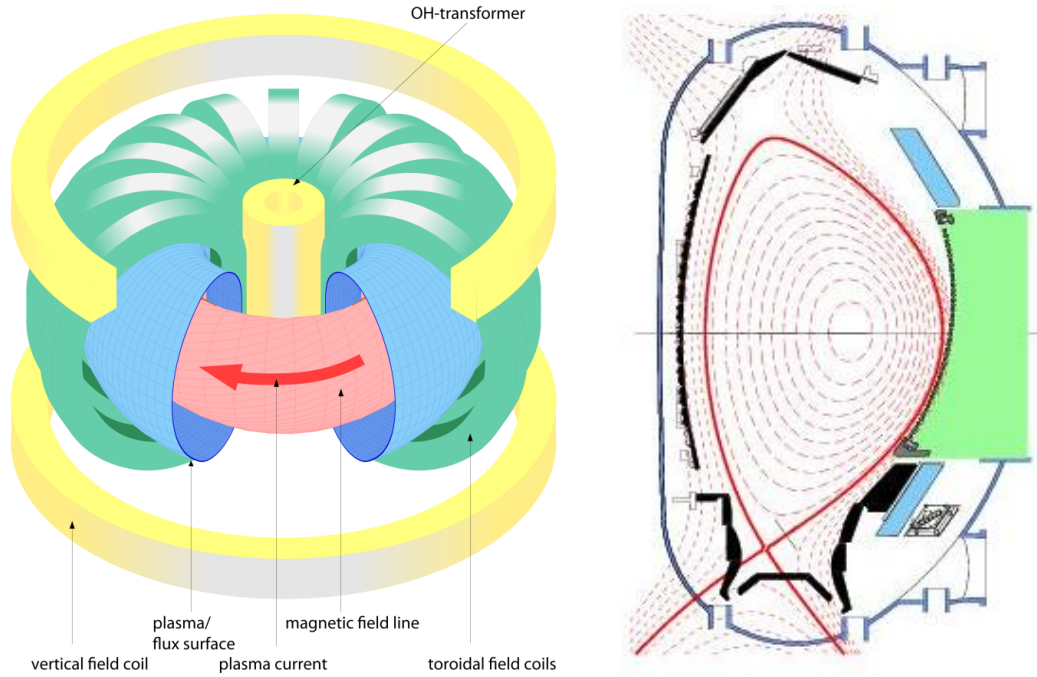
Figure 1.1.: Tokamak ASDEX Upgrade. Left: the toroidal plasma chamber of the tokamak with closed magnetic field lines lying on one surface (red). Right: a cut through the torus. The red lines are cuts through the surfaces the magnetic field lines are lying on. The surfaces inside the bold one are closed within the chamber. The bold surface (called separatrix) is the first to hit the tokamak walls at the bottom. [Pictures taken from AUG gallery.]

where B is the magnetic field strength, e the electron charge and m_e the electron mass. This frequency is referred to as electron-cyclotron frequency. Waves which are in resonance with this cyclotron frequency or higher harmonics have the ability of transferring their energy to the plasma and drive an electric current. Typically, the required frequency is of the order of $100\,\mathrm{GHz}$[2] and thus millimeter wave beams are considered. In general, the magnetic field decreases from the symmetry axis of the tokamak outwards: $B \equiv B(R)$ where R is the distance to the symmetry axis. Therefore, properly tuning the microwave frequency, the distance R where the wave gets absorbed can be chosen. Varying the injection angle of the beam, it can also be determined the vertical location of absorption and the amount of driven current. Together, this allows to target at a magnetic surface.

---

[2]The electron-cyclotron frequency can be obtained from the simple formula $\nu[\mathrm{GHz}] = 28B[\mathrm{T}]$.

In a plasma there also might be regions where no propagating wave exists for a given frequency. They are referred to as evanescent regions. Instead of propagating, a wave launched from outside the plasma mainly gets reflected at the boundary of evanescent regions, referred to as cut-off layer. In the reflectometry technique, this property is exploited: A beam might be launched with injection parameters such that it gets reflected. Then, the reflected beam can be measured and conclusions on the plasma properties might be drawn for diagnostics purposes.

The calculation of electromagnetic waves in the electron-cyclotron frequency range usually employs the fact that the wavelength is much smaller than the typical scale associated to the variation of the plasma parameters [3], [4], [5]. In the presence of fluctuations of the plasma parameters on short scales (like those caused for example by plasma turbulence) or in the vicinity of a cut-off layer, however, this treatment becomes invalid. It is the aim of this thesis to address this issue. Previous work on scattering of electromagnetic waves from fluctuations with application to tokamak plasmas is based on simplified models on wave propagation and on diffusive models [6], [7], which are not always clearly justified. Calculations based on the solution of the full wave equations are available only in limited cases. However, there are several hints that wave scattering can play a significant role in determining the region illuminated by the beam.

In this thesis, a mathematically consistent treatment based on the Wigner-Weyl calculus in analogy to [8], [9] is developed and implemented in a new code, able to produce accurate results for the electromagnetic wave field amplitude near cut-off layers and in the presence of background fluctuations of arbitrary wavelength, provided that their amplitude remains small enough to allow the use of the perturbative approach described in chapter 3.

This thesis begins with a chapter on the theoretical background, where the fundamental physical equations to describe propagation of electromagnetic waves are presented and the mathematical concept of symbol calculus is reviewed. The need for a suitable phase space representation for the wave is displayed. In the next chapter, based on this framework, an equation describing the beam propagation in phase space is developed. This is referred to as wave kinetic equation. The derivation is performed in analogy to [9]. However, considering waves in anisotropic media, the theory
properties of the equation are extensively discussed. A way to deduce physical quantities like the electric field energy density or the power absorption is presented. A basis for the implementation

in the new simulation code is a numerical scheme for the solution of the wave kinetic equation. Two possible schemes are presented in the numerics chapter. In both schemes, the reduction to physical quantities is split into a Monte-Carlo part and a direct part in a different way. After a brief presentation of the newly implemented code (WKBeam) for the simulation, it follows a chapter on benchmarking tests. An investigation of the results for simplified models confirms the accuracy of the code, also near turning points and under the presence of fluctuations. Last, in the applications chapter, results of the simulation for realistic tokamak heating and reflectometry applications are shown. The effect of fluctuation is compared to the estimate in [6]. These first results confirm the importance of wave scattering for the propagation of mm-wave beams in particular in large (reactor-like) devices.

2

Theoretical background

In this chapter, the problem under consideration is stated and the necessary theoretical background is reviewed. First, the equations describing the wave propagation in magnetized plasmas are introduced. It will be seen that a suitable mathematical framework is the Wigner-Weyl symbol calculus, which is introduced and applied to the wave equation under investigation. Furthermore, the standard geometrical optics approximation is recalled.

2.1. Electromagnetic wave propagation in plasmas

The aim of this section is to give an overview of the fundamental equations needed to describe the propagation of electromagnetic waves in a plasma. In addition, the assumptions we make on the problem are discussed.

The propagation of electromagnetic waves is described using as a starting point Maxwell's equations. The reader might refer to the standard textbook of Jackson [10]. In cgs-units,

2. Theoretical background

Maxwell's equations read

$$\nabla \cdot D = 4\pi \rho^{\text{ext}}, \tag{2.1a}$$

$$\nabla \cdot B = 0, \tag{2.1b}$$

$$\nabla \times E + \frac{1}{c}\frac{\partial B}{\partial t} = 0, \tag{2.1c}$$

$$\nabla \times H = \frac{4\pi}{c}j^{\text{ext}} + \frac{1}{c}\frac{\partial D}{\partial t}, \tag{2.1d}$$

where E and H denote the electric and magnetic field, respectively. Throughout this work, c denotes the speed of light in free space. The magnetic induction B is implicitly given by

$$H = B - 4\pi M, \tag{2.2a}$$

where M is the magnetization. The electric displacement is

$$D = E + 4\pi P, \tag{2.2b}$$

with the polarization P. The magnetization and the polarization depend on the electromagnetic field (E, B) and describe the response of the medium under investigation to an electromagnetic disturbance. The last two equations complement Maxwell's equations with the physics of the medium and, therefore, are called constitutive equations. Maxwell's equations are invariant under the gauge transformation

$$M' = M - \frac{1}{c}\frac{\partial V}{\partial t}, \tag{2.3a}$$

$$P' = P + \nabla \times V \tag{2.3b}$$

for the magnetization and polarization, V being an arbitrary vector field [11]. Hence, one is free to move to the primed quantities without changing physics. For this thesis, it is assumed that the gauge V is chosen so that the magnetization vanishes, hence, $H = B$. Furthermore no external

current density j^{ext} nor charges ρ^{ext} are considered so that the systems (2.1) and (2.2) reduce to

$$\nabla \times (\nabla \times E) + \frac{1}{c^2} \frac{\partial^2 D}{\partial t^2} = 0, \tag{2.4a}$$

$$D = E + 4\pi P, \tag{2.4b}$$

with the polarization field P describing the whole response of the medium.

In the case of wave propagation in plasmas, in general, the polarization response $P(t, r)$ at the time t and point r does not only depend on the electric field $E(t, r)$ at (t, r), but it depends on all previous instants $t' < t$ [11], [12]; this is referred to as memory effect or temporal non-locality. Furthermore, the dependence on the electric field is non-local: The response may depend on the electric field at any point r' as far as the distance $|r - r'|$ can be covered in time $t - t'$ without breaking the assumptions of causality. This means (t', r') must be situated inside the backward light cone of (t, r). In summary, $D(t, r)$ depends on $E(t', r')$ where $c |r - r'| \leq t - t'$ so that causality is fulfilled. In this thesis, we limit ourselves to the case of a linear response of the medium, which is a well-justified assumption for the kind of waves we are going to investigate. Such a linear relationship can be written in the form

$$D(t, r) = \int \varepsilon(t, r, t', r') E(t', r') \mathrm{d}t' \mathrm{d}r', \tag{2.5}$$

where $\varepsilon(t, r, t', r')$ is referred to as dielectric kernel. Here, due to causality, this kernel should vanish in case $c |r - r'| > t - t'$, but usually ε has contributions only in the center of the light cone, i.e. for $c |r - r'| \gg t - t'$.

In this thesis, a steady state solution is considered. This means that the dielectric kernel depends only on t and t' via their difference $t - t'$, namely, $\varepsilon(t, r, t', r') \equiv \varepsilon(t - t', r, r')$. Then, equation (2.5) amounts to a convolution in time. According to the convolution theorem, for the Fourier transformed functions

$$E(\omega, r) = \int e^{i\omega t} E(t, r) \mathrm{d}t, \tag{2.6}$$

$$D(\omega, r) = \int e^{i\omega t} D(t, r) \mathrm{d}t, \tag{2.7}$$

and, upon changing to the coordinate $\tau = t - t'$,

$$\varepsilon(\omega, r, r') = \int e^{i\omega\tau} \varepsilon(\tau, r, r') \mathrm{d}\tau, \tag{2.8}$$

the operation of convolution in time is translated to a simple multiplication in the frequency domain with the result that

$$D(\omega, r) = \int \varepsilon(\omega, r, r') E(\omega, r') \mathrm{d}r'. \tag{2.9}$$

Here, ω is the angular frequency of the wave. In the frequency domain, the memory effect in the response operator yields a frequency-dependent kernel, i.e. temporal dispersion. Physically, this response is related to a displacement of charged particles in the medium provoked by the electromagnetic wave field. Then, memory effects arise due to the inertia of those particles [13].

As wave beams with one constant frequency (monochromatic beams) are considered in this work, ω is a fixed parameter of the problem and the wave equation system (2.4) reads

$$\nabla \times (\nabla \times E(\omega, r)) - \frac{\omega^2}{c^2} D(\omega, r) = 0, \tag{2.10a}$$

$$D(\omega, r) = \int \varepsilon(\omega, r, r') E(\omega, r') \mathrm{d}r'. \tag{2.10b}$$

This is a closed system which, in principle, can be solved for the electric field E.

For plasmas, rather than the kernel $\varepsilon(\omega, r, r')$, we have information on its Fourier transform

$$\varepsilon(\omega, r, k) = \int e^{-ik \cdot s} \varepsilon(\omega, r, r - s) \, \mathrm{d}s, \tag{2.11}$$

which is referred to as the local dielectric tensor [3]. In the case of a uniform medium, the only space dependence is via $s = r - r'$. The Fourier transform is performed with respect to this distance, which is in analogy to the temporal Fourier transformation in (2.8). Instead, for a non-uniform medium, the space dependence r appears explicitly also in the local dielectric tensor. Analogously to the definition of temporal dispersion, the non-locality of the response yields a dielectric tensor which depends on k and this is by definition spatial dispersion. Therefore, spatial dispersion is equivalent to the non-locality of the response. When, in particular, a medium has a

local response,

$$\varepsilon(\omega, r, r') = \varepsilon(\omega, r)\delta(r - r'),\tag{2.12}$$

the corresponding dielectric tensor obtained from (2.11) reads

$$\varepsilon(\omega, r, k) = \varepsilon(\omega, r),\tag{2.13}$$

which is independent of k. In this case, wave equation (2.10) reduces to a differential equation for E which does not involve any integral operator. Physically, the response (2.10b) can be explained by a spread of the particle velocities due to finite temperature: The particles remember the impact of the electromagnetic field along all points on their trajectory (t', r'), which is different for each particle due to the thermal velocity spread. As an example, this effect is not present in the cold-plasma approximation [12], where the response becomes local. For the purpose of this work, the general plasma dielectric tensor is employed. It is also referred to as kinetic dielectric tensor, given the fact that it can be derived from the kinetic theory of the microscopic dynamics of plasma particles [4].

One common simplification is the adiabatic approximation for the dielectric tensor $\varepsilon(\omega, r, k)$ of a plasma. It consists in the use of a dielectric tensor $\varepsilon(\omega, k; n, B_0, T)$ computed for the case of a homogeneous plasma with constant equilibrium density n, magnetic field B_0 and temperature T and introducing spatial dependence through plasma parameters; that is, $\varepsilon(\omega, r, k) = \varepsilon(\omega, k; n(r), B_0(r), T(r))$, where $n(r)$, $B_0(r)$ and $T(r)$ are the equilibrium profiles of plasma parameters. Then, the space dependence of the dielectric tensor is present via the parameters of the medium, but their spatial derivatives are neglected. This approach is a good approximation when plasma parameters are slowly varying. In order to give a measure of the variations of a parameter $f(r)$, a typical length scale L, measuring the gradients is introduced, namely

$$|\nabla f| \approx \left|\frac{f}{L}\right|,\tag{2.14}$$

for $f = n, B_0, T$. This length L is used to introduce normalized coordinates

$$x := \frac{r}{L}.\tag{2.15}$$

2. Theoretical background

In terms of such normalized coordinates, the wave equation (2.4a) for the electric field $E(\omega, r)$ and the electric displacement $D(\omega, r)$ reads

$$\nabla_x \times (\nabla_x \times E) - \frac{\omega^2 L^2}{c^2} D = 0. \tag{2.16}$$

One can see that the dimensionless parameter

$$\kappa := \frac{\omega L}{c} = k_0 L \tag{2.17}$$

appears naturally. Here, k_0 is the wave number in free space which can be used as a reference value for the wave vector k. Let us define a normalized quantity

$$N := \frac{ck}{\omega}, \tag{2.18}$$

which is referred to as refractive index vector. From now on, all functions will be written in terms of functions of x (instead of r) and N (instead of k). This has as a consequence that in Fourier transformations the parameter κ appears explicitly. For example, for the Fourier transform of a function f, one has

$$\hat{f}(N) = \int e^{-i\kappa N \cdot x} f(x) \mathrm{d}x, \tag{2.19a}$$

and for the inverse Fourier transform

$$f(x) = \left(\frac{\kappa}{2\pi}\right)^m \int e^{i\kappa x \cdot N} \hat{f}(N) \mathrm{d}N. \tag{2.19b}$$

Here, m denotes the dimensionality and is $m = 3$ for the case of electromagnetic wave propagation in a physical space. Furthermore, the angular frequency ω and the parameter κ both are fixed parameters of the problem. In this work, for simplicity of writing, they will no longer be listed as an argument in any functions. The wave equation (2.10) in terms of the just defined normalized

coordinates reads

$$\nabla_x \times (\nabla_x \times E(x)) - \kappa^2 D(x) = 0, \tag{2.20a}$$

$$D(x) = \int \varepsilon(x, x') E(x') \mathrm{d}x'. \tag{2.20b}$$

Let us note that this wave equation is somehow mixed: the first term on the l.h.s. of equation (2.20a) consists in a partial differential operator applied to the wave field E while the second term is an integral operator present through (2.20b). The wave equation can be written in terms of a single integral operator, namely

$$\int \left[(\nabla_x \otimes \nabla_x - \Delta_x) \, \delta(x - x') - \varepsilon(x, x') \right] E(x') \mathrm{d}x' = 0, \tag{2.21}$$

where $\delta(x)$ is the Dirac's δ-function. Here, the Graßmann identity

$$a \times (b \times c) = b(a \cdot c) - (a \cdot b)c \tag{2.22}$$

is used for the partial differential operators. After integration, the first term in square brackets amounts to $\nabla_x \times (\nabla_x \times E)$. Upon introducing the Fourier transform of the square brackets with respect to $s = x - x'$, namely,

$$d(x, N) = N^2 - N \otimes N - \varepsilon(x, N), \tag{2.23}$$

wave equation (2.21) reads

$$\left(\frac{\kappa}{2\pi} \right)^3 \int e^{i\kappa(x-x')\cdot N} d(x, N) E(x') \mathrm{d}N \mathrm{d}x' = 0. \tag{2.24}$$

The dimensionality for the Fourier transform is fixed to $m = 3$ due to the physical problem. It is worth recalling that both, $d(x, N)$ and $E(x')$, depend on both the frequency and the parameter κ, although such dependence is suppressed in the notation.

Operators of the form (2.24) are well-known in the mathematical literature as semiclassical pseudo-differential operators [14]. The adjective "semiclassical" refers to the explicit dependence on the parameter κ in the Fourier transform (2.19), as opposite to the standard definition. In this section, such an operator has appeared naturally in the wave equation. However, no mathematical

details were given. The next section is dedicated to the general mathematical framework of such pseudo-differential operators.

In this work, we will address equation (2.20) in the high-frequency limit $\kappa \to \infty$, which is also called semiclassical limit, in analogy with quantum mechanics [14]. For the special case of microwave beams in fusion plasmas, we have $\kappa \gg 1$ and hence the asymptotic solution is a good approximation of the real physical situation.

2.2. Pseudo-differential operators

In the last section, a pseudo-differential operator was identified in the wave equation for microwave beams. Here, we have to make up for the mathematical details which were skipped in this physics section. The ideas summarized here can be found in [8], [14] and also nicely reviewed in [15]. Since they are applicable not just to the special case of wave propagation in plasmas, a general wave equation is considered and specified to physically relevant equations later on.

2.2.1. Definition of symbols and multi-index notation

The formulation of pseudo-differential operators in general is presented in the next section, where we shall need a specific class of functions referred to as symbols. For sake of clearness, in this section the definition of symbols is explicitly given. As stated in [15], a smooth function $p(x, N)$ is called symbol of order μ, if

$$\left| \partial_x^\alpha \partial_N^\beta p(x, N) \right| \leq C_{\alpha,\beta} \left(1 + |N| \right)^{\mu - |\beta|} \tag{2.25}$$

with some constant $C_{\alpha,\beta}$. Thus, symbols are basically defined as smooth and polynomially bounded functions. In this definition as well as in following parts of the work, the multi-index notation is used. For an m-dimensional space, a multi-index α is a m-tuple $\alpha = (\alpha_1, \ldots, \alpha_m)$ of non-negative integers α_i. Let α, β be multi-indices, then the following definitions apply:

- componentwise sum (difference):

$$\alpha \pm \beta := (\alpha_1 \pm \beta_1, \ldots, \alpha_m \pm \beta_m), \tag{2.26a}$$

14

- partial order:

$$\alpha < \beta :\Leftrightarrow \alpha_i < \beta_i \ \forall i = 1, \ldots, m, \tag{2.26b}$$

- definition of an absolute value:

$$|\alpha| := \alpha_1 + \cdots + \alpha_m, \tag{2.26c}$$

- definition of a factorial:

$$\alpha! := \alpha_1! \cdots \alpha_m!, \tag{2.26d}$$

- definitions of powers for a variable $x \in \mathbb{R}^m$:

$$x^\alpha := x_1^{\alpha_1} \cdots x_m^{\alpha_m}, \tag{2.26e}$$

- definition of derivatives with respect to the components of $x \in \mathbb{R}^m$:

$$\partial_x^\alpha := \partial_{x_1}^{\alpha_1} \cdots \partial_{x_m}^{\alpha_m}. \tag{2.26f}$$

2.2.2. Definition of pseudo-differential operators

In this section, pseudo-differential operator calculus is introduced. As it is done in [8], a general wave equation

$$D(\psi)(x) = 0 \tag{2.27}$$

is considered. Here, $\psi \equiv \psi(x)$ is a function $\psi : \mathbb{R}^m \to \mathbb{R}^n$ (so $x \in \mathbb{R}^m$ and $\psi(x) \in \mathbb{R}^n$). Therefore, the operator D acting on the wave field is an $n \times n$ matrix of operators. The "double-bracket" notation in (2.27) means that the operator D acts on ψ and the result is evaluated at point x. The kernel $d(x, x') \in \mathbb{R}^n \times \mathbb{R}^n$ of the operator D is defined such that

$$D(\psi)(x) = \int d(x, x')\psi(x')\mathrm{d}x'. \tag{2.28}$$

15

2. Theoretical background

The Fourier transformed of this kernel with respect to the distance $s = x - x'$ reads

$$d(x, N) = \int e^{-i\kappa N \cdot s} d(x, x - s) \mathrm{d}s. \tag{2.29}$$

This is a function on phase space coordinates (x, N). In general, if this function fulfils the requirement for a symbol (2.25), the operator D is by definition a pseudo-differential operator and $d(x, N)$ is referred to as the symbol of this operator. For the case of plasma waves presented in section 2.1, the Fourier transform $d(x, N)$ of the wave operator kernel is given in (2.23). The first two parts actually are polynomials and therefore are symbols. The last term is the dielectric tensor which is assumed to be well-behaved. For waves in plasmas, this assumption is justified by the smooth plasma profiles yielding a smooth dielectric tensor and by the fact that for large wave vectors $|N| \to \infty$, the waves do not feel the plasma any more, so that the dielectric tensor of free space is approached. This is polynomially bounded and, thus, also the plasma dielectric tensor is. In summary, $d(x, N)$ is a symbol and hence for the problem of microwave propagation, pseudo-differential operator calculus applies.

It must be noted that the relationship between operators and symbols is not unique. It is necessary to introduce a label in order to distinguish different kinds of these mathematical objects. Symbols constructed via (2.29) are called L-symbols. Here, L stands for "left" and recalls the fact that the position argument x for the symbol is just the left one of the kernel. In this thesis, L-symbols are denoted with small case letters.

Formally, the operation of constructing a symbol $a(x, N)$ given a pseudo-differential operator A is called symbol map

$$\sigma^L : A \mapsto a(x, N). \tag{2.30}$$

Here, the superscript L reminds one to use the transformation (2.29) to construct an L-symbol. The inverse operation, namely the construction of an operator given its symbol, is called quantization rule and, again, there are several ways how this can be done. One is the left side quantization rule. Given any symbol $a(x, N)$, the outcoming operator applied on a test function f yields

$$a(x, -\frac{i}{\kappa}\nabla_x)f(x) = \left(\frac{\kappa}{2\pi}\right)^m \int e^{i\kappa(x-x')\cdot N} a(x, N) f(x') \mathrm{d}x' \mathrm{d}N. \tag{2.31}$$

Here, the notation for the operator on the l.h.s. is a formal way of writing which should not be confused with any function at arguments x and $-\frac{i}{\kappa}\nabla_x$. It should be rather more considered as an object which is defined by its effect on a function f given on the r.h.s. Operators constructed upon the L-quantization rule (2.31) are denoted with small case letters in this work.

If the symbol under consideration is an L-symbol constructed as it is presented in (2.29), the quantization rule (2.31) just recovers the original operator, i.e.

$$a(x, N) = d(x, N) \Rightarrow a(x, -\frac{i}{\kappa}\nabla_x) = D. \tag{2.32}$$

The L-symbol and L-quantization rule presented above are the ones which are relatively straight forward to understand, and a special case is the symbol (2.23) for plasma wave propagation. The main results of this thesis, however, rely upon an alternative definition. Due to its useful properties, deriving from its symmetric construction, the so-called Weyl symbol,

$$A(x, N) = \int e^{-i\kappa N \cdot s} a\left(x + \frac{s}{2}, x - \frac{s}{2}\right) \mathrm{d}s, \tag{2.33}$$

is introduced, where $a(x, x')$ is the kernel of a given operator A. Throughout this thesis, capital letters are used for Weyl symbols in order to distinguish them from the L-symbols denoted by small case letters. The symbol map appropriate to the previously defined Weyl symbols,

$$\sigma^W : A \mapsto A(x, N), \tag{2.34}$$

takes the operator and computes its Weyl symbol, according to equation (2.33). In analogy to the left quantization rule (2.31), there is the Weyl quantization rule which, given the Weyl symbol $D(x, N)$ of an operator D, provides the operator itself, i.e.

$$A(x, N) = D(x, N) \Rightarrow A(x, -\frac{i}{\kappa}\nabla_x) = D. \tag{2.35}$$

This quantization rule, again, is defined via the action of this operator on a test function f:

$$A(x, -\frac{i}{\kappa}\nabla_x)f(x) = \left(\frac{\kappa}{2\pi}\right)^m \int e^{i\kappa(x-x')\cdot N} A\left(\frac{x+x'}{2}, N\right) f(x')\mathrm{d}x'. \tag{2.36}$$

17

2. Theoretical background

Here, the inversion of equation (2.33) is used to express the kernel of the operator $A(x, -\frac{i}{\kappa}\nabla_x)$. Operators constructed with the Weyl quantization rule are denoted with capital letters in the framework of this thesis.

The remaining part of this section is devoted to specific issues arising from the application of the Weyl symbols to the problem of wave propagation considered in this work. The main ideas, again, follow [8].

In equation (2.23) the L-symbol corresponding to the wave equation for wave beam propagation is found. It was mentioned that the Weyl symbol is used instead. So a direct relation between L-symbols and Weyl symbols is needed in order to compute the latter. In principle, it is clear what to do: The Weyl symbol $A(x, N)$ is computed with the Weyl symbol map (2.34) for a given pseudo-differential operator with kernel $a(x, x')$, explicitly formulated in terms of a Fourier transformation of the kernel in equation (2.33). Once the symbol $a(x, N)$ is known, its kernel is obtained from (2.29). The derivation of a final formula linking $a(x, N)$ and $A(x, N)$ is a little technical and therefore moved to appendix A.1. The final result is

$$A(x, N) = e^{\frac{i}{2\kappa}\partial_N \cdot \partial_x} a\,(x, N)\,. \tag{2.37}$$

Here, the partial derivatives at the exponent are a formal way of writing which makes sense only if the exponential is expressed in terms of its Taylor series.

As a particular case which will be needed, when

$$a(x, N) = a_1(x) + a_2(N), \tag{2.38}$$

then the derivatives in the exponential (2.37), being mixed derivatives acting on x and N, will vanish and therefore only the zeroth order term of the Taylor series of the exponential contributes. This means that the left symbol and the Weyl symbol are the same, i.e.

$$A(x, N) = a(x, N) = a_1(x) + a_2(N). \tag{2.39}$$

For later reference let us write a formula which allows to find the Weyl symbol $C(x, N)$ of the composition of two operators A and B with Weyl symbols $A(x, N)$ and $B(x, N)$. Again, the

technical computation is moved to appendix A.2. The final formula is

$$
\begin{aligned}
C(x, N) =& A(x, N) \star B(x, N) = \\
& A(x, N)\, e^{\frac{i}{2\kappa} \left[\overleftarrow{\partial_x} \cdot \overrightarrow{\partial_N} - \overleftarrow{\partial_N} \cdot \overrightarrow{\partial_x} \right]} B(x, N).
\end{aligned}
\tag{2.40}
$$

The operation denoted by "$\star$" is called Moyal-Weyl product. The arrows on the partial differential operators indicate the direction in which the operators act.

2.2.3. Differential operators in the framework of pseudo-differential operator calculus

Pseudo-differential operators can be considered a generalization of differential operators: One can express differential operators in the form of pseudo-differential operators. Actually, for the case of the electromagnetic wave equation, the first term on the l.h.s. of (2.21) was formulated in terms of a symbol in (2.23). In this section, a general argument is presented. A good overview on this topic is also provided in [15].

A general partial differential operator of order μ in multi-index notation is expressed as

$$
D = \sum_{|\alpha| \leq \mu} \left(-\frac{i}{\kappa} \right)^{|\alpha|} p_\alpha(x) \partial_x^\alpha.
\tag{2.41}
$$

Here, $p_\alpha(x)$ are bounded functions with bounded derivatives on x. This operator acting on a generic function f, in terms of the kernel $d(x, x')$, yields the result

$$
D(f)(x) = \int d(x, x') f(x') \mathrm{d}x'.
\tag{2.42}
$$

Therefore, the kernel of the differential operator is explicitly given by

$$
d(x, x') = \sum_{|\alpha| \leq \mu} \left(-\frac{i}{\kappa} \right)^{|\alpha|} p_\alpha(x) \partial_x^\alpha \delta(x - x'),
\tag{2.43}
$$

which can be verified by direct substitution. Derivatives of the δ-distribution must be considered in a weak sense, as reviewed in appendix B.

Symbol map (2.29) applied to the operator D with kernel (2.43) yields

$$d(x, N) = \sum_{|\alpha| \leq \mu} \left(-\frac{i}{\kappa} \right)^{|\alpha|} p_\alpha(x) \int e^{-i\kappa N \cdot s} \partial_s^\alpha \delta(s) \mathrm{d}s. \tag{2.44}$$

This integral is computed by parts and the result reads

$$d(x, N) = \sum_{|\alpha| \leq \mu} p_\alpha(x) N^\alpha. \tag{2.45}$$

The function $d(x, N)$ computed in this last equation, being a polynomial in N with smooth and uniformly bounded coefficients $p_\alpha(x)$, is a symbol. Therefore, in general, differential operators can be considered as pseudo-differential operators. Furthermore the symbols of differential operators are easily constructed replacing the partial differential operator $-\frac{i}{\kappa}\partial_x$ by the conjugate variable N.

2.3. Geometrical optics and ray tracing

The aim of this section is to present the standard geometrical optics approximation for wave propagation. Geometrical optics provides asymptotic solutions in the high-frequency limit $\kappa \to \infty$, where κ is the dimensionless parameter defined in (2.17) and it can be considered a cornerstone of semiclassical methods. It shows the Hamiltonian structure which controls the behavior of the wave field in the semiclassical limit and, hence, makes it possible to use ray tracing methods [3], [5]. In this section, we shall review the basic ideas of geometrical optics for the simple case of transverse electromagnetic waves in isotropic media. This simplification allows us to avoid unessential technical difficulties, while retaining the basic ingredients of the theory. For transverse waves in isotropic, spatially non-dispersive media, the response operator (2.20b) simplifies to a multiplication with a scalar function $\varepsilon(x)$. Hence, the wave equation (2.20) reduces to the Helmholtz equation

$$\Delta_x E(x) + \kappa^2 \varepsilon(x) E(x) = 0, \tag{2.46}$$

where $\nabla_x \cdot E \equiv 0$ has been accounted for.

The high-frequency limit suggests the use of the **W**entzel-**K**ramers-**B**rillouin (WKB) ansatz for the electric field, which is

$$E(x) = e^{i\kappa S(x)} \left[A_0(x) + \frac{1}{\kappa} A_1(x) + \dots \right]. \tag{2.47}$$

Here, $S(x)$ is a scalar function called eikonal. It represents the phase of the wave. Instead, the functions $A_j(x)$, $j \geq 0$ representing the polarization and the amplitude of the field, are vector valued. They introduce explicitly the expansion of the amplitude in different orders in κ^{-1}. In analogy with the plane wave, for which

$$E(x) \propto e^{i\kappa N \cdot x}, \tag{2.48}$$

the local refractive index is defined as

$$N(x) = \nabla_x S(x). \tag{2.49}$$

It is worth noting that the eikonal establishes a relationship between the position x and the refractive index $N(x)$: At every spatial position x, this relation uniquely defines a value for the refractive index $N(x)$. The substitution of the WKB ansatz (2.47) into the wave equation (2.46) after separating different orders of $\kappa \to \infty$, yields for the first two equations in the hierarchy

$$\mathcal{O}(\kappa^2): \quad (\nabla_x S(x))^2 - \varepsilon(x) = 0, \tag{2.50a}$$

$$\mathcal{O}(\kappa): \quad 2\nabla_x A_0(x) \cdot \nabla_x S(x) + A_0(x)\Delta_x S(x) = 0. \tag{2.50b}$$

For each point x, the first equation (2.50a), also referred to as eikonal equation, defines the refractive index $N(x)$, whereas, given this refractive index, the second equation (2.50b) describes the wave amplitude to lowest order in the WKB ansatz (2.47). A set of eikonal and amplitude to lowest order (S, A_0) which solves the system (2.50) solves the wave equation (2.46) in the limit $\kappa \to \infty$ with a remainder of order κ^{-2}. Equation (2.50a) is called local dispersion relation. For a homogeneous medium, a plane wave (2.48) solves the wave equation (2.46) and, by definition, as dispersion relation an equation is considered which defines the refractive index so that a solution for the wave equation exists. In the context of the WKB ansatz, the adjective "local" refers to

the fact that the refractive index to solve the wave equation might depend on the position x, i.e. $N \equiv N(x)$.

The local dispersion relation (2.50a) has the structure of a Hamilton-Jacobi equation, which is discussed in some details in appendix C, cf. equation (C.8). The relevant Hamiltonian is

$$H(x, N) = N^2 - \varepsilon(x). \tag{2.51}$$

Therefore, a solution of the nonlinear first-order partial differential equation (2.50) can be obtained in terms of Hamilton orbits. Hamiltonian orbits are the trajectories in phase space obtained from Hamilton's equations of motion (C.1) as, again, discussed in appendix C. More specifically, on an antenna plane, boundary conditions for the wave equation (2.46) are known. This includes a knowledge on the phase, called eikonal S in the framework of the WKB approximation and allows us to construct initial conditions for Hamilton's equations of motion with Hamiltonian (2.51). Such equations then are ordinary differential equations which can be solved by using standard numerical techniques. The projection of the resulting Hamiltonian orbits from phase space into configuration space determines a bundle of curves in the physical space called geometrical optics rays. These constitute the light rays in basic optics descriptions. The solution of Hamilton's equations of motion in the framework of geometrical optics if often referred to as "ray tracing".

One finds that Hamiltonian orbits resulting from the ray tracing procedure span a hypersurface of the form $(x, N(x))$ with geometrical optics refractive index vector as given in (2.49), usually called Lagrangian manifold. The bundle of geometrical optics rays defines a velocity field on the physical space, which is given by

$$v_x = \nabla_N H(x, N) = 2N(x). \tag{2.52}$$

Upon accounting for (2.52), equation (2.50b) can be written in the form

$$v_x \cdot \nabla_x A_0 + \frac{1}{2} \left(\nabla_x \cdot v_x \right) A_0 = 0. \tag{2.53}$$

This equation describes the evolution of the lowest order amplitude A_0. We can see that A_0 is transported along geometrical optics rays. Multiplied with A_0^*, equation (2.50b) takes the form of

a steady-state continuity equation, namely,

$$\nabla_x \cdot \left(v_x \left| A_0 \right|^2 \right) = 0. \tag{2.54}$$

This last equation expresses the conservation of the beam energy at the leading order in the limit $\kappa \to \infty$. Note that no sources or dissipation is present in (2.46). The exact energy transport of the electric field is proportional to the normalized Poynting flux:

$$F(x) = \frac{1}{i\kappa} \left(E^\dagger(x) \nabla_x E(x) - \nabla_x E^\dagger(x) E(x) \right). \tag{2.55}$$

Analogously to [16], the WKB ansatz for lowest order in κ^{-1} yields $F = F_0 + \mathcal{O}(\kappa^{-1})$ with

$$F_0(x) = 2 \left| A_0(x) \right|^2 \nabla_x S(x) = \left| A_0(x) \right|^2 v_x(x). \tag{2.56}$$

Here, the velocity (2.52) and the definition of the refractive index (2.49) have been accounted for. This shows that (2.54) describes energy conservation within the geometrical optics approximation.

The fact that equations (2.50) can be solved by tracing a set of rays makes geometrical optics computationally very efficient. Ray tracing codes have been the main tool for the study of waves in inhomogeneous plasmas in the short wavelength limit. Nevertheless, the approach of geometrical optics breaks down in some situations. Two examples in a two-dimensional geometry $x = (\mathrm{x}, \mathrm{y})$ are displayed in figure 2.1 which shows the bundle of rays (a,c) and the corresponding Hamiltonian orbits in phase space (b,d), for the case of two-dimensional propagation of beams in presence of a focal point (a,b) and of a turning point (c,d). In both cases the beam is launched from the line $\{\mathrm{x} = 0\}$ and propagates towards the negative x-axis. Hamiltonian orbits are smooth trajectories without crossings. Their congruence determines a hypersurface in the phase space. When such hypersurface can be written in the form (2.49), we readily have a solution of (2.50a) as presented in appendix C. One can see that this is not the case near $(\mathrm{x} = -0.25, \mathrm{y} = 0)$ for figure 2.1 (b) and near $(\mathrm{x} = -0.5, \mathrm{y})$ for figure 2.1 (d). The corresponding geometrical optics rays are obtained by projecting Hamiltonian orbits into the configuration space and are shown in figure 2.1 (a,c). For the situation of a focal point shown on top, all rays cross at $(\mathrm{x} = -0.25, \mathrm{y} = 0)$ thus violating the requirement (2.49) for which at every point x we can have only one value of N. This leads to a vanishing beam width at this focal point for which

the continuity equation (2.54) predicts an infinite amplitude. Both, the zero beam width as well as the divergent amplitude, are unphysical for finite frequencies. A more detailed analysis [17] reveals that the geometrical optics ray tracing method does not account for diffractive effects that are crucial near focal points. For the case of a turning point shown in figure 2.1 (c), the rays are reflected at x = −0.5. Again, just at the point where the rays change their direction, several values for N are present which cannot properly be described using geometrical optics. The points where such projection singularities occur are called caustics. For a more mathematical study on caustic points, the reader might refer to [18].

It was seen in this section that geometrical optics is a simple approach which allows to compute the electric field in the semiclassical limit. However, the results projected on configuration space are inadequate for several situations as for example focal points or turning points. The physical meaning of the WKB ansatz for the wave field consists in assuming that for each point x only one value $N(x)$ for the refractive index is present and hence, the field locally near each point can be approximated by a plane wave. In order to unfold the projection singularities, one should resolve different values N of the refractive index at each configuration space point x. In the next section, a quantity is presented which provides a phase space description of the electric field and hence is suitable for such purposes.

Focal point:
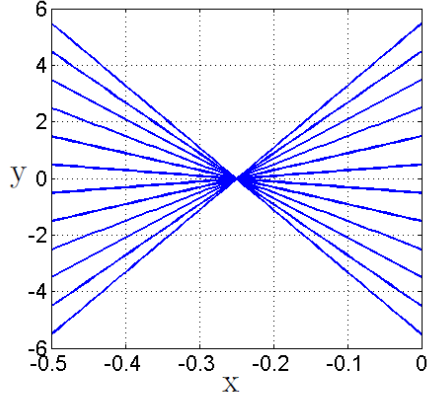
(a) rays in configuration space: (b) orbits in phase space:
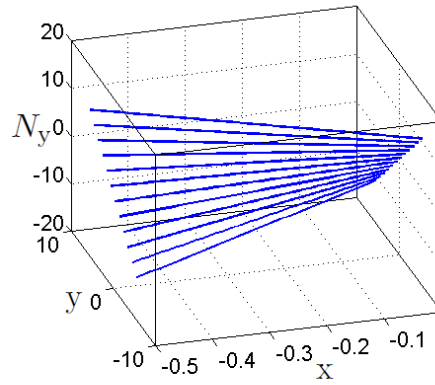
Turning point:
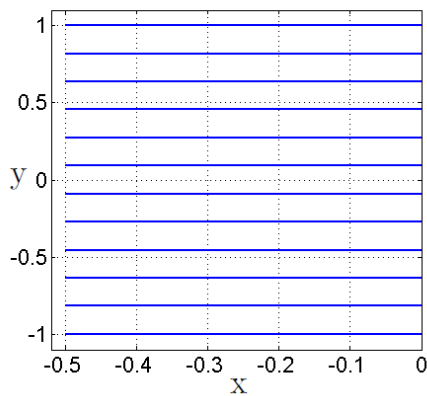
(c) rays in configuration space: (d) orbits in phase space:
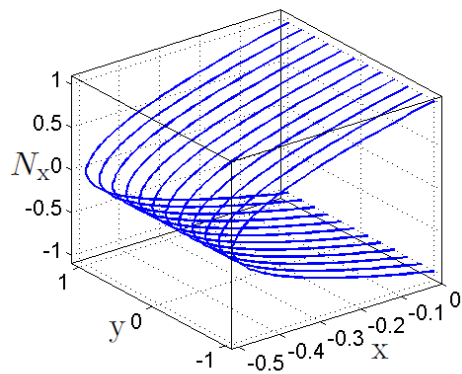
Figure 2.1.: Two-dimensional geometrical optics rays (a,c) and the corresponding Hamiltonian orbits (b,d) in phase space. The Lagrangian manifold is visible as a congruence of the orbits. They are launched at x = 0 and propagate to the left. Two different situations are shown: On top (a,b) the rays show a focal point. At the bottom (c,d), the media is such that a turning point is present.

2.4. Spectral operator and Wigner function

In the last section, it was seen that geometrical optics is a fundamental tool for simulations of high frequency waves and yet it is limited by the singularities of the projection from phase space to configuration space. A phase space description not restricting the distribution of rays to a Lagrangian manifold should solve the problem. In this section, a representation of the wave field in phase space is introduced. Furthermore, its connection to symbol calculus is presented. Again, the concept is not restricted to the electric field and the general field ψ is considered.

Let us begin with the spectral operator W (also referred to as density operator in quantum mechanics) of the wave field $\psi \equiv \psi(x)$ under investigation. This is defined in terms of its kernel

$$w(x, x') = \psi(x)\psi(x')^\dagger, \tag{2.57}$$

where "$\dagger$" denotes the Hermitian conjugate (i.e. the complex conjugate of the transpose). If the corresponding operator is applied to a test function $f(x)$, the result is the projection of f on the wave field ψ, namely

$$W(f)(x) = \int w(x, x')f(x')\mathrm{d}x' = \psi(x)\int \psi(x')^\dagger f(x')\mathrm{d}x'. \tag{2.58}$$

It is convenient to introduce the notation

$$W = \psi\psi^\dagger \tag{2.59}$$

for the operator W, where $\psi\psi^\dagger$ should be interpreted as a tensor product in the space of functions $\{\psi\}$, which is (2.58).

The symbol map (2.29) applied to the spectral operator yields

$$w(x, N) = \int e^{-i\kappa N \cdot s} w(x, x - s)\mathrm{d}s = e^{-i\kappa N \cdot x}\psi(x)\hat{\psi}^\dagger(N). \tag{2.60}$$

It is worth noting that $w(x, N)$ might not be a symbol in the sense of section 2.2.1. Nevertheless the Fourier transform implied by the definition of σ^L (2.29) makes sense also for operators more general than pseudo-differential operators. With abuse of language, we shall call $w(x, N)$ symbol of W, but the reader should be aware of the difference.

In the last step, the Fourier transform (2.19a) of the wave field $\hat{\psi}(N)$ has been inserted, splitting the symbol $w(x, N)$ into a product of the wave field itself and its Fourier transformed. Therefore, it is clear that it is significantly different from zero near phase space points (x, N) where both $\psi(x)$ as well as $\hat{\psi}(N)$ are significant. Thus, this symbol gives a statement on the phase space distribution of the electric field and therefore, in principle, could be used as a phase space representation.

On the other hand, the construction of $w(x, N)$ requires both $\psi(x)$ and $\hat{\psi}(N)$, with similar projection singularities as encountered in geometrical optics [8]. It turns out that the symmetrized version of the symbol of the spectral operator, referred to as Weyl symbol, does not show this problem of unexpected singularities. Moreover, as it will be seen later on in this section, a relatively easy physical interpretation for the Weyl symbol can be given. The Weyl symbol of the spectral operator is obtained by applying the symbol map (2.34) on the kernel $w(x, x')$, with the result

$$W(x, N) = \int e^{-i\kappa N \cdot s} \psi\left(x + \frac{s}{2}\right) \psi^\dagger\left(x - \frac{s}{2}\right) \mathrm{d}s. \tag{2.61}$$

This equation is also referred to as Wigner transform. As for (2.60), $W(x, N)$ is not a symbol in the sense of section 2.2.1; indeed, it is generally a singular distribution. However, the word "symbol" referred to $W(x, N)$ is an abuse of language which is common in literature. The phase space representation $W(x, N)$ of the wave field is also called Wigner function of the wave field, although, when ψ is a vector, $W(x, N)$ is a matrix. It has the nice properties relating its partial integrals to physical and spectral energy distributions, namely

$$\left(\frac{\kappa}{2\pi}\right)^m \int \mathrm{Tr}\, W(x, N)\mathrm{d}N = |\psi(x)|^2, \tag{2.62a}$$

$$\int \mathrm{Tr}\, W(x, N)\mathrm{d}x = \left|\hat{\psi}(N)\right|^2, \tag{2.62b}$$

for a wave field in an m-dimensional space. Here, Tr denotes the trace of a matrix. In case of the electric field, $\psi = E$, integral (2.62a) yields the electric field energy density (energy density resolved in x), whereas the second integral (2.62b) provides the spectrum of the electric field (energy density resolved in N). Therefore, the Wigner function would be a good candidate as a phase space energy density. Unfortunately, in general, the Wigner function might become

negative, thus such interpretation is not generally appropriate. One refers to the Wigner function as an energy quasi-density in phase space. However, we remember that the Wigner function integrated as is done in (2.62) behaves like an energy density in phase space.

To get familiar with the Wigner function, in the following two examples are presented. In the second one, in particular, the Wigner function becomes negative at some points.

2.4.1. Example 1: Geometrical optics ansatz

In the WKB ansatz (2.47) for geometrical optics, to lowest order in κ^{-1}, the electric field is approximated by

$$E(x) = A_0(x)e^{i\kappa S(x)}. \tag{2.63}$$

For simplicity, we shall assume that $E(x)$ and $A_0(x)$ are scalar fields, implying that the polarization of the electric field is fixed. Formula (2.61) with $\psi = E$ provides the Wigner function of the electric field

$$W(x, N) = \int e^{-i\kappa N \cdot s + i\kappa S(x+s/2) - i\kappa S(x-s/2)} A_0\left(x + \frac{s}{2}\right) A_0^\dagger\left(x - \frac{s}{2}\right) \mathrm{d}s. \tag{2.64}$$

It is assumed that the amplitude $A(x)$ and the refractive index vector $N(x) = \nabla_x S(x)$ are slowly varying in space. Therefore, a Taylor expansion of the amplitude to zeroth order and of the eikonal to first order are appropriate with a remainder $\mathcal{O}(\kappa^{-1})$:

$$W(x, N) = \int e^{-i\kappa(N - \nabla_x S) \cdot s} |A_0(x)|^2 \, \mathrm{d}s + \mathcal{O}(\kappa^{-1}). \tag{2.65}$$

Given the fact that the only s-dependence in the integral is at the exponent, it can be computed analytically and one finds

$$W(x, N) = \left(\frac{2\pi}{\kappa}\right)^m |A(x)|^2 \, \delta(N - \nabla_x S) + \mathcal{O}(\kappa^{-1}). \tag{2.66}$$

For a physical electric field, the dimensionality must be set to $m = 3$. The result in (2.66) shows again that the restriction of the geometrical optics ansatz consists in taking one value for the refractive index N for each position x, as it is expressed here by the δ-distribution.

2.4.2. Example 2: Superposition of plane waves

Here an example is presented which shows the problem of the interpretation of the Wigner function as an energy density in phase space. Let the electric field be the superposition of two plane waves,

$$E(x) = e^{i\kappa x \cdot N_0} + e^{-i\kappa x \cdot N_0}, \tag{2.67}$$

with refractive indices N_0 and $-N_0$, respectively. Computing the Wigner function (2.61) yields

$$W(x, N) = \left(\frac{2\pi}{\kappa}\right)^m [\delta(N - N_0) + \delta(N + N_0) + 2\cos(2\kappa x \cdot N_0)\,\delta(N)] \tag{2.68}$$

and from this Wigner function the electric field energy density, obtained via (2.62a), is

$$|E(x)|^2 = 2 + 2\cos(2\kappa x \cdot N_0). \tag{2.69}$$

The first two terms in (2.68) reproduce the phase space energy density contributions one would have expected for the two plane waves which are singularly supported at the prescribed values of the refractive index, i.e. $N = N_0$ and $N = -N_0$. In addition, the term $2\cos(2\kappa x \cdot N_0)\,\delta(N)$ appears, which leads to the well-known interference pattern in the energy density (2.69). It is centered at $N = 0$ and oscillatory in x which means that W might become negative when $N = 0$. Such negative values for the Wigner function are incompatible with the interpretation of W as a phase space energy density. However, when the limit $\kappa \to \infty$ is considered, the oscillation period asymptotically goes to zero. Therefore, integrating the Wigner function even on a small interval, the oscillatory part will vanish because positive and negative contributions cancel out. Nevertheless, it can be proven that in the semiclassical limit $\kappa \to \infty$, the Wigner function approaches a well-defined positive measure on phase space, the calculation of which is the main purpose of this work.

3

The wave kinetic equation

The previous chapter contains an overview on pseudo-differential operator calculus, symbol calculus and basic ideas from geometrical optics. In addition, a phase space representation of the wave field in terms of the Wigner function is presented. Equations describing the behavior of the Wigner function in phase space are now required.

In this chapter, such equations are derived. We begin with the simple case of propagation without absorption and fluctuations of the medium. Next, also these two effects are included and a discussion on some special related topics follows. The chapter is completed by the outline of a framework for a phase space description of wave beams: This comprises the extension of physical boundary conditions for the wave field to phase space, as well as the reconstruction of physical observables from the Wigner function.

3.1. Weyl phase space representation of the wave equation

In this section, the evolution equation for the Wigner function is derived from the wave equation, neglecting absorption and short scale fluctuations. These physical effects are introduced later in section 3.2. The derivation follows the work of McDonald [8].

Let us begin with an abstract wave equation of the form

$$D\psi = 0, \tag{3.1}$$

where D is a pseudo-differential operator referred to as dispersion operator. It is assumed that this operator is Hermitian and, thus, also its Weyl symbol $D(x, N)$ is a Hermitian matrix. Physically, such an assumption does not allow us to describe the effect of absorption, which corresponds to a non-Hermitian part in the wave equation operator. However, it is useful to present the basic idea of phase space formulation of the wave equation for a simpler problem first.

The abstract vector $D\psi$ is multiplied with its adjoint from the right, the multiplication being in the sense of the tensor product defined in equation (2.58). The result is

$$D\psi\psi^\dagger D^\dagger = 0. \tag{3.2}$$

Multiplied from the right with the inverse $\left(D^\dagger\right)^{-1}$ it yields

$$D\psi\psi^\dagger = 0. \tag{3.3}$$

Here, the spectral operator W as defined in (2.58) is identified:

$$DW = 0. \tag{3.4}$$

This shows that, if a non-vanishing solution W is considered, the dispersion operator is singular and the inverse D^{-1} cannot be properly defined. Hence, the step from (3.2) to (3.3) is not trivial to justify. For the moment, we note that even if the inverse itself does not exist, it can be given sense to it in terms of propagators, addressed in section 3.4, so that formally we can assume that the inverse exists.

Equation (3.4) is translated into an equation involving the Weyl symbol $D(x, N)$ of the dispersion operator and the Wigner function $W(x, N)$ of the wave upon making use of the symbol map (2.34) and the symbol product rule (2.40), with the result

$$D(x, N) \star W(x, N) = D(x, N) e^{\frac{i}{2\kappa} \left[\overleftarrow{\partial_x} \cdot \overrightarrow{\partial_N} - \overleftarrow{\partial_N} \cdot \overrightarrow{\partial_x} \right]} W(x, N) = 0. \tag{3.5}$$

When the Taylor series of the exponential is used, equation (3.5) becomes

$$\sum_{k=0}^{\infty} \frac{1}{k!} \left(\frac{i}{2\kappa} \right)^k D(x, N) \left(\overleftarrow{\partial_x} \cdot \overrightarrow{\partial_N} - \overleftarrow{\partial_N} \cdot \overrightarrow{\partial_x} \right)^k W(x, N) \sim 0, \tag{3.6}$$

in the sense of asymptotic series in the semiclassical limit $\kappa \to \infty$. Specifically, the sign "$\sim$" is used instead of the equality to recall that asymptotic series do not converge to a unique sum, but have a remainder of order $\mathcal{O}(\kappa^{-\infty})$, this is, smaller than $\mathcal{O}(\kappa^{-n})$ for every positive n.

It was stated in section 2.1 that for the case of millimeter wave propagation in fusion plasmas, the background parameters are such that the semiclassical limit is a reasonable approximation. If also fluctuations which might have a much shorter scale length are considered, this could no longer be true, requiring a special treatment for fluctuations presented in the next section.

In the limit $\kappa \to \infty$, different orders of κ^{-1} can be separated. The two leading orders for equation (3.6) read

$$\mathcal{O}(1) : \qquad D(x, N) W(x, N) = 0, \tag{3.7a}$$

$$\mathcal{O}(\kappa^{-1}) : \quad -\frac{i}{2\kappa} D(x, N) \left(\overleftarrow{\partial_x} \cdot \overrightarrow{\partial_N} - \overleftarrow{\partial_N} \cdot \overrightarrow{\partial_x} \right) W(x, N) = 0. \tag{3.7b}$$

In equation (3.7) both $D(x, N)$ and $W(x, N)$ are matrices, and a matrix product is implied. In addition one should note that the derivation of (3.7) by direct separation of orders in (3.6) is not entirely rigorous, as a perturbation series for W should be employed instead. However, it is possible to show [19] that equation (3.7) correctly determines the semiclassical limit of the Wigner function; hence, $W(x, N)$ in (3.7) should be interpreted as the semiclassical limit of the Wigner function.

The $\mathcal{O}(1)$ equation (3.7a) yields a non-vanishing solution for the Wigner function W only on the surface defined by $\det D(x, N) = 0$. This is called dispersion variety. Equation (3.7a) is therefore equivalent to the dispersion equation. In this thesis, with some abuse of language, it

is also referred to as dispersion relation for simplicity. The $\mathcal{O}(\kappa^{-1})$ equation (3.7b), using the definition of the Poisson brackets (C.4), states

$$\{D, W\} = 0. \tag{3.8}$$

Let us remark that, for matrix-valued arguments, Poisson brackets imply a matrix multiplication, namely,

$$\{D, W\}_{ij} = \{D_{ik}, W_{kj}\} = \partial_N D_{ik} \partial_x W_{kj} - \partial_x D_{ik} \partial_N W_{kj}, \tag{3.9}$$

with Einstein's sum convention.

  Equation (3.8) has the form of a steady state kinetic equation and will yield the evolution of the Wigner function from an antenna plane into phase space, cf. chapter 4. It will alternatively be referred to as evolution equation or wave kinetic equation. In principle, formulas (3.7) being simple enough, would be a good starting point for further calculations.

3.2. Derivation of the wave kinetic equation for dispersive, weakly dissipative, and random media

In the last section, the idea how an equation describing the Wigner function can be formulated was presented. However, the effect of fluctuations could not be treated directly, because random fluctuations might have short scale oscillations breaking the limit $\kappa \to \infty$. Moreover, inclusion of wave absorption breaks the Hermiticity of the dispersion operator. In this section, instead, a somewhat more sophisticated approach is used. Fluctuations are treated separately and the limit $\kappa \to \infty$ is only considered when it is appropriate. In addition, the limit of weak dissipation is considered. The derivation follows basically [9]. The underlying idea for the separation of different orders was presented in [20] years before and consists in dividing the operator D into one contribution D_0, a separate contribution δD_F containing the (possibly short scale length) fluctuations of the medium and a third part $\delta^2 D_A$ containing the effect of absorption, i.e.

$$D = D_0 + \delta D_F + \delta^2 D_A. \tag{3.10}$$

3.2. Derivation of the wave kinetic equation for dispersive, weakly dissipative, and random media

The parameter δ plays the role of an ordering parameter. It will be assumed small, reflecting the assumption of a weakly fluctuating and dissipative medium. This ordering is discussed in more detail later in this section. The lowest-order part of the wave operator D_0 as well as the fluctuating part D_F are assumed to be Hermitian, whereas the absorption part D_A is described by an anti-Hermitian operator.

The wave equation written in terms of this perturbed operator is

$$\left(D_0 + \delta D_F + \delta^2 D_A\right)\psi = 0. \tag{3.11}$$

In analogy to the previous section, this wave equation is multiplied with its adjoint from the right, with the result that

$$\left(D_0 + \delta D_F + \delta^2 D_A\right)\psi\psi^\dagger \left(D_0^\dagger + \delta D_F + \delta^2 D_A^\dagger\right) = 0. \tag{3.12}$$

Here, we properly put the adjoint signs also to the Hermitian operator D_0. Analogously to the last section, when the inverse of D_0 is considered, propagators are involved and D_0^{-1} and $\left(D_0^\dagger\right)^{-1}$ must be distinguished, cf. section 3.4. Instead, the "$\dagger$" is dropped for the operator D_F, accounting for its Hermiticy and regularity.

Again, the spectral operator $W = \psi\psi^\dagger$ is identified in equation (3.12). Multiplying with D_0^{-1} from the left and with $\left(D_0^\dagger\right)^{-1}$ from the right, one obtains

$$W = W_0 - \delta\left(W D_F \left(D_0^\dagger\right)^{-1} + D_0^{-1} D_F W\right)$$
$$- \delta^2 \left(D_0^{-1} D_F W D_F \left(D_0^\dagger\right)^{-1} + D_0^{-1} D_A W + W D_A^\dagger \left(D_0^\dagger\right)^{-1}\right), \tag{3.13}$$

where contributions of order $\mathcal{O}(\delta^3)$ and higher are neglected. The term W_0 has been added on the r.h.s. so that when fluctuations and absorption vanish ($\delta = 0$), the Wigner function W is a solution of the corresponding wave equation (3.4), labeled with an index "0" in this section:

$$D_0 W_0 = 0. \tag{3.14}$$

3. The wave kinetic equation

As a consistency check, let us do the step backwards from (3.13) to (3.12), i.e. multiplying equation (3.13) with D_0 from the left and with $D_0^\dagger$ from the right. This makes the additional term W_0 disappear and justifies its introduction by hand in (3.13).

Equation (3.13) contains the random term D_F accounting for random fluctuation of the medium. Therefore, the solution W is a random variable: In correspondence of a realization D_F of the random fluctuation of the medium we find a solution W; moreover, a sample of the random field D_F will produce a sample of solutions for the spectral operator W, characterized by a certain distribution. Here we are only interested in a deterministic equation that describes the average of W. With this aim equation (3.13) is averaged over several realizations of the fluctuations, denoted by $\mathbb{E}(\cdot)$. It is assumed that the mean value of the fluctuation vanishes, i.e.

$$\mathbb{E}(D_F) = 0. \tag{3.15}$$

On the r.h.s. of equation (3.13), there are products of W and D_F. When it comes to the computation of the average $\mathbb{E}(\cdot)$ of such terms, there is the difficulty that the solution W will depend on the realization of the fluctuation D_F and, thus, W and D_F are not statistically independent. This problem can easily be avoided by using equation (3.13) iteratively to remove W from the r.h.s. until only terms dependent on W_0 and terms of order $\mathcal{O}(\delta^3)$ and higher are left. Neglecting those high-order terms, the result yields

$$\begin{aligned}
W = {}& W_0 - \delta D_0^{-1} D_F W_0 - \delta W_0 D_F \left(D_0^\dagger\right)^{-1} \\
& + \delta^2 D_0^{-1} D_F D_0^{-1} D_F W_0 + \delta^2 D_0^{-1} D_F W_0 D_F \left(D_0^\dagger\right)^{-1} \\
& + \delta^2 W_0 D_F \left(D_0^\dagger\right)^{-1} D_F \left(D_0^\dagger\right)^{-1} - \delta^2 D_0^{-1} D_A W_0 - \delta^2 W_0 D_A^\dagger \left(D_0^\dagger\right)^{-1}.
\end{aligned} \tag{3.16}$$

Next the averaging of the wave equation over fluctuation realizations is performed. According to (3.15), all terms linear in D_F will vanish, but the average of higher powers of D_F must be retained, with the result

$$\begin{aligned}
\mathbb{E}(W) = {}& W_0 + \delta^2 D_0^{-1} \mathbb{E}\left(D_F D_0^{-1} D_F\right) W_0 + \delta^2 D_0^{-1} \mathbb{E}\left(D_F W_0 D_F\right) \left(D_0^\dagger\right)^{-1} \\
& + \delta^2 W_0 \mathbb{E}\left(D_F \left(D_0^\dagger\right)^{-1} D_F\right) \left(D_0^\dagger\right)^{-1} \\
& - \delta^2 D_0^{-1} D_A W_0 - \delta^2 W_0 D_A^\dagger \left(D_0^\dagger\right)^{-1}.
\end{aligned} \tag{3.17}$$

3.2. Derivation of the wave kinetic equation for dispersive, weakly dissipative, and random media

Multiplying with D_0 from the left, the equation simplifies to

$$D_0 \mathbb{E}(W) = \delta^2 \mathbb{E}\left(D_F D_0^{-1} D_F\right) W_0 + \delta^2 \mathbb{E}\left(D_F W_0 D_F\right)\left(D_0^\dagger\right)^{-1} - \delta^2 D_A W_0. \tag{3.18}$$

Here, the wave equation for the non-fluctuating and non-dissipative case (3.14) has been accounted for. It is seen that, as a consequence of the ordering of equation (3.10), the effects of fluctuations and absorption enter at the same order in δ. Equation (3.17) allows us to compute the spectral operator averaged over fluctuation realizations $\mathbb{E}(W)$, given the non-perturbed solution W_0; the difference between the two is

$$\mathbb{E}(W) - W_0 = \mathcal{O}(\delta^2). \tag{3.19}$$

As we restrict ourselves to orders of $\mathcal{O}(\delta^2)$, W_0 on the right in equation (3.18) can be replaced with $\mathbb{E}(W)$ with negligible fourth order corrections. This provides a closed equation describing $\mathbb{E}(W)$:

$$D_0 \mathbb{E}(W) = \delta^2 \mathbb{E}\left(D_F D_0^{-1} D_F\right)\mathbb{E}(W) + \delta^2 \mathbb{E}\left(D_F \mathbb{E}(W) D_F\right)\left(D_0^\dagger\right)^{-1} - \delta^2 D_A \mathbb{E}(W). \tag{3.20}$$

As pointed out in section 2.1, considering wave propagation in plasmas, equation (3.20) is an integro-differential equation. It describes the average spectral operator $\mathbb{E}(W)$, and it has deterministic coefficients. When such coefficients depend weakly on the position x, semiclassical asymptotics can be applied even though D_F in the original equation (3.11) exhibits short-scale random variations.

In analogy to the previous section, equation (3.20) can be formulated in terms of Weyl symbols and the Wigner function using the Moyal-Weyl product rule (2.40):

$$D_0 \star \mathbb{E}(W) = \delta^2 \mathbb{E}\left(\sigma^W\left(D_F D_0^{-1} D_F\right)\right) \star \mathbb{E}(W) + \delta^2 \mathbb{E}\left(\sigma^W\left(D_F \mathbb{E}(W) D_F\right)\right) \star D_0^{-1}$$
$$- \delta^2 D_A \star \mathbb{E}(W). \tag{3.21}$$

The products involving fluctuations $D_F A D_F$ with $A = D_0^{-1}$ or $A = \mathbb{E}(W)$ on the r.h.s. are referred to as triple products. Note that the average operator $\mathbb{E}$ commutes with the symbol map σ^W, thus, changing the order of application has no effect on the result.

3. The wave kinetic equation

As a next step, these triple products are investigated: The effect of an operator $D_F A D_F$ on a test function $f(x)$ is computed explicitly. First, the effect of D_F is discussed, then A acts on the result of this operation, and at last D_F is applied on the left. It is assumed that the operator D_F containing the fluctuations is local and does not involve differential operators. This will suffice for the applications considered in this thesis. The Weyl symbol map (2.33) shows that in this case the Weyl symbol $D_F(x, N)$ of D_F does not depend on N, i.e. $D_F(x, N) \equiv D_F(x)$. The action of the operator on a test function $f(x)$ then simply consists in the multiplication with the Weyl symbol:

$$D_F(f)(x) = D_F(x)f(x). \tag{3.22}$$

Also A given in terms of its Weyl symbol $A(x, N)$ applied on this result, according to the Weyl quantization rule (2.36), yields

$$(AD_F)(f)(x) = \left(\frac{\kappa}{2\pi}\right)^m \int e^{i\kappa(x-x')\cdot N} A\left(\frac{x+x'}{2}, N\right) D_F(x')f(x')\mathrm{d}N\mathrm{d}x'. \tag{3.23}$$

The last application of D_F again just being a multiplication with $D_F(x)$ gives the final result

$$(D_F A D_F)(f)(x) = \left(\frac{\kappa}{2\pi}\right)^m \int e^{i\kappa(x-x')\cdot N}$$
$$\times D_F(x)A\left(\frac{x+x'}{2}, N\right) D_F(x')f(x')\mathrm{d}N\mathrm{d}x'. \tag{3.24}$$

In this last formula the kernel of the triple product $D_F A D_F$

$$(D_F A D_F)(x, x') = \left(\frac{\kappa}{2\pi}\right)^m \int e^{i\kappa(x-x')\cdot N} D_F(x)A\left(\frac{x+x'}{2}, N\right) D_F(x')\mathrm{d}N \tag{3.25}$$

is identified. The symbol map (2.33) yields the corresponding Weyl symbol

$$\sigma^W(D_F A D_F)(x, N) = \left(\frac{\kappa}{2\pi}\right)^m \int e^{i\kappa(N'-N)\cdot s}$$
$$\times D_F\left(x + \frac{s}{2}\right) A(x, N) D_F\left(x - \frac{s}{2}\right) \mathrm{d}N'\mathrm{d}s. \tag{3.26}$$

When symbol calculus was presented in section 2.2, it was stated that the Weyl symbols we are dealing with are matrix-valued functions and it is not obvious if they commute. However, the

fluctuations are an input for the simulation. Thus, it is advantageous to rearrange the symbols in (3.26) such that fluctuations are singled out. Therefore, the matrix multiplication is written out explicitly in terms of matrix components using Einstein's summation convention on repeated indices:

$$
\begin{aligned}
\sigma^W \left(D_F A D_F \right)_{ij} (x, N) = \left(\frac{\kappa}{2\pi} \right)^m \int e^{i\kappa(N'-N)\cdot s} \\
\times D_{F,ia} \left(x + \frac{s}{2} \right) D_{F,bj} \left(x - \frac{s}{2} \right) A_{ab} (x, N) \, \mathrm{d}N' \mathrm{d}s.
\end{aligned}
\tag{3.27}
$$

After applying the statistical average operator $\mathbb{E}$ which commutes with both integrals, and formally exchanging the order of integration, fluctuations are entirely described by

$$
G_{iabj}(x, \Delta N) = \left(\frac{\kappa}{2\pi} \right)^m \int e^{-i\kappa \Delta N \cdot s} \mathbb{E} \left(D_{F,ia} \left(x + \frac{s}{2} \right) D_{F,bj} \left(x - \frac{s}{2} \right) \right) \mathrm{d}s,
\tag{3.28}
$$

which is up to a prefactor the Wigner transformation applied to the two-point fluctuation correlation function $\mathbb{E} \left(D_{F,ia}(x) D_{F,bj}(x') \right)$. With definition (3.28), formula (3.27) for the Weyl symbol of the triple product simplifies to the convolution

$$
\sigma^W \left(\mathbb{E} \left(D_F A D_F \right) \right)_{ij} (x, N) = \int G_{iabj}(x, N - N') A_{ab} (x, N) \, \mathrm{d}N'.
\tag{3.29}
$$

One should note that A is usually singular in the cases we are considering; in fact, if A is either the propagator D_0^{-1} or the averaged Wigner function $\mathbb{E}(W)$, $A(x, N)$ is singular on the dispersion variety. On the other hand, $G(x, N)$ is typically smooth, so that the convolution regularizes A. The result $\sigma^W \left(\mathbb{E} \left(D_F A D_F \right) \right)$ is assumed to be a symbol, an assumption which is fulfilled in the cases of interest. This justifies the use of the Moyal-Weyl formula in (3.21), which upon accounting for (3.29) yields

$$
\begin{aligned}
(D_0 \star \mathbb{E}(W))_{ij} (x, N) = \delta^2 \left[\int G_{iabk}(x, N - N') D_{0,ab}^{-1}(x, N') \mathrm{d}N' \right] \star \mathbb{E}(W)_{kj}(x, N) \\
+ \delta^2 \left[\int G_{iabk}(x, N - N') \mathbb{E}(W)_{ab} (x, N') \, \mathrm{d}N' \right] \star \left(D_0^\dagger \right)_{kj}^{-1} (x, N) \\
- \delta^2 D_{A,ik}(x, N) \star \mathbb{E}(W)_{kj}(x, N).
\end{aligned}
\tag{3.30}
$$

3. The wave kinetic equation

At this point there are two ordering parameters involved in the theory. One is δ, which measures the strength of fluctuations and of absorption and is assumed to be small. The other is κ, which, in the short wavelength limit, is assumed to be large and enters through the Moyal-Weyl products. A simple ordering is suggested in [20], namely:

$$\kappa^{-1} = \delta^2 \tag{3.31}$$

The ordering of absorption effects to be $\mathcal{O}\left(\kappa^{-1}\right)$ as compared to the Hamiltonian part of the dispersion operator describing wave propagation is customary in the theory of high-frequency waves in plasmas [3], [4], [5]. Physically, this is appropriate for weak effects of fluctuation and absorption. Considering zeroth order terms $\mathcal{O}(1)$ of equation (3.30), the r.h.s. does not give any contribution and one obtains

$$D_0(x, N)\mathbb{E}(W)(x, N) = 0. \tag{3.32a}$$

This is the dispersion relation already found in section 3.1 for the case without fluctuations and absorption. So the solutions $\mathbb{E}(W)(x, N)$ are still singularly restricted to the dispersion variety $\det D_0(x, N) = 0$. For the order $\mathcal{O}(\kappa^{-1})$ equation, terms of order $\mathcal{O}(\delta^2)$ have to be kept on the r.h.s., with the result that

$$
\begin{aligned}
-\frac{i}{2}\left\{D_0(x, N), \mathbb{E}(W)(x, N)\right\}_{ij} = \int & G_{iabk}(x, N - N') \\
\times & \left[D_{0,ab}^{-1}(x, N')\mathbb{E}(W)_{kj}(x, N)\right. \\
& \left.+ \mathbb{E}(W)_{ab}\left(x, N'\right)\left(D_0^\dagger\right)_{kj}^{-1}(x, N)\right]\mathrm{d}N' \\
- & D_{A,ik}(x, N)\mathbb{E}(W)_{kj}(x, N). \tag{3.32b}
\end{aligned}
$$

Here, again the definition of the Poisson bracket (C.4) is used. This last equation is the wave kinetic equation in case fluctuations and absorption are present.

In this section, applying the semiclassical limit whenever appropriate, dispersion relation (3.32a) and an evolution equation (3.32b) for the statistically averaged Wigner function of the wave field are derived. The effects of fluctuations and absorption are taken into account under the assumption that their level measured by δ and δ^2 fulfils $\delta^2 \approx \kappa^{-1}$. As a matter of fact, the

functions involved are tensors because the wave field under investigation is vector-valued. In the next section, it will be seen how the problem can be decomposed in normal modes so that a scalar description is appropriate. One more point needs to be discussed further, namely, the existence of the formal inverse D_0^{-1}. This issue is delayed to section 3.4.

3.3. Mode decomposition

In the last section, the dispersion relation (3.32a) and the wave kinetic equation (3.32b) have been derived. They describe the propagation of the Wigner function of the wave field. As vector valued waves are considered, the Wigner function is a tensor. It would be easier to deal with scalar functions. In this section, a mode decomposition of the vector valued wave field is performed. Furthermore, we shall prove that the scalar functions that describe the modes independently are real valued. Therefore, the wave equation is projected on the eigenmodes of the wave field. Note that this section reviews a sketch of the derivation, which involves a lengthy calculation [21].

We consider the asymptotic series expansion of the averaged Wigner matrix, thus splitting the different orders of $\mathbb{E}(W)$, i.e.

$$\mathbb{E}(W)(x, N) = W^{(0)}(x, N) + \frac{1}{\kappa} W^{(1)}(x, N) + \mathcal{O}\left(\kappa^{-2}\right), \tag{3.33}$$

with the zeroth order contribution $W^{(0)}$ representing the semiclassical limit we are interested in. Here, $W^{(1)}$ is the first-order corrector which we do not compute explicitly; it is however important to check that corrections remain bounded so that (3.33) makes sense as an asymptotic series. With the perturbation series (3.33), the first two orders of wave equation (3.30) read

$$D_0(x, N)W^{(0)}(x, N) = 0, \tag{3.34a}$$

$$D_0(x, N)W^{(1)}(x, N) = V(W^{(0)})(x, N), \tag{3.34b}$$

where $V(W)$ contains the Poisson bracket as well as fluctuations and absorption:

$$V(W^{(0)})_{ij}(x, N) = V_P(W^{(0)})_{ij}(x, N) + V_F(W^{(0)})_{ij}(x, N) + V_A(W^{(0)})_{ij}(x, N) \tag{3.35}$$

3. The wave kinetic equation

with

$$V_P(W^{(0)})_{ij}(x,N) = \frac{i}{2}\left\{D_0(x,N),W^{(0)}(x,N)\right\}_{ij} \tag{3.36a}$$

$$V_F(W^{(0)})_{ij}(x,N) = \int G_{iabk}(x,N-N')\left[D_{0,ab}^{-1}(x,N')(W)_{0,kj}(x,N)\right.$$

$$\left.+ W_{0,ab}(x,N')\left(D_0^\dagger\right)_{kj}^{-1}(x,N)\right]\mathrm{d}N' \tag{3.36b}$$

$$V_A(W^{(0)})_{ij}(x,N) = -D_{A,ik}(x,N)W_{0,kj}(x,N). \tag{3.36c}$$

Since the averaged Wigner matrix is Hermitian, we are interested in Hermitian solutions of (3.34). Let $e_\alpha(x,N)$ ($\alpha = 1,2,\ldots,n$) be the set of ortho-normal basis vectors which diagonalize $D_0(x,N)$. Then, it follows from equation (3.34a) that a Hermitian solution $W^{(0)}$ is also diagonal in this basis, so that it is appropriate to write

$$D_0(x,N) = \sum_\alpha H_\alpha(x,N)e_\alpha(x,N)e_\alpha^\dagger(x,N), \tag{3.37a}$$

$$W^{(0)}(x,N) = \sum_\alpha w_\alpha(x,N)e_\alpha(x,N)e_\alpha^\dagger(x,N) \tag{3.37b}$$

with H_α and w_α being the eigenvalues of D_0 and $W^{(0)}$, respectively. Then, equation (3.34a) takes the form of decoupled scalar equations,

$$H_\alpha(x,N)w_\alpha(x,N) = 0 \tag{3.38}$$

for $\alpha = 1,\ldots,n$ (no implicit sum). This is the dispersion relation for the decomposed modes labelled by α. It states that the Wigner function $w_\alpha(x,N)$ for mode α is singularly supported on the dispersion surface $H_\alpha(x,N) = 0$ corresponding to mode α.

Unlike the previously presented matrices, the first-order contribution $W^{(1)}$ is not necessarily diagonal, but it can be decomposed using e_α as a basis, namely

$$W^{(1)}(x,N) = \sum_{\alpha,\beta} w_{\alpha\beta}^{(1)}(x,N)e_\alpha(x,N)e_\beta^\dagger(x,N). \tag{3.39}$$

We wish to construct Hermitian-valued solutions even including the first-order approximation. This is obtained from a Hermitian first order corrector matrix $W^{(1)}$. The condition that $W^{(1)}$ is

Hermitian implies that the coefficients $w_{\alpha\beta}^{(1)}$ in equation (3.39) must be of the form

$$w_{\alpha\beta}^{(1)} = w_{\beta\alpha}^{(1)*}, \tag{3.40}$$

where the "*" denotes complex conjugation. With Hermitian solutions, the first-order equation (3.34b) and its Hermitian conjugate projected on $e_\alpha^\dagger$ from the left and on e_β from the right read

$$H_\alpha w_{\alpha\beta}^{(1)} = e_\alpha^\dagger V e_\beta, \tag{3.41a}$$

$$H_\beta w_{\alpha\beta}^{(1)} = e_\alpha^\dagger V^\dagger e_\beta. \tag{3.41b}$$

Equation (3.41b) is subtracted from equation (3.41a), with the result that

$$\alpha = \beta: \quad 0 = e_\alpha^\dagger \left(V - V^\dagger \right) e_\alpha, \tag{3.42a}$$

$$\alpha \neq \beta: \quad w_{\alpha\beta}^{(1)} = \frac{e_\alpha^\dagger \left(V - V^\dagger \right) e_\beta}{H_\alpha - H_\beta}. \tag{3.42b}$$

Here, the condition for $\alpha \neq \beta$ has been divided by $H_\alpha - H_\beta$, assuming that no degeneracy of the eigenvalues H_α is present, so that this difference never vanishes. Physically, this assumption implies that no mode conversion occurs in the considered phase space domain. In this thesis linear mode conversion [22] is not considered as typically it is not an issue for the applications under consideration.

Equations (3.42) are necessary conditions that must be fulfilled for Hermitian solutions to exist. Condition (3.42b) explicitly provides the off-diagonal parts of $W^{(1)}$. We next have to see if this $W^{(1)}$ solves wave equation (3.34b), which would mean that, indeed, the off-diagonal terms given in (3.42b) are a solution for the wave equation to first order. Multiplying equation (3.42b) by H_α one obtains

$$H_\alpha w_{\alpha\beta}^{(1)} = \frac{H_\alpha e_\alpha^\dagger V e_\beta - H_\alpha e_\alpha^\dagger V^\dagger e_\beta}{H_\alpha - H_\beta}. \tag{3.43}$$

Note that a comparison of (3.41a) multiplied with H_β and (3.41b) multiplied with H_α yields

$$H_\beta e_\alpha^\dagger V e_\beta = H_\alpha e_\alpha^\dagger V^\dagger e_\beta. \tag{3.44}$$

3. The wave kinetic equation

This relation is used to replace the second term in the numerator in (3.43), yielding

$$H_\alpha w^{(1)}_{\alpha\beta} = \frac{H_\alpha e^\dagger_\alpha V e_\beta - H_\beta e^\dagger_\alpha V e_\beta}{H_\alpha - H_\beta} = e^\dagger_\alpha V e_\beta. \tag{3.45}$$

Hence, the r.h.s. of wave equation (3.41a) is recovered. This shows that, indeed, the off-diagonal terms of the Hermitian $W^{(1)}$ solve the equation.

In order to obtain the wave kinetic equation, V from (3.35) is substituted into the necessary condition for the diagonal terms (3.42a). Let us split the computation in the Poisson bracket part, fluctuation part and absorption part and start with the last one: Upon defining a real valued absorption coefficient

$$\gamma_\alpha := e^\dagger_\alpha \left[\frac{i}{2}(D_A - D^\dagger_A) \right] e_\alpha, \tag{3.46}$$

the projection on part (3.36c) reads

$$e^\dagger_\alpha \left(V_A(W^{(0)}) - V^\dagger_A(W^{(0)}) \right) e_\alpha = 2i\gamma_\alpha w_\alpha. \tag{3.47}$$

For the part describing fluctuations, we first need to specify the "inverse"

$$D^{-1}_0(x, N) = \sum_\alpha \frac{e_\alpha(x, N)e^\dagger_\alpha(x, N)}{H_\alpha(x, N) - i\epsilon}. \tag{3.48}$$

Here, in the denominator a small imaginary contribution $-i\epsilon$ is added by hand. The inverse is obtained in the limit $\epsilon \to 0$. However, this imaginary part ensures existence of the inverse even if vanishing eigenvalues are considered. A more detailed discussion on this issue follows in section 3.4. Then, inserting (3.36b) into condition ((3.42a)) yields

$$e^\dagger_\alpha \left(V_F(W^{(0)}) - V^\dagger_F(W^{(0)}) \right) e_\alpha = \int \sum_\beta G_{\alpha\beta}(x, N, N')$$
$$\times \left[\frac{w_\alpha(x, N)}{H_\beta(x, N') - i\epsilon} + \frac{w_\beta(x, N')}{H_\alpha(x, N) + i\epsilon} - \text{c.c.} \right] dN' \tag{3.49}$$

where "c.c." denotes the complex conjugate part and

$$G_{\alpha\beta}(x, N, N') := e^\dagger_{\alpha,i}(x, N)e_{\alpha,k}(x, N)e^\dagger_{\beta,a}(x, N')e_{\beta,b}(x, N')G_{iabk}(x, N - N'). \tag{3.50}$$

One can verify that $G_{\alpha\beta}(x, N, N')$ is real-valued as a consequence of the condition $D_F = D_F^\dagger$. The term in square brackets in (3.49) is purely imaginary, hence,

$$
\begin{aligned}
e_\alpha^\dagger \left(V_F(W^{(0)}) - V_F^\dagger(W^{(0)}) \right) e_\alpha = 2i \int \sum_\beta G_{\alpha\beta}(x, N, N') \\
\times \operatorname{Im} \left[\frac{w_\alpha(x, N)}{H_\beta(x, N') - i\epsilon} + \frac{w_\beta(x, N')}{H_\alpha(x, N) + i\epsilon} \right] \mathrm{d}N' \quad (3.51)
\end{aligned}
$$

Finally, the Poisson bracket part is found to be [21]

$$
e_\alpha^\dagger \left(V_P(W^{(0)}) - V_P^\dagger(W^{(0)}) \right) e_\alpha = i \left\{ H_\alpha, w_\alpha \right\}. \quad (3.52)
$$

Inserting equations (3.47), (3.51) and (3.52) into condition (3.42a) via the decomposition (3.35) yields the mode-decomposed wave kinetic equation

$$
\begin{aligned}
-\frac{i}{2} \left\{ H_\alpha(x, N), w_\alpha(x, N) \right\} = i \int \sum_\beta G_{\alpha\beta}(x, N, N') \\
\times \operatorname{Im} \left[\frac{w_\alpha(x, N)}{H_\beta(x, N') - i\epsilon} + \frac{w_\beta(x, N')}{H_\alpha(x, N) + i\epsilon} \right] \mathrm{d}N' \\
+ i\gamma_\alpha(x, N) w_\alpha(x, N). \quad (3.53)
\end{aligned}
$$

It can be seen that also the Wigner function of mode β has an impact on the evolution of mode α. This is interpreted as mode-to-mode scattering due to the presence of fluctuations. For the case of waves in plasmas, on one hand, the modes are assumed to be non-degenerate and the different branches of the dispersion variety in phase space well-distinguished by a minimum distance ΔN_{modes} at a given point x. For the problem of fluctuations in fusion plasmas, we assume that the fluctuation spectrum $G(x, N, N')$ is such that the "gap" ΔN_{modes} to change mode is not bridged, i.e. $G(x, N, N')$ decreases fast with increasing $N - N'$ and for $|N - N'| \geq \Delta N_{\text{modes}}$, the contribution is negligible. In this work, we neglect mode-to-mode scattering, assuming that fluctuations act in a region of the plasma where the modes are well separated. A general estimate of the validity of this assumption is left for future work. Note that there is no theoretical necessity for this simplifications. Mode-to-mode scattering is turned off by imposing

$$
G_{\alpha\beta}(x, N, N') = G_\alpha(x, N, N')\delta_{\alpha\beta}, \quad (3.54)
$$

where $\delta_{\alpha\beta}$ is Kronecker's delta. This fluctuation spectrum is substituted into wave kinetic equation (3.53) and multiplied with $2i$. The result reads

$$\{H_\alpha(x, N), w_\alpha(x, N)\} = \mathcal{S}_\alpha(w_\alpha)(x, N) - 2\gamma_\alpha(x, N)w_\alpha(x, N). \tag{3.55}$$

Here, Einstein's summation convention does not apply, so there is no sum on α. The operator $\mathcal{S}_\alpha$ acting on w_α,

$$\mathcal{S}_\alpha(w_\alpha)(x, N) := -2 \int G_\alpha(x, N, N')$$
$$\times \operatorname{Im}\left[\frac{w_\alpha(x, N)}{H_\alpha(x, N') - i\epsilon} + \frac{w_\alpha(x, N')}{H_\alpha(x, N) + i\epsilon}\right] dN', \tag{3.56}$$

is defined. It is referred to as scattering operator and, integrated on the refractive index N, vanishes. Physically, this expresses the fact that energy is conserved in the presence of fluctuations, which are described by $\mathcal{S}_\alpha$.

Summarizing, in this section, the wave kinetic equation has been projected on the eigenmodes of the dispersion matrix $D_0(x, N)$, so that (3.38) and (3.55) form a set of dispersion relation and wave kinetic equation for scalar Wigner functions w_α labeled by a mode index α. In case the solution under consideration is a superposition of those eigenmodes of the dispersion operator, owing to the linearity of the wave equation, the problem can be solved for the eigenmodes independently and the single contributions are added up. In writing (3.55), mode-to-mode scattering has been neglected; when this approximation fails, the more general expression $G_{\alpha\beta}$ should be kept in equation (3.53).

The problem of a non-defined inverse of D_0 under the integral in (3.32b) was solved for the mode decomposed equation (3.55) by adding a small imaginary part to the denominator of vanishing eigenvalues. However, convergence of the integral in the limit $\epsilon \to 0$ should be studied further. This is the issue of the following section.

3.4. Singular integrals

In the previous section, a set of equations for the scalar Wigner function has been derived, namely the dispersion relation (3.38) and, upon neglecting mode-to-mode scattering, the wave kinetic
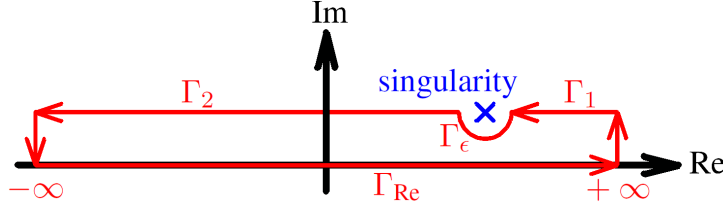
Figure 3.1.: Complex plane with considered integration path (red) and singularity (blue). The part along the real axis is denoted Γ_{Re}. Together with the contributions Γ_1 and Γ_2 parallel to the real axis, the semi circle Γ_ϵ around the singularity and the contributions parallel to the imaginary axis for infinite real parts, a closed path in the complex plane is obtained.

equation (3.55). There, fluctuations are accounted for in an integral which originally involved the inverse of the eigenvalue $H_\alpha^{-1}(x, N)$. This inverse, not being defined, was regularized by adding an imaginary contribution $-i\epsilon$. In the limit $\epsilon \to 0$, the non-defined inverse is recovered. However, after integration, the result might converge. In this section, in analogy to [9], we analyze the convergence of the integral describing fluctuations in the scattering operator (3.56) in the limit $\epsilon \to 0$.

Note that this regularization procedure is well-known in physics in the framework of propagators, e.g. in the field of quantum electrodynamics [23]. However, in this physical problem, the sign of the imaginary part is determined by causality. Instead, we are solving a steady state equation and no such argument can be applied. Therefore in this thesis we pick the sign which yields reasonable results.

First, an integral on generic functions f and g which has the same structure as in (3.56) is investigated, namely

$$I_\epsilon = \int_{-\infty}^{+\infty} \frac{f(x)}{g(x) - i\epsilon} \mathrm{d}x. \tag{3.57}$$

Let the function g in the denominator exhibit a zero point at $x_0 \in \mathbb{R}$, i.e. $g(x_0) = 0$. Now, the integration path in figure 3.1 is considered. A decomposition of the integration in the single contributions along Γ_1, Γ_2 and Γ_ϵ yields

$$\oint \frac{f(x)}{g(x) - i\epsilon} \mathrm{d}x = \int_{\Gamma_{\text{Re}}} \frac{f(x)}{g(x) - i\epsilon} \mathrm{d}x + \int_{\Gamma_1 + \Gamma_2} \frac{f(x)}{g(x) - i\epsilon} \mathrm{d}x + \int_{\Gamma_\epsilon} \frac{f(x)}{g(x) - i\epsilon} \mathrm{d}x, \tag{3.58}$$

3. The wave kinetic equation

where the contributions at Re $x \to \pm\infty$ are negligible in the limit $\epsilon \to 0$ and residue theorem states that the integral along the closed path vanishes. Equation (3.58) can be solved for the integral along the real axis (3.57):

$$I_\epsilon = \int_{\Gamma_{\text{Re}}} \frac{f(x)}{g(x) - i\epsilon} \mathrm{d}x = -\int_{\Gamma_1 + \Gamma_2} \frac{f(x)}{g(x) - i\epsilon} \mathrm{d}x - \int_{\Gamma_\epsilon} \frac{f(x)}{g(x) - i\epsilon} \mathrm{d}x. \tag{3.59}$$

In the limit $\epsilon \to 0$, the first integral on the r.h.s. is denoted principle value integral

$$\mathcal{P} \int \frac{f(x)}{g(x)} \mathrm{d}x = -\lim_{\epsilon \to 0} \int_{\Gamma_1 + \Gamma_2} \frac{f(x)}{g(x) - i\epsilon} \mathrm{d}x, \tag{3.60}$$

and the second integral can be computed with the residue theorem. It is only half a circle around the singularity at $x_0 + i\epsilon$ and hence the integral yields half the contribution of the pole of order one at the singularity, i.e.

$$-\lim_{\epsilon \to 0} \int_{\Gamma_\epsilon} \frac{f(x)}{g(x) - i\epsilon} \mathrm{d}x = i\pi \lim_{\epsilon \to 0} \text{Res} \frac{f(x_0 + i\epsilon)}{g(x_0 + i\epsilon)} = i\pi \frac{f(x_0)}{\partial g / \partial x (x_0)}. \tag{3.61}$$

With these results, the integral I_ϵ in the limit $\epsilon \to 0$ reads

$$I_0 = \mathcal{P} \int \frac{f(x)}{g(x)} \mathrm{d}x + i\pi \frac{f(x_0)}{\partial g / \partial x (x_0)}. \tag{3.62}$$

The second contribution may also be written in terms of an integral on a δ-distribution, namely:

$$I_0 = \mathcal{P} \int \frac{f(x)}{g(x)} \mathrm{d}x + i\pi \int f(x)\delta\left(g(x)\right) \mathrm{d}x. \tag{3.63}$$

Given real valued functions f and g, the principal value is purely real, whereas the contribution of the singularity is purely imaginary.

After the foregoing discussion on the generic integral (3.57), we go back to the scattering operator (3.56). Note that the integral involved there recovers the structure of (3.57) and hence is computed analogously to (3.63):

$$\mathcal{S}_\alpha(w_\alpha)(x, N) = 2\pi \int G_\alpha(x, N, N')\left[w_\alpha\left(x, N'\right)\delta\left(H_\alpha(x, N)\right)\right.$$
$$\left. - w_\alpha(x, N)\delta\left(H_\alpha(x, N')\right)\right]\mathrm{d}N'. \tag{3.64}$$

In this scattering operator, the minus sign in front of the second term in squared brackets is put, because the complex conjugate of the denominator is considered. In addition, the principal value parts, yielding real contributions, are dropped in (3.56), where uniquely the imaginary part of the square brackets contributes to the wave kinetic equation.[1]

In the scattering operator (3.64), one singular δ-distribution is integrated away, namely $\delta\left(H_\alpha(x, N')\right)$, whereas the other one, $\delta\left(H_\alpha(x, N)\right)$, is not involved in the integration and hence remains a singular contribution. Therefore, also the l.h.s. of the wave kinetic equation (3.55) should be singular. We note that the Wigner function is indeed singular due to the dispersion relation (3.38). The singularity can be made appear explicitly by splitting the Wigner function into a well-behaved, regular function $\tilde{w}_\alpha(x, N)$ and the singularity in terms of a δ-distribution, i.e.

$$w_\alpha(x, N) = \tilde{w}_\alpha(x, N)\delta(H_\alpha(x, N)). \tag{3.65}$$

Substituted into the Poisson brackets on the l.h.s. of equation (3.55), they become

$$\{H_\alpha(x, N), \tilde{w}_\alpha(x, N)\delta(H_\alpha(x, N))\} = \{H_\alpha(x, N), \tilde{w}_\alpha(x, N)\}\,\delta(H_\alpha(x, N)). \tag{3.66}$$

Here, the simplified Leibnitz rule (C.7b) and the fact that $\{H_\alpha(x, N), H_\alpha(x, N)\} \equiv 0$ due to anti-symmetry of the Poisson brackets (C.7a) is used. Formula (3.66) makes sense in terms of distributions. The derivatives of the δ-distribution involved in the Poisson brackets must be seen as derivatives in a weak sense as reviewed in appendix B. The splitting of Poisson brackets (3.66) together with scattering operator (3.64) inserted into the wave kinetic equation (3.55) yield

$$\delta(H_\alpha(x, N))\left\{H_\alpha(x, N), \tilde{w}_\alpha(x, N)\right\} = \left\{2\pi\int G_\alpha(x, N, N')\delta(H_\alpha(x, N'))\right.$$
$$\times\left[\tilde{w}_\alpha\left(x, N'\right) - \tilde{w}_\alpha(x, N)\right]\mathrm{d}N'$$
$$\left. - 2\gamma_\alpha(x, N)\tilde{w}_\alpha(x, N)\right\}\delta(H_\alpha(x, N)). \tag{3.67}$$

---

[1]The real part (principal part of the integral) contributes to equation (3.34b) for the corrector $W^{(1)}$, which is not solved in practice.

A necessary condition imposed by this equation is

$$\{H_\alpha(x, N), \tilde{w}_\alpha(x, N)\} = 2\pi \int G_\alpha(x, N, N')\delta(H_\alpha(x, N'))$$
$$\times \left[\tilde{w}_\alpha(x, N') - \tilde{w}_\alpha(x, N)\right] \mathrm{d}N'$$
$$- 2\gamma_\alpha(x, N)\tilde{w}_\alpha(x, N) \tag{3.68}$$

for all $(x, N) \in \{(x', N') : H_\alpha(x', N') = 0\}$.

This last equation now describes well-behaved functions $\tilde{w}_\alpha(x, N)$. The dimensionality is reduced to $2m - 1$ because one component of (x, N) is fixed by the condition $H_\alpha(x, N) = 0$. The dispersion relation is intrinsic in (3.65), where the singular contribution of the Wigner function is split up.

In this section, we have seen that a physical interpretation can be given to the mathematically not defined integrals in the scattering operator (3.56). It was recognized that they give rise to a singularity which is consistent with the one due to dispersion relation. A wave kinetic equation for well-behaved functions with the dispersion relation already intrinsic (3.68) was derived in order to point out the meaning of the singular integrals. When the numerical solution is considered, however, a more practical starting point is the dispersion relation (3.38) and wave kinetic equation (3.55) derived in the previous section. The singularity in the integral then is written out explicitly using the scattering operator (3.64).

3.5. Boundary value problem for the steady-state wave kinetic equation

Within the last sections, the dispersion relation and the wave kinetic equation were extensively discussed. In the formulation (3.38) and (3.55) for mode decomposed wave fields, they constitute a set of equations which describes the behavior of the scalar Wigner function for one single wave mode. In order to solve these equations, some boundary condition for this Wigner function is needed.

For the considered physical problem, the wave field on an antenna plane is assumed to be known. For the moment, the geometry of the antenna plane is taken as in figure 3.2 (a). It is represented by the set $A = \{x = (\mathrm{x}, \mathrm{y}) \in \mathbb{R} \times \mathbb{R}^{m-1} : \mathrm{x} = 0\}$. The geometric object representing the antenna

(a) antenna in configuration space:
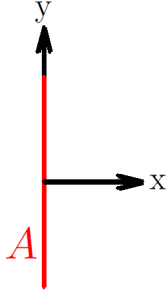
(b) antenna in phase space:
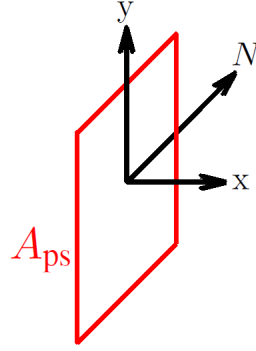
Figure 3.2.: Geometry of the antenna plane (red) (a) in configuration space and (b) extended to phase space. The spatial dimensions $y \in \mathbb{R}^{m-1}$ and the refractive index $N \in \mathbb{R}^m$ are shown as if they were only one dimensional due to illustrative limitations.

plane in phase space is the set $A_{ps} = \{(x, y, N) \in \mathbb{R} \times \mathbb{R}^{m-1} \times \mathbb{R}^m : x = 0\}$. Once the wave field is known on the physical antenna plane A, the Wigner transform (2.61) allows to compute the scalar Wigner functions $\tilde{w}_\alpha(x = 0, y, N_y)$ of the initial field with $N_y \in \mathbb{R}^{m-1}$ being the component of the refractive index N corresponding to the coordinates y. At last, the dispersion relation (3.65) gives the Wigner function $w_\alpha(x, N)|_{A_{ps}}$.

As a summary, equations (3.38) and (3.55) together with this boundary condition pose a boundary value problem for the Wigner function $w_\alpha(x, N)$:

$$H_\alpha(x, N)w_\alpha(x, N) = 0, \tag{3.69a}$$

$$\{H_\alpha(x, N), w_\alpha(x, N)\} = \mathcal{S}_\alpha(w_\alpha)(x, N) - 2\gamma_\alpha(x, N)w_\alpha(x, N), \tag{3.69b}$$

$$w_\alpha(x, N)|_{A_{ps}} = \text{known boundary value.} \tag{3.69c}$$

The absorption coefficient is given in (3.46) and the scattering operator can be found in (3.64).

The simplifying geometry presented in this section is not appropriate for applications in tokamaks. Therefore, it is generalized to more realistic situations in section 7.2. However, this generalization consists basically in a rotation of coordinate axis and therefore does not contain any interesting physics.

3.6. Reconstructing physical observables

In the last section, it was shown how boundary conditions for the Wigner function are formulated and, hence, how one moves from the physically posed boundary conditions in configuration space to phase space. To complete a framework for the phase space description of wave beams, in the end, also the way backwards needs to be done: Once the Wigner function in phase space is known, it must be reduced to meaningful physical observables.

It is postulated here that such physical observables are computed as integrals of the form

$$\langle A \rangle_\Omega = \left(\frac{\kappa}{2\pi} \right)^m \int_\Omega A(x, N) w(x, N) \mathrm{d}x \mathrm{d}N. \tag{3.70}$$

The integration area is $\Omega = \mathcal{W} \times \mathcal{V}$ where x and N run on $\mathcal{W}$ and $\mathcal{V}$, respectively. An integral of the form (3.70) provides the value of $A(x, N)$ (called observable in this thesis) weighted with the Wigner function w on the area Ω. Here, $w(x, N)$ is the scalar Wigner function of a specific pre-selected wave mode. Integrals (2.62) averaged over a volume are special cases of (3.70), obtained by the special choice of the integration area $\mathcal{V} = \mathbb{R}^m$ or $\mathcal{W} = \mathbb{R}^m$ for (2.62a) or (2.62b), respectively. If, in addition, the observable $A(x, N)$ is slowly varying, the interpretation of the Wigner function as an energy density is appropriate. Instead, interference effects might be missed if the observation area is chosen small in all direction, this is $\kappa \Delta x \lesssim 1$ and $\kappa \Delta N \lesssim 1$ for the typical edge lengths Δx and ΔN of $\mathcal{W}$ and $\mathcal{V}$, respectively. This was pointed out in example 2.4.2.

In the following some observables are considered and their physical meaning is shown.

- The simplest observable is $A(x, N) \equiv 1$. In this case, integral (3.70) is

$$\langle 1 \rangle_{\mathcal{W} \times \mathcal{V}} = \left(\frac{\kappa}{2\pi} \right)^m \int_{\mathcal{W} \times \mathcal{V}} w(x, N) \mathrm{d}x \mathrm{d}N \tag{3.71}$$

  This is just the phase space energy density summed up over the phase space volume $\mathcal{W} \times \mathcal{V}$. Therefore, $\langle 1 \rangle_{\mathcal{W} \times \mathcal{V}}$ yields the energy inside this volume. We consider the fixed point $\bar{x}$, and the area

$$\mathcal{W} \subseteq \{ x \in \mathbb{R}^m : |x - \bar{x}| \leq d \}, \tag{3.72a}$$

$$\mathcal{V} = \mathbb{R}^m, \tag{3.72b}$$

with $d \ll L_w$, where L_w is the variational length of the Wigner function,

$$\left| \frac{w(x, N)}{L_w} \right| \approx |\nabla_x w(x, N)| . \tag{3.73}$$

Then, integral (3.71) is a good approximation for

$$\langle 1 \rangle_{\mathcal{W} \times \mathcal{V}} \approx \left(\frac{\kappa}{2\pi} \right)^m |\mathcal{W}| \int_{\mathbb{R}^m} w(\bar{x}, N) \mathrm{d}N. \tag{3.74}$$

Here

$$|\mathcal{W}| = \int_{\mathcal{W}} \mathrm{d}x \tag{3.75}$$

is the volume of $\mathcal{W}$ and it is assumed that $w(x, N)$ does not change significantly when x is moved around inside the area $\mathcal{W}$. This is true by definition of the variational length L_w (3.73) for the Wigner function and the area $\mathcal{W}$ (3.72a). In (3.74), the integral (2.62a) is recovered. This yields the norm of the wave field amplitude squared which is, in case we are dealing with an electric field, proportional to the electric field energy density and hence a physically meaningful observable. Therefore, we call the integral (3.74) built upon the observable 1 the normalized energy density

$$\mathcal{E}(x) := \left(\frac{\kappa}{2\pi} \right)^m \int_{\mathbb{R}^m} w(x, N) \mathrm{d}N. \tag{3.76}$$

Here, the adjective "normalized" recalls the fact that no physical units are involved.

- Another interesting point is the construction of the energy flow. To this aim, the wave kinetic equation (3.69b) is integrated on N. Under this integration, the scattering operator (3.56) vanishes, as stated before. The result yields

$$\int \{H, w\} (\bar{x}, N) \mathrm{d}N = -2 \int \gamma(\bar{x}, N) w(\bar{x}, N) \mathrm{d}N. \tag{3.77}$$

For the derivatives of the Poisson brackets as defined in (C.4), the product rule is applied:

$$\begin{aligned} \{H, w\} (x, N) &= \partial_N H(x, N) \partial_x w(x, N) - \partial_x H(x, N) \partial_N w(x, N) \\ &= \partial_x \left(\partial_N H(x, N) w(x, N) \right) - \partial_N \left(\partial_x H(x, N) w(x, N) \right). \end{aligned} \tag{3.78}$$

Here, the second derivatives of H cancel out. This result is substituted into integral (3.77) and the second term does not contribute due to the fact that $w(x, N)$ is assumed to vanish at the boundaries $N \to \pm\infty$. The remaining parts are

$$\partial_x \int \partial_N H w \mathrm{d}N = -2 \int \gamma w \mathrm{d}N. \tag{3.79}$$

Defining the normalized energy flux $F(x)$ and the absorption $\gamma(x)$

$$F(x) := \left(\frac{\kappa}{2\pi}\right)^m \int \partial_N H(x, N) w(x, N) \mathrm{d}N, \tag{3.80}$$

$$\gamma(x) := 2 \left(\frac{\kappa}{2\pi}\right)^m \frac{\int \gamma(x, N) w(x, N) \mathrm{d}N}{\mathcal{E}(x)}, \tag{3.81}$$

equation (3.79) has the shape of a continuity equation

$$\nabla_x \cdot F(x) + \gamma(x)\mathcal{E}(x) = 0. \tag{3.82}$$

For absorption turned off, $\gamma(x) \equiv 0$, the energy flux is conserved. Instead, if absorption is turned on, it constitutes either an energy drain when $\gamma(x) > 0$ or an energy source when $\gamma(x) < 0$. Upon taking as observables the group velocity of the wave field, i.e. $A(x, N) \equiv \partial_N H(x, N)$ and the absorption coefficient $A(x, N) \equiv 2\gamma(x, N)$, an approximation for the flux $F(x)$ and the absorption $\gamma(x)$ at some point x can be given. As integration area for integral (3.70), still (3.72) is used.

In this section it was seen that physically meaningful quantities are computed in terms of integral (3.70). In particular, the absorbed power will be interesting for heating in tokamaks when applications are considered.

Still, a numerical scheme to solve the wave kinetic equation needs to be presented. The next chapter is dedicated to this issue. As it was seen here, the Wigner function is not needed pointwise, but always integrated over some phase space area. A numerical scheme which is especially powerful for the computation of such integrals should be used.

4

Numerics

In the theory chapter 3, the Wigner function for a mode-decomposed wave field is described by the dispersion relation (3.38) and the wave kinetic equation (3.53). It was noted in section 3.4 that the dispersion relation restricts the Wigner function to the class of functions singularly supported on the dispersion surface whereas the evolution equation has the form of a steady state kinetic equation. Considering the physical problem of microwave beam propagation with dimensionality $m = 3$, the wave kinetic equation is a six-dimensional partial differential equation to be solved for a singular solution. Furthermore, it involves the integral scattering operator (3.56) which describes the effect of fluctuations. The boundary condition posed in section 3.5 belongs to the problem.

We note that a numerical solver for such boundary value problems based on a standard discretization technique will not work in practice. In order to apply such a solver, first one should remove the singularity. This in principle is possible as it was presented in section 3.4. Also the dimensionality then would be reduced to $2m-1 = 5$. Anyway, this is a quite high dimensionality;
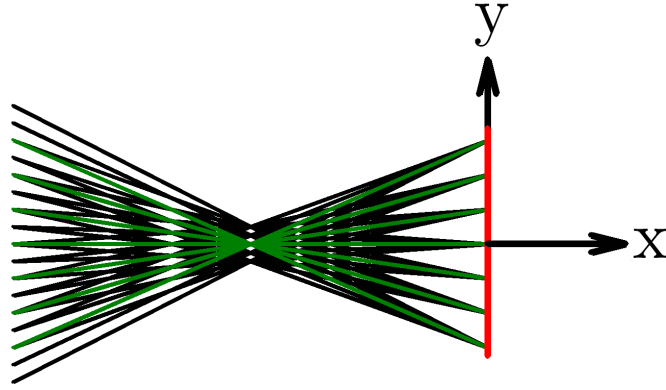
Figure 4.1.: Antenna plane in configuration space with launched rays. Green rays are the geo-
metrical optics rays, the black ones are the configuration-space projections of the
Hamiltonian orbits required for the numerical schemes for the wave kinetic equation.
The initial conditions are such that a focal point is present.

furthermore a global parametrization of the dispersion variety would be required in such reduction
approach. Together with the integral operator involved, it would make the partial differential
equation solver at least numerically expensive. Therefore, in this chapter, numerical schemes are
presented which are more powerful for the purpose of this work. They are especially good when
physical observables are computed as in (3.70).

In the framework of this thesis, two approaches have been developed. The one presented in
section 4.1 solves the wave kinetic equation for the Wigner function. It turns out that, even if
in principle this approach could be extended to the case when fluctuations are present, it is not
particularly appropriate. However, it can be considered a basis for section 4.2, where a scheme
which is also able to cope with fluctuations in a natural way, is presented. The procedure there
is to solve slightly modified equations and to use the result of those to compute the Wigner
function. Both methods are based on a Monte-Carlo scheme and in section 4.3, an estimate for
the statistical uncertainty of the result is given.

Both numerical schemes require tracing Hamiltonian orbits in phase space, introduced in
appendix C. This amounts in solving exactly the same equations as in the geometrical optics ray
tracing method, cf. section 2.3, namely Hamilton's equations of motion (C.1). For this reason, the
expression "ray tracing" is copied from geometrical optics, even if phase space orbits are meant
instead of rays, with abuse of the vocabulary defined in appendix C. However, the reader should
be warned of an important difference: The geometrical optics method allows only to launch

one ray from each point on the physical antenna plane in the projection to configuration space. Instead, in general, there is no such restriction for the phase space description solved in this chapter. It will be seen in the following sections that both numerical schemes, indeed, will use a distribution of initial parameters spread over the antenna plane in phase space, i.e. for a given point x in configuration space various initial values for the refractive index N are considered. A sketch of ray trajectories with initial parameters as in the geometrical optics approach and with initial parameters as suggested by the numerical schemes solving the wave kinetic equation is shown in figure 4.1, pointing out the difference.

Given the fact that in this chapter only one mode α for vector valued wave fields is considered, the mode label is no longer needed and dropped. All functions which are discussed belong to this specific, preselected mode.

4.1. Direct approach

This section is dedicated to a first numerical scheme to solve the wave kinetic equation without scattering by fluctuations. This is referred to as direct approach, considered as a basis for the next section, where fluctuations are introduced.

For fluctuations turned off, the wave kinetic equation (3.55) reads

$$\{H(x, N), w(x, N)\} = -2\gamma(x, N)w(x, N), \tag{4.1}$$

where, again, the index α labeling the mode is dropped. The dispersion relation (3.38) and the boundary condition posed in section 3.5 are additional requirements the solution must fulfil.

It is reviewed in appendix C that the evolution of the Wigner function along Hamiltonian orbits $(x(\tau), N(\tau))$ is given by the Poisson brackets, i.e.

$$\frac{\mathrm{d}w\left(x(\tau), N(\tau)\right)}{\mathrm{d}\tau} = \{H, w\}\left(x(\tau), N(\tau)\right). \tag{4.2}$$

They are expressed in terms of equation (4.1). This yields the ordinary differential equation

$$\frac{\mathrm{d}w\left(x(\tau), N(\tau)\right)}{\mathrm{d}\tau} = -2\gamma\left(x(\tau), N(\tau)\right)w\left(x(\tau), N(\tau)\right). \tag{4.3}$$

4. Numerics

In appendix C, Liouville's theorem is discussed. It states that Hamiltonian orbits started from different points in phase space do not cross. Let $(0, y_0, N_0)$ be a point on the antenna plane A_{ps} extended in the phase space, and let $(x(\tau, y_0, N_0), N(\tau, y_0, N_0))$ be the solution of Hamilton's equation (C.1) with the Hamiltonian $H(x, N)$ relevant for the considered mode. Since Hamiltonian orbits do not cross, we can regard the function $(\tau, y_0, N_0) \mapsto (x(\tau, y_0, N_0), N(\tau, y_0, N_0))$ as a coordinate transformation in the full phase space.

Given the evolution equation (4.3) along Hamiltonian orbits, the natural choice of coordinates is (τ, y_0, N_0). The equation is integrated and the result yields

$$w(\tau, y_0, N_0) = \exp\left\{-2\int_0^\tau \gamma(\tau', y_0, N_0)\mathrm{d}\tau'\right\} w(\tau = 0, y_0, N_0). \tag{4.4}$$

We suppose that the rays are launched on the phase-space antenna plane A_{ps}. This means $(\tau = 0, y_0, N_0)$ maps to a point (x, N) on the phase space antenna plane. Therefore, $w(\tau = 0, y_0, N_0)$ is known from the boundary condition. Then formula (4.4) provides the Wigner function at any given point in phase space (τ, y_0, N_0). It is worth noting that solution (4.4) automatically satisfies the dispersion relation (3.65), as, by construction (cf. section 3.5) $w(\tau = 0)$ does, and the Hamiltonian is conserved along the orbit which is solution to Hamilton's equations of motion.

The physical observables are computed in terms of the integral (3.70). Given the solution of the Wigner function parametrized with (τ, y_0, N_0) as in (4.4), for the integration it is more appropriate to change to the coordinates (τ, y_0, N_0):

$$\int_\Omega A(x, N)w(x, N)\mathrm{d}x\mathrm{d}N = \int_{\Omega'} A(\tau, y_0, N_0)w(\tau, y_0, N_0)\,|J(\tau, y_0, N_0)|\,\mathrm{d}\tau\mathrm{d}y_0\mathrm{d}N_0. \tag{4.5}$$

Here, the integration area Ω' for (τ, y_0, N_0) is meant to cover the corresponding area Ω for (x, N), i.e.

$$\Omega' := \{(\tau, y_0, N_0) : (x(\tau, y_0, N_0), N(\tau, y_0, N_0)) \in \Omega\}. \tag{4.6}$$

In addition, the Jacobian of the coordinate transformation is defined by

$$|J(\tau, y_0, N_0)| := \left|\frac{\partial(x, N)}{\partial(\tau, y_0, N_0)}\right|. \tag{4.7}$$

The next important point for the computation of the integral is to find an expression for the Jacobian along the orbits. Therefore, as an abbreviation for the two sets of coordinates

$$u := (x, N) \in \mathbb{R}^{2m}, \tag{4.8a}$$

$$v := (\tau, \mathrm{y}_0, N_0) \in \mathbb{R}^{2m} \tag{4.8b}$$

is introduced. The Jacobian matrix in this notation is

$$J_{ij} = \frac{\partial u_i}{\partial v_j}, \tag{4.9}$$

where $i, j = 1, \ldots, m$ are the matrix indices. The evolution equation of the Jacobian matrix components J_{ij} reads

$$\frac{\mathrm{d}}{\mathrm{d}\tau} J_{ij} = \frac{\partial}{\partial \tau} \frac{\partial u_i}{\partial v_j} = \frac{\partial}{\partial v_j} \frac{\partial u_i}{\partial \tau}. \tag{4.10}$$

We note that the evolution of the coordinates u is obtained from Hamilton's equations of motion (C.1). They can be cast into the form

$$\frac{\mathrm{d}u_i}{\mathrm{d}\tau} = M_{ij} \frac{\partial H}{\partial u_j}. \tag{4.11}$$

with the matrix

$$M_{ij} = \begin{pmatrix} 0 & -\mathbb{I}_m \\ \mathbb{I}_m & 0 \end{pmatrix}, \tag{4.12}$$

containing the m-dimensional identity matrix denoted by $\mathbb{I}_m$. Substituting the time derivatives (4.11) into (4.10) yields

$$\frac{\mathrm{d}}{\mathrm{d}\tau} J_{ij} = \frac{\partial}{\partial v_j} M_{ik} \frac{\partial H}{\partial u_k}. \tag{4.13}$$

As M is a constant matrix, it can be put in front of the partial differential operator. Moreover, the derivative with respect to v_j using chain rule is replaced with derivatives with respect to u_k.

4. Numerics

Then, the evolution of the Jacobian matrix along a Hamiltonian orbit (4.13) is given by

$$\frac{\mathrm{d}}{\mathrm{d}\tau} J_{ij} = M_{ik} \frac{\partial^2 H}{\partial u_l \partial u_k} \frac{\partial u_l}{\partial v_j} = M_{ik} \frac{\partial^2 H}{\partial u_l \partial u_k} J_{lj}. \tag{4.14}$$

Equation (4.14) now is an ordinary differential (matrix) equation with the solution

$$J(\tau, \mathrm{y}_0, N_0) = \exp\left\{ \int_0^\tau M\mathcal{D}^2 H \mathrm{d}\tau' \right\} J_0(\mathrm{y}_0, N_0), \tag{4.15}$$

where $\mathcal{D}^2 H$ is the Hessian matrix of H. Furthermore, the Jacobian matrix at $\tau = 0$ is denoted with J_0. For the integral (4.5), only the determinant of the Jacobian matrix is needed. The structure of matrix equation (4.15) is

$$A = e^B C \tag{4.16}$$

with A, B, C matrices. The equation relating the correspondend determinants is

$$|A| = e^{\mathrm{Tr}\, B} |C|. \tag{4.17}$$

Upon accounting for this identity, the evolution of the Jacobian deduced from (4.15) reads

$$|J(\tau, \mathrm{y}_0, N_0)| = \exp\left\{ \int_0^\tau \mathrm{Tr}\left(M\mathcal{D}^2 H \right) \mathrm{d}\tau' \right\} |J_0(\mathrm{y}_0, N_0)|. \tag{4.18}$$

Given the definition of M (4.12), it can directly be verified that the integrand inside the exponential on the r.h.s. vanishes identically. Therefore, the Jacobian determinant remains constant along the Hamiltonian orbits and in the integral (4.5), it is replaced with the initial value:

$$I = \int_\Omega A(x, N) w(x, N) \mathrm{d}x \mathrm{d}N$$
$$= \int_{\Omega'} A(\tau, \mathrm{y}_0, N_0) w(\tau, \mathrm{y}_0, N_0) |J_0(\mathrm{y}_0, N_0)| \, \mathrm{d}\tau \mathrm{d}\mathrm{y}_0 \mathrm{d}N_0. \tag{4.19}$$

The integration area Ω' is defined in (4.6). The Jacobian at time $\tau = 0$ is easy to compute, assuming that the antenna is in free space where the ray trajectories are known analytically and hence the relation between the sets of coordinates u and v is known.

For the computation of integrals as in (4.19), a mixed approach is employed. The Wigner function $w(\tau, y_0, N_0)$ is known along Hamiltonian orbits. This means that, for fixed values of y_0 and N_0, it is known continuously for all τ from the ray tracing technique, which allows us to compute the τ-integration directly as integrals along Hamiltonian orbits. Instead, for the integration on initial conditions (y_0, N_0), a Monte-Carlo strategy is employed. The Monte-Carlo approximation for integrals

$$\int_{\mathcal{A}} g(z) \mathrm{d}z \approx \frac{1}{n_0} \sum_{\substack{i=1 \\ z_i \in \mathcal{A}}}^{n_0} \frac{g(z_i)}{p(z_i)} \tag{4.20}$$

can be found in several textbooks (e.g. in [24]). Here, n_0 samples of values $z_1, \ldots, z_{n_0}$ are generated following $p(z)$ as a probability distribution and z is any set of coordinates. As it will be seen in section 4.3, the approximation is good if n_0 is large. For the integral I (4.19), the Monte-Carlo sum yields

$$I \approx \frac{1}{n_0} \int \sum_{\substack{i=1 \\ (y_i, N_i) \in \Omega'_{y,N}(\tau)}}^{n_0} \frac{A(\tau, y_i, N_i) w(\tau, y_i, N_i) \left| J_0(y_i, N_i) \right|}{p(y_i, N_i)} \mathrm{d}\tau. \tag{4.21}$$

Here, n_0 Hamiltonian orbits labeled with $i = 1, \ldots, n_0$ are launched on the antenna plane with initial phase space coordinates $(x = 0, y_i, N_i)$ following for the initial parameters the probability distribution $p(y, N)$ and $\Omega'_{y,N}(\tau)$ labels a projection of the area Ω' on the y and N-coordinates, i.e.

$$\Omega'_{y,N}(\tau) := \left\{ (y, N) \in \mathbb{R}^{2m-1} : (\tau, y, N) \in \Omega \right\}. \tag{4.22}$$

The natural choice of the probability distribution $p(y, N)$ is given by the initial Wigner distribution $w(\tau = 0, y, N)$. With this choice orbits are initialized on the intersection of the extended antenna plane A_{ps} and the dispersion variety of the considered mode.

In this section a scheme is presented which is appropriate to compute directly physical observables in terms of the integral (3.70). This scheme works for the case when fluctuations are not present. However, the solution given here is based on the relation between the coordinates (τ, y_0, N_0) and (x, N). When fluctuations are turned on, it will be seen in the next section that the Hamiltonian trajectories should be modified to take this effect into account. Then, the coordinate

transformation is no longer naturally present via the ray tracing technique. This obstacle, in principle, could be overcome just by tracing additional orbits to establish the coordinate transformation. However, this would make the implementation ineffective and complicated.

4.2. Indirect approach

In this section, a different numerical scheme is presented which is not based on an orbit-following coordinate transformation and hence can be generalized in a more straight forward way to the case when fluctuations are present. Like the one in the previous section, it is based on a ray tracing strategy. The separation of integration variables into one which can be computed along the rays and the others to compute in terms of a Monte-Carlo estimator is achieved not solving the boundary value problem posed in (3.69), but a slightly modified problem: The initial value problem with evolution equation

$$\frac{\partial f}{\partial \tau}(\tau, x, N) + \{H, f\}(\tau, x, N) = \mathcal{S}(f)(\tau, x, N) - 2\gamma(x, N)f(\tau, x, N) \tag{4.23}$$

and known initial condition $f(\tau = 0, x, N)$ is considered. This evolution equation is basically the same as the one valid for the boundary value problem, but it is extended with a τ-dependence by hand. The solution $f \equiv f(\tau, x, N)$ for the moment is a generic time-dependent function which does not have any physical meaning.

The scattering operator can be written in the form

$$\mathcal{S}(f)(\tau, x, N) = \int \sigma(x, N', N)f(\tau, x, N')\mathrm{d}N' - \Sigma(x, N)f(\tau, x, N), \tag{4.24}$$

where

$$\sigma(x, N, N') = 2\pi G(x, N, N')\delta\left(H(x, N')\right), \tag{4.25a}$$

$$\Sigma(x, N) = \int \sigma(x, N, N')\mathrm{d}N'. \tag{4.25b}$$

In order to prove this form of the scattering operator, one needs the identity

$$G(x, N, N') = G(x, N', N), \tag{4.26}$$

which states that the kernel $G(x, N, N')$ is symmetric under exchange of N and N'. In turn, this symmetry property follows from the definition of $G_{\alpha\beta}(x, N, N')$ (3.50), together with the property

$$G_{iabj}(x, N' - N) = G_{bjia}(x, N - N').\qquad(4.27)$$

This can directly be verified upon accounting for the definition (3.28).

For the time-dependent problem (4.23), a Monte-Carlo scheme is known [24]. The main steps in this section are hence first to find a solution $f(\tau, x, N)$ using this scheme, next to see how, out of this result, a solution for $w(x, N)$ can be constructed and how the boundary condition for w and the initial condition for f are related. And finally, as usual, the Wigner function must be reduced to observables by means of (3.70).

Let us start discussing the relationship between solutions of (4.23) and the orbits of a specific stochastic process for the case $\gamma = 0$, i.e. when the medium is lossless. This generalizes the relationship between Poisson brackets and Hamiltonian orbits addressed in appendix C. The effect of absorption is then introduced by a suitable weight along each realization of the stochastic process, as discussed in reference [24].

The relevant stochastic process $(\mathcal{X}(\tau), \mathcal{N}(\tau))$ is defined as follows. First, a Poisson process $\{\tau_k\}$ is generated with mean $\bar{\Sigma} = \sup \Sigma(x, N)$; this defines values $\tau = \tau_k$ for the parameter τ and thus intervals $[\tau_k, \tau_{k+1})$. In each interval $(\mathcal{X}(\tau), \mathcal{N}(\tau))$ is a classical solution of the Hamiltonian equations of motion with initial condition $(\mathcal{X}(\tau_k), \mathcal{N}(\tau_k))$, namely

$$\frac{\mathrm{d}\mathcal{X}}{\mathrm{d}\tau} = \partial_N H(\mathcal{X}, \mathcal{N}),\qquad(4.28a)$$

$$\frac{\mathrm{d}\mathcal{N}}{\mathrm{d}\tau} = -\partial_x H(\mathcal{X}, \mathcal{N}).\qquad(4.28b)$$

At each boundary point $\tau = \tau_k$ a jump may be applied. The jump involves the refractive index variable $\mathcal{N}$ and not the position $\mathcal{X}$, as the scattering operator $\mathcal{S}$ describes wave-vector scattering only. The probability of a jump event at the point (x, N) is given by $\Sigma(x, N)/\bar{\Sigma}$. If a jump event occurs at the phase-space location (x, N), the new momentum is drawn from the local distribution of probability $\sigma(x, N, \cdot)/\Sigma(x, N)$. It is possible to prove that the probability distribution of orbits

$p(\tau, x, N)$ of such process satisfies the Fokker-Planck equation ([24], section 2.5.2).

$$\frac{\partial p}{\partial \tau}(\tau, x, N) + \{H, p\}(\tau, x, N) = \mathcal{S}(p)(\tau, x, N), \qquad (4.29)$$

which is just equation (4.23) with $\gamma = 0$. Since $p(\tau, x, N)$ is a probability distribution we must have

$$\int p(\tau, x, N)\mathrm{d}x\mathrm{d}N = 1, \qquad (4.30)$$

and it is enough to fix the normalization of $p(\tau = 0, x, N)$ as (4.29) preserves the phase space integral of $p(\tau, x, N)$.

Given $f(\tau = 0, x, N)$, one can set

$$\alpha p(\tau = 0, x, N) = f(\tau = 0, x, N), \text{ with } \alpha = \int f(\tau = 0, x, N)\mathrm{d}x\mathrm{d}N, \qquad (4.31)$$

and the solution of equation (4.29) with the initial condition $p(\tau = 0, x, N)$ is related to the solution $f(\tau, x, N)$ of (4.23) with $\gamma = 0$ and the initial condition $f(\tau = 0, x, N)$ via (4.31). This relation is used to evaluate expectation values of physical observables over a phase-space domain Ω, namely

$$\int_\Omega A(x, N)f(\tau, x, N)\mathrm{d}x\mathrm{d}N = \alpha \int_\Omega A(x, N)p(\tau, x, N)\mathrm{d}x\mathrm{d}N, \text{ with } \gamma = 0, \qquad (4.32)$$

where the probability distribution $p(\tau, x, N)$ can be sampled by tracing the orbits of the stochastic process $(\mathcal{X}(\tau), \mathcal{N}(\tau))$. More specifically, an estimator for such expectation values is built by sampling the initial distribution $p(\tau = 0, x, N)$ with n_0 initial parameters $\{(x_i, N_i)\}_{i=1}^{n_0}$ in phase space and then tracing the orbits of the above-described stochastic process; the orbit originating from (x_i, N_i) is denoted $(\mathcal{X}_i(\tau), \mathcal{N}_i(\tau))$. By construction, for every $\tau \geq 0$, the set of points $\{\mathcal{X}_i(\tau), \mathcal{N}_i(\tau)\}_{i=1}^{n_0}$ is a sample drawn from the distribution $p(\tau, x, N)$, hence

$$\int_\Omega A(x, N)f(\tau, x, N)\mathrm{d}x\mathrm{d}N \approx \frac{\alpha}{n_0} \sum_{(\mathcal{X}_i(\tau), \mathcal{N}_i(\tau)) \in \Omega} A(\mathcal{X}_i(\tau), \mathcal{N}_i(\tau)), \text{ with } \gamma = 0, \qquad (4.33)$$

where the sum extends to all orbits such that $(\mathcal{X}_i(\tau), \mathcal{N}_i(\tau)) \in \Omega$ at the considered τ.

In presence of absorption ($\gamma \neq 0$), each orbit is weighted by the "amount of losses" along the trajectory, namely

$$\mathcal{W}_i(\tau) = e^{-2 \int_0^\tau \gamma(\mathcal{X}_i(\tau'), \mathcal{N}_i(\tau')) \mathrm{d}\tau'}. \tag{4.34}$$

The general form of (4.32) accounting for both scattering and dissipation is

$$\int_\Omega A(x, N) f(\tau, x, N) \mathrm{d}x \mathrm{d}N \approx \frac{\alpha}{n_0} \sum_{(\mathcal{X}_i(\tau), \mathcal{N}_i(\tau)) \in \Omega} A(\mathcal{X}_i(\tau), \mathcal{N}_i(\tau)) \mathcal{W}_i(\tau). \tag{4.35}$$

A proof of the general form can be found in [24], section 3.2, theorem 2.5.4.[1]

Next, a solution for $w(x, N)$ based on function f which solves evolution equation (4.23) should be constructed. Therefore, this last equation is formulated for the Fourier transform of f in the variable τ, i.e.

$$\hat{f}(u, x, N) = \int e^{-iu\tau} f(\tau, x, N) \mathrm{d}\tau. \tag{4.36}$$

Here the variable u is used for the dual of τ; it may be understood as a frequency associated to τ, but it should not be confused with the physical frequency ω. Derivatives with respect to τ are replaced by $-iu$ in the Fourier transformed equation with the result that

$$-iu\hat{f}(u, x, N) + \left\{ H, \hat{f} \right\}(u, x, N) = \mathcal{S}(\hat{f})(u, x, N) - 2\gamma(x, N)\hat{f}(u, x, N). \tag{4.37}$$

Here, the Poisson bracket, the scattering operator and absorption are not affected by the Fourier transformation because they are independent of τ. Now it is obvious that this equation, in case $u = 0$, is just the same as the steady state evolution equation (3.69b) for $w(x, N)$. Therefore, a solution for the Wigner function w can be found in the form

$$w(x, N) = \hat{f}(u = 0, x, N) = \int f(\tau, x, N) \mathrm{d}\tau, \tag{4.38}$$

given the fact that $f(\tau, x, N)$ fulfils its evolution equation (4.23).

---

[1]Note that in this textbook only the proof for the special case $\Omega = \mathbb{R}^{2m}$ with a differentiable observable $A \in C^1$ is presented. The theorem, however, is applied to the more general case $\Omega \subseteq \mathbb{R}^{2m}$ in this thesis.

4. Numerics

If $f(\tau, x, N)$ is singularly supported on a dispersion surface, i.e. on the surface $H(x, N) = 0$, by construction also w is so. Instead, it is not straight forward to find initial conditions for f which reproduce desired boundary conditions for w. As a simplification, the functions f under investigation are restricted to a certain class: Let us consider only initial conditions which are singularly supported on the antenna plane defined in 3.5, i.e.

$$f(\tau = 0, \mathrm{x}_0, \mathrm{y}_0, N_0) = \delta(\mathrm{x}_0) f_0(\mathrm{y}_0, N_0). \tag{4.39}$$

This is an arbitrary assumption and will be justified by the fact that even under this constraint, any boundary condtition for w can be reproduced. In other word, no generality is lost by imposing this condition on the auxiliary function f.

We assume that near the antenna plane there is a non-fluctuating and dissipation free medium, so neither scattering events nor absorption take place and the Hamiltonian orbits starting at $x_0 = (\mathrm{x}_0, \mathrm{y}_0)$ around the antenna are given by Hamilton's equation of motion (C.1a), namely in integrated form

$$\mathrm{x} = \mathrm{x}_0 + \Delta\mathrm{x}(\tau), \tag{4.40a}$$

$$\mathrm{y} = \mathrm{y}_0 + \Delta\mathrm{x}(\tau), \tag{4.40b}$$

where the covered distance is

$$\Delta\mathrm{x}(\tau) := \int_0^\tau \frac{\partial H_a}{\partial N_\mathrm{x}} d\tau', \tag{4.41a}$$

$$\Delta\mathrm{y}(\tau) := \int_0^\tau \frac{\partial H_a}{\partial N_\mathrm{y}} d\tau' \tag{4.41b}$$

with the Hamiltonian H_a around the antenna plane. Then, around the antenna plane the solution of (4.23) is

$$f(\tau, x, N) = f(\tau = 0, \mathrm{x}_0, \mathrm{y}_0, N_0) = \delta\left(\mathrm{x} - \Delta\mathrm{x}(\tau)\right) f_0(\mathrm{y} - \Delta\mathrm{y}(\tau), N) \tag{4.42}$$

and the corresponding Wigner function obtained from (4.38) and restricted to the antenna plane reads

$$w(\mathrm{x} = 0, \mathrm{y}, N) = \int \delta\left(-\Delta\mathrm{x}(\tau)\right) f_0(\mathrm{y} - \Delta\mathrm{y}(\tau), N)\mathrm{d}\tau = \frac{f_0(\mathrm{y}, N)}{|v_\mathrm{x}|}. \qquad (4.43)$$

Here, the integral is easily performed thanks to the δ-distribution involved. Solved for f_0 and taking into account the definitions (4.41), this last equation reads

$$f_0(\mathrm{y}, N) = \left|\frac{\partial H_a(\mathrm{x} = 0, \mathrm{y}, N)}{\partial N_\mathrm{x}}\right| w(\mathrm{x} = 0, \mathrm{y}, N) \qquad (4.44)$$

and provides the initial condition for f given the boundary condition for w. Although there is this restriction to a special class of functions f, still any kind of boundary conditions for w can be reproduced. This shows that, by using (4.23) with initial conditions (4.39) and (4.44), the boundary value problem (3.69) can be solved with no loss of generality except placing the antenna in a region where no scattering and absorption take place.

As a last point, the reduction of the Wigner function to physical observables (3.70) must be performed. For this purpose, in the integral, the Wigner function is written in terms of f:

$$\int_\Omega A(x, N)w(x, N)\mathrm{d}x\mathrm{d}N = \int \int_\Omega A(x, N)f(\tau, x, N)\mathrm{d}x\mathrm{d}N\mathrm{d}\tau, \qquad (4.45)$$

where the phase-space and τ-integration have been exchanged and equation (4.38) is used. The inner integral over phase space is replaced by the Monte-Carlo estimator (4.35) with the result that

$$\int_\Omega A(x, N)w(x, N)\mathrm{d}x\mathrm{d}N \approx \int \left[\frac{\alpha}{n_0} \sum_{(\mathcal{X}_i(\tau), \mathcal{N}_i(\tau)) \in \Omega} A(\mathcal{X}_i(\tau), \mathcal{N}_i(\tau))\mathcal{W}_i(\tau)\right] \mathrm{d}\tau. \qquad (4.46)$$

If $\mathcal{Q}_i$ denotes the i-th orbit of the stochastic process, i.e.

$$\mathcal{Q}_i = \{(\mathcal{X}_i(\tau), \mathcal{N}_i(\tau)) : \tau \geq 0\}, \qquad (4.47)$$

and

$$I_{i,\Omega} = \{\tau : (\mathcal{X}_i(\tau), \mathcal{N}_i(\tau)) \in \Omega\} \qquad (4.48)$$

is the interval in τ for which the point $(\mathcal{X}_i(\tau), \mathcal{N}_i(\tau))$ on ray i stays within Ω, the sum and the integral can be exchanged as follows:

$$\int \sum_{(\mathcal{X}_i(\tau), \mathcal{N}_i(\tau)) \in \Omega} A(\mathcal{X}_i(\tau), \mathcal{N}_i(\tau)) \mathcal{W}_i(\tau) \mathrm{d}\tau = \sum_{\mathcal{Q}_i \cap \Omega \neq \emptyset} \int_{I_{i,\Omega}} A(\mathcal{X}_i(\tau), \mathcal{N}_i(\tau)) \mathcal{W}_i(\tau) \mathrm{d}\tau. \quad (4.49)$$

The simplest numerical procedure is chosen for the remaining integral over the τ-interval $I_{i,\Omega}$, namely, a Riemann quadrature based on the τ-stepping points τ_j used in generating a numerical approximation $(\mathcal{X}_{i,j}, \mathcal{N}_{i,j}) \approx (\mathcal{X}_i(\tau_j), \mathcal{N}_i(\tau_j))$. At last, upon accounting for (4.46), (4.49) and the above-mentioned approximation we have

$$\int_\Omega A(x, N) w(x, N) \mathrm{d}x \mathrm{d}N \approx \frac{\alpha}{n_0} \sum_{\substack{\mathcal{Q}_i \cap \Omega \neq \emptyset \\ \tau_j \in I_{i,\Omega}}} A(\mathcal{X}_{i,j}, \mathcal{N}_{i,j}) \mathcal{W}_i(\tau_j) \Delta\tau_j, \quad (4.50)$$

where $\Delta\tau_j = \tau_{j+1} - \tau_j$ is the local step in τ.

The practical implementation of formula (4.50) requires a ray tracing and a binning procedure: Once numerical approximations $(\mathcal{X}_{i,j}, \mathcal{N}_{i,j})$ of the orbits $\mathcal{Q}_i$ are generated by a ray tracing procedure, and the domain Ω, also referred to as bin, is selected, one has to find which orbits cross Ω and what is the crossing interval $I_{i,\Omega}$. The implementation of both ray tracing and binning is described in chapter 5.

The Monte-Carlo estimator (4.50) can be considered the final result of this section, from which the expectation value of physical observables, i.e. the l.h.s., may be deduced, inserting quantities on the r.h.s. known from ray tracing.

4.3. Statistical uncertainty

The numerical approaches presented in the last two sections are partly based on Monte-Carlo estimators which are random variables and hence are subject to a statistical uncertainty. The aim of this section is to provide an estimate of the statistical uncertainty. This will provide a feeling for the reliability of the result. Furthermore, when benchmarks are performed, possible deviations of a solution with respect to the reference solution can be compared to the statistical uncertainty as a consistency check.

The Monte-Carlo estimators (4.21) or (4.50) have the structure of a sum like

$$I = \frac{1}{n_0} \sum_{i=1}^{n_0} I_i.$$

(4.51)

The terms in the sum are obtained from a statistical process and hence the sum is a random variable. Here, I_i/n_0 is the contribution of a single ray i. The empirical variance of the single ray contributions can be introduced as [24]

$$V_I = \frac{1}{n_0 - 1} \sum_{i=1}^{n_0} (I_i - I)^2 .$$

(4.52)

The only input for this expression are the single contributions I_i of the Monte-Carlo sum (4.51). This allows to determine the quantity without big additional efforts. It is shown then that the statistical uncertainty of the Monte-Carlo estimator is given by

$$\sigma_I = \sqrt{\frac{V_I}{n_0}}.$$

(4.53)

The well-known dependence $\sigma_I \propto n_0^{-1/2}$ can be identified here, which results in a slowly decreasing statistical uncertainty when more and more rays are traced.

4.4. Change of Hamiltonian

The numerical schemes presented in this chapter are based on Hamiltonian ray tracing, where according to (3.37a) the eigenvalue of the Weyl symbol $D_0(x, N)$ of the dispersion operator D_0 for the appropriate mode serves as Hamiltonian H. It is clear that, if the Hamiltonian $H(x, N)$ is multiplied by some non-vanishing function $\xi(x, N)$, the orbits in the dispersion variety $\{H(x, N) = 0\}$ remain the same, but the parameter τ along the orbits changes, cf. the Hamilton equations of motion (C.1). There is one natural choice of the Hamiltonian, namely the one obtained from the wave equation directly as explained in section 3.3, which provides correct results. However, Hamilton's equations of motion (C.1) might simplify for a Hamiltonian multiplied by some $\xi(x, N)$, especially when the plasma dispersion tensor for magnetized plasmas (7.22) is involved, leading to complicated eigenvalues which are solutions of a cubic equation, but yielding an easier Hamiltonian (7.34) when the multiplication technique is applied. Here it is

shown how to rescale properly the various terms in Hamilton equations of motion and the wave kinetic equation to obtain correct results with such rescaled Hamiltonians, following [21].

The natural Hamiltonian is denoted $H(x, N)$ and a modified Hamiltonian

$$\tilde{H}(x, N) := \xi(x, N) H(x, N) \tag{4.54}$$

is considered. It is assumed that the evolution of a generic phase-space quantity $A(\tau, x, N)$ along a Hamiltonian orbit is given by

$$\frac{\mathrm{d}A}{\mathrm{d}\tau} = \frac{\partial A}{\partial \tau} + \{H, A\} = \eta(A), \tag{4.55}$$

where $A(x, N)$ is assumed to be singularly supported on dispersion surfaces and $\eta(A)$ is some operator η applied on A. This is the structure of evolution equations present in both numerical schemes, namely (4.2) and (4.3) with $A \equiv w$ and (4.23) with $A \equiv f$. For the case of propagation in fluctuating and weakly dissipative media discussed in chapter 3, the operator η is composed by the effect of fluctuation described by $\mathcal{S}(\cdot)$, cf. (3.56) and the absorption coefficient γ (3.46).

Next, the Poisson bracket involving the modified Hamiltonian $\tilde{H}(x, N)$ is computed. We remind the reader that A is considered singularly supported, requiring a treatment of the Poisson brackets in the weak sense of distributions. As reviewed in appendix B, the integral representation of this distribution is considered: Applied on the test function Φ, it reads

$$\left\{\tilde{H}, A\right\}(\Phi) = \int \Phi(x, N) \left\{\tilde{H}, A\right\}(x, N) \mathrm{d}x \mathrm{d}N \tag{4.56}$$

with the generating function $\left\{\tilde{H}, A\right\}(x, N)$. Writing out the Poisson brackets (C.4) explicitly yields

$$
\begin{aligned}
\int \Phi \left\{\tilde{H}, A\right\} \mathrm{d}x \mathrm{d}N &= \int \Phi \left(\frac{\partial(\xi H)}{\partial n} \frac{\partial A}{\partial x} - x \leftrightarrow N\right) \mathrm{d}x \mathrm{d}N \\
&= \int \Phi \left(\xi \frac{\partial H}{\partial N} \frac{\partial A}{\partial x} + \frac{\partial \xi}{\partial N} H \frac{\partial A}{\partial x} - x \leftrightarrow N\right) \mathrm{d}x \mathrm{d}N.
\end{aligned}
\tag{4.57}
$$

Here, the notation "$x \leftrightarrow N$" stands for a repetition with x and N interchanged in derivatives. The arguments (x, N) have been dropped for simplicity. In the next step, the second term is

integrated by parts over x (N for the interchanged terms), leading to

$$\int \Phi \left\{ \tilde{H}, A \right\} \mathrm{d}x \mathrm{d}N = \int \left(\Phi \xi \frac{\partial H}{\partial N} \frac{\partial A}{\partial x} - \frac{\partial}{\partial x} \left(\Phi \frac{\partial \xi}{\partial N} H \right) A - x \leftrightarrow N \right) \mathrm{d}x \mathrm{d}N$$

$$= \int \left(\Phi \xi \frac{\partial H}{\partial N} \frac{\partial A}{\partial x} - \Phi \frac{\partial \xi}{\partial N} \frac{\partial H}{\partial x} A - x \leftrightarrow N \right) \mathrm{d}x \mathrm{d}N. \qquad (4.58)$$

In the second line of this equation, the product rule has been applied for the second term. Note that contributions which involve the product HA vanish, due to the assumption of singular support of A on the $H \equiv 0$ surface. The surviving terms can be combined as two Poisson brackets, namely

$$\int \Phi \left\{ \tilde{H}, A \right\} \mathrm{d}x \mathrm{d}N = \int \Phi \left(\xi \left\{ H, A \right\} + \left\{ H, \xi \right\} A \right) \mathrm{d}x \mathrm{d}N. \qquad (4.59)$$

So dropping the integral, in the sense of distributions, for the Poisson bracket of the modified Hamiltonian $\tilde{H}$, one finds

$$\left\{ \tilde{H}, A \right\} = \left\{ \xi H, A \right\} = \xi \left\{ H, A \right\} + \left\{ H, \xi \right\} A. \qquad (4.60)$$

Here, the first term on the r.h.s. is the rescaled Poisson bracket involving the natural Hamiltonian and the second term accounts for the evolution of the prefactor ξ. Defining a modified time parameter $\tilde{\tau}$ along the rays such that

$$\frac{\mathrm{d}A}{\mathrm{d}\tilde{\tau}} = \frac{\partial A}{\partial \tilde{\tau}} + \left\{ \tilde{H}, A \right\}, \qquad (4.61\mathrm{a})$$

$$\frac{\partial A}{\partial \tilde{\tau}} = \xi \frac{\partial A}{\partial \tau}, \qquad (4.61\mathrm{b})$$

equation (4.60) reads

$$\frac{\mathrm{d}A}{\mathrm{d}\tilde{\tau}} = \xi \frac{\partial A}{\partial \tau} + \xi \left\{ H, A \right\} + \left\{ H, \xi \right\} A. \qquad (4.62)$$

For the first Poisson bracket the natural evolution equation (4.55) is inserted. The second Poisson bracket is replaced with

$$\left\{ H, \xi \right\} = \frac{\xi}{\xi} \left\{ H, \xi \right\} = \frac{1}{\xi} \left(\left\{ \xi H, \xi \right\} - \left\{ \xi, \xi \right\} H \right) = \frac{1}{\xi} \left\{ \tilde{H}, \xi \right\}. \qquad (4.63)$$

Here, rules (C.7b) and (C.7a) for Poisson brackets have been applied as well as the definition of $\tilde{H}$ (4.54) in the last step. With the modified time parameter (4.61), equation (4.62) reads

$$\frac{\mathrm{d}A}{\mathrm{d}\tilde{\tau}} = \xi\eta(A) + \frac{1}{\xi}\frac{\mathrm{d}\xi}{\mathrm{d}\tilde{\tau}}A. \tag{4.64}$$

This equation shows the additional term $\mathrm{d}\log\xi/\mathrm{d}\tilde{\tau}$ which should be added to the numerical weight (4.34). It is however possible to account for the contribution of $\log\xi$ in a simple way. A different quantity

$$\tilde{A}(x, N) := g^{-1}(x, N)A(x, N) \tag{4.65}$$

which is linear in A is considered. It is easy to show that by properly choosing g, an evolution equation for $\tilde{A}$ without any additional term can be formulated: Substituting (4.65) into (4.64) yields

$$\frac{\mathrm{d}A}{\mathrm{d}\tilde{\tau}} = g\frac{\mathrm{d}\tilde{A}}{\mathrm{d}\tilde{\tau}} + \frac{\mathrm{d}g}{\mathrm{d}\tilde{\tau}}\tilde{A} = \xi\eta(g\tilde{A}) + \frac{g}{\xi}\frac{\mathrm{d}\xi}{\mathrm{d}\tilde{\tau}}\tilde{A}. \tag{4.66}$$

For the choice $g(x, N) \equiv \xi(x, N)$, one has the simpler evolution equation

$$\frac{\mathrm{d}\tilde{A}}{\mathrm{d}\tilde{\tau}} = \eta(\xi\tilde{A}), \tag{4.67}$$

which is in desired form. This equation can be solved with the numerical schemes to determine $\tilde{A}$. Then A is obtained directly from equation (4.65).

Note that in the theory chapter on the wave kinetic equation 3, the Hamiltonian also explicitly appeared in the scattering operator, cf. (3.64), and that the natural Hamiltonian is meant. If for any reason an other Hamiltonian is in use, it must be accounted for this with the aid of the correction factor at this point as well, yielding the fully corrected scattering cross section

$$\sigma_\alpha(x, N, N') := 2\pi G_\alpha(x, N, N')\xi(x, N)\xi(x, N')\delta\left(\tilde{H}_\alpha(x, N')\right). \tag{4.68}$$

Here the factor $\xi(x, N)$ absorbs the necessary rescaling in the evolution equation and the factor $\xi(x, N')$ accounts for the use of the tilded Hamiltonian in Dirac's delta.

5
Implementation

In this chapter, the implementation of the second numerical scheme described in section 4.2 is summarized. First, the implemented equations and the structure of the code are presented. In a later section, more details on the implementation from the computer science point of view are provided. A user guide can be found in appendix E.

Given the fact that the code is based on the wave kinetic equation and that it considers the semiclassical limit, which is related to the WKB approximation, it will be referred to as wave kinetic code or alternatively as WKBeam, standing for **W**ave **K**inetic **Beam** tracing code.

5.1. Physical structure of the code

In this section, the implemented equations are summarized. The structure follows the computational one, i.e. the extension of boundary conditions to phase space first, then the ray tracing technique and at last the reduction to physical observables.

5.1.1. Boundary conditions and initial conditions for the rays

The physical boundary condition for the simulation is the electric field at the antenna plane, the geometry of which is discussed in section 3.5. The use of coordinates $x = (\mathrm{x}, \mathrm{y})$ with the meaning of the direction normal to the antenna plane $\mathrm{x} \in \mathbb{R}$ and the coordinates in the antenna plane $\mathrm{y} \in \mathbb{R}^{m-1}$, where m is the dimensionality of the problem, is helpful and allows us to generalize the antenna plane to the tokamak requirements, cf. section 7.2. As a first step in the code, initial conditions for the rays to be traced are generated. Relevant quantities are reviewed in this section and the implemented probability distribution is formulated.

In the code, for simplicity a Gaussian beam profile on the antenna plane is used. This is realistic enough for later tokamak applications [25]. Furthermore, it allows an analytical computation of the Wigner function on the antenna plane. The calculation is reported in appendix D, with the Wigner function (D.11)

$$w(\mathrm{x} = 0, \mathrm{y}, N) = \frac{2^m \pi^{(m+1)/2}}{\kappa^{(m-1)/2}\sqrt{\det \Phi}} e^{-\kappa \mathrm{y} \cdot \Phi \mathrm{y} - \kappa[(N_{\mathrm{y},0} - N_\mathrm{y}) + S\mathrm{y}] \cdot \Phi^{-1}[(N_{\mathrm{y},0} - N_\mathrm{y}) + S\mathrm{y}]}$$
$$\times \, \delta(N_\mathrm{x} - N_{\mathrm{x},0}) \tag{5.1}$$

as a result. The value $N_{\mathrm{x},0} \equiv N_{\mathrm{x},0}(\mathrm{y}, N_\mathrm{y}))$ is fixed by the dispersion relation as a function of $(\mathrm{y}, N_\mathrm{y})$. The implementation allows us to choose between $m = 2$ or $m = 3$. The input parameters describing the beam profile are in this case the initial beam cross section, described by the matrix Φ and the initial curvature radius of the beam wave front, information which is contained in the matrix S, cf., again, appendix D.

As discussed in section 4.2, the probability distribution for initial parameters (x_i, N_i) for the ray tracing is $p(\tau = 0, x, N)$. Upon accounting for the relation to the function f (4.31), the restriction to the antenna plane (4.39) and the matching to the Wigner function on the antenna plane (4.44), this probability distribution reads

$$p(x, N) = \frac{1}{\alpha} |v_\mathrm{x}| \, \delta(\mathrm{x}) w(\mathrm{x} = 0, \mathrm{y}, N), \tag{5.2}$$

with a normalization constant α, discussed later in this section. Here, v_{x} is the x-component of the ray velocity projected on configuration space, defined as

$$v_{\mathrm{x}} := \frac{\partial H_a}{\partial N_{\mathrm{x}}}. \tag{5.3}$$

As a standard Hamiltonian around the antenna plane, the free space Hamiltonian

$$H_a(x, N) = N^2 - 1 \tag{5.4}$$

is considered. The only situation presented within this thesis where this is not a good choice is the lens-like medium, section 6.2, where Hamiltonian (6.19) must be used.

Around the antenna plane, via equation (C.11), (5.4) yields the velocity

$$|v_{\mathrm{x}}| = 2N_{\mathrm{x}}. \tag{5.5}$$

Inserting this velocity component and Wigner function (5.1) into (5.2) provides the probability distribution

$$p(x, N) \propto |N_{\mathrm{x}}| \, \delta(\mathrm{x}) \delta(N_{\mathrm{x}} - N_{\mathrm{x},0}) e^{-\kappa \mathrm{y} \cdot \Phi \mathrm{y} - \kappa[(N_{\mathrm{y},0} - N_{\mathrm{y}}) + S\mathrm{y}] \cdot \Phi^{-1}[(N_{\mathrm{y},0} - N_{\mathrm{y}}) + S\mathrm{y}]}. \tag{5.6}$$

For implementation purposes (Metropolis-Hastings algorithm, see appendix F), the normalization constant for this probability distribution is not important and is not further addressed here. It is obvious that this function can be factorized into

$$p(x, N) = \delta(\mathrm{x}) \delta(N_{\mathrm{x}} - N_{\mathrm{x},0}) p_{\mathrm{y}}(\mathrm{y}, N_{\mathrm{y}}) \tag{5.7}$$

with a function uniquely dependent on $(\mathrm{y}, N_{\mathrm{y}})$

$$p_{\mathrm{y}}(\mathrm{y}, N_{\mathrm{y}}) \propto |N_{\mathrm{x},0}(\mathrm{y}, N_{\mathrm{y}})| \, e^{-\kappa \mathrm{y} \cdot \Phi \mathrm{y} - \kappa[(N_{\mathrm{y},0} - N_{\mathrm{y}}) + S\mathrm{y}] \cdot \Phi^{-1}[(N_{\mathrm{y},0} - N_{\mathrm{y}}) + S\mathrm{y}]}, \tag{5.8}$$

where $N_{\mathrm{x},0}(\mathrm{y}, N_{\mathrm{y}})$ is obtained as a solution of dispersion relation with $H_a(x, N)$ as Hamiltonian. Due to the δ-distributions in (5.7), $\mathrm{x} = 0$ and, once the values y and N_{y} are chosen, also $N_{\mathrm{x}} = N_{\mathrm{x},0}$ are fixed, which is also how they are determined in the code. Instead, $(\mathrm{y}, N_{\mathrm{y}})$ follow

the probability distribution (5.8), which is not a standard one and hence requires Metropolis-Hastings algorithm for its sampling. This algorithm is reviewed in appendix F. It internally needs to propose random numbers, following a probability distribution labeled with "proposal", which should be as close as possible to the probability density function $p(y, N_y)$. We choose

$$p_{\text{proposal}}(y, N_y) = \frac{1}{|N_{x,0}(y, N_y)|} p_y(y, N_y), \tag{5.9}$$

which, indeed, is close to $p_y(y, N_y)$ if the rays leave the antenna plane mainly in x-direction, i.e. $|N_{x,0}(y, N_y)| \approx 1$.

5.1.2. Phase space description

From a mathematical point of view, the scheme presented in section 4.2 for the solution of the wave kinetic equation requires the integration of ordinary differential equations, namely Hamilton's equations of motion (C.1) and the evolution of $\mathcal{W}$ in differential form of (4.34), i.e. the set of equations

$$\frac{d\mathcal{X}_i}{d\tau} = \partial_N H(\mathcal{X}_i, \mathcal{N}_i), \tag{5.10a}$$

$$\frac{d\mathcal{N}_i}{d\tau} = -\partial_x H(\mathcal{X}_i, \mathcal{N}_i), \tag{5.10b}$$

$$\frac{d\mathcal{W}_i}{d\tau} = -2\gamma(x, N)\mathcal{W}_i. \tag{5.10c}$$

Note that, unlike the derivation in the numerics chapter 4, equations (5.10) are integrated along a constant interval $\Delta\tau$ and all scattering kicks which may occur during this step are applied after the integration on $\Delta\tau$, cf. figure 5.1. This scheme is a good approximation to the numerical scheme described in section 4.2 when the step $\Delta\tau$ is small. The single computational steps are explained in more detail in the following.

The integration is discretised using the Runge-Kutta method. For a detailed description on the numerics behind, the reader may refer to the textbook [26]. Given the initial values $\mathcal{X}_i(\tau_k)$, $\mathcal{N}_i(\tau_k)$ and $\mathcal{W}_i(\tau_k)$ at τ_k and their derivatives $\frac{d\mathcal{X}_i}{d\tau}, \frac{d\mathcal{N}_i}{d\tau}, \frac{d\mathcal{W}_i}{d\tau}$, the Runge-Kutta solver provides the values at a later step $\tau_{k+1} = \tau_k + \Delta\tau$, i.e. $\mathcal{X}(\tau_{k+1}), \mathcal{N}_i(\tau_{k+1})$ and $\mathcal{W}_i(\tau_{k+1})$, for a chosen step $\Delta\tau$. In the adaptive Runge-Kutta method, $\Delta\tau$ is internally subdivided into smaller steps so that a specified tolerance of the result is reached. After each integration step, a scattering event
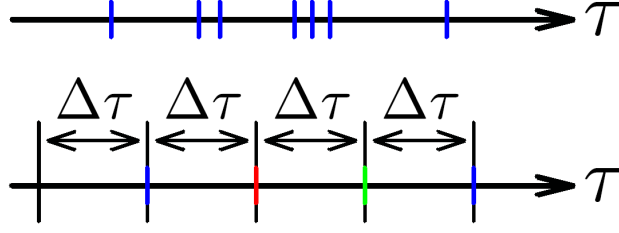
Figure 5.1.: Comparison of the scattering scheme described in the numerics chapter and the implementation. Blue marks: one scattering event, red mark: two scattering events, green mark: three scattering events. On top: τ-axis with one sample of scattering events along the evolution of a ray, simulated by means of a Poisson process as described in section 4.2. Below: Implemented procedure. The integration is subdivided into intervals $\Delta\tau$ which are not interrupted by scattering; all scattering kicks which should be performed during the interval are applied at the end instead.

might be performed to simulate the effect of fluctuations. For this purpose, an integer random number N_S is generated according to a Poisson distribution with mean $\Sigma_{\mathrm{max}}\Delta\tau$ for each ray i after each integration step k, where Σ_{max} is a guess for an upper limit of the total scattering cross section $\Sigma(\mathcal{X}_i(\tau_k), \mathcal{N}_i(\tau_k))$, defined in (4.25b). The number N_S is the maximum number of kicks in the interval $\Delta\tau$ for the current realization. Note that, in case we can afford it numerically, as a guess for the upper limit Σ_{max} the scattering cross section Σ itself may be taken. In order to decide how many scattering kicks actually are performed, N_S uniformly distributed numbers p_i within $[0, 1)$ are generated and for each a scattering kick is applied if and only if $p_i < \Sigma/\Sigma_{\mathrm{max}}$. Note that the above-described procedure generates $n_S \leq N_S$ scattering kicks for the ray i after the integration step k, with n_S following a Poisson distribution with mean value $\Sigma\Delta\tau$, but requires evaluating the total scattering cross section Σ not after each step, but only in case $N_S \neq 0$. If the probability distribution σ for choosing a new value for the refractive index at each jump is not a standard function, Metropolis-Hastings algorithm (described in appendix F) is applied.

As an output of the ray tracing, the trajectories $(\mathcal{X}_i(\tau_k), \mathcal{N}_i(\tau_k))$ and the value $\mathcal{W}_i(\tau_k)$ are stored in an output file for a discrete sample of moments τ_k with the step $\Delta\tau$ in between. In addition, transformed trajectories $T(\mathcal{X}_i(\tau_k), \mathcal{N}_i(\tau_k))$ with some coordinate transformation T may be saved. This is the information required for the reduction to physical observables, presented in the next section.
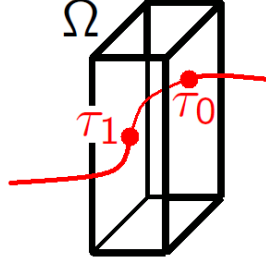
Figure 5.2.: One Hamiltonian orbit (red) entering the volume Ω (referred to as bin) for a parameter τ_0 and leaving for τ_1.

5.1.3. Reconstructing physical observables

The reconstruction of physical observables in terms of integral (3.70) is also called binning. In the code, it is done as a post-processing, so the ray trajectories are read and the Monte-Carlo estimator (4.50) is computed. In figure 5.2, one Hamiltonian orbit which crosses a bin is shown. The code executes a linear interpolation between the discrete steps τ_k where the trajectory of orbit i $(\mathcal{X}_i(\tau_k), \mathcal{N}_i(\tau_k))$ and the value $\mathcal{W}_i(\tau_k)$ are known from ray tracing and recognizes the intersections of the orbits with the bin boundaries. Thereby, the parameter τ when the orbit enters and leaves the bin τ_0 and τ_1 are estimated. The Monte-Carlo estimator for the integral to be computed is given by (4.50). The constant α, defined in (4.31) and involved as a prefactor in the Monte-Carlo sum, upon accounting for (4.39) and (4.44), reads

$$\alpha = \int |v_x|\, w(x = 0, y, N)\mathrm{d}y\mathrm{d}N. \tag{5.11}$$

Inserting the Wigner function on the antenna plane (5.1) and the x-velocity component (5.5), this yields

$$\alpha = 2\left(\frac{2\pi}{\kappa}\right)^m \int \sqrt{1 - N_y^2} \prod_{i=1}^{m-1} e^{-\kappa \frac{D_i}{D_i^2 + S_i^2}(N_{i,0} - N_i)^2} \mathrm{d}N_y, \tag{5.12}$$

where $N_y = (N_1, \ldots, N_{m-1})$ and D_i and S_i include information on the initial beam width and the initial curvature radius, as defined in appendix D. This integral must be computed numerically. Calculating the Monte-Carlo estimator then amounts in summing up all the ray contributions, obtained from the just presented quantities.

As a special case, if the absorption coefficient is taken as observable, i.e. $A(x, N) = 2\gamma(x, N)$, the corresponding Monte-Carlo estimator (4.46) reads

$$\langle 2\gamma \rangle_\Omega = 2 \left(\frac{\kappa}{2\pi} \right)^m \int \left[\frac{\alpha}{n_0} \sum_{(\mathcal{X}_i(\tau), \mathcal{N}_i(\tau)) \in \Omega} \gamma(\mathcal{X}_i(\tau), \mathcal{N}_i(\tau)) \mathcal{W}_i(\tau) \right] \mathrm{d}\tau, \qquad (5.13)$$

involving explicit information on the medium in γ also on the r.h.s. It would be beneficial if in the post-processing, no information on the medium is explicitly needed. Therefore we note that taking into account the evolution of $\mathcal{W}_i$ (5.10c), a factor γ may be obtained by applying a derivation with respect to τ:

$$\langle 2\gamma \rangle_\Omega = - \left(\frac{\kappa}{2\pi} \right)^m \int \left[\frac{\alpha}{n_0} \sum_{(\mathcal{X}_i(\tau), \mathcal{N}_i(\tau)) \in \Omega} \frac{\mathrm{d}\mathcal{W}_i(\tau)}{\mathrm{d}\tau} \right] \mathrm{d}\tau. \qquad (5.14)$$

Upon accounting for the fundamental theorem of calculus, this simplifies to

$$\langle 2\gamma \rangle_\Omega = - \left(\frac{\kappa}{2\pi} \right)^m \frac{\alpha}{n_0} \sum_{(\mathcal{X}_i(\tau), \mathcal{N}_i(\tau)) \in \Omega} \mathcal{W}_i(\tau) \Bigg|_{\tau = \tau_{i,0}}^{\tau_{i,1}} \qquad (5.15)$$

This expression requires no explicit knowledge of the absorption coefficient γ, information which is present via the change of $\mathcal{W}$ through a bin, simplifying the implementation and improving performance in terms of computational time.

In the previous discussion a single area Ω (bin) has been considered. Obviously, the code, in principle, is not restricted to only one such area, but it can deal with a whole set of integration volumes Ω_α, defined by

$$\Omega_\alpha = \left\{ (x, N) \in \mathbb{R}^{2m} : \frac{\alpha_i}{n_i} \leq \frac{T_i(x, N) - a_i^{\min}}{a_i^{\max} - a_i^{\min}} < \frac{\alpha_i + 1}{n_i} \text{ with } i = 1, \dots, \mu \right\}. \qquad (5.16)$$

Here, α is a μ-dimensional multi-index $\alpha = (\alpha_1, \dots, \alpha_\mu)$ and $T : \mathbb{R}^{2m} \to \mathbb{Y} \subset \mathbb{R}^\mu \times \mathbb{R}^{2m-\mu}$ a transformation to appropriate coordinates, where only the first μ components are resolved. The boundaries of the area under consideration are defined by $a_i^{\min}$ and $a_i^{\max}$ in i-th direction, subdivided into n_i bins. As an example, for the benchmarking tests, see chapter 6, two-dimensional Cartesian coordinates (x, y) are appropriate. If we wish to resolve these two spatial coordinates, the relevant dimensionality for the binning is $\mu = 2$ and the transformation under consideration

is

$$T_1(x, N) = \mathrm{x}, \tag{5.17a}$$

$$T_2(x, N) = \mathrm{y}. \tag{5.17b}$$

Then, the areas for the binning are squares

$$\Omega_{\mu\nu} = \left\{ (x, N) \in \mathbb{R}^{2m} : \frac{\mu}{n_{\mathrm{x}}} \leq \frac{\mathrm{x} - \mathrm{x}^{\min}}{\mathrm{x}^{\max} - \mathrm{x}^{\min}} < \frac{\mu + 1}{n_{\mathrm{x}}}, \right.$$
$$\left. \frac{\nu}{n_{\mathrm{y}}} \leq \frac{\mathrm{y} - \mathrm{y}^{\min}}{\mathrm{y}^{\max} - \mathrm{y}^{\min}} < \frac{\nu + 1}{n_{\mathrm{y}}} \right\}. \tag{5.18}$$

with integer labels μ and ν referring to the x- and y-direction, respectively.

5.2. Implementation of the code

In this section, a few details, from a computer-science point of view, for the numerical implementation of WKBeam are given. The code is written in the high-level language python [27] with the scientific libraries numpy and scipy [28]. Parallelization, cf. section 5.2.1, is achieved by the MPI protocol [29] through the mpi4py-package [30]. Being a script language, python is rather slow. In order to speed up the code, some expensive parts are moved to cython [31] and precompiled.

Note that WKBeam consists of two parts which are launched independently: One is referred to as ray tracing part and provides as an output a set of ray trajectories with attached quantities, namely $\mathcal{W}_i$ and $T(\mathcal{X}_i(\tau_k), \mathcal{N}_i(\tau_k))$, as described in section 5.1.2. A second part, called binning part of WKBeam, reads this ray trajectories and does the reconstruction of physical observables, presented in section 5.1.3.

In the following, the rough structure of these two independent parts of the code is discussed. In particular, some comments on the runtime are presented. Typically, the ray tracing data which is created on 16 cores with a runtime of $2\,\mathrm{h}$ is binned in a few minutes using one single core. All simulations performed for this master thesis where processed on the Linux Compute Cluster of the Rechenzentrum Garching [32].

(a) master core:

```
┌─────────────────────────────────────┐
│ generate initial conditions and send │
│ those to the slave cores             │
└─────────────────────────────────────┘
                 │
                 ▼
┌─────────────────────────────────────┐
│ for all initial conditions sent:     │
└─────────────────────────────────────┘
      ┌──────────────────────────────┐
      │ wait for the slave cores'     │
      │ answers containing the ray    │
      │ trajectories and collect those│
      └──────────────────────────────┘
                 │
                 ▼
┌─────────────────────────────────────┐
│ write the output file containing     │
│ the collected results                │
└─────────────────────────────────────┘
```

(b) slave core:

```
┌─────────────────────────────────────┐
│ wait for initial conditions          │
│ from master core                     │
└─────────────────────────────────────┘
                 │
                 ▼
┌─────────────────────────────────────┐
│ for all initial conditions received: │
└─────────────────────────────────────┘
      ┌──────────────────────────────┐
      │ integrate ray trajectory      │
      │ and send back result to       │
      │ master core                   │
      └──────────────────────────────┘
```

Figure 5.3.: Program flow for (a) master core and (b) slave core.

5.2.1. Ray tracing part of the code

In section 4.3, the statistical uncertainty of physical results was presented and it was pointed out that it decreases with the square root of the number of rays. Running the code, we find that a reasonable number of rays is of the order of 10^5, see also section 7.5. Assuming that it takes about $100\,\text{ms}$ to trace a ray, the total runtime amounts to several hours. For this reason the ray tracing is parallelized: The set of initial conditions is split into several parts, each passed to a different CPU referred to as "slave core" via MPI interface. The slave cores perform the ray tracing and communicate the ray trajectories back to a core called "master core", which is in charge of writing the output file. One master core is responsible for at most seven slave cores. If there are more, several master cores are present and several output files are written. An upper limit for the number of slave cores per master core is required, because too many slave cores overburden the master core, thus forming a bottleneck. In python, for this purpose, the mpi4py package is available. It labels all cores which are part of the MPI environment with an index, used in the implementation to decide whether the source code for a master or a slave core is called. The structure of the codes for both is also displayed in figure 5.3.

A study of the strong scaling of the parallelization is presented in figure 5.4. The plot shows the runtime T of the ray tracing code, run for a standard case with a reduced number of rays, making use of various numbers n of cores in a doubly logarithmic plot. The jobs are processed via a queue which distributes available resources to the users of the computer cluster, providing the runtime as an output once the code has finished.
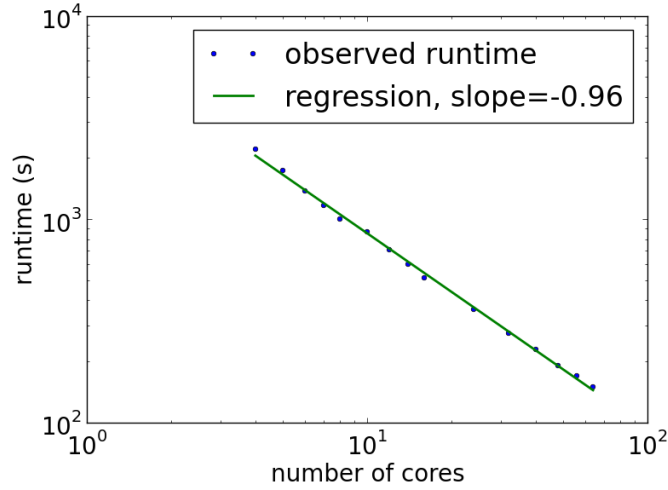
Figure 5.4.: Doubly logarithmic plot of runtime versus number of cores. On top of that, a linear regression is performed with slope -0.96.

The slope in figure 5.4 is -0.96 which almost corresponds to the ideal scaling law

$$T \propto n^{-1}. \qquad (5.19)$$

This is the typical scaling whenever no communication is needed between different cores, as it is the case for the WKBeam code, except for the communication of the initial parameters for the rays and the results. This data transfer, however, is negligible and does not spoil the good scaling.

A user guide for this part of the code is presented in appendix E.1.

5.2.2. Binning part of the code

Once the ray tracing is performed and the output files are available, the physical observables can be computed, cf. section 5.1.3. The corresponding part of the WKBeam code is referred to as binning. This part of the code, as an input, uniquely requires the output files of the ray tracing part and does not involve any python objects, which allows us to fully move the code to cython and precompile it. The code is fast enough so that no parallelization is required.

A users guide for the binning code can be found in appendix E.2.

6

Benchmarking: simplified models

Before applying the theory derived previously to realistic situations in tokamak plasmas, benchmarking tests must be performed to check that the code is free from programming errors. Moreover, such tests allow one to clarify the limitations of the code due e.g. to the semiclassical limit, the Monte-Carlo uncertainty (4.53) and the approximation in the calculation of physical observables (3.74) under simple and controllable conditions. This chapter is dedicated to those tests. Several simplified models have been considered. For each of these, analytical solutions can be constructed, or at least other well-established numerical schemes can be used as a crosscheck. In each section, the input quantities for the numerical scheme as well as a sketch of the derivation of a reference solution are described. Fluctuations and absorption first are turned off and introduced in section 6.4. For later applications, it is of special interest to be aware of the impact of numerical parameters to choose when the simulation is run, e.g. the number of rays and the bin size. A study of this issue is delayed to section 6.5. However we note here that for the

benchmarks reasonable parameters which allow us to resolve the effects under investigation are chosen.

In this chapter, the antenna plane is, as presented in section 3.5, the $x = 0$ plane and beams are launched so that they propagate towards negative values of x. This simulates the low-field side injection in tokamak plasmas described in section 7.2, when no tilt of the antenna plane is considered. In all benchmarks, two-dimensional geometries with coordinates $x = (x, y) \in \mathbb{R}^2$ are considered. As in the previous chapters, the calculations are presented in terms of normalized coordinates in this thesis. Instead, the implementation deals with lengths in centimeter units. The reader is reminded that those results are obtained simply by replacing in the equations κ with k_0 and the normalized position x with the natural position r. The length scale of possibly involved background variations is denoted L, in consistency with (2.14).

6.1. Free space

In this section the simplest situation is considered, i.e. the propagation of electromagnetic waves in free space. Neither absorption nor fluctuations are present.

The wave equation (2.10) for this case reads

$$\left[\Delta_x + \kappa^2 \right] E(x) = 0. \tag{6.1}$$

It was made use of the fact that free space is isotropic and hence the electric field can be described as a scalar. Furthermore, the response of free space is local and the dielectric operator is nothing more than the identity. Therefore, equation (6.1) has the form of a Helmholtz equation. The corresponding L-symbol, as was explained in section 2.2, is obtained by replacing the partial derivative ∂_x in the dispersion operator with $-i\kappa N$ and hence is given by

$$d(x, N) = 2N^2 - 2. \tag{6.2}$$

Here, a constant prefactor of $-\frac{2}{\kappa^2}$ has been introduced. This is an arbitrary choice which leads to a non-trivial factor ξ, cf. equation (6.4) thus allows to test the rescaling procedure presented in section 4.4. The L-symbol (6.2) depends uniquely on N and can hence be cast to the form (2.38).

So, according to section 2.2.2, the corresponding Weyl symbol is identical, i.e.

$$H(x, N) = d(x, N) = 2N^2 - 2. \tag{6.3}$$

Investigating scalar waves, this Weyl symbol is a matrix of dimensionality 1 and thus equivalent to its eigenvalue which is considered as Hamiltonian. Comparison of Hamiltonian (6.3) with the Hamiltonian considered around the antenna plane (5.4) yields the correction factor, cf. equation (4.54),

$$\xi(x, N) \equiv 2. \tag{6.4}$$

In order for this case to be a useful benchmark, a reference solution of the partial differential equation (6.1) must be obtained. To this aim, the coordinates are split into $x = (\mathrm{x}, \mathrm{y})$. Like in section 3.5, $\mathrm{y} \in \mathbb{R}$ is the coordinate parallel to the antenna plane. A Fourier transform with respect to y is performed, i.e.

$$\hat{E}(\mathrm{x}, N_\mathrm{y}) = \int e^{-i\kappa N_\mathrm{y} \cdot \mathrm{y}} E(\mathrm{x}, \mathrm{y}) d\mathrm{y}. \tag{6.5}$$

This is substituted into the wave equation (6.1) with the result

$$\left(\partial_\mathrm{x}^2 + \kappa^2 \left(1 - N_\mathrm{y}^2 \right) \right) \hat{E}(\mathrm{x}, N_\mathrm{y}) = 0. \tag{6.6}$$

Now, x being one dimensional, this last equation is an ordinary differential equation. Integrated it yields

$$\hat{E}(\mathrm{x}, N_\mathrm{y}) = e^{-i\kappa \sqrt{1 - N_\mathrm{y}^2} \mathrm{x}} \hat{E}(\mathrm{x} = 0, N_\mathrm{y}). \tag{6.7}$$

Note that (6.6) is a differential equation of second order, thus yielding two independent solutions with refractive indices $N_\mathrm{x} = \pm\sqrt{1 - N_\mathrm{y}^2}$, representing two possible branches of the dispersion relation. The one relevant to propagation toward the negative x-axis considered in (6.7) is $N_\mathrm{x} = -\sqrt{1 - N_\mathrm{y}^2}$.

In this solution, the Fourier transformed electric field on the antenna plane $\hat{E}(\mathrm{x} = 0, N_\mathrm{y})$ is involved as a boundary condition. The field on the antenna plane itself has the usual Gaussian beam

profile (D.1) with vanishing central refractive index $N_{y,0}$ and the central amplitude normalized to $A = 1$, i.e.

$$E(\mathrm{x} = 0, \mathrm{y}) = e^{\frac{i}{2}\kappa \mathrm{y} \cdot S\mathrm{y} - \frac{1}{2}\kappa \mathrm{y} \cdot \Phi \mathrm{y}}. \tag{6.8}$$

For the two-dimensional case with propagation perpendicular to the antenna plane considered here, the matrices Φ and S in fact are scalars and the same as their eigenvalues, with the notation introduced in appendix D implying $\Phi = D$. The wave field (6.8) can be Fourier transformed analytically, yielding the boundary condition for (6.7):

$$\hat{E}(\mathrm{x} = 0, N_y) = \int e^{-i\kappa N_y \cdot \mathrm{y}} E(\mathrm{x} = 0, \mathrm{y})\mathrm{dy} = \left(\frac{2\pi}{D - iS}\right)^{1/2} e^{-\frac{1}{2}\kappa \frac{N_y^2}{D - iS}}. \tag{6.9}$$

In order to compute the electric field in space $E(\mathrm{x}, \mathrm{y})$, the inverse Fourier transform of (6.7) is computed. It reads

$$E(\mathrm{x}, \mathrm{y}) = \left(\frac{\kappa}{2\pi (D - iS)}\right)^{1/2} \int e^{i\kappa \mathrm{y} \cdot N_y} e^{-i\kappa \sqrt{1 - N_y^2}\mathrm{x}} e^{-\frac{1}{2}\kappa \frac{N_y^2}{D - iS}} \mathrm{d}N_y. \tag{6.10}$$

Due to the square root in the exponential, an analytical computation of this integral cannot be performed. However, a useful approximation is obtained if the power spectrum of the beam, i.e. the norm squared of (6.9)

$$\left|\hat{E}(\mathrm{x} = 0, N_y)\right|^2 = \frac{2\pi}{D^2 + S^2} e^{-\frac{1}{2}\frac{\kappa D}{D^2 + S^2} N_y^2} \tag{6.11}$$

is analyzed. It is identified to be a Gaussian distribution centered around $N_y = 0$ with width $\sigma = \sqrt{\frac{D^2 + S^2}{\kappa D}}$. Apart from situations in which the beam is extremely focused (S large) or the beam width is of the order of the wave length ($D/\kappa \gtrsim 1$), the spectral width is much smaller then 1. This means that only small values of N_y contribute to the solution, making it appropriate to use the Taylor expansion

$$\sqrt{1 - N_y^2} = 1 - \frac{1}{2}N_y^2 + \mathcal{O}\left(N_y^4\right) \tag{6.12}$$

(a) result of the WKBeam code:

(b) difference WKBeam - reference solution:

(c) statistical uncertainty of WKBeam:
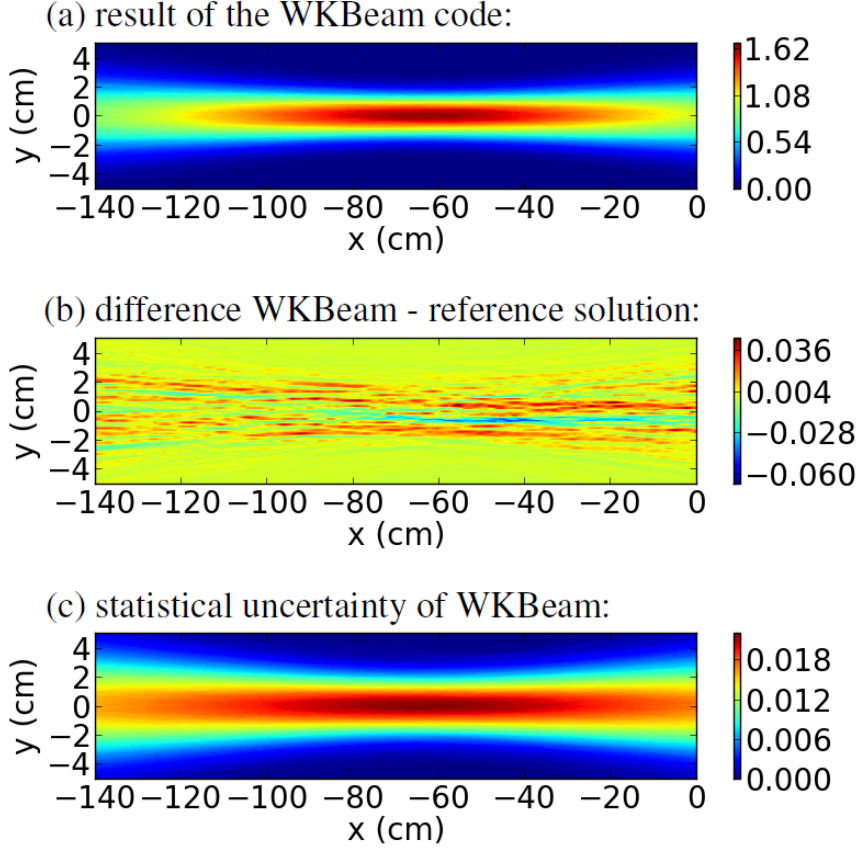
Figure 6.1.: Beam in free space with frequency $f = 140\,\text{GHz}$, initial beam width $w = 3\,\text{cm}$ and initial curvature radius $R = 100\,\text{cm}$. $n_0 = 100000$ rays have been traced and the size of the bins is $\Delta x = 1.5\,\text{cm}$ and $\Delta y = 0.29\,\text{cm}$. It is shown: (a) the result obtained by the wave kinetic code, (b) the difference to the analytical reference solution, (c) the statistical uncertainty.

and neglect fourth order terms. This is called paraxial approximation and allows us to compute the integral in (6.10) analytically, with the electric field as a result:

$$E(\mathrm{x},\mathrm{y}) = \frac{1}{\left(1 - (iD + S)\,\mathrm{x}\right)^{1/2}} e^{-i\kappa\mathrm{x} - \frac{\kappa}{2}\frac{\mathrm{y}^2}{\frac{1}{D - iS} - i\mathrm{x}}}. \tag{6.13}$$

The norm squared which is compared to the result of the wave kinetic code is

$$|E(\mathrm{x},\mathrm{y})|^2 = \frac{1}{\left((1 - S\mathrm{x})^2 + (D\mathrm{x})^2\right)^{1/2}} e^{-\frac{\kappa D\mathrm{y}^2}{(1 - S\mathrm{x})^2 + (D\mathrm{x})^2}}. \tag{6.14}$$

A set of beam parameters satisfying the paraxial approximation (in physical units, appropriate in the code: typical frequency of microwaves in tokamak applications $f = 140\,\text{GHz}$, initial beam width of $w = 3\,\text{cm}$ (large compared to the wave length), slightly focused by a curvature radius of $R = 100\,\text{cm}$) is chosen. The results are presented in figure 6.1. The result of WKBeam (a) is computed in terms of the Monte-Carlo estimator (4.50) and its statistical uncertainty (c) is given by (4.53). It can be seen that the difference between the analytical, paraxial solution and the numerical one (b) is close to zero and of the order of magnitude of the statistical uncertainty. Furthermore, this difference shows an erratic behavior typical for statistical processes. The wave kinetic code nicely reproduces, up to the statistical uncertainty, the reference solution.

6.2. Lens-like medium

As a next simplified model, a medium with space-dependent refractive index

$$n^2(\text{y}) = 1 - \text{y}^2 \tag{6.15}$$

is considered in this section. This refractive index allows non-evanescent wave propagation only for $|\text{y}| \leq 1$. The wave equation, describing a two-dimensional scalar wave field, reads

$$\left(\frac{\partial^2}{\partial \text{x}^2} + \kappa^2 \left(1 + \frac{1}{\kappa^2} \frac{\partial^2}{\partial \text{y}^2} - \text{y}^2 \right) \right) E(\text{x}, \text{y}) = 0. \tag{6.16}$$

With the same arguments as in the previous section on free space, the Hamiltonian to be employed for the ray tracing is obtained by replacing ∂_x with $-i\kappa N$, leading to

$$H(\text{x}, \text{y}, N_\text{x}, N_\text{y}) = 2 \left(N_\text{x}^2 + N_\text{y}^2 - 1 + \text{y}^2 \right) \tag{6.17}$$

with the correction factor defined in (4.54)

$$\xi(x, N) \equiv 2, \tag{6.18}$$

where as a Hamiltonian around the antenna plane (5.4) is not appropriate and replaced by the Hamiltonian considered natural for this benchmark in the sense of section 4.4

$$H_a(\mathrm{x}, \mathrm{y}, N_{\mathrm{x}}, N_{\mathrm{y}}) = N_{\mathrm{x}}^2 + N_{\mathrm{y}}^2 - 1 + \mathrm{y}^2. \tag{6.19}$$

A reference solution to the wave equation (6.16) can be calculated. We recognize that its y-part looks like the harmonical oscillator problem in quantum mechanics. The ansatz

$$E(\mathrm{x}, \mathrm{y}) = E_{\mathrm{x}}(\mathrm{x}) E_{\mathrm{y}}(\mathrm{y}) \tag{6.20}$$

substituted into equation (6.16) allows to separate it in independent equations for x and y, namely the system

$$\left(\frac{\partial^2}{\partial \mathrm{x}^2} + \kappa^2 \right) E_{\mathrm{x}}(\mathrm{x}) = \kappa^2 C E_{\mathrm{x}}(\mathrm{x}), \tag{6.21a}$$

$$\left(\mathrm{y}'^2 - \frac{\partial^2}{\partial \mathrm{y}'^2} \right) E_{\mathrm{y}'}(\mathrm{y}') = C' E_{\mathrm{y}'}(\mathrm{y}') \tag{6.21b}$$

with some constant $C \in \mathbb{R}$ and the definition of rescaled quantities

$$\mathrm{y}' := \sqrt{\kappa} \mathrm{y}, \tag{6.22a}$$

$$C' := \kappa C. \tag{6.22b}$$

The x-equation (6.21a) is an ordinary differential equation with constant coefficients and easy to solve. The result reads

$$E_{\mathrm{x}}(\mathrm{x}) = A e^{-i\kappa\sqrt{1-C}\mathrm{x}} \tag{6.23}$$

with an amplitude A if propagation to the left is assumed, determining the sign of the exponential in analogy to the free space section 6.1.

For the y-part (6.21b), solutions are provided in [33] in terms of the Hermite polynomials $H_n(\mathrm{y}')$. For any $n \in \mathbb{N}_0$, the Hermite-Gaussian mode

$$E_{\mathrm{y}',n}(\mathrm{y}') = H_n(\mathrm{y}') e^{-\frac{1}{2}\mathrm{y}'^2} \tag{6.24}$$

6. Benchmarking: simplified models

solves the wave equation. The corresponding constant $C' = C'_n$ depends on the mode index n and, in quantum mechanics, has the physical meaning of energy. It is given by

$$C'_n = 2n + 1 \quad \text{with } n \in \mathbb{N}_0. \tag{6.25}$$

The wave equation is linear, so a general solution is found as a superposition of these eigenmodes, namely

$$E(\mathrm{x}, \mathrm{y}) = \sum_{n=0}^{\infty} A_n e^{-i\kappa\sqrt{1 - \frac{2n+1}{\kappa}}\mathrm{x}} H_n\left(\sqrt{\kappa}\mathrm{y}\right) e^{-\frac{1}{2}\kappa\mathrm{y}^2}. \tag{6.26}$$

Here, A_n are coefficients to be determined given the boundary condition $E(\mathrm{x} = 0, \mathrm{y})$. The model of a lens-like medium being also discussed in [34], the computation of the coefficients A_n may be borrowed from there: We recall orthogonality of Hermite polynomials

$$\int e^{-\mathrm{y}'^2} H_m(\mathrm{y}') H_n(\mathrm{y}') \mathrm{dy}' = 2^n n! \sqrt{\pi} \delta_{mn} \tag{6.27}$$

and recover this integral when integrating on y the electric field on the antenna plane $E(\mathrm{x} = 0, \mathrm{y})$ obtained from (6.26) multiplied by the m-th Hermite-mode

$$E_{\mathrm{y},m}(\mathrm{y}') = H_m(\mathrm{y}') e^{-\frac{1}{2}\mathrm{y}'^2}. \tag{6.28}$$

Kronecker's δ then simplifies the sum, with the result that

$$\int e^{-\frac{1}{2}\kappa\mathrm{y}^2} H_m(\sqrt{\kappa}\mathrm{y}) E(\mathrm{x} = 0, \mathrm{y}) \mathrm{dy} = 2^m m! \sqrt{\frac{\pi}{\kappa}} A_m. \tag{6.29}$$

Solved for the coefficients, this reads

$$A_m = \frac{1}{2^m m!} \sqrt{\frac{\kappa}{\pi}} \int e^{-\frac{1}{2}\kappa\mathrm{y}^2} H_m(\sqrt{\kappa}\mathrm{y}) E(\mathrm{x} = 0, \mathrm{y}) \mathrm{dy}. \tag{6.30}$$

As initial conditions, a Gaussian beam profile as considered in appendix D is chosen. In this section, only beams of vanishing initial phase-front curvature, i.e. $S = 0$, and with vanishing central refractive index in the antenna plane are studied. Under these conditions, the electric field

on the antenna plane (D.1) simplifies to

$$E(\mathrm{x}=0,\mathrm{y}) = e^{-\frac{1}{2}\kappa D \mathrm{y}^2}. \tag{6.31}$$

The coefficients (6.30) are then, in terms of the normalized y',:

$$A_m = \frac{1}{2^m m!} \int e^{-\frac{1}{2}(1+D)\mathrm{y'}^2} H_m(y') \mathrm{dy}'. \tag{6.32}$$

These integrals are computed recursively in [34], with the result

$$A_{2l} = \frac{1}{(2l)!!2^l} \frac{\left(\frac{1}{\gamma}-1\right)^l}{\sqrt{\gamma}}, \tag{6.33a}$$

$$A_{2l+1} = 0, \tag{6.33b}$$

where $\gamma := 1 + D$. Upon making use of the floor function defined as

$$\lfloor f \rfloor := \max \left\{ n \in \mathbb{Z} : n \leq f \right\}, \tag{6.34}$$

according to (6.26) modes n with

$$n > \lfloor \frac{\kappa - 1}{2} \rfloor =: n_0 \tag{6.35}$$

are evanescent and, fading away exponentially on the length scale of the wave length, do not contribute considerably far from the antenna plane. Therefore, these modes are neglected and only the first n_0 are taken into account.

Let us discuss the periodicity in x-direction of the wave field amplitude of the reference solution (6.26). At a given position x, the phase shift $\Delta\phi_{mn}$ between two Hermite-modes m and n, is

$$\Delta\phi_{mn} = \kappa \left(\sqrt{1 - \frac{2m+1}{\kappa}} - \sqrt{1 - \frac{2n+1}{\kappa}} \right) \mathrm{x}. \tag{6.36}$$

A periodicity in x is purely determined by this phase shift, cf. (6.26). The condition for the superposition of the Hermite-modes to be periodic is that, for $\mathrm{x} = p$ with a period p, $\Delta\phi_{mn}$ is a multiple of 2π for any m and n. Regarding these phase shifts (6.36) containing square roots, we

6. Benchmarking: simplified models

note that in general the ratio of $\Delta\phi_{mn}$ and $\Delta\phi_{m'n'}$ is not rational for $(m,n) \neq (m',n')$, making it impossible that all are multiples of 2π for the same value of x. This means that the solution in general is not periodic. However, it can be shown that in the limit $\kappa \to \infty$, a periodic solution is obtained: The square roots in the phase shift (6.36) then may be Taylor expanded, i.e. up to first-order terms $\mathcal{O}(\kappa^{-1})$

$$\Delta\phi_{mn} = (n-m)\mathrm{x} + \frac{(2n+1)^2 - (2m+1)^2}{8\kappa}\mathrm{x}. \tag{6.37}$$

Upon neglecting the second term on the r.h.s and taking into account that only even numbers n and m are considered, cf. (6.33), the phase shift is a multiple of 2π for $\mathrm{x} = \pi$, determining the periodicity of the solution, $p = \pi$. The second term may be neglected for small $|\mathrm{x}|$, namely

$$|\Delta\mathrm{x}| \ll \frac{\kappa}{\tilde{n}_0^2} \tag{6.38}$$

for $\tilde{n}_0$ the number of relevant modes with non-negligible amplitude (6.33a). For beams propagating over a larger distance, however, the first-order term spoils periodicity.

In the following, results are presented, again, in physical units. For the test runs of the simulation, first a very high frequency, $f = 14000\,\mathrm{GHz}$, and an initial beam width of $w = 0.1\,\mathrm{cm}$ are used. With a typical variational length scale of the refractive index $L = 3\,\mathrm{cm}$. The amplitude in (6.33a) drops fast with increasing index, justifying the assumption that the number of relevant modes $\tilde{n}_0$ is of order 1. Then, the above-presented parameters, yielding $\kappa \approx 9 \cdot 10^3$, ensure a periodic solution over the whole observation range. The results are presented in figure 6.2. The difference between WKBeam and the reference solution (b) is close to zero. This confirms that the wave kinetic code produces reasonable results for the chosen set of parameters. In addition it is confirmed that the result (a) is periodic in x, with a period $p = 9.4\,\mathrm{cm}$.

Next, the beam is simulated for another set of parameters, for which we expect a faster breakdown of the periodicity: The frequency is reduced by a factor of 100, i.e. $f = 140\,\mathrm{GHz}$, causing also a reduction of the parameter κ. In addition, the initial beam width is multiplied by a factor of 10, $w = 1\,\mathrm{cm}$. This leaves the parameter D unchanged, cf. (D.13a). According to (6.32) this results in similar contributions of Hermite-modes as compared to the beam parameters before. Hence, also the number of relevant modes $\tilde{n}_0$ is equivalent. Even if the high-frequency limit $\kappa \approx 90 \gg 1$ is still fulfilled, a periodic solution is predicted by (6.38) only for $|\Delta\mathrm{x}| \ll 30\,\mathrm{cm}$.
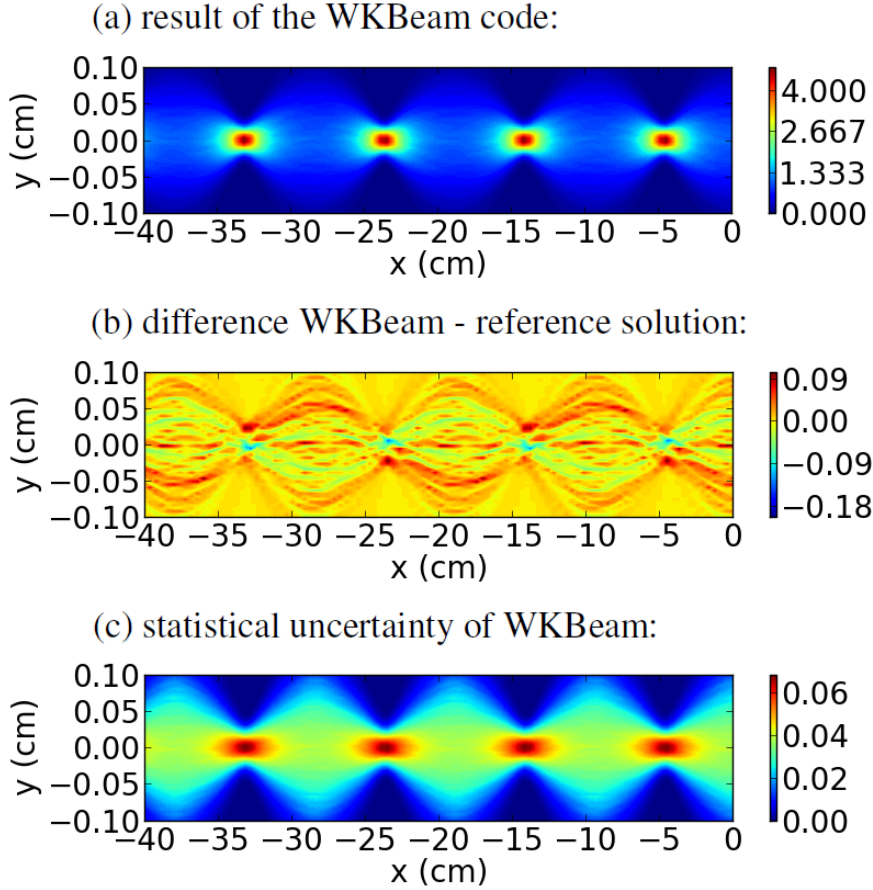
(a) result of the WKBeam code:

(b) difference WKBeam - reference solution:

(c) statistical uncertainty of WKBeam:

Figure 6.2.: Beam in a lens-like medium $L = 3\,\text{cm}$ with frequency $f = 14000\,\text{GHz}$, initial beam width $w = 0.1\,\text{cm}$. $n_0 = 20000$ rays have been traced and the size of the bins is $\Delta x = 0.4\,\text{cm}$ and $\Delta y = 0.004\,\text{cm}$. It is shown: (a) the result obtained by the wave kinetic code, (b) the difference to the analytical reference solution, (c) the statistical uncertainty.

The results can be seen in figure 6.3. In this figure, two effects can be discovered: Indeed, solution (a) is no longer periodic, as it was foreseen considering the input parameters for the beam. Furthermore, the difference (b) of the outcome of WKBeam (a) to the reference solution is significantly larger than the statistical uncertainty (c), pointing to an inaccuracy beyond this uncertainty. The semiclassical limit may serve as an explanation: The spots seen in the difference plot (b) show a typical interference pattern with a scale of $d = 0.2\,\text{cm} \approx \lambda$. This can be attributed to the interference of the Hermite-Gaussian modes composing the beam. As addressed in section 2.4.2, the semiclassical limit of the Wigner function is defined in weak sense only,
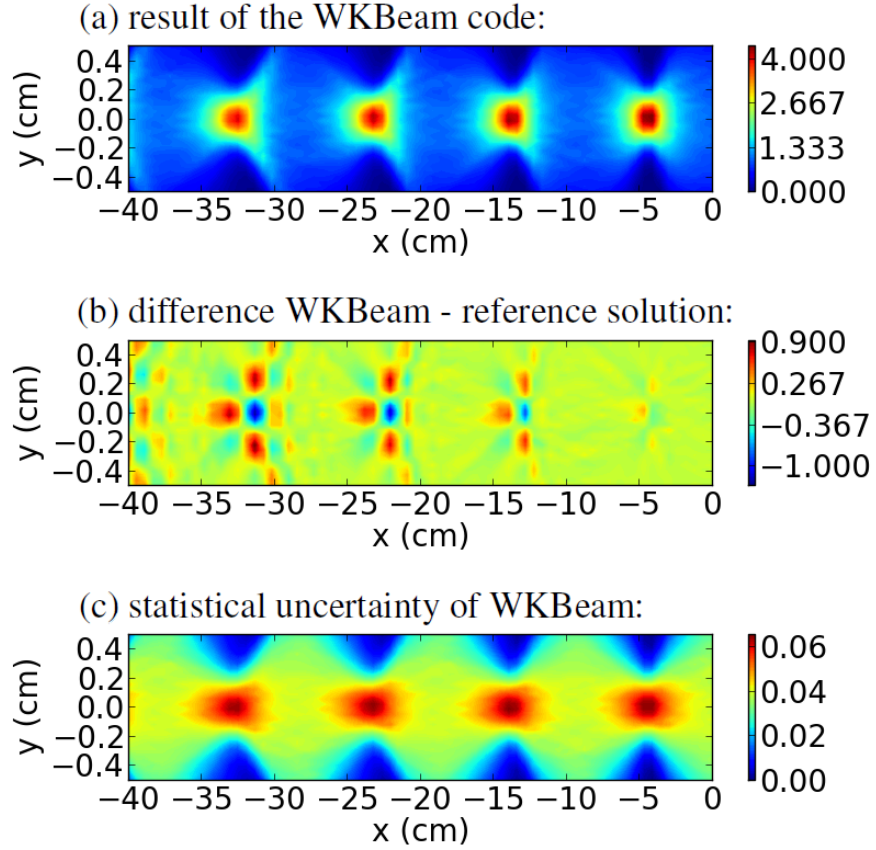
(a) result of the WKBeam code:

(b) difference WKBeam - reference solution:

(c) statistical uncertainty of WKBeam:

Figure 6.3.: Beam in a lens-like medium $L = 3\,\mathrm{cm}$ with frequency $f = 140\,\mathrm{GHz}$, initial beam width $w = 1\,\mathrm{cm}$. $n_0 = 20000$ rays have been traced and the size of the bins is $\Delta x = 0.57\,\mathrm{cm}$ and $\Delta y = 0.033\,\mathrm{cm}$. It is shown: (a) the result obtained by the wave kinetic code, (b) the difference to the analytical reference solution, (c) the statistical uncertainty.

implying an average of such interference pattern over a scale length of several wave length λ. This effect is discussed further in the next example. Such interference effects in principle are also present for the parameters used in figure 6.2. However, the wave length there was $\lambda = 2 \cdot 10^{-3}\,\mathrm{cm}$, which is too small to be resolved with the chosen bin size, such that the approximation of the semiclassical limit does not lead to inaccuracies.

6.3. Linear layer

The simplified model under investigation in this section has a linearly decreasing squared refractive index for propagation to the left, i.e.

$$n^2(\mathrm{x}) = 1 + \mathrm{x}. \tag{6.39}$$

This medium does not allow beam propagation beyond a cut-off layer, this means for $\mathrm{x} < -1$, where $n(\mathrm{x})$ becomes imaginary. This model is interesting particularly with regard to reflectometry applications in tokamak plasmas, because reflections can be reproduced. The wave equation with refractive index (6.39) yields

$$\left(\frac{\partial^2}{\partial \mathrm{x}^2} + \frac{\partial^2}{\partial \mathrm{y}^2} + \kappa^2 (1 + \mathrm{x}) \right) E(\mathrm{x}, \mathrm{y}) = 0. \tag{6.40}$$

The Hamiltonian for the wave kinetic code is constructed in analogy to the free space case in section 6.1 and yields

$$H(\mathrm{x}, \mathrm{y}, N_\mathrm{x}, N_\mathrm{y}) = 2 \left(N_\mathrm{x}^2 + N_\mathrm{y}^2 - 1 - \mathrm{x} \right) \tag{6.41}$$

where the correction factor is, again,

$$\xi(x, N) \equiv 2. \tag{6.42}$$

For the construction of a reference solution, we refer to [35]. A Fourier transformation with respect to y of the wave equation is performed. This leads to

$$\left(\frac{\partial^2}{\partial \mathrm{x}'^2} - \mathrm{x}' \right) \hat{E}(\mathrm{x}', N_\mathrm{y}) = 0. \tag{6.43}$$

Here, the rescaled coordinate

$$\mathrm{x}' = -\kappa^{2/3} \left(1 + \mathrm{x} - N_\mathrm{y}^2 \right) \tag{6.44}$$

has been introduced. Since N_y is a constant of motion in this case, equation (6.43) is the well-known Airy equation with the solution referred to as Airy function $Ai(x')$. Hence, the Fourier transformed wave field reads

$$\hat{E}(x, N_y) = f(N_y)Ai\left(-\kappa^{2/3}\left(1 + x - N_y^2\right)\right).$$ (6.45)

The function $f(N_y)$ contains the boundary conditions, i.e. the electric field at the antenna plane. Note that, in case the beam gets reflected and comes back to the antenna plane, only the originally launched contribution $E_B(y)$, i.e. the contribution propagating in negatice x-direction, must be taken into account, for consistency with the wave kinetic code. Around the antenna plane, i.e. $x \approx 0$, we have $x' \approx -\kappa^{2/3}\left(1 - N_y^2\right) \gg 1$, which justifies the following approximation: As discussed in [36], in the regime $x' \ll -1$, the Airy function can be approximated with

$$Ai(x') \approx \frac{\sin\left(\frac{2}{3}(-x')^{3/2} + \frac{\pi}{4}\right)}{\sqrt{\pi}(-x')^{1/4}}.$$ (6.46)

In this approximation, the contribution propagating in negative x-direction is obtained if the sin-function is replaced with the right exponential, i.e.

$$\sin(\cdot) \rightarrow \frac{1}{2i}e^{i(\cdot)}.$$ (6.47)

This inserted into (6.45) results in

$$\hat{E}(x, N_y) = f(N_y)\frac{e^{-\frac{2}{3}\kappa\left(1+x-N_y^2\right)^{3/2}}}{2\sqrt{\pi}\kappa^{2/3}\left(1 + x - N_y^2\right)^{1/4}}.$$ (6.48)

For $x = 0$, this expresses the spectrum of the wave field considered as boundary condition on the antenna plane. Solved for $f(N_y)$ and inserted into (6.45), the previous equation leads to

$$\hat{E}(x, N_y) = 2\sqrt{\pi}\kappa^{2/3}\frac{\left(1 - N_y^2\right)^{1/4}}{e^{-\frac{2}{3}\kappa\left(1-N_y^2\right)^{3/2}}}Ai\left(-\kappa^{2/3}\left(1 + x - N_y^2\right)\right)\hat{E}(x = 0, N_y).$$ (6.49)
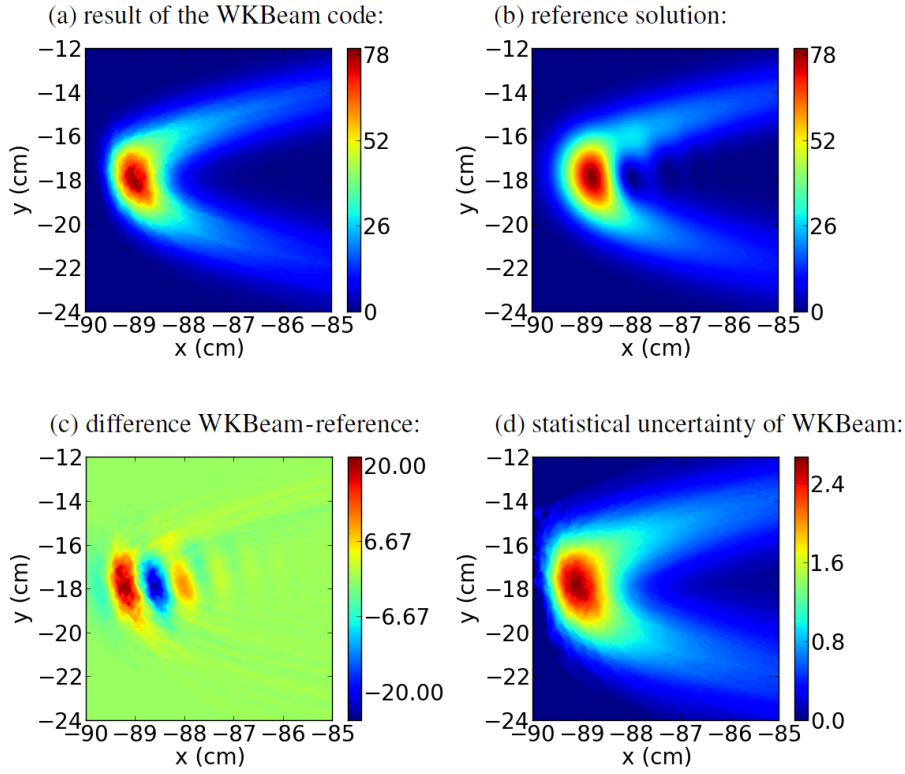
Figure 6.4.: Beam in a linear layer with inhomogenity scale $L = 90\,\mathrm{cm}$, frequency $f = 140\,\mathrm{GHz}$, initial beam width $w = 6\,\mathrm{cm}$ and initial curvature radius $R = 180\,\mathrm{cm}$. $n_0 = 10000$ rays have been traced and the size of the bins is $\Delta x = 0.031\,\mathrm{cm}$ and $\Delta y = 0.15\,\mathrm{cm}$. The beam is launched at $(x = 0, y = 0)$ with an injection angle of $5.7°$ with respect to the negative x-axis. Around the turning point it is shown: (a) the result from the wave kinetic code, (b) the reference solution, (c) the difference between WKBeam and the reference solution and (d) the statistical uncertainty of the wave kinetic code.

The inverse Fourier transform provides the wave field

$$E(\mathrm{x}, \mathrm{y}) = \frac{\kappa^{5/3}}{\sqrt{\pi}} \int \frac{\left(1 - N_\mathrm{y}^2\right)^{1/4}}{e^{-\frac{2}{3}\kappa\left(1 - N_\mathrm{y}^2\right)^{3/2}}} \mathrm{Ai}\left(-\kappa^{2/3}\left(1 + \mathrm{x} - N_\mathrm{y}^2\right)\right) \hat{E}(\mathrm{x}, N_\mathrm{y})\mathrm{d}N_\mathrm{y}. \qquad (6.50)$$

The electric field on the antenna plane is assumed to be (D.1).

As a consistency check, let us assume that wave propagation around $\mathrm{x} \approx 0$ is studied, with the physical meaning of a negligible influence of the refractive index variation. Then approximation (6.46) and, upon assuming propagation to the left also (6.47) is appropriate for the remaining
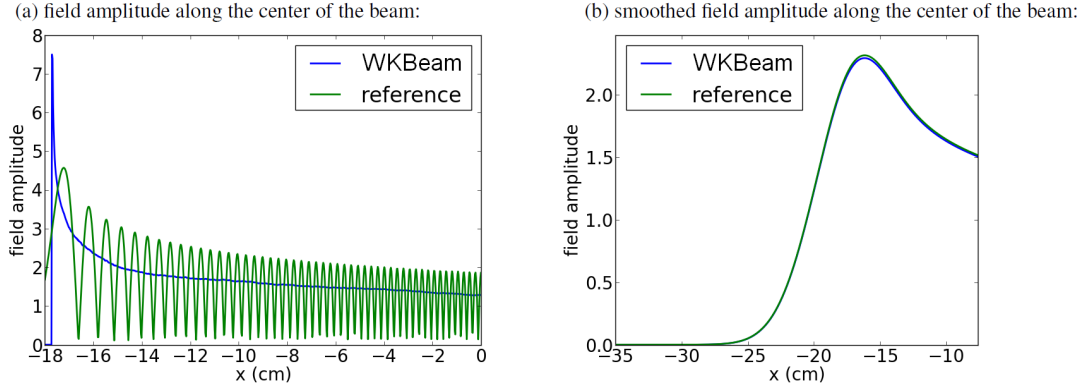
(a) field amplitude along the center of the beam:

(b) smoothed field amplitude along the center of the beam:

Figure 6.5.: Beam propagating in a linear layer with $L = 17.7\,\text{cm}$, frequency $f = 64\,\text{GHz}$, initial beam width $w = 3.19\,\text{cm}$ and initial curvature radius $R = 512\,\text{cm}$. $n_0 = 10000$ rays have been traced and the size of the bins is $\Delta\text{x} = 0.023\,\text{cm}$ and $\Delta\text{y} = 0.13\,\text{cm}$. The injection is parallel to the x-axis. It is shown (a) field amplitude along the center of the, i.e. the x-axis, (b) data from (a) smoothed according to equation (6.53).

Airy function in (6.50), with the result that

$$E(\text{x}, \text{y}) = \frac{\kappa}{2\pi} \int e^{i\kappa \text{y} N_\text{y}} \left(\frac{1 - N_\text{y}^2}{1 + \text{x} - N_\text{y}^2} \right)^{1/4} e^{-\frac{2}{3} i\kappa \left[\left(1 + \text{x} - N_\text{y}^2\right)^{3/2} - \left(1 - N_\text{y}^2\right)^{3/2} \right]} \, dN_\text{y}. \qquad (6.51)$$

We should recover formula (6.10) for free space in this limit. Indeed, a Taylor expansion of the expression in the exponent around $\text{x} \approx 0$ yields

$$\left(1 + \text{x} - N_\text{y}^2\right)^{3/2} - \left(1 - N_\text{y}^2\right)^{3/2} \approx \frac{3}{2}\sqrt{1 - N_\text{y}^2}\,\text{x} \qquad (6.52)$$

with the expected consequence.

As an example, in figure 6.4 the results for the case of a reflected beam are shown, with (6.50) as a reference solution and the integral computed numerically. It can be seen that in the reference solution (b) an interference pattern is visible. Instead, it is absent in the weak semiclassical limit $\kappa \to \infty$ considered in the wave kinetic code (a). Therefore, the difference (c) exceeds by far the statistical uncertainty (d). However, the shape of the beam intensity is well reproduced by the wave kinetic code.

The smaller the injection angle is chosen, the more the interference pattern is pronounced. The WKBeam code even produces results for zero injection angle, presented in figure 6.5. Again,

the interference pattern which is present for the reference solution up to the antenna plane is not reproduced by the wave kinetic code, cf. figure 6.5 (a). In addition, the numerical result drops to zero at the cut-off layer $x = 17.7\,\text{cm}$ whereas the reference solution shows an evanescent field contribution even beyond. Instead, there is a good agreement in (b), where the result is smoothed over the interval $s = 2\,\text{cm} \gg 0.47\,\text{cm} = \lambda$, large compared to the free space wave length $\lambda = 2\pi/k_0$. The smoothing is realized by mean of a convolution:

$$A^2_{\text{smooth}}(x, y) = \int e^{-\frac{1}{2}\frac{(x-x')^2+(y-y')^2}{s^2}} A^2(x', y')dx'dy'. \tag{6.53}$$

Hence, also for the reflectometry case, the smoothed amplitude is an accurate quantity. The formalism adapted in the wave kinetic code, however, does not allow a reproduction of the detailed interference pattern exhibited by the exact solution.

6.4. Fluctuations in free space

The benchmarks presented in previous sections do not involve fluctuations. Here, a simplified model of a random media is presented to test the numerical scattering scheme for fluctuations, namely the wave equation

$$\left(\frac{\partial^2}{\partial x^2} + \frac{\partial^2}{\partial y^2} + \kappa^2(1 + \delta n^2(x, y))\right) E(x, y) = 0. \tag{6.54}$$

Once again, the dimensionality is specified to $m = 2$ and scalar waves are considered. Therefore, all matrix-valued quantities reduce to scalars. Fluctuations are introduced via a random contribution to the refractive index $\delta n^2(x, y)$. For the special case of no fluctuations, $\delta n^2(x, y) \equiv 0$, wave equation (6.54) reduces to the free space wave equation (6.1). Hence, the free space Hamiltonian (6.3) is still an appropriate choice with correction factor $\xi = 2$. The fluctuating part $\delta n^2(x, y)$ in the wave equation is a simple function of the coordinates (x, y), not involving any complicated operators. For the fluctuation part of the dispersion symbol, this yields

$$D_F(x, N) = \sqrt{\kappa}\delta n^2(x), \tag{6.55}$$

6. Benchmarking: simplified models

where the ordering parameter δ, cf. equation (3.10), is accounted for by the prefactor $\sqrt{\kappa}$ on the r.h.s. The following statistical properties are considered:

$$\mathbb{E}\left(\delta n^2(x,y)\right) = 0, \tag{6.56a}$$

$$\mathbb{E}\left(\delta n^2(x,y)\delta n^2(x',y')\right) = \Delta^2 e^{-\frac{(x-x')^2}{4\Delta x^2}-\frac{(y-y')^2}{4\Delta y^2}}. \tag{6.56b}$$

The first property (6.56a) states that the mean value of the fluctuations vanishes. The two-point correlation function (6.56b) inserted into (3.28) yields the spectral scattering amplitude

$$G(x,N) = \frac{\kappa^3 \Delta^2}{\pi}\Delta x \Delta y\, e^{-\kappa^2\left(\Delta x^2 N_x^2 + \Delta y^2 N_y^2\right)}. \tag{6.57}$$

Then, the scattering cross section as presented in (4.68) yields

$$\sigma(x,N,N') = 8\pi G(x,N-N')\delta\left(H(x,N')\right). \tag{6.58}$$

The parameter Σ for the Poisson process which produces scattering events is obtained as an integral on the scattering cross section σ, cf. equation (4.25b). Inserting the Hamiltonian (6.3) into (6.58) and integrating in N_x-direction on Dirac's delta, this integral reads

$$\Sigma(x,N) = 2\pi \int \left.\frac{G(x,N-N')}{|N_x'|}\right|_{N_x'=-\sqrt{1-N_y'^2}} dN_y'. \tag{6.59}$$

Note that Dirac's delta in (6.58) in principle, yields a contributions for all branches of the dispersion variety, i.e. for $N_x' = \pm\sqrt{1-N_y'^2}$. However, for this benchmark a beam composed by orbits propagating to the left, i.e. $N_x = -1 + \mathcal{O}\left(N_y^2\right)$, is considered and the chosen parameters ($\kappa\Delta x \approx 2.6$, cf. figure 6.7) suppress large jumps in the refractive index of the order $\Delta N_x \approx 2$, which could lead to backscattering. This is seen in the fluctuation spectrum (6.57), where the factor $e^{-\kappa^2\Delta x^2 \Delta N_x^2} \approx 10^{-12}$ is present. In turn such jumps would be required for the orbits to reach the positive branch with $N_x' = 1 + \mathcal{O}\left(N_y'^2\right)$, justifying that we restrict ourselves to the branch $N_x' = -\sqrt{1-N_y'^2}$ in (6.59). The remaining integral in (6.59) can be computed numerically, with G provided by equation (6.57).

Once a scattering event is produced, according to the numerical scheme in section 4.2, the new refractive index N' is chosen following as a probability density $\sigma(x,N,N')$, defined in (6.58).

Upon accounting for the free space Hamiltonian, this probability distribution is

$$\sigma(x, N, N') \propto \frac{G(x, N - N')}{|N'_\text{x}|} \delta\left(N'_\text{x} + \sqrt{1 - N'^2_\text{y}}\right).$$ (6.60)

Given the fact that prefactors are not of importance here, they are dropped and the equation is restricted to a proportionality statement. As mentioned also in section 5.1.2, the probability distribution is no standard distribution, so no standard functions can be used to generate the required random numbers. Therefore, the value for N'_y is generated with Metropolis-Hastings algorithm, see appendix F, where

$$p_\text{proposal} \propto e^{-\kappa^2 \Delta\text{y}^2\left(N_\text{y} - N'_\text{y}\right)^2}$$ (6.61)

serves as proposal probability distribution required by the algorithm. Once the value for N'_y is picked, N'_x is determined by the dispersion relation for Hamiltonian (6.3):

$$N'_\text{x} = -\sqrt{1 - N'^2_\text{y}},$$ (6.62)

as expressed by the δ-distribution in (6.60).

To construct a reference solution, snapshots of the fluctuation $\delta n^2(x)$ are generated randomly so that the statistical properties (6.56) are fulfilled. The original wave equation (6.54) is solved for every single set of fluctuations and the resulting electric field amplitude squared is averaged. This quantity then is suitable to be compared with the wave kinetic code. Of course, given the complexity of equation (6.54) for each realization of the fluctuations δn^2, a numerical solution is required. As a model for the fluctuations, δn^2 is represented in Fourier series

$$\delta n^2(\text{x}, \text{y}) = \sum_{a,b} \Phi_{a,b} e^{i\pi a \frac{\text{y}}{\text{y}_0}} e^{2\pi i b \frac{\text{x}}{\text{x}_0}},$$ (6.63)

where $\Phi_{a,b}$ are random numbers. The wave equation is solved by the spectral method in the variable y transversal to the propagation direction. Specifically, the electric field in such mode decomposition reads

$$E(\text{x}, \text{y}) = \sum_m E_m(\text{x}) e^{i\pi m \frac{\text{y}}{\text{y}_0}},$$ (6.64)

6. Benchmarking: simplified models

yielding the wave equation

$$\left(\frac{\partial^2}{\partial x^2} - \frac{\pi^2 m^2}{y_0^2} + \kappa^2\right) E_m(x) + \kappa^2 \sum_{a,b} \Phi_{m-a,b} e^{2\pi i b \frac{x}{x_0}} E_a(x) = 0. \tag{6.65}$$

Equation (6.65) being of second order must be equipped with two boundary conditions. The beam is launched at $x = 0$ and assumed to propagate to the left, so the electric field on the antenna plane at $x = 0$ is mode-decomposed and $E_m(x = 0)$ serve as boundary conditions. Physically, the second condition to be modeled is the information that the beam propagates to the left. In equation (6.65) this can be described by introducing an absorption layer with non-vanishing absorption coefficient $\gamma(x)$ for $x \in (x_{\min}, -x_0)$ by hand, where $x_{\min} < 0$ determines the left boundary for the numerical solver and $-x_0 < 0$. It is assumed that this layer completely absorbs the beam intensity so that the observed beam is purely propagating in the negative x-direction and the boundary condition $E_m(x_{\min}) = 0$ applies at $x = x_{\min}$. Instead, the solution is not affected by the absorption in the range $x_0 < x < 0$, so in this area the solution for the wave equation (6.65) without absorption is obtained. The wave equation with absorption reads

$$\left(\frac{\partial^2}{\partial x^2} + i\gamma(x) - \frac{\pi^2 m^2}{y_0^2} + \kappa^2\right) E_m(x) + \kappa^2 \sum_{a,b} \Phi_{m-a,b} e^{2\pi i b \frac{x}{x_0}} E_a(x) = 0. \tag{6.66}$$

This equation with the above-stated boundary condition constitutes a two-point boundary value problem on the interval $[x_{\min}, 0]$, which is solved by a finite element library.

Note that absorption might not be perfect, causing a small contribution of the beam which gets reflected at the boundary $x = x_{\min}$. This can make appear an interference pattern on top of the desired solution, cf. figure 6.7 and 6.7 (f).

Here, fluctuations are fully characterized by the coefficients $\Phi_{a,b}$. They are chosen randomly with a distribution such that the properties (6.56) are fulfilled. For the random generation, the ansatz

$$\Phi_{a,b} = \tilde{\Phi}_{a,b} e^{i\alpha_{a,b}} \tag{6.67a}$$

is used. Here, $\tilde{\Phi}_{a,b}$ are deterministic coefficients to be determined later on and

$$\alpha_{a,b} = \alpha_a^{(\mathrm{x})} + \alpha_b^{(\mathrm{y})} \tag{6.67b}$$

are random phases picked according to

$$\alpha_a^{(i)} = -\alpha_{-a}^{(i)} \text{ uniformly distributed in } \in [0, 2\pi) \text{ for } a \geq 0,$$

$$\text{with superscript } (i) = (\mathrm{x}), (\mathrm{y}) \tag{6.67c}$$

Ansatz (6.67) reproduces the stochastic properties (6.56). In fact, the average of the fluctuation in terms of mode decomposition (6.63) reads

$$\mathbb{E}\left(\delta n^2(\mathrm{x}, \mathrm{y})\right) = \sum_{a,b} e^{i\pi a \frac{\mathrm{y}}{\mathrm{y}_0}} e^{2\pi i b \frac{\mathrm{x}}{\mathrm{x}_0}} \tilde{\Phi}_{a,b} \mathbb{E}\left(e^{i\alpha_{a,b}}\right). \tag{6.68}$$

Here, the ansatz (6.67a) is used and the averaging only applies on the random numbers (6.67c). The way the random numbers are constructed (6.67c) ensures that this expectation value vanishes, in agreement with (6.56a).

 Next, the mean value of the two-point correlation function (6.56b) is evaluated: This fixes the deterministic coefficients $\tilde{\Phi}_{a,b}$. Substituting (6.63) into (6.56b) yields

$$\mathbb{E}(\delta n^2(\mathrm{x}, \mathrm{y})\delta n^2(\mathrm{x}', \mathrm{y}')) = \sum_{a,b,a',b'} \tilde{\Phi}_{a,b}\tilde{\Phi}_{a',b'}^* e^{i\pi \frac{a\mathrm{y} - a'\mathrm{y}'}{\mathrm{y}_0}} e^{2\pi i \frac{b\mathrm{x} - b'\mathrm{x}'}{\mathrm{x}_0}}$$

$$\times \mathbb{E}\left(e^{i(\alpha_a^{(\mathrm{x})} - \alpha_{a'}^{(\mathrm{x})})}\right) \mathbb{E}\left(e^{i(\alpha_b^{(\mathrm{y})} - \alpha_{b'}^{(\mathrm{y})})}\right). \tag{6.69}$$

Since the coefficients $\alpha_a^{(\mathrm{x})}$ and $\alpha_b^{(\mathrm{y})}$ are chosen in a statistically independent way, the expectation value can be split as in equation (6.69). As an example, the average $\mathbb{E}\left(e^{i(\alpha_a^{(\mathrm{x})} - \alpha_{a'}^{(\mathrm{x})})}\right)$ running on the x-component is discussed; the y-part can be treated analogously. Three cases are distinguished:

- $a \neq a'$ and $a \neq -a'$: The random numbers $\alpha_a^{(\mathrm{x})}$ and $\alpha_{a'}^{(\mathrm{x})}$ are statistically independent, the average yields

$$\mathbb{E}\left(e^{i(\alpha_a^{(\mathrm{x})} - \alpha_{a'}^{(\mathrm{x})})}\right) = \mathbb{E}\left(e^{i\alpha_a^{(\mathrm{x})}}\right) \mathbb{E}\left(e^{-i\alpha_{a'}^{(\mathrm{x})}}\right) = 0. \tag{6.70a}$$

103

6. Benchmarking: simplified models

- $a = -a'$: According to (6.67c), the random numbers fulfil $\alpha_a^{(x)} = -\alpha_{a'}^{(x)}$. The average reads

$$\mathbb{E}\left(e^{i(\alpha_a^{(x)} - \alpha_{a'}^{(x)})}\right) = \mathbb{E}\left(e^{2i\alpha_a^{(x)}}\right) = 0. \tag{6.70b}$$

- $a = a'$: obviously, $\alpha_a^{(x)} = \alpha_{a'}^{(x)}$ and the average is

$$\mathbb{E}\left(e^{i(\alpha_a^{(x)} - \alpha_a^{(x)})}\right) = \mathbb{E}(1) = 1. \tag{6.70c}$$

In summary, we find

$$\mathbb{E}\left(e^{i(\alpha_a^{(x)} - \alpha_{a'}^{(x)})}\right) = \delta_{a,a'}, \tag{6.71a}$$

where $\delta_{a,a'}$ is Kronecker's delta and, in analogy,

$$\mathbb{E}\left(e^{i(\alpha_b^{(y)} - \alpha_{b'}^{(y)})}\right) = \delta_{b,b'}. \tag{6.71b}$$

These results are substituted in equation (6.69) with the result

$$\mathbb{E}(\delta n^2(\mathrm{x}, \mathrm{y})\delta n^2(\mathrm{x}', \mathrm{y}')) = \sum_{a,b} \left|\tilde{\Phi}_{a,b}\right|^2 e^{i\pi a\frac{\mathrm{y}-\mathrm{y}'}{\mathrm{y}_0}} e^{2\pi i b\frac{\mathrm{x}-\mathrm{x}'}{\mathrm{x}_0}}, \tag{6.72}$$

where on the right no random variables occur any longer. Mathematically, equation (6.72) is a decomposition into a Fourier series of the two-point correlation function. Given the two-point correlation function (6.56b), the Fourier coefficients $\left|\tilde{\Phi}_{a,b}\right|^2$, upon accounting for the substitution $\tilde{\mathrm{x}} = \mathrm{x} - \mathrm{x}'$ and $\tilde{\mathrm{y}} = \mathrm{y} - \mathrm{y}'$, read

$$\left|\tilde{\Phi}_{a,b}\right|^2 = \frac{\Delta^2}{2\mathrm{x}_0\mathrm{y}_0} \int_{-\mathrm{x}_0/2}^{\mathrm{x}_0/2} e^{-\frac{\tilde{\mathrm{x}}^2}{4\Delta\mathrm{x}^2} - 2\pi i a\frac{\tilde{\mathrm{x}}}{\mathrm{x}_0}} \, \mathrm{d}\tilde{\mathrm{x}} \int_{-\mathrm{y}_0}^{\mathrm{y}_0} e^{-\frac{\tilde{\mathrm{y}}^2}{4\Delta\mathrm{y}^2} - \pi i b\frac{\tilde{\mathrm{y}}}{\mathrm{y}_0}} \, \mathrm{d}\tilde{\mathrm{y}}. \tag{6.73}$$

The integrals can be computed analytically if the integration boundaries are placed to infinity. This is a good approximation with the assumption of a small fluctuation correlation length, i.e. $\Delta\mathrm{x} \ll \mathrm{x}_0$ and $\Delta\mathrm{y} \ll \mathrm{y}_0$, since it affects the tails of the Gaussian in the integral, with the result

that

$$\left|\tilde{\Phi}_{a,b}\right|^2 = 2\pi\Delta^2 \frac{\Delta\text{x}\Delta\text{y}}{\text{x}_0\text{y}_0} e^{-\pi^2\left[4\frac{\Delta\text{x}^2}{\text{x}_0^2}a^2+\frac{\Delta\text{y}^2}{\text{y}_0^2}b^2\right]}. \tag{6.74}$$

This condition for the coefficients $\tilde{\Phi}_{a,b}$, yielding real and positive numbers for their norm squared, can be fulfilled, justifying ansatz (6.67a) to reproduce the two-point correlation function (6.56b). Equation (6.74) then determines the norm of the deterministic fluctuation coefficients. The coefficient for one realization of fluctuations $\Phi_{a,b}$ is given by (6.67a), where the deterministic number $\tilde{\Phi}_{a,b}$ is multiplied with a random phase. Therefore, the phase of $\tilde{\Phi}$ has no importance. Without any restriction, the coefficients $\tilde{\Phi}$ are chosen to be the real and positive square root of (6.74):

$$\tilde{\Phi}_{a,b} = \sqrt{2\pi\frac{\Delta\text{x}\Delta\text{y}}{\text{x}_0\text{y}_0}}\Delta e^{-\pi^2\left[2\frac{\Delta\text{x}^2}{\text{x}_0^2}a^2+\frac{1}{2}\frac{\Delta\text{y}^2}{\text{y}_0^2}b^2\right]}. \tag{6.75}$$

The result of one run of the full wave solver is the electric field $E_i(\text{x}, \text{y})$. Here, i labels the run. The averaged field energy density for K runs is computed as

$$\mathbb{E}\left(|E(\text{x},\text{y})|^2\right) = \frac{1}{K}\sum_{k=1}^{K}|E_k(\text{x},\text{y})|^2. \tag{6.76}$$

The corresponding statistical uncertainty is estimated by

$$\sigma_{|E|^2}(\text{x},\text{y}) = \frac{1}{K}\sqrt{\sum_{k=1}^{K}\left(|E_k(\text{x},\text{y})|^2 - \mathbb{E}\left(|E(\text{x},\text{y})|^2\right)\right)^2}. \tag{6.77}$$

In this section, two test runs for different sets of parameters are presented. For the beam frequency, $f = 50\,\text{GHz}$ is chosen. The initial beam width is $w = 1.5\,\text{cm}$, the initial curvature radius $R = 20\,\text{cm}$. This yields a good focusing, compensating for the spreading of the beam due to diffractive effects so that in the range of observation $\text{x}[\text{cm}] \in [-10, 0]$, without fluctuations, an approximately constant beam amplitude is obtained. The fluctuation correlation lengths are $\Delta\text{x} = \Delta\text{y} = 0.25\,\text{cm}$. For the mode decomposition, 80 modes in x-direction and 19 modes in y-direction are in use.

(a) fluctuations δn^2:

(b) beam without fluctuations:
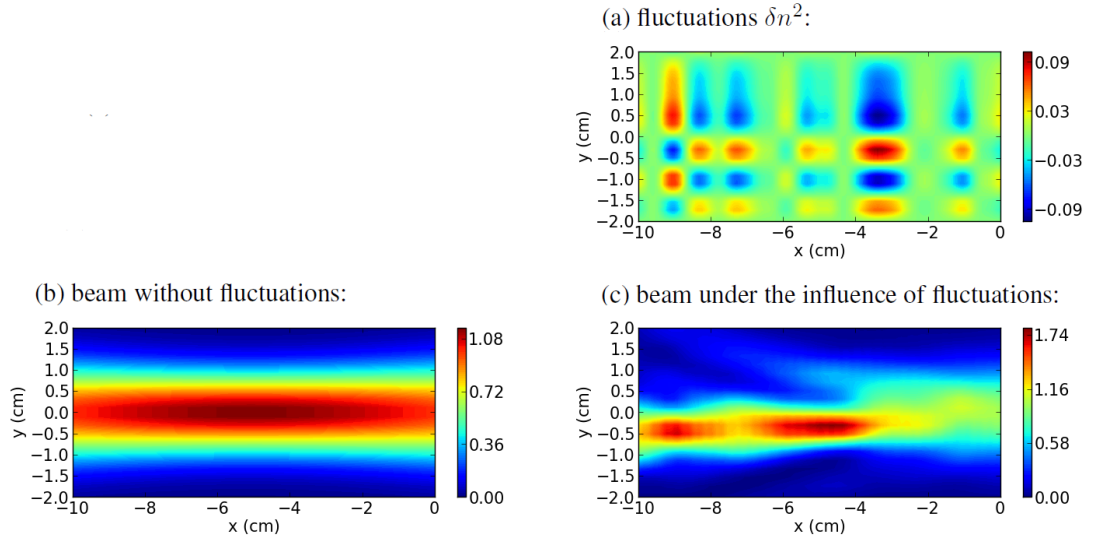
(c) beam under the influence of fluctuations:

Figure 6.6.: Beam launched at x = 0 and propagating to the left with and without the effect of fluctuation. (a) deviation of the squared refractive index n^2 due to the randomly generated fluctuation with parameters $\Delta = 0.05$, $\Delta x = \Delta y = 0.25$ cm, (b) beam intensity for fluctuations turned off, (c) beam intensity, when the fluctuations (a) are taken into account.

In figure 6.6, as an example, the effect of fluctuations on the beam propagation is shown for the turbulence realization presented in the first panel (a). In part (b) on the left, the beam for free space without fluctuations is displayed, whereas on the right, the result of one single run of the full wave solver is shown (c). The fluctuation is randomly generated as described before with the parameter determining the strength of fluctuation $\Delta = 0.05$. It can be seen that the beam under the influence of fluctuations has no longer the nice, Gaussian shape it has in free space. Around x = -3.5 cm there is a relatively strong gradient of δn^2 pointing downward, deflecting the main contribution of the beam to the bottom. In addition, the beam propagates through the positive density blob centered at x = -3.5 cm, y = -0.25 cm, acting like a lens focusing the beam. This increases the beam intensity to a maximum value of around 1.75, exceeding the maximal intensity of around 1 for the beam neglecting fluctuations, cf. figure 6.6, (b).

To allow a comparison with the wave kinetic code, 1380 runs of the full wave solver for different realizations of the fluctuations have been performed and the average (6.76) has been computed according to (6.76). For $\Delta = 0.05$, the result is shown in figure 6.7. The effect of the fluctuation is seen best in the comparison (e) to the analytical free space solution without fluctuations which

is well reproduced by the wave kinetic code in the absence of fluctuations. The difference shown there vanishes on the antenna plane at x = 0, where the beam is launched and hence not yet affected by any properties of the medium. Instead, after propagation through the fluctuating region, the beam intensity is increased at its boundaries and decreased in the center, corresponding to a spreading of the beam. The decrease is by about 20% of the maximum beam intensity. Most important for the benchmarking is that the difference (f) between the wave kinetic code and the full wave solver is only 3% of the maximum beam intensity. This is the order of magnitude of the statistical uncertainty of both, full wave solver (b) and wave kinetic code (d), and one order of magnitude smaller then the effect of fluctuations (e), indicating that the effect of fluctuations is well-resolved and the results are correct. In figure 6.8 the same comparison is presented for a higher level of fluctuations, $\Delta = 0.1$. The higher level of fluctuation increases its effect on the beam. Still, the comparison of kinetic code and full wave solver gives satisfactory results.

(a) result of the full wave solver:

(b) uncertainty of the full wave solver:

(c) result of the WKBeam code:

(d) uncertainty of WKBeam:

(e) effect of fluctuation:
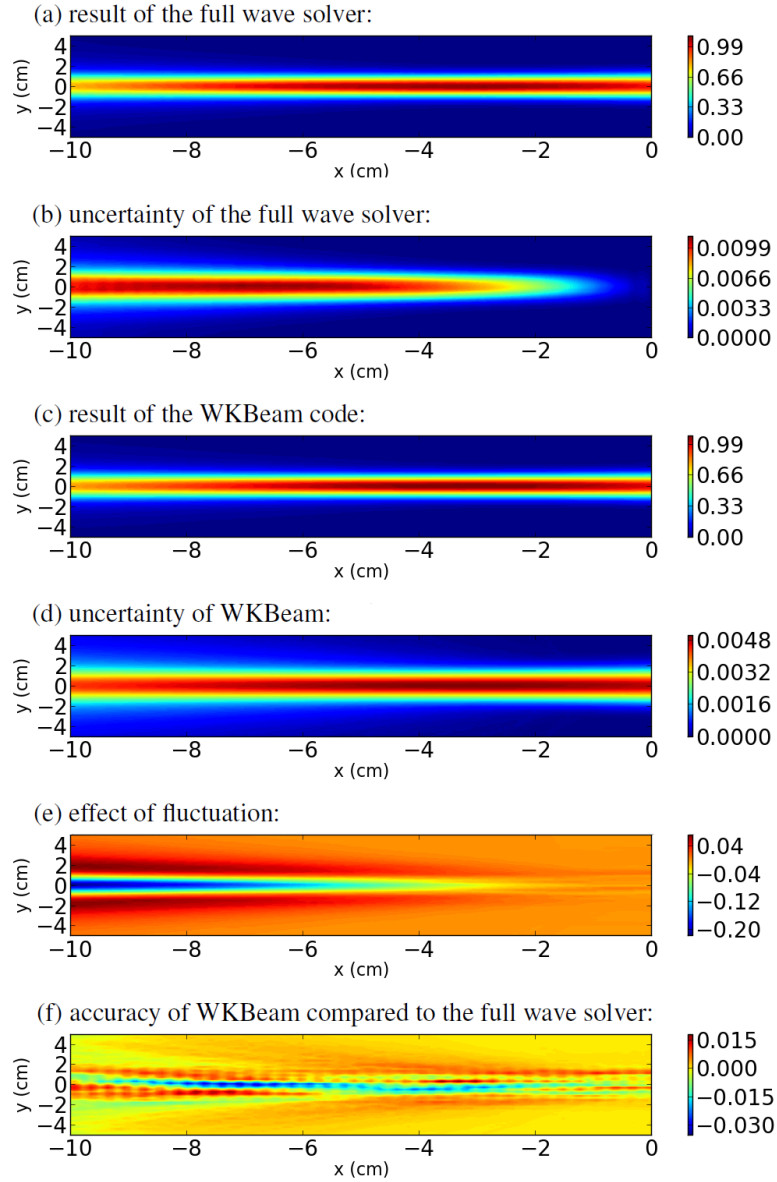
(f) accuracy of WKBeam compared to the full wave solver:

Figure 6.7.: Results for a beam in free space with fluctuation strength $\Delta = 0.05$, fluctuation correlation lengths $\Delta x = \Delta y = 0.25 \, \text{cm}$, beam frequency $f = 50 \, \text{GHz}$, initial beam width $w = 1.5 \, \text{cm}$ and initial curvature radius $R = 20 \, \text{cm}$. It is shown: (a) the averaged result of the full wave solver and (b) its statistical uncertainty, (c) the results produced by WKBeam with (d) the corresponding statistical uncertainty, (e) the difference between the wave kinetic code and the analytical result neglecting fluctuations and (f) the difference between the wave kinetic code and the full wave solver, an interference pattern aligned with the y-direction is observed, due to the effect discussed after equation (6.66).
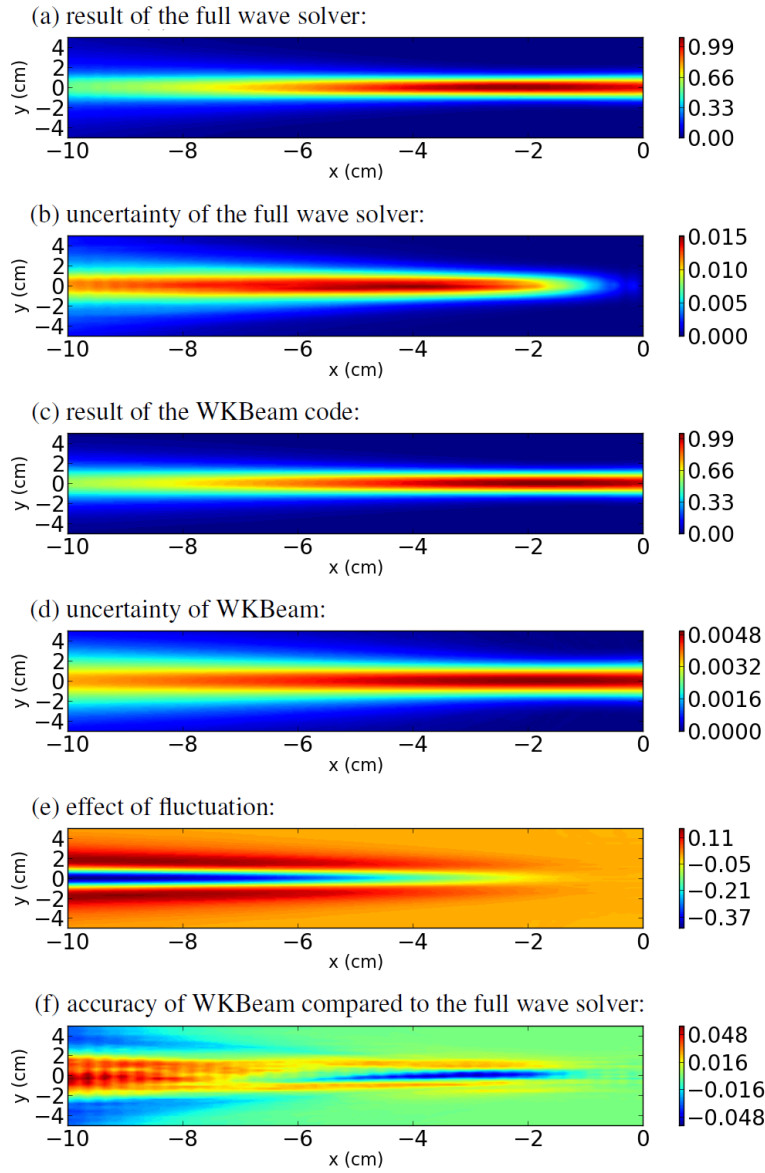
(a) result of the full wave solver:

(b) uncertainty of the full wave solver:

(c) result of the WKBeam code:

(d) uncertainty of WKBeam:

(e) effect of fluctuation:

(f) accuracy of WKBeam compared to the full wave solver:

Figure 6.8.: Results for a beam in free space with fluctuation strength $\Delta = 0.1$, fluctuation correlation lengths $\Delta x = \Delta y = 0.25 \, \text{cm}$, beam frequency $f = 50 \, \text{GHz}$, initial beam width $w = 1.5 \, \text{cm}$ and initial curvature radius $R = 20 \, \text{cm}$. It is shown: (a) the averaged result of the full wave solver and (b) its statistical uncertainty, (c) the results produced by WKBeam with (d) the corresponding statistical uncertainty, (e) the difference between the wave kinetic code and the analytical result neglecting fluctuations and (f) the difference between the wave kinetic code and the full wave solver, an interference pattern aligned with the y-direction is observed, due to the effect discussed after equation (6.66).

6.5. Convergence test

As announced in the introduction to this chapter, we shall discuss the impact of numerical parameters on the result of the wave kinetic code, i.e. the number of rays and the number of bins, defining their edge lengths. For this analysis, a beam with frequency $f = 50\,\text{GHz}$, initial beam width $w = 1.5\,\text{cm}$ and initial curvature radius $R = 20\,\text{cm}$ is launched and observed in an area x[cm] $\in [-10, 0]$ and y[cm] $\in [-9, +9]$. The beam propagates in free space. With the chosen parameters, the beam has an approximately constant width over the whole observation range. We define

$$\text{Error}_{\text{L2}} := \frac{\int \left[|E(\text{x}, \text{y})|^2 - |E_{\text{ref}}(\text{x}, \text{y})|^2 \right]^2 \text{dxdy}}{\int |E_{\text{ref}}(\text{x}, \text{y})|^4 \text{dxdy}}. \tag{6.78}$$

and refer to this expression as error norm. It is one single number which expresses the global accuracy of the solution of the wave kinetic code $|E(\text{x}, \text{y})|^2$ in comparison with the analytical reference solution $|E_{\text{ref}}(\text{x}, \text{y})|^2$, cf. (6.14). If and only if both are the same, the error norm vanishes. An estimate of the error norm in terms of the statistical uncertainty reads

$$\text{Uncertainty}_{\text{L2}} := \frac{\int \sigma_{E^2}^2(\text{x}, \text{y})\text{dxdy}}{\int |E_{\text{ref}}(\text{x}, \text{y})|^4 \text{dxdy}}. \tag{6.79}$$

Here, σ_{E^2} denotes the standard deviation of the Monte-Carlo estimator for E^2 (4.53). In case statistical uncertainty is the only source of inaccuracies, (6.78) and (6.79) are the same.

Performing a scan over the number of traced rays and the number of bins, we obtain the results in figure 6.9. The number of bins is given by $n_b = n_{\text{x}} n_{\text{y}}$, where n_{x} and n_{y} denote the number of subdivisions of the area under investigation in x-direction and y-direction, respectively. For the test presented here, these subdivisions are chosen such that $n_{\text{x}} = n_{\text{y}}$.

It is seen that, in general, the more rays are traced the lower the statistical uncertainty is. This result was predicted by section 4.3. The error shows the same behavior. Comparing error norm and statistical uncertainty, it is conspicuous that for a large number of bins, they are the same. This is because then the bins are small and the approximation made in (3.74), namely the assumption that the wave field amplitude is constant over the whole bin, is a good approximation such that the only inaccuracy is due to statistics. Instead, if only few bins are taken, at some point, more specificly $\log_{10} n_b \approx 3.55$, corresponding to 60 bins in each direction, the error norm explodes,
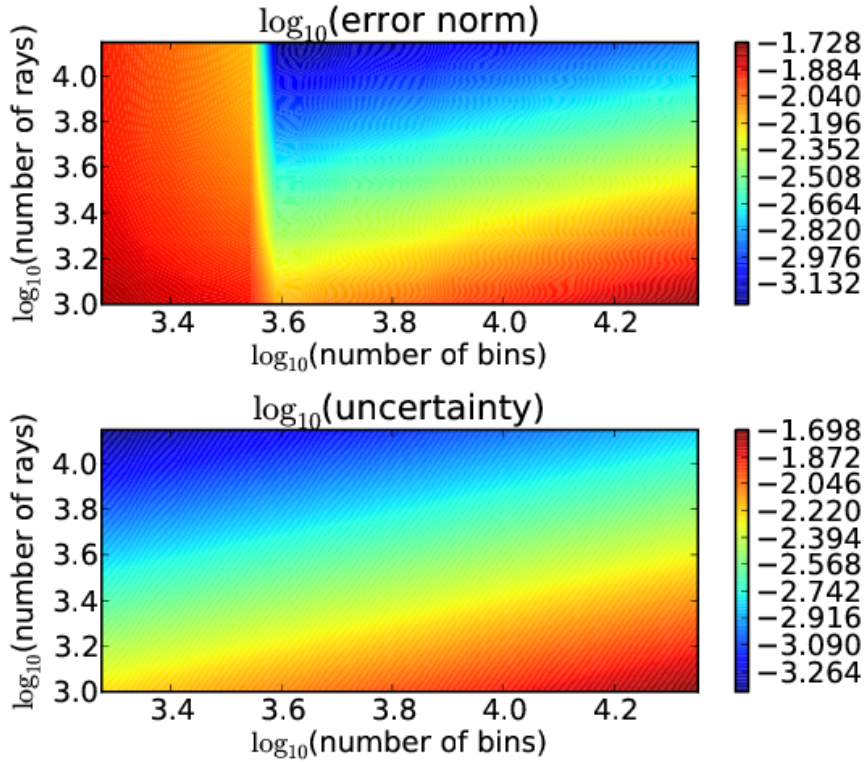
Figure 6.9.: Top: Error norm. Bottom: statistical uncertainty. Both depending on the number of traced rays n_0 and the number of bins covering the observation area n_b.

while the statistical uncertainty still decreases. This can be explained by the growing bin size which is, at some point, just too rough to reproduce the fine structure of the beam. Instead, inside each bin the contributions of a lot of rays are summed up, leading to a small statistical uncertainty. Here, this is the case when $\Delta y = 0.3 \, \text{cm}$, which starts to be comparable to the beam width $w = 1.5 \, \text{cm}$. The precise formulation of a criteria for the automatic determination of the maximum bin size allowed before the error explodes is left for future work. However, as a guideline for this thesis, we say that the bin size should be considerably smaller then the structures to resolve. For such parameters, this section has shown that the error is as large as expected from the statistical uncertainty.

7

Results for tokamak plasmas

The benchmarking in the previous chapter has showed that the wave kinetic code WKBeam yields results that are in satisfactory agreement with the reference solutions. Therefore, we can now exploit the code for real, physical tokamak situations. The equations involved in such situations are more complicated than those describing the simplified models. Furthermore, the simple geometry with the antenna plane well-aligned to Cartesian coordinate axis considered for the benchmarks is no longer appropriate.

The geometry for physical situations is three dimensional, so for the applications in this chapter, $m = 3$ is specified, with a Cartesian coordinate vector $x = (\mathrm{x}, \mathrm{y}, \mathrm{z})$ and a Cartesian refractive index vector $N = (N_\mathrm{x}, N_\mathrm{y}, N_\mathrm{z})$.

This chapter is organized as follows: First, the geometry of the tokamak and the antenna plane are presented as well as some useful coordinate transformations. Next, there is a discussion on the lowest-order contribution of the dispersion tensor D_0 for magnetized plasmas and a Hamiltonian is constructed. This is followed by the model for fluctuations and absorption.
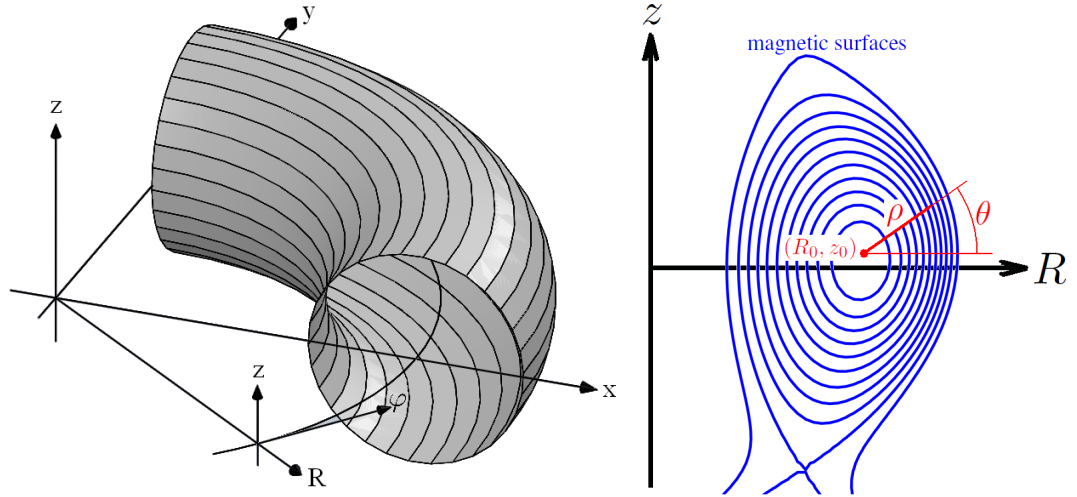
Figure 7.1.: Left: Section of the "donut"-shaped tokamak. The Cartesian coordinate system (x, y, z) has its origin on the axis of rotation. In each poloidal plane, a coordinate system (R, φ, z) is localized. The R-axis points radially outwards, the φ-axis in toroidal direction and the z-axis is the z-axis of the Cartesian coordinate system. Right: Coordinates in one poloidal plane. The magnetic surfaces suggest the use of a coordinate system (ρ, θ) in the poloidal plane. The point (R_0, z_0) is the position of the magnetic axis.

7.1. Tokamak geometry

The wave kinetic equation is formulated in terms of Cartesian coordinates. However, the tokamak has a special toroidal symmetry which suggests the use of a cylindrical coordinate system. So both, the Cartesian as well as the cylindrical coordinate system, are in use and a coordinate transformation is needed. To illustrate how coordinates are defined, the "donut"-shaped tokamak with the attached coordinate systems is shown on the left in figure 7.1. A cut through the tokamak tube containing the R- and z-axis is called poloidal plane, whereas the direction perpendicular to it is referred to as toroidal direction. The toroidal symmetry of the tokamak involves every equilibrium quantity including the background plasma profiles. For our purposes, these are the electron density n_e, the magnetic field B and the electron temperature T_e. The magnetic field is such that the field lines lie on closed surfaces called magnetic surfaces. The central magnetic surface collapsing to a single line, is called magnetic axis. The cut of the magnetic surfaces and the magnetic axis through the poloidal plane is shown on the right in figure 7.1. The surfaces can be labeled e.g. with the magnetic flux Ψ flowing through them or alternatively with $\rho = \sqrt{\Psi}$.

Hence, an alternative coordinate system in the poloidal plane (ρ, θ) is introduced, where $\rho = \sqrt{\Psi}$ and θ is the angle as shown in figure 7.1. Note that the flux in this thesis is normalized so that $\rho = \Psi = 0$ on the magnetic axis and $\rho = \Psi = 1$ at the separatrix (last close flux surface). The coordinate ρ it is also referred to as normalized minor radius coordinate, which is motivated by the fact that it measures the distance from the magnetic axis under the simplifying approximations of circular magnetic surfaces and a constant magnetic field. Given the fact that the electron density and the temperature equilibrate fast on magnetic surfaces [37], it is appropriate to assume that they are functions on ρ only. Instead, the magnetic field depends on (R, z). However, the larger (toroidal) component of the magnetic field is in first approximation a function of R only, and decreases as $1/R$ away from the z-axis.

Given the Cartesian coordinates (x, y, z), the components (R, z) of the cylindrical coordinate system are given by the following relations obtained from geometry:

$$\begin{pmatrix} R \\ z \end{pmatrix} = \begin{pmatrix} \sqrt{x^2 + y^2} \\ z \end{pmatrix}. \tag{7.1}$$

Given a vector A in components (A_R, A_φ, A_z), the transformation to Cartesian coordinates is a simple rotation around the z-axis, i.e.

$$\begin{pmatrix} A_x \\ A_y \\ A_z \end{pmatrix} = \begin{pmatrix} \cos\varphi & -\sin\varphi & 0 \\ \sin\varphi & \cos\varphi & 0 \\ 0 & 0 & 1 \end{pmatrix} \begin{pmatrix} A_R \\ A_\varphi \\ A_z \end{pmatrix}. \tag{7.2}$$

with the rotation angle

$$\varphi = \arctan\frac{y}{x}. \tag{7.3}$$

In later applications, e.g. section 7.5, the beam propagation usually is considered close to the xz-plane, defined by $\varphi = 0$. Let us note that in this specific case, the unit vectors e_R, e_φ and e_z of the cylindrical coordinate system correspond to e_x, e_y and e_z in the Cartesian coordinate system, respectively.

7.2. Orientation of the antenna plane

The antenna plane is not necessarily aligned to the Cartesian coordinate system as presented in section 3.5. Instead, for tokamak applications, the antenna is considered to be a plane containing the point $x_a = (x_a, y_a, z_a)$ with an orientation specified by two angles ϑ and ϕ, called poloidal and toroidal angles, respectively. The unit vector normal to the antenna plane in terms of Cartesian coordinates, in ASDEX Upgrade convention, is

$$n = \begin{pmatrix} n_x \\ n_y \\ n_z \end{pmatrix} = \begin{pmatrix} -\cos\vartheta\cos\phi \\ -\cos\vartheta\sin\phi \\ -\sin\vartheta \end{pmatrix}. \tag{7.4}$$

For the generation of initial ray conditions, a Cartesian coordinate system $(\xi_1, \xi_2, \xi_\perp)$ is attached to the antenna plane. The direction perpendicular to the antenna plane is labeled with an index "$\perp$" whereas the directions which span the plane are indexed with "1" and "2". The origin is set at x_a. Then, in terms of these coordinates, the geometry of section 3.5 is appropriate and the corresponding Cartesian coordinates are obtained from the coordinate transformation

$$\begin{pmatrix} x \\ y \\ z \end{pmatrix} = T(\vartheta, \phi) \begin{pmatrix} \xi_1 \\ \xi_2 \\ \xi_\perp \end{pmatrix} + \begin{pmatrix} x_a \\ y_a \\ z_a \end{pmatrix}. \tag{7.5}$$

Here,

$$T(\vartheta, \phi) = \begin{pmatrix} -\sin\vartheta\cos\phi & \sin\phi & -\cos\vartheta\cos\phi \\ \sin\vartheta\sin\phi & -\cos\phi & -\cos\vartheta\sin\phi \\ -\cos\vartheta & 0 & -\sin\vartheta \end{pmatrix} \tag{7.6}$$

is a rotation matrix and it is accounted for the shift (x_0, y_0, z_0). In analogy, the refractive index vector is rotated:

$$\begin{pmatrix} N_x \\ N_y \\ N_z \end{pmatrix} = T(\vartheta, \phi) \begin{pmatrix} N_{a1} \\ N_{a2} \\ N_{a\perp} \end{pmatrix}. \tag{7.7}$$

For the tokamak ITER (under construction), another convention has been introduced [38]: It is obtained by replacing the angles in $T(\vartheta, \phi)$ by tilded versions, defined as

$$\tilde{\vartheta} = -\arcsin\left(\sin\vartheta\cos\phi\right), \tag{7.8a}$$

$$\tilde{\phi} = -\arctan\frac{\tan\phi}{\cos\vartheta}. \tag{7.8b}$$

7.3. Coordinates aligned to the magnetic field

The plasma in a tokamak is anisotropic due to the presence of a magnetic field B. However, we will see, cf. section 7.4.1, that the local properties of the plasma are invariant under changes of the gyrophase ϕ_N, introduced later in this section in (7.10). This suggests to introduce a coordinate system aligned to the magnetic field and to express the refractive index in the dispersion operator symbol in terms of the components $N_{\perp 1}$ and $N_{\perp 2}$ perpendicular to the magnetic field and $N_{\parallel}$ parallel to it. The basis vectors of the two coordinate systems in use are denoted with $(e_{\mathrm{x}}, e_{\mathrm{y}}, e_{\mathrm{z}})$ and $(e_{\perp 1}, e_{\perp 2}, e_{\parallel})$.

The transformation can be written in terms of a rotation $Q^T(x)$, which is in matrix notation

$$\begin{pmatrix} N_{\perp 1} \\ N_{\perp 2} \\ N_{\parallel} \end{pmatrix} = Q^T \begin{pmatrix} N_x \\ N_y \\ N_z \end{pmatrix}, \tag{7.9}$$

where Q^T is the transpose of Q, which, in turn, is defined as the rotation matrix transforming from the field-aligned frame to the Cartesian frame. In addition, we introduce polar coordinates $(N_{\perp}, \phi_N)$ in the plane perpendicular to the magnetic field:

$$N_{\perp 1} = \cos(\phi_N)N_{\perp}, \tag{7.10a}$$

$$N_{\perp 2} = \sin(\phi_N)N_{\perp}. \tag{7.10b}$$

As an example, upon accounting for the expression of Q derived in (7.19), if the magnetic field is oriented in y-direction (approximately corresponding to the toroidal direction for standard beam

parameters, cf. section 7.2) the coordinate transformations (7.9) and (7.10) amount to

$$N_{\mathrm{x}} = \sin(\phi_N)N_\perp, \tag{7.11a}$$

$$N_{\mathrm{z}} = -\cos(\phi_N)N_\perp. \tag{7.11b}$$

Hence $\phi_N = 0$ corresponds to a refractive index pointing in negative z-direction.

As a next step, we shall compute the rotation matrix Q. This is possible based upon information on the orientation of B only. Let us note that the coordinate transformation (7.9) is applicable to any vector, including the magnetic field B itself:

$$\begin{pmatrix} B_{\mathrm{x}} \\ B_{\mathrm{y}} \\ B_{\mathrm{z}} \end{pmatrix} = Q \begin{pmatrix} B_{\perp 1} \\ B_{\perp 2} \\ B_\| \end{pmatrix}. \tag{7.12}$$

This expresses the Cartesian components of the magnetic field in terms of the field aligned components. Of course, the magnetic field does not have any component perpendicular to itself, so $B_{\perp 1} = B_{\perp 2} = 0$, and we obtain

$$B = |B|\, Q e_\|. \tag{7.13}$$

Here, the norm of the magnetic field is $|B|$ and the direction is contained in the rotation matrix Q. Equation (7.13) can be considered as a condition to be solved for Q. Dividing by $|B|$ it reads

$$\frac{B}{|B|} = Q e_\| = Q|_{\text{last column}}. \tag{7.14}$$

The most general ansatz for the rotation Q is the parametrization with the three Euler angles α, β and γ as follows:

$$Q = R_3(\alpha)R_2(\beta)R_3(\gamma). \tag{7.15}$$

Here $R_3(\xi)$ denotes a rotation around the third axis, i.e. the z- or $\|$-direction, by an angle ξ with matrix representation

$$R_3(\xi) = \begin{pmatrix} \cos\xi & \sin\xi & 0 \\ -\sin\xi & \cos\xi & 0 \\ 0 & 0 & 1 \end{pmatrix} \qquad (7.16a)$$

and $R_2(\xi)$ denotes a rotation around the second axis with matrix representation

$$R_2(\xi) = \begin{pmatrix} \cos\xi & 0 & \sin\xi \\ 0 & 1 & 0 \\ -\sin\xi & 0 & \cos\xi \end{pmatrix}. \qquad (7.16b)$$

When these matrices are substituted into (7.14), we find

$$\frac{B}{|B|} = \begin{pmatrix} \cos\alpha\sin\beta \\ -\sin\alpha\sin\beta \\ \cos\beta \end{pmatrix}, \qquad (7.17)$$

which is a condition for the angles α and β, with the solution

$$\alpha = -\arctan\frac{B_\mathrm{y}}{B_\mathrm{x}}, \qquad (7.18a)$$

$$\beta = \arcsin\frac{\sqrt{B_\mathrm{x}^2 + B_\mathrm{y}^2}}{|B|}. \qquad (7.18b)$$

It is worth noting that the vector $(0, 0, B_\|)$, which represents the magnetic field in the field-aligned frame, is invariant under rotation around the third axis, $R_3(\gamma)$. Hence, (7.14) does not constrain the angle γ. Therefore, this angle should be arbitrary. Indeed, it does not appear in condition (7.17). Hence, without loss of generality, we set $\gamma = 0$, with the final result

$$Q = R_3(\alpha)R_2(\beta) = \begin{pmatrix} \cos\alpha\cos\beta & \sin\alpha & \cos\alpha\sin\beta \\ -\sin\alpha\cos\beta & \cos\alpha & -\sin\alpha\sin\beta \\ -\sin\beta & 0 & \cos\beta \end{pmatrix}. \qquad (7.19)$$

7.4. Weyl symbol for electron-cyclotron waves

In this section, the Weyl symbol $D(x, N)$ of the wave equation operator for electron-cyclotron wave propagation in tokamak plasmas is discussed. For the framework of this thesis, it was presented in section 3.2 that this operator is split into a part referred to as dispersion operator $D_0(x, N)$, one part $\delta D_F(x, N)$ describing the fluctuations and a contribution $\delta^2 D_A(x, N)$ which describes the effect of absorption. For the case of waves in magnetized plasmas, the symbols involved are matrices and $D_0(x, N)$ must be diagonalized as explained in section 3.3 to simplify to a scalar problem. This section is split into several parts, where the above-mentioned contributions are presented separately.

7.4.1. Cold-plasma dispersion

The eigenvalue of $D_0(x, N)$ corresponding to the mode under investigation is considered as natural Hamiltonian in the ray tracing code. In this subsection, D_0 for magnetized plasmas is computed and a Hamiltonian is constructed.

 For the propagation of electron-cyclotron waves it is customary to use the cold-plasma approximation for $D_0(x, N)$ [11], [12], [13]. This is appropriate as far as the beam is far from resonances. Hot-plasma effects determine the resonant absorption of the wave, see section 7.4.6. A discussion on this approximation can be found e.g. in [12]. The cold-plasma dielectric tensor is

$$\varepsilon_\text{z} = \begin{pmatrix} S & iD & 0 \\ -iD & S & 0 \\ 0 & 0 & P \end{pmatrix}. \tag{7.20}$$

The index z indicates that this dielectric tensor is expressed in a frame where B is aligned to the z-axis. The tensor in generic coordinates can be obtained by applying the coordinate transformation expressed by the matrix Q (7.19). The coefficients S, D and P are functions of the (electron)

plasma frequency ω_p and the (electron) cyclotron frequency Ω as follows:

$$P = 1 - \frac{\omega_p^2}{\omega^2}, \tag{7.21a}$$

$$S = 1 - \frac{\omega_p^2}{\omega^2 - \Omega^2}, \tag{7.21b}$$

$$D = \frac{\omega\Omega}{\omega^2 - \Omega^2}\frac{\omega_p^2}{\omega^2}. \tag{7.21c}$$

The electron plasma frequency is $\omega_p = \sqrt{\frac{n_e e^2}{\epsilon_0 m_e}}$ where n_e is the electron number density, e is the negative electron charge ($e > 0$), m_e the electron mass and ϵ_0 the vacuum permitivity. The cyclotron frequency in MKSA-units reads $\Omega = \frac{e|B|}{m_e}$, where $|B|$ is the norm of the magnetic field. Note that since n_e and $|B|$ are space-dependent, also ε is. The L-symbol $d_0(x, N)$ of the dispersion operator is obtained by means of (2.23). Upon accounting for its structure, discussed in equation (2.38), the Weyl symbol $D_0(x, N)$ is equivalent,

$$D_0(x, N) = -N \otimes N + N^2 \mathbb{I}_3 - \varepsilon(x). \tag{7.22}$$

The Hamiltonian for the ray tracing, in principle, is found by computing the eigenvalue λ_α of this matrix for the mode α to be traced. This requires solving the cubic dispersion relation

$$\det\left(D_0(x, N) - \lambda\mathbb{I}_3\right) = 0 \tag{7.23}$$

and is not trivial. Anyway, it was seen in section 4.4 that it can be multiplied with any non-vanishing function and still a correct solution can be obtained with a rescaling procedure. Given the fact that the determinant of a matrix is just the product of the eigenvalues, the determinant of (7.22) would be an appropriate choice for the Hamiltonian which is much simpler to compute than the eigenvalue. Therefore, as a relatively easy starting point, the Hamiltonian

$$H'(x, N) = \det D_0(x, N) \tag{7.24}$$

is considered. This determinant is computed as follows: First, the dispersion matrix is transformed to the coordinate system aligned to the magnetic field, i.e.

$$D_{0,z} = Q^T D_0 Q = \left(Q^T N\right) \otimes \left(Q^T N\right) - N^2 \mathbb{I}_3 - \varepsilon_z. \tag{7.25}$$

With the rotation Q a unitary matrix, the determinant is not affected by such transformations, i.e.

$$\det D_{0,z} = \det D_0. \tag{7.26}$$

Inserting Q defined in (7.9) and the dielectric tensor (7.20) into (7.25), the dispersion matrix reads

$$D_{0,z} = \begin{pmatrix} N^2 - N_{\perp 1}^2 - S & -N_{\perp 1} N_{\perp 2} - iD & -N_{\perp 1} N_{\parallel} \\ -N_{\perp 1} N_{\perp 2} + iD & N^2 - N_{\perp 2}^2 - S & -N_{\perp 2} N_{\parallel} \\ -N_{\perp 1} N_{\parallel} & -N_{\perp 2} N_{\parallel} & N^2 - N_{\parallel}^2 - P \end{pmatrix}. \tag{7.27}$$

It is worth noting that here no assumption is made on the orientation of N in the plane perpendicular to the local magnetic field. If, in addition, one sets the gyrophase ϕ_N so that $N_{\perp 2} = 0$ the tensor (7.27) reduces to the well-known from [12]. The determinant of the dispersion tensor (7.27) is an appropriate choice for the Hamiltonian:

$$H'(x, N) = SN_{\perp}^4 - \left[\left(S - N_{\parallel}^2\right)(S + P) - D^2\right] N_{\perp}^2$$
$$+ P\left[\left(S - N_{\parallel}^2\right)^2 - D^2\right]. \tag{7.28}$$

The Hamiltonian presented in (7.28) is seen to be a polynomial of second order in $N_{\perp}^2$. With the parameters

$$\mathcal{A} := S, \tag{7.29a}$$
$$\mathcal{B} := (S + P)N_{\parallel}^2 - SP + D^2 - S^2, \tag{7.29b}$$
$$\mathcal{C} := S^2 P - D^2 P - 2SPN_{\parallel}^2 + PN_{\parallel}^4 \tag{7.29c}$$

dependent on x and $N_\parallel$, equation (7.28) amounts to

$$H'(x, N) = \mathcal{A}(x)N_\perp^4 + \mathcal{B}(x, N_\parallel)N_\perp^2 + \mathcal{C}(x, N_\parallel). \tag{7.30}$$

The construction of this Hamiltonian was relatively straight forward. However, as it stands, it is not a good choice for the ray tracing code. First of all, in free space, the electron density vanishes and the Hamiltonian (7.30) reduces to

$$H'(x, N) = \left(N^2 - 1\right)^2, \tag{7.31}$$

showing a second-order zero. Hence, whenever the Hamiltonian vanishes, also the derivatives with respect to N, and hence the ray velocity defined in (C.1a), vanish.

The second problem is that the Hamiltonian presented in (7.28) is valid for all plasma modes. In case they are degenerate, as for example in free space, there is no way to properly choose the mode. Instead, a different behavior of the mode shows up once the plasma is reached. Therefore, employing the Hamiltonian (7.28) would require a special treatment of the free space region around the plasma.

In the following, a different Hamiltonian is presented which solves immediately both problems mentioned before. It is constructed based on (7.28) as a starting point. In equation (7.30) the structure of the Hamiltonian as a polynomial of second order in $N_\perp^2$ is obvious. In general, it is easy to compute the two roots of such a polynomial, which allows to write it in terms of a product of two linear factors, i.e.

$$H'(x, N) = S\left(N_\perp^2 - N_\perp^2(+1, x, N_\parallel)\right)\left(N_\perp^2 - N_\perp^2(-1, x, N_\parallel)\right), \tag{7.32}$$

where $N_\perp^2(\sigma, x, N)$ denotes the root labeled with $\sigma = \pm 1$ (corresponding to the single modes) of the equation $H'(x, N) = 0$ solved for $N_\perp^2$

$$N_\perp^2(\sigma, x, N) = -\frac{\mathcal{B}}{2\mathcal{A}} + \sigma\sqrt{\frac{\mathcal{B}^2}{4\mathcal{A}^2} - \frac{\mathcal{C}}{\mathcal{A}}}. \tag{7.33}$$

The different modes which arise from the cold-plasma dispersion relation are discussed e.g. in [12]. The mode labeled with $\sigma = +1$ in this thesis there is referred to as O-mode (ordinary

mode), whereas $\sigma = -1$ is the X-mode (extraordinary mode). For propagation perpendicular to the background magnetic field, these modes are characterised by an electric wave field pointing in the direction of B and perpendicular to B, respectively. If, as a Hamiltonian appropriate for the mode σ,

$$H^\sigma(x, N) = 2 \left(N_\perp^2 - N_\perp^2(\sigma, x, N_\parallel) \right) = 2N_\perp^2 + \frac{1}{\mathcal{A}} \left(\mathcal{B} - \sigma \sqrt{\mathcal{B}^2 - 4\mathcal{A}\mathcal{C}} \right), \qquad (7.34)$$

is employed, it is exclusively valid for the mode σ. Thus, the mode can properly be chosen by specifying the index σ. Also the slow propagation for degenerate modes is no longer present for this Hamiltonian. If free space ($n_e = 0$) is considered, the free space Hamiltonian

$$H^\sigma(x, N) = 2 \left(N^2 - 1 \right) \qquad (7.35)$$

is recovered, cf. (6.3).

The Hamiltonian (7.34) is the one used in the ray tracing module of the wave kinetic code. The remaining part of this section is dedicated to some issues of special interest for the implementation.

It can be seen in (7.35) that for free space parameters, the Hamiltonian does not depend on σ. This is clear because there the modes are degenerated. Also (7.34) should not depend on σ for free space. This is the case when the involved square root vanishes. The definition of the parameters (7.29) and (7.21) are substituted into the square root and a lengthy but straight forward computation shows

$$\sqrt{\mathcal{B}^2 - 4\mathcal{A}\mathcal{C}} = |D| \sqrt{4PN_\parallel^2 + \frac{\Omega^2}{\omega^2} \left(N_\parallel^2 - 1 \right)^2}. \qquad (7.36)$$

For this simpler expression for the square root it is obvious that it vanishes for free space where $D = 0$.

One numerically troublesome point could arise when $S = 0$. This happens in the plasma when $\omega^2 = \omega_p^2 + \Omega^2$, which is known as the upper hybrid resonance [12]. For the $\sigma = -1$ mode, such a parameter leads to a blow up in the Hamiltonian (7.34). Instead, for the $\sigma = +1$ mode, a Taylor expansion of the square root around $\mathcal{A} = 0$ yields

$$H^{+1}(x, N) = 2N_\perp^2 + \frac{\mathcal{B}}{\mathcal{A}} \left(1 - 1 + 2\frac{\mathcal{A}\mathcal{C}}{\mathcal{B}^2} + \mathcal{O}(\mathcal{A}^2) \right) = 2N_\perp^2 + \frac{\mathcal{C}}{\mathcal{B}} + \mathcal{O}(\mathcal{A}). \qquad (7.37)$$

So, divergence cancels out. In any case, when numerical computations are involved and the Taylor expansion is not performed, the Hamiltonian is composed by a term of order $\mathcal{O}(\mathcal{A})$ divided by $\mathcal{A}$. In the limit $\mathcal{A} \to 0$, this will cause numerical errors and must be avoided. Therefore, instead of $\mathcal{A}^{-1}$, a regularized inverse

$$\mathcal{A}_{\text{reg}}^{-1} = \frac{\mathcal{A}}{\mathcal{A}^2 + \epsilon^2} \tag{7.38}$$

is used. Here, ϵ is a small constant. This inverse of $\mathcal{A}$ does not blow up any longer for small $\mathcal{A}$, but it is bounded by the values $\pm\frac{1}{2\epsilon}$. The error of this regularized inverse of $\mathcal{A}$ compared to the correct value is given by

$$\left| \frac{1}{\mathcal{A}} - \frac{\mathcal{A}}{\mathcal{A}^2 + \epsilon^2} \right| = \left| \frac{\epsilon^2}{\mathcal{A}(\mathcal{A}^2 + \epsilon^2)} \right| \leq \left| \frac{\epsilon^2}{\mathcal{A}} \right|. \tag{7.39}$$

As can be seen, for large $\mathcal{A}$ this vanishes. For $\mathcal{A}$ close to zero the use of the regularized inverse avoids terms in the Hamiltonian blowing up. In the limit $\epsilon \to 0$, the non-regularized inverse is found. Therefore, the regularized result should converge to the correct result in this limit. A convergence study can be found in section 7.4.4.

7.4.2. Correction factor for the Hamiltonian

According to the theory developed in section 3.3, the Hamiltonian corresponding to the mode with eigenvector e_α of the dispersion operator is its eigenvalue

$$\lambda_\alpha(x, N) = e_\alpha^\dagger(x, N) D_0(x, N) e_\alpha(x, N). \tag{7.40}$$

Instead, the Hamiltonian $H^\alpha(x, N)$ given by (7.34) is employed in the numerical solution. The latter can be written as the eigenvalue multiplied by a non-vanishing function as in (4.54):

$$H^\alpha(x, N) = \xi(x, N)\lambda_\alpha(x, N). \tag{7.41}$$

It is the aim of this section to compute this factor for the cold-plasma case. This is done in two steps: First, the correction factor $\xi_1(x, N)$ relating $\lambda_\alpha(x, N)$ to the determinant $H'(x, N)$ is

computed, i.e.

$$H'(x, N) = \xi_1(x, N)\lambda_\alpha(x, N). \tag{7.42}$$

To this goal, we note that the determinant of a matrix is the product of its eigenvalues $\lambda_\beta(x, N)$, i.e.

$$H'(x, N) = \det D_0(x, N) = \prod_\beta \lambda_\beta(x, N) = \lambda_\alpha(x, N) \prod_{\beta \neq \alpha} \lambda_\beta(x, N). \tag{7.43}$$

On the other hand, the matrix of cofactors $C(x, N)$ of the dispersion matrix can be expanded on the basis of the eigenvectors:

$$C(x, N) = \sum_\alpha \left(\prod_{\beta \neq \alpha} \lambda_\beta(x, N) \right) e_\alpha(x, N) e_\alpha^\dagger(x, N). \tag{7.44}$$

The trace of $C(x, N)$ reads

$$\operatorname{Tr} C(x, N) = \sum_\mu e_\mu^\dagger(x, N) C(x, N) e_\mu(x, N) = \sum_\alpha \left(\prod_{\beta \neq \alpha} \lambda_\beta(x, N) \right). \tag{7.45}$$

Since the eigenvalue $\lambda_\alpha(x, N)$ vanishes on phase space points (x, N) along the considered trajectories, the last sum only has one contribution:

$$\operatorname{Tr} C|_{\lambda_\alpha = 0}(x, N) = \prod_{\beta \neq \alpha} \lambda_\beta(x, N). \tag{7.46}$$

With this result, a comparison of (7.43) and (7.42) yields the factor

$$\xi_1(x, N) = \operatorname{Tr} C(x, N), \tag{7.47}$$

where it is implied that (x, N) satisfies the dispersion relation $\lambda_\alpha(x, N) = 0$ which will always be the case.

Next, the factor $\xi_2(x, N)$ relating the determinant to the final Hamiltonian (7.34), i.e.

$$H(x, N) = \xi_2(x, N)H'(x, N), \tag{7.48}$$

126

is obtained by a comparison of $H'(x, N)$ in (7.32) and $H(x, N)$ in (7.34): For the mode σ one has

$$\xi_2(x, N) = \frac{2}{S\left(N_\perp^2 - N_\perp^2(-\sigma, x, N_\parallel)\right)}. \tag{7.49}$$

Finally, the correction factor as a whole is given by

$$\xi(x, N) = \xi_1(x, N)\xi_2(x, N) = \frac{2\operatorname{Tr} T(x, N)}{S\left(N_\perp^2 - N_\perp^2(-\sigma, x, N_\parallel)\right)}. \tag{7.50}$$

The explicit calculation is, again, straight forward but lengthy. Therefore, here only the results are reported, computed with the help of the matrix of cofactors presented in [11]. The results are:

$$\xi^{\sigma=+1} = \frac{\frac{\left(2\left(\frac{\Omega^2}{\omega^2}-2\right)N_\parallel^2 - \frac{\Omega}{\omega}\left(D+\frac{\Omega}{\omega}\right)\right)^2}{\left(\frac{\Omega}{\omega}N_\parallel^2 + D + \sqrt{4PN_\parallel^2 + \frac{\Omega^2}{\omega^2}\left(N_\parallel^2-1\right)^2}\right)}D - \frac{\Omega^2}{\omega^2}D}{\sqrt{4PN_\parallel^2 + \frac{\Omega^2}{\omega^2}\left(N_\parallel^2 - 1\right)^2}} - 2, \tag{7.51a}$$

$$\xi^{\sigma=-1} = \frac{-\left(\frac{\Omega}{\omega}N_\parallel^2 + D + \sqrt{4PN_\parallel^2 + \frac{\Omega^2}{\omega^2}\left(N_\parallel^2-1\right)^2}\right)^2\frac{D}{S^2} + \frac{\Omega^2}{\omega^2}D}{\sqrt{4PN_\parallel^2 + \frac{\Omega^2}{\omega^2}\left(N_\parallel^2 - 1\right)^2}} - 2 \tag{7.51b}$$

for the mode $\sigma = +1$ and $\sigma = -1$, respectively.

7.4.3. Derivatives of the Hamiltonian

In section 7.4.1, the Hamiltonian for the ray tracing in tokamak plasmas was derived. Actually, not the Hamiltonian enters the Hamilton equations of motion (C.1), but its derivatives with respect to $x = (\mathrm{x}, \mathrm{y}, \mathrm{z})$ and $N = (N_\mathrm{x}, N_\mathrm{y}, N_\mathrm{z})$. In this section, the computation of these derivatives is sketched.

We start with the derivatives with respect to N. The Hamiltonian (7.34) is given in terms of the components of the refractive index parallel and perpendicular to the magnetic field. Hence, chain

7. Results for tokamak plasmas

rule is used:

$$\partial_N H = \frac{\partial H}{\partial N_\parallel} \partial_N N_\parallel + \frac{\partial H}{\partial N_\perp} \left(\frac{\partial N_\perp}{\partial N_{\perp 1}} \partial_N N_{\perp 1} + \frac{\partial N_\perp}{\partial N_{\perp 2}} \partial_N N_{\perp 2} \right)$$
$$= \frac{\partial H}{\partial N_\parallel} \left(Q e_\parallel \right)^T + \frac{\partial H}{\partial N_\perp} \left(\cos(\phi_N) \left(Q e_{\perp 1} \right)^T + \sin(\phi_N) \left(Q e_{\perp 2} \right)^T \right). \tag{7.52}$$

Here, the rotation (7.9) is used to express $(N_{\perp 1}, N_{\perp 2}, N_\parallel)$ in terms of (N_x, N_y, N_z). Furthermore, the transformation to polar coordinates (7.10) allows us to compute $\frac{\partial N_\perp}{\partial N_{\perp 1}}$ and $\frac{\partial N_\perp}{\partial N_{\perp 2}}$.

Next, the derivatives of the Hamiltonian with respect to x are computed. The terms depending on position are the parameters $\mathcal{A}$, $\mathcal{B}$, $\mathcal{C}$ via their dependency on electron density n_e and magnetic field B and $N_\perp$ and $N_\parallel$ via the rotation Q. Therefore, using chain rule again, the derivatives of H with respect to the spatial coordinates x are obtained by

$$\partial_x H = \frac{\partial H}{\partial \mathcal{A}} \left(\frac{\partial \mathcal{A}}{\partial \mathrm{R}} \partial_x \mathrm{R} + \frac{\partial \mathcal{A}}{\partial \mathrm{z}} \partial_x \mathrm{z} \right) + \frac{\partial H}{\partial \mathcal{B}} \left(\frac{\partial \mathcal{B}}{\partial \mathrm{R}} \partial_x \mathrm{R} + \frac{\partial \mathcal{B}}{\partial \mathrm{z}} \partial_x \mathrm{z} \right)$$
$$+ \frac{\partial H}{\partial \mathcal{C}} \left(\frac{\partial \mathcal{C}}{\partial \mathrm{R}} \partial_x \mathrm{R} + \frac{\partial \mathcal{C}}{\partial \mathrm{z}} \partial_x \mathrm{z} \right) + \frac{\partial H}{\partial N_\perp} \partial_x N_\perp + \frac{\partial H}{\partial N_\parallel} \partial_x N_\parallel. \tag{7.53}$$

The transformation between the Cartesian coordinate system $x = (\mathrm{x}, \mathrm{y}, \mathrm{z})$ and (R, z) (7.1) yields the derivatives

$$\partial_x \mathrm{R} = \begin{pmatrix} \frac{\mathrm{x}}{\mathrm{R}} \\ \frac{\mathrm{y}}{\mathrm{R}} \\ 0 \end{pmatrix}, \qquad \partial_x \mathrm{z} = \begin{pmatrix} 0 \\ 0 \\ 1 \end{pmatrix}. \tag{7.54}$$

The derivatives of the parameters $\mathcal{A}$, $\mathcal{B}$ and $\mathcal{C}$ are obtained immediately, if their dependence on $n_e \equiv n_e(\mathrm{R}, \mathrm{z})$ and $|B| \equiv |B|(\mathrm{R}, \mathrm{z})$ is written out and chain rule is applied. Then, the terms describing the dependence of the Hamiltonian on the parameters $\mathcal{A}$, $\mathcal{B}$ and $\mathcal{C}$ in equation (7.53) are known. Still, $\partial_x N_\perp$ and $\partial_x N_\parallel$ need to be computed. Since the space dependence appears via the rotation matrix Q parametrized in (7.19) by the Euler angles (α, β), the chain rule is applied again:

$$\partial_x N_i = \frac{\partial N_i}{\partial \alpha} \frac{\partial \alpha}{\partial x} + \frac{\partial N_i}{\partial \beta} \frac{\partial \beta}{\partial x} \tag{7.55}$$

with an index $i = \perp, \parallel$. After inserting the parametrization (7.19) into the transformation (7.9), the components $N_\perp$ and $N_\parallel$ are expressed in terms of the Euler angles α and β,

$$N_\parallel = N_\mathrm{x} \cos\alpha \sin\beta - N_\mathrm{y} \sin\alpha \sin\beta + N_\mathrm{z} \cos\beta, \tag{7.56a}$$

$$\begin{aligned} N_\perp = \Big[&\left(\cos^2\alpha\cos^2\beta + \sin^2\alpha\right) N_\mathrm{x}^2 + \left(\sin^2\alpha\cos^2\beta + \cos^2\alpha\right) N_\mathrm{y}^2 \\ &+ \sin^2\beta N_\mathrm{z}^2 + 2\sin\alpha\cos\alpha\sin^2\beta N_\mathrm{x} N_\mathrm{y} \\ &+ 2\left(\sin\alpha N_\mathrm{y} - \cos\alpha N_\mathrm{x}\right)\sin\beta\cos\beta N_\mathrm{z}\Big]^{1/2}, \end{aligned} \tag{7.56b}$$

yielding the derivatives $\frac{\partial N_i}{\partial\alpha}$ and $\frac{\partial N_i}{\partial\beta}$. The Euler angles have been derived in equations (7.18). There, the magnetic field components $(B_\mathrm{x}, B_\mathrm{y}, B_\mathrm{z})$, obtained from $(B_\mathrm{R}, B_\varphi, B_\mathrm{z})$ via the transformation (7.2), enter. With these magnetic field components, the Euler angles read

$$\alpha = -\arctan\frac{B_\varphi}{B_\mathrm{R}} - \arctan\frac{\mathrm{y}}{\mathrm{x}}, \tag{7.57a}$$

$$\beta = \arcsin\frac{\sqrt{B_\mathrm{R}^2 + B_\varphi^2}}{|B|}. \tag{7.57b}$$

Here, it was made use of additional theorems for trigonometric functions. The derivatives of the Euler angles are hence

$$\partial_x\alpha = -\frac{B_\mathrm{R}\partial_x B_\varphi - B_\varphi\partial_x B_\mathrm{R}}{B_\mathrm{R}^2 + B_\varphi^2} - \frac{\mathrm{x}\partial_x\mathrm{y} - \mathrm{y}\partial_x\mathrm{x}}{\mathrm{R}^2}, \tag{7.58a}$$

$$\partial_x\beta = -\frac{\partial_x B_\mathrm{z} - \frac{B_\mathrm{z}}{B_\mathrm{R}^2 + B_\varphi^2}\left(B_\mathrm{R}\partial_x B_\mathrm{R} + B_\varphi\partial_x B_\varphi\right)}{\sqrt{B_\mathrm{R}^2 + B_\varphi^2} + \frac{B_\mathrm{z}^2}{\sqrt{B_\mathrm{R}^2 + B_\varphi^2}}}. \tag{7.58b}$$

The space dependence of the magnetic field B on (R, z) is known from input files, yielding the spatial derivatives

$$\partial_x B = \frac{\partial B}{\partial\mathrm{R}}\partial_x\mathrm{R} + \frac{\partial B}{\partial\mathrm{z}}\partial_x\mathrm{z}, \tag{7.59}$$

where (7.54) provides $\partial_x\mathrm{R}$ and $\partial_x\mathrm{z}$.

7.4.4. Symmetries and tests of the Hamiltonian

The Hamiltonian (7.34) and its derivatives used in the Hamilton equations of motion (C.1) involve relatively cumbersome expressions. This could easily cause bugs in the implementation. Therefore, once the ray tracing is implemented, some tests need to be performed for debugging purposes. Moreover, we shall study the convergence of the results in the limit of the regularization parameter $\epsilon \to 0$, cf. (7.38), as promised in section 7.4.1.

One test the ray tracing routine must pass consists in constructing quantities which should be conserved along the Hamiltonian orbits and to check if, indeed, they are. As mentioned in appendix C, the Hamiltonian itself is conserved and, hence, is one such quantity. Another is found upon applying Noether theorem. It states that each symmetry of a system under investigation leads to a conservation law. A symmetry present in the tokamak is the invariance under rotations around the z-axis. The Hamiltonian does not depend on the toroidal angle φ and remains unchanged under such rotations by a small angle $\delta\varphi$, i.e.

$$\delta H = \frac{\partial H}{\partial \varphi} \delta\varphi = 0. \tag{7.60}$$

The change of the Hamiltonian in general can be expressed as

$$\delta H = \frac{\partial H}{\partial x}\delta x + \frac{\partial H}{\partial y}\delta y + \frac{\partial H}{\partial z}\delta z + \frac{\partial H}{\partial N_x}\delta N_x + \frac{\partial H}{\partial N_y}\delta N_y + \frac{\partial H}{\partial N_z}\delta N_z = 0, \tag{7.61}$$

where a rotation around the z-axis leads z and N_z unchanged, i.e. $\delta z = \delta N_z = 0$ and the shifts in the xy-plane to first order $\mathcal{O}(\delta\varphi)$ read

$$\delta x = -y\delta\varphi, \tag{7.62a}$$

$$\delta y = x\delta\varphi, \tag{7.62b}$$

$$\delta N_x = -N_y\delta\varphi, \tag{7.62c}$$

$$\delta N_y = N_x\delta\varphi. \tag{7.62d}$$

Substituted into (7.61), the variation of the Hamiltonian yields

$$\delta H = \left(-y\frac{\partial H}{\partial x} + x\frac{\partial H}{\partial y} - N_y\frac{\partial H}{\partial N_x} + N_x\frac{\partial H}{\partial N_y}\right)\delta\varphi = 0. \tag{7.63}$$

Since $\delta\varphi$ is arbitrary, the expression within the brackets must vanish. The partial derivatives of the Hamiltonian are replaced using Hamilton's equations of motion (C.1). The result reads

$$\mathrm{y}\frac{dN_\mathrm{x}}{d\tau} - \mathrm{x}\frac{dN_\mathrm{y}}{d\tau} - N_\mathrm{y}\frac{d\mathrm{x}}{d\tau} + N_\mathrm{x}\frac{d\mathrm{y}}{d\tau} = \frac{d}{d\tau}\left(\mathrm{y}N_\mathrm{x} - \mathrm{x}N_\mathrm{y}\right) = 0. \tag{7.64}$$

We define

$$N_\varphi := \mathrm{y}N_\mathrm{x} - \mathrm{x}N_\mathrm{y} \tag{7.65}$$

referred to as toroidal refractive index component and note that it should be conserved along Hamiltonian orbits.

We run the ray tracing routine for one specific set of initial conditions and obtain the evolution of H and N_φ along the ray which is shown in figure 7.2. The important point is the variation of the Hamiltonian and the toroidal refractive index component along the ray through the plasma. In this test the "time step" $\Delta\tau$ is adapted automatically by the Runge-Kutta solver in order to meet the prescribed error tolerance. It is seen that the conservation of the toroidal refractive index component is within the order of 10^{-9}. It improves, when a smaller integrator tolerance is chosen. The Hamiltonian stays within a bound of order 10^{-4}, but does not further improve significantly with smaller tolerances. For analytical plasma profiles, we observe better convergence of the error of the value of the Hamiltonian with the tolerance; therefore we attribute this behavior to imprecisions in the numerical interpolation of the plasma profiles. For the case of N_φ, on the contrary, the results are better as the invariance under toroidal rotations is enforced by construction in the interpolant. Indeed, since plasma profiles are given as functions on (R, z) based on interpolation of tables in the input files, the background profiles are extended to the tokamak volume by exploiting the symmetry of the torus so that the rotational invariance is present independently of interpolation inaccuracies. Hence, the conservation of the toroidal refractive index component in the code is restricted only to the Runge-Kutta solver. A further test for the ray tracing consists in comparing ray trajectories of the wave kinetic code with trajectories obtained from the well-tested [39] TORBEAM code [40]. For different initial parameters, such a comparison is displayed in figure 7.3. The vacuum-plasma boundary is located at $\mathrm{x} = 215\,\mathrm{cm}$. There, the rays get deflected. One can see that the torbeam ray trajectory and the trajectory of the new wave kinetic code are in good agreement.

(a) conservation of Hamiltonian:
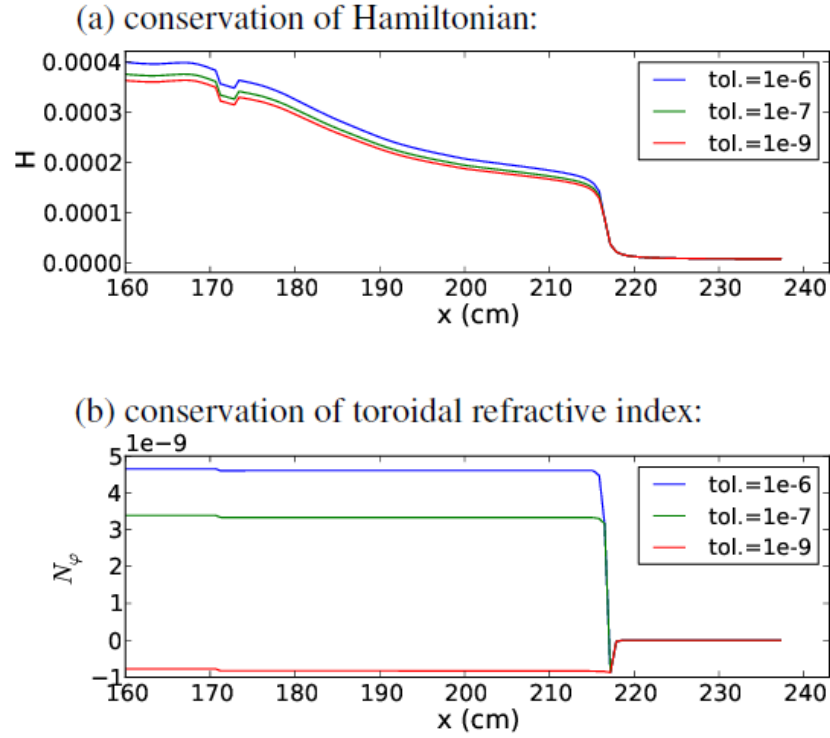

(b) conservation of toroidal refractive index:

Figure 7.2.: Evolution of (a) the Hamiltonian H and (b) the toroidal refractive index component along a ray launched at x = 238 cm. A scan of tolerances for the Runge-Kutta solver is shown. The initial conditions are chosen such that the initial values of H and N_φ vanish. The plasma profiles of AUG #25485 are used, cf. appendix G. The jump at about x = 218 cm corresponds to the plasma boundary.

Finally, the convergence of the trajectories in the limit $\epsilon \to 0$ for the regularization parameter (7.38) is investigated in figure 7.4. Frequency is decreased so that a region with $S = 0$ is crossed. It is seen that there is not a clear difference between the ray trajectories for different values of ϵ. Instead, the conservation of the Hamiltonian starting from the point were $S = 0$ is influenced by this parameter and improves for smaller ϵ. However, the Hamiltonians for $\epsilon = 3 \cdot 10^{-4}$ and $\epsilon = 1 \cdot 10^{-3}$ are very close one to the other even beyond this point and show a satisfactory conservation. More test runs with even smaller parameters up to $\epsilon = 1 \cdot 10^{-7}$ have been performed and are not distinguishable to the $\epsilon = 3 \cdot 10^{-4}$ run, confirming convergence. Based on this result we usually fix $\epsilon = 1 \cdot 10^{-6}$.
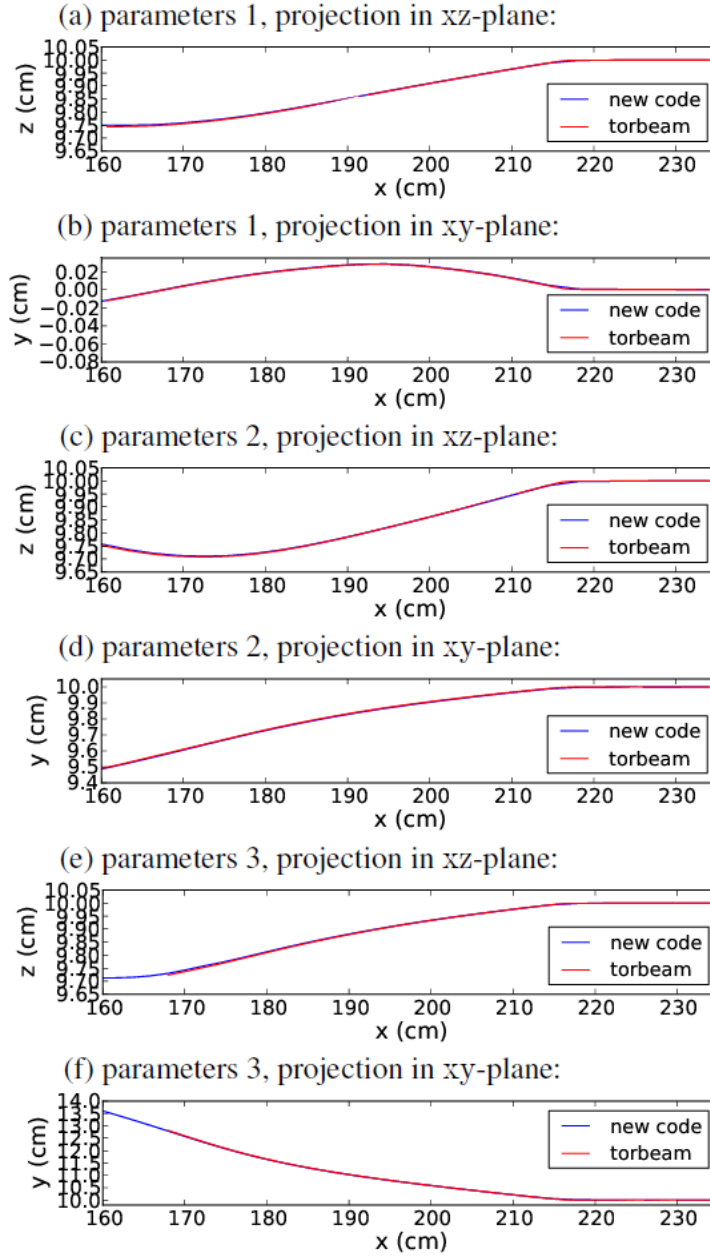
Figure 7.3.: Comparison of TORBEAM rays with the trajectories of the wave kinetic code for different initial ray coordinates and wave modes. The considered frequency is $f = 140\,\mathrm{GHz}$. The initial propagation direction is the negative x-axis for all rays. The initial position (x, y, z) and wave mode are: (a,b) $x = 238\,\mathrm{cm}$, $y = 0\,\mathrm{cm}$, $z = 10\,\mathrm{cm}$, O-mode, (c,d) $x = 238\,\mathrm{cm}$, $y = 10\,\mathrm{cm}$, $z = 10\,\mathrm{cm}$, O-mode, (e,f) $x = 238\,\mathrm{cm}$, $y = 10\,\mathrm{cm}$, $z = 10\,\mathrm{cm}$, X-mode. The plasma profiles are taken from AUG #25485, cf. appendix G.

(a) projection of trajectory in Rz-plane:

(b) projection of trajectory in Ry-plane:

(c) conservation of Hamiltonian:

(d) plasma parameter S:
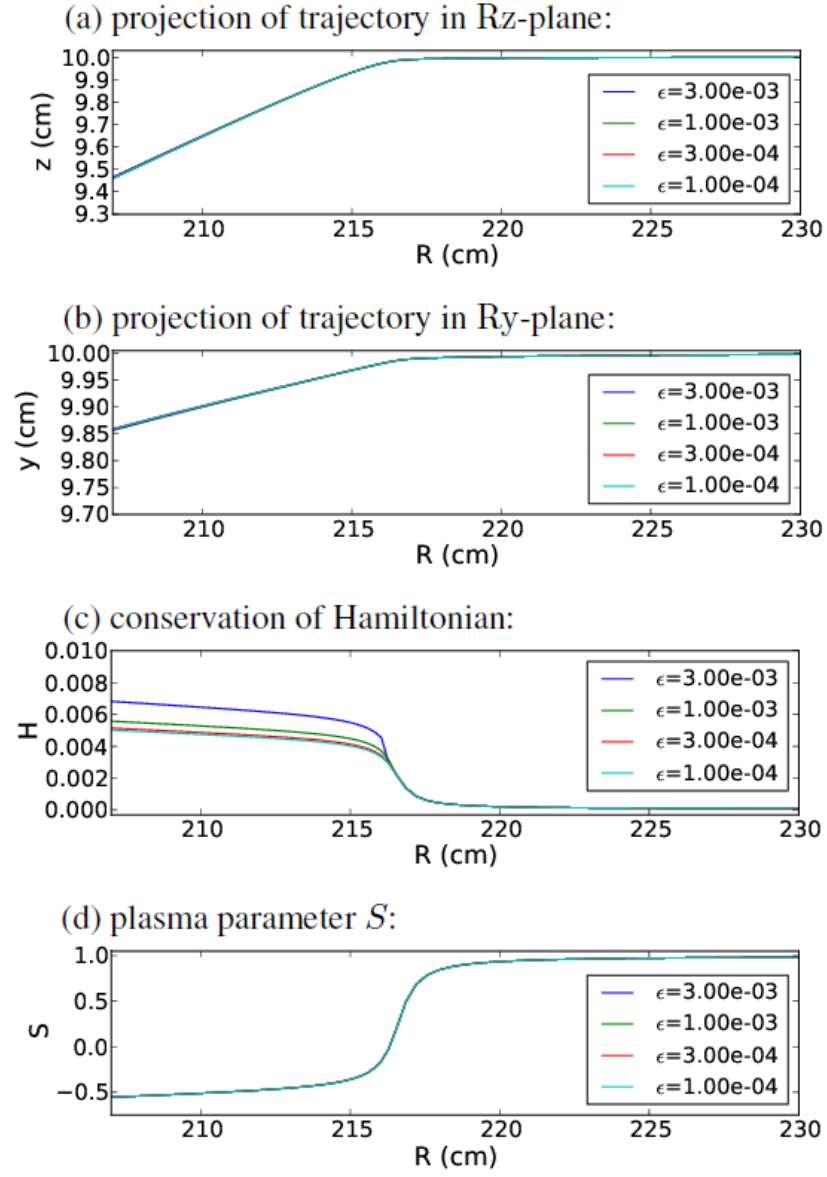
Figure 7.4.: Influence of the regularization parameter ϵ. Ray is launched at $x = 238\,\text{cm}$, $y = 10\,\text{cm}$, $z = 10\,\text{cm}$, a frequency $f = 85\,\text{GHz}$ and O-mode propagation are considered. (a,b) Projection of the ray trajectory in Rz- and Ry-plane, (c) conservation of Hamiltonian, (d) plasma parameter S. The plasma profiles are taken from AUG #25485, cf. appendix G.

7.4.5. Fluctuation model

This section is dedicated to the issue of fluctuations in tokamak plasmas. Their effect on the microwave beam is described via the part δD_F in the wave operator. In this work, it is assumed that the fluctuation in the wave operator arises mainly due to electron density fluctuations, i.e.

$$D_F(x) = \sqrt{\kappa}\,(\mathbb{I} - \varepsilon(x))\,\frac{\delta n_e(x)}{n_e(x)}. \tag{7.66}$$

Here, $\delta n_e(x)$ describes the random deviation of the background electron density n_e at point x. This should not be confused with the refractive index fluctuation δn^2 in section 6.4. Note that the prefactor $\sqrt{\kappa}$ in (7.66) is needed to compensate for the explicit factor $\delta = \kappa^{-1/2}$, as it was the case in section 6.4 on fluctuations in free space. Substituted into the spectrum of fluctuations (3.28), this reads

$$G_{iabj}(x, N - N') = \frac{\kappa^4}{(2\pi)^3}\,(\mathbb{I} - \varepsilon(x))_{ia}\,(\mathbb{I} - \varepsilon(x))_{bj}$$
$$\times \frac{1}{n_e} \int e^{-i\kappa(N-N')\cdot s} \mathbb{E}\left(\delta n_e\left(x + \frac{s}{2}\right)\delta n_e\left(x - \frac{s}{2}\right)\right) \mathrm{d}s. \tag{7.67}$$

Here, it is assumed that ε is slowly varying in x and, thus, is well-approximated with the Taylor expansion around x to lowest order:

$$\varepsilon\left(x \pm \frac{s}{2}\right) \approx \varepsilon(x). \tag{7.68}$$

The Wigner transform of the (relative) electron density fluctuations is denoted by

$$\Gamma(x, N - N') = \int e^{-i\kappa(N-N')\cdot s} \mathbb{E}\left(\delta n_e\left(x + \frac{s}{2}\right)\delta n_e\left(x - \frac{s}{2}\right)\right) \mathrm{d}s. \tag{7.69}$$

The mode decomposition is performed as described in section 3.3 and only one single mode is taken into consideration. The scattering cross section (4.68) to be inserted into the scattering operator (4.24) with rescaled Hamiltonian, cf. section 4.4, hence reads

$$\sigma(x, N, N') := \frac{\kappa^4}{(2\pi)^2}\,\frac{1}{n_e^2}\,\left|e^{\dagger}(x, N)\,(\mathbb{I} - \varepsilon)\,e(x, N')\right|^2 \Gamma(x, N - N')$$
$$\times \xi(x, N)\xi(x, N')\delta\left(H(x, N')\right). \tag{7.70}$$

7. Results for tokamak plasmas

Note that the rescaling factors ξ to account for a Hamiltonian different from the natural choice are included in this expression. In addition, $e(x, N) \equiv e_\alpha(x, N)$ denotes the normalized eigenvector of the wave mode α under consideration.

The code requires information on the electron density fluctuations in the plasma. This information is provided in terms of the two-point correlation function $\mathbb{E}\left(\delta n_e\left(x + \frac{s}{2}\right)\delta n_e\left(x - \frac{s}{2}\right)\right)$ inserted into (7.69). In principle the information may be obtained from any source, i.e. experimental measurements, turbulence simulations or models. As a simple starting point, for the two-point correlation function we use the model

$$\frac{1}{n_e^2}\mathbb{E}\left(\delta n_e\left(x + \frac{s}{2}\right)\delta n_e\left(s - \frac{s}{2}\right)\right) = \Delta^2 F^2(x)e^{-\frac{1}{2}s\cdot\Xi(x)s}. \tag{7.71}$$

Let us remark that r.h.s. of (7.71) expresses the two-point correlation of relative fluctuations. In analogy to the model (6.56b) for fluctuations in free space, the parameter Δ determines the strength of fluctuations and the factor

$$F(x) \equiv F(\rho) = e^{-\frac{(\rho-\rho_0)^2}{\Delta\rho_F^2}}, \tag{7.72}$$

specifying the extension of the fluctuations, where the width in normalized minor radius units is determined by $\Delta\rho_F$ and the center of fluctutations is at $\rho = \rho_0$. In the applications described below, the fluctuation layer is typically centered at the separatrix, i.e. $\rho_0 = 1$. The short scale dependency of the two-point correlation function (7.71) is present via the factor $e^{-\frac{1}{2}s\cdot\Xi(x)s}$. Here, in a coordinate system aligned to the magnetic field, the matrix $\Xi(x)$ contains on its diagonals the two-point correlation lengths $L_\perp(x)$ and $L_\parallel(x)$ of the fluctuation in direction perpendicular and parallel to the magnetic field, respectively, i.e.

$$\Xi(x) = \text{diag}\left\{\Xi_\perp(x), \Xi_\perp(x), \Xi_\parallel(x)\right\} = \text{diag}\left\{L_\perp^{-2}(x), L_\perp^{-2}(x), L_\parallel^{-2}(x)\right\}. \tag{7.73}$$

Given the fact that usually the electron density fluctuation correlation length is much larger parallel to the magnetic field then perpendicular to it, it makes sense to distinguish those two directions. Note that in principle the theory would also allow us to assume two different correlation lengths in the poloidal plane. However, for this first model we restict ourselves to one single value.

136

This model is motivated by the one used in [41] and adapted to the wave kinetic code. It allows us to compute the fluctuation spectrum (7.69) analytically, employing equation (7.71):

$$\Gamma(x, \Delta N) = (2\pi)^{3/2} \frac{\Delta^2 F^2(x)}{\sqrt{\Xi_\perp^2(x)\Xi_\parallel(x)}} e^{-\frac{\kappa^2}{2}\left[\frac{\Delta N_{\perp 1}^2 + \Delta N_{\perp 2}^2}{\Xi_\perp(x)} + \frac{\Delta N_\parallel^2}{\Xi_\parallel(x)}\right]}. \tag{7.74}$$

Substituted into (4.68), the scattering cross section reads

$$\sigma(x, N, N') = \frac{\kappa^4}{\sqrt{2\pi}} \frac{\Delta^2 F^2(x)}{\sqrt{\Xi_\perp(x)^2\Xi_\parallel(x)}} \left| e^\dagger(x, N)\,(\mathbb{I} - \varepsilon)\,e(x, N') \right|^2$$

$$\times \xi(x, N)\xi(x, N')e^{-\frac{\kappa^2}{2}\left[\frac{\Delta N_{\perp 1}^2 + \Delta N_{\perp 2}^2}{\Xi_\perp(x)} + \frac{\Delta N_\parallel^2}{\Xi_\parallel(x)}\right]} \delta\left(H(x, N')\right). \tag{7.75}$$

For the numerical scheme, the intensity $\Sigma(x, N)$ for the Poisson process which produces scattering events is expressed in equation (4.25b). The Dirac's δ-function and the Hamiltonian (7.34) in the scattering cross section allow us to immediately perform the $N'_\perp$-integration, if as integration variables the field aligned coordinates introduced in section 7.3 are used:

$$\Sigma(x, N) = \frac{\kappa^4}{4\sqrt{2\pi}} \frac{\Delta^2 F^2(x)}{\sqrt{\Xi_\perp(x)^2\Xi_\parallel(x)}} \int \left| e^\dagger(x, N)\,(\mathbb{I} - \varepsilon)\,e(x, N') \right|^2 \xi(x, N)\xi(x, N') \times$$

$$\times \left. e^{-\frac{\kappa^2}{2}\left[\frac{\Delta N_{\perp 1}^2 + \Delta N_{\perp 2}^2}{\Xi_\perp(x)} + \frac{\Delta N_\parallel^2}{\Xi_\parallel(x)}\right]} \right|_{N'_\perp = N_\perp(N'_\parallel)} \mathrm{d}N'_\parallel \mathrm{d}\phi'_N. \tag{7.76}$$

Here, $N_\perp(N'_\parallel)$ denotes the refractive index (7.33) which fulfils the dispersion relation. The remaining two-dimensional integral cannot be calculated analytically. Therefore, it would be quite time consuming to compute it after each integration step in the code. For the Poisson process, therefore, an upper limit Σ_{max} of the total scattering cross section Σ is used, as it is suggested in section 4.2. Let us recall that this strategy requires an evaluation of the exact value of Σ only if a Poisson event happens, which saves computational time. The needed upper limit is the product of a rough approximation Σ_{guess} for Σ, obtained from (7.76), evaluated under simplifying assumptions and approximations, and a user parameter g, i.e.

$$\Sigma_{\mathrm{max}}(x, N) = \Sigma_{\mathrm{guess}}(x, N)g. \tag{7.77}$$

The reader should be aware of the fact that the simplifying assumptions in Σ_{guess} are not always well-justified. However, we are rather interested in a reasonable guess for the order of magnitude of Σ then in the exact number, ensuring the important condition $\Sigma_{\text{max}} \geq \Sigma$ by a proper choice of the parameter g. To this aim, O-mode propagation purely perpendicular to the magnetic field is considered. Then, the polarization is taken so that $e(x, N') = e_{\parallel}$, and the projection of the fluctuation matrix D_F to the eigenvectors simplifies to

$$e^{\dagger}(x, N) \left(\mathbb{I} - \varepsilon \right) e(x, N') \approx 1 - P. \tag{7.78}$$

We have assumed further that fluctuations change the propagation direction only by a small amount, yielding $N \approx N'$. One also has $\xi(x, N) \approx \xi(x, N')$, so that

$$\Sigma_{\text{guess}}(x, N) = \frac{\kappa^3}{4} \frac{\Delta^2 F^2(x)}{\Xi_{\perp}(x)} \left(1 - P(x) \right)^2 \xi^2(x, N) \int e^{-\kappa^2 N_{\perp}^2 \frac{1 - \cos \Delta \phi_N}{\Xi_{\perp}(x)}} \mathrm{d}\Delta \phi_N. \tag{7.79}$$

Here, the $N'_{\parallel}$-integration has been performed analytically and the perpendicular refractive index components are written in terms of polar coordinates. In the exponential, $\cos \Delta \phi_N$ is Taylor expanded to second order, making it possible to perform the last remaining integration, with the result

$$\Sigma_{\text{guess}}(x, N) = \frac{\sqrt{2\pi} \kappa^2}{4} \frac{\Delta^2 F^2(x)}{\sqrt{\Xi_{\perp}(x)} N_{\perp}} \xi^2(x, N) \left(1 - P(x) \right)^2. \tag{7.80}$$

If as an example the exact value of Σ and the value of the guess Σ_{guess} are compared along a single ray trajectory, it turns out that they are typically in good agreement up to errors of a few per cent. We usually fix the parameter $g = 2$, which ensures that, indeed, Σ_{max} is an upper bound.

7.4.6. Absorption model

The last part of the dispersion symbol which needs to be discussed is the absorption part $\delta^2 D_A$. A model for absorption is derived in the frame of hot-plasma theory where the plasma particles are not assumed to move coherently at the same speed, but also their thermal velocity distribution is properly accounted for. Solving this hot-plasma dispersion relation, naturally an anti-Hermitian part emerges in the dielectric tensor, leading to absorption. Thermal effects are depicted in a kinetic theory where the plasma particles are characterized not only by their position x, but also

by their velocity v. This is properly described in the Vlasov equation. A good overview on the hot-plasma dispersion relation can be found in [42]. A full review on how to compute the absorption coefficient (3.46) is presented in [4]. For the code, an already existing absorption routine [43] is implemented. This point is not further addressed in the frame of this thesis.

7.5. Results

The remaining part of this chapter is dedicated to the results obtained from the WKBeam code under realistic tokamak conditions. First, the equations are studied under an approximation in order to compare the effect of fluctuations with previous works. Next, the code is run with various parameters for ASDEX Upgrade (AUG) and ITER plasma profiles. As a final result, the effect of fluctuations on absorption profiles, cf. section 7.5.2, and beams in reflectometry runs, section 7.5.3, are discussed.

7.5.1. Comparison with previous works

Due to the complexity of the problem, only few publications address the issue of beam propagation in tokamak plasmas including electron density fluctuations. In this section, we refer to a recent paper by Tsironis et al. [6], where a rough estimate based on a heuristic model of electron density blobs demonstrates the importance of the effect of fluctuations. A weak electron density ($\omega_p \ll \omega$) is considered. The field propagation is described in terms of a diffusion equation for the electric field energy distribution $F(\alpha, l)$, i.e.

$$\partial_l F(\alpha, l) = \frac{\partial}{\partial \alpha} \left(D_\alpha^{\mathrm{Tsironis}} \frac{\partial F(\alpha, l)}{\partial \alpha} \right) . \tag{7.81}$$

Here α denotes the propagation angle from the x-axis, i.e.

$$\tan \alpha = \frac{v_{\mathrm{y}}}{v_{\mathrm{x}}} \tag{7.82}$$

with the velocity $(v_{\mathrm{x}}, v_{\mathrm{y}})$ and l the length the rays have traveled through the fluctuating medium. Constant background plasma parameters and O-mode propagation purely perpendicular to the

magnetic field are assumed. The diffusion coefficient derived by Tsironis et al. is

$$D_\alpha^{\text{Tsironis}} = \frac{\sqrt{2\pi^3}}{32} \frac{\omega_p^4}{\omega^4} \frac{\delta n_e^2}{n_e^2} \frac{1}{L_b},$$

(7.83)

where δn_e is the electron density deviation in the center of a blob, n_e is the background electron density and L_b is the typical blob size. This analytic result is shown below to be included in our theory, as a special limiting case.

For comparison reasons, in this section, a diffusion equation is derived starting from the wave kinetic equation. The same conditions as in [6] are considered: Propagation of the O-mode purely perpendicular to the magnetic field $B = |B| e_z$ with a constant background density n_e. The appropriate eigenvalue of the dispersion tensor (7.27) for this case reads

$$H(N) = N_\perp^2 - P = N_\perp^2 - 1 + \frac{\omega_p^2}{\omega^2},$$

(7.84)

considered as Hamiltonian in this section. In the sense of section 4.4, this yields the trivial correction factor $\xi(x, N) \equiv 1$. The assumption of propagation purely perpendicular to B reduces the dimensionality of the problem to $m = 2$, so the position is described by $x = (x, y) \in \mathbb{R}^2$ and the refractive index by $N = (N_x, N_y) \in \mathbb{R}^2$.

We start with the wave kinetic equation formulated for the Wigner function with removed singularity, i.e. equation (3.68). An implicit condition in this equation is dispersion relation (3.38), which fixes in terms of polar coordinates

$$N_x = N_\perp \cos \phi_N,$$

(7.85a)

$$N_y = N_\perp \sin \phi_N,$$

(7.85b)

the $N_\perp$-component of the refractive index:

$$N_\perp = N_\perp' = \sqrt{1 - \frac{\omega_p^2}{\omega^2}}.$$

(7.86)

Hence, dimensionality of the refractive index is further reduced by one and the remaining component ϕ_N of the polar coordinates fully characterizes the refractive index. Disregarding

absorption, the wave kinetic equation (3.68) then reads

$$\{H(N), \tilde{w}(x, \phi_N)\} = \int \left[\tilde{\sigma}(x, \phi_N', \phi_N)\tilde{w}(x, \phi_N') - \tilde{\sigma}(x, \phi_N, \phi_N')\tilde{w}(x, \phi_N) \right] \mathrm{d}\phi_N'. \quad (7.87)$$

Here $\tilde{w}$ is the Wigner function with removed singularity as defined in (3.65) and $\tilde{\sigma}(x, \phi_N, \phi_N')$ is the simplified scattering cross section in terms of ϕ_N and ϕ_N' appropriate for the simplified two-dimensional propagation where also singularities are removed. It is obtained from the general scattering cross section presented in section 7.4.5, i.e. (7.75), adapted to the purposes of this section: An infinite parallel correlation length ensures that the rays stay inside the poloidal plane and do not get deflected with non-vanishing components parallel to the magnetic field. Furthermore, it is evaluated at values $N_\perp = N_\perp'$ which satisfy dispersion relation (7.86), i.e. in general

$$\tilde{\sigma}(x, \phi_N, \phi_N') = \left. \int \sigma(x, N, N') \mathrm{d}N_\parallel' \right|_{N_\perp = N_\perp' = \sqrt{1 - \frac{\omega_p^2}{\omega^2}}}. \quad (7.88)$$

With (7.75) inserted, this reads

$$\tilde{\sigma}(x, \phi_N, \phi_N') = \frac{1}{2} \left[(\mathbb{I} - P) \frac{\delta n_e}{n_e} \right]^2 \frac{\kappa^3}{\Xi_\perp} e^{-\frac{\kappa^2 N_\perp^2}{\Xi_\perp}\left(1 - \cos(\phi_N - \phi_N')\right)}, \quad (7.89)$$

where δn_e is the maximum of the electron density fluctuations. Here, the projection of the fluctuation part of the dispersion tensor (7.66) for O-mode propagation perpendicular to B

$$e^\dagger(x, N) (\mathbb{I} - \varepsilon) e(x, N') \approx 1 - P \quad (7.90)$$

is used as in (7.78), where P is defined in (7.21a). Furthermore, if $\kappa^2 N_\perp^2 / \Xi_\perp \gg 1$, which is the case for the considered parameters, cf. figure 7.5, only terms $|1 - \cos(\phi_N - \phi_N')| \ll 1$ yield a non-negligible exponential in the scattering cross section (7.89), so that the Taylor approximation

$$1 - \cos(\phi_N - \phi_N') \approx \frac{1}{2}(\phi_N - \phi_N')^2 \quad (7.91)$$

7. Results for tokamak plasmas

is appropriate. This is the assumption of small angle scattering. If also the approximation of small electron density $N_\perp \approx 1$ is used, cf. (7.86), the scattering cross section (7.89) simplifies to

$$\tilde{\sigma}(x, \phi_N, \phi'_N) = \frac{1}{2} \frac{\omega_p^4}{\omega^4} \frac{\delta n_e^2}{n_e^2} \frac{\kappa^3}{\Xi_\perp} e^{-\frac{\kappa^2}{2\Xi_\perp} \left(\phi_N - \phi'_N\right)^2}. \tag{7.92}$$

With this scattering cross section, which has been obtained under the same condition as in [6], we shall derive a diffusion equation, to be compared to (7.81). For this aim, in the general transport equation, i.e. the wave kinetic equation (7.87), a Taylor expansion for $\tilde{w}(x, \phi'_N)$ around $\phi'_N = \phi_N$ is performed up to the second order, i.e.

$$\begin{aligned}
\tilde{w}(x, \phi'_N) = \tilde{w}(x, \phi_N) &+ \frac{\partial \tilde{w}(x, \phi_N)}{\partial \phi_N}(\phi'_N - \phi_N) \\
&+ \frac{1}{2} \frac{\partial^2 \tilde{w}(x, \phi_N)}{\partial \phi_N^2}(\phi'_N - \phi_N)^2 + \mathcal{O}\left((\phi'_N - \phi_N)^3\right).
\end{aligned} \tag{7.93}$$

Physically, again, this is a small scattering angle approximation. Note that the small scattering angle limit applied in (7.91), where scattering angles should be small compared to unity, is valid for AUG and ITER parameters. However, for the Taylor expansion (7.93), unity might not be the right scale to compare. In fact we have no precise error control for the Taylor approximation and, thus, are not able to provide a precise condition on the scattering angles such that the error becomes negligible. For a rough estimate let us assume that the typical variational scale of $\tilde{w}$ is $\phi_{\tilde{w}}$, in the sense of

$$\left|\frac{\mathrm{d}^k \tilde{w}(x, \phi_N)}{\mathrm{d}\phi_N^k}\right| \approx \left|\frac{\tilde{w}(x, \phi_N)}{\phi_{\tilde{w}}^k}\right|. \tag{7.94}$$

Then the Taylor series makes sense as an asymptotic series when jumps $\Delta\phi_N = \phi'_N - \phi_N$ are small compared to this scale, i.e. $|\phi'_N - \phi_N| \ll \phi_{\tilde{w}}$. A proof of convergence is presented on the level of the associated stochastical process later on in this section. However, the AUG and ITER parameters used for figure 7.5 lead to $\left|\frac{\phi'_N - \phi_N}{\phi_{\tilde{w}}}\right| \approx 0.9$ and $\left|\frac{\phi'_N - \phi_N}{\phi_{\tilde{w}}}\right| \approx 0.01$, respectively, indicating that the expansion (7.93) might be inaccurate for ASDEX Upgrade. Here, the variational scale of $\tilde{w}$ is approximated by the initial width of the distribution, i.e. $\phi_{\tilde{w}} \approx \Delta\phi_{\text{init}}$.

Anyway, neglecting terms of order $\mathcal{O}\left((\phi'_N - \phi_N)^3\right)$, the Taylor expansion (7.93) inserted into (7.92) yields the evolution equation

$$\{H(N), \tilde{w}(x, \phi_N)\} = \frac{1}{2} \int \tilde{\sigma}(x, \phi_N, \phi'_N)\, (\phi'_N - \phi_N)^2 \, \mathrm{d}\phi'_N \frac{\partial^2 \tilde{w}(x, \phi_N)}{\partial \phi_N^2}. \qquad (7.95)$$

Here, due to $\tilde{\sigma}(x, \phi_N, \phi'_N) = \tilde{\sigma}(x, \phi'_N, \phi_N)$, cf. the explicit expression (7.92), zeroth order terms of the Taylor approximation cancel out and first-order terms vanish under the integral. Hence, the last equation only involves derivatives of the Wigner function of second order on the r.h.s. and has the same structure as (7.81), which is a diffusion equation. We refer to this equation as "diffusive limit", because it is obtained from the general equation under a limit of small scattering angles, characteristic of diffusive effects. The scattering cross section $\tilde{\sigma}$ (7.92) substituted into the integral in (7.95) can be computed analytically, with the result

$$\{H(N), \tilde{w}(x, \phi_N)\} = \frac{\partial}{\partial \phi_N} \left(\frac{\sqrt{2\pi}}{4} \frac{\omega_p^4}{\omega^4} \frac{\delta n_e^2}{n_e^2} \frac{1}{L_\perp} \frac{\partial \tilde{w}(x, \phi_N)}{\partial \phi_N} \right). \qquad (7.96)$$

The diffusion coefficient obtained from this diffusive equation is

$$D_{\phi_N} = \frac{\sqrt{2\pi}}{4} \frac{\omega_p^4}{\omega^4} \frac{\delta n_e^2}{n_e^2} \frac{1}{L_\perp}. \qquad (7.97)$$

We identify the two-point correlation length $L_\perp$ with the typical blob size L_b in the Tsironis model. This is physically motivated by the fact that both are a scale for the fluctuation. In addition, the propagation angle α, defined in (7.82), coincides with the angle of the refractive index ϕ_N, introduced in (7.85): This is implied in Hamilton's equation of motion (C.1a) for the two-dimensional geometry, where $H(x, N) \equiv H(x, N_\perp)$ does not depend on ϕ_N, so that the refractive index points in direction of propagation. This makes the diffusion coefficient derived in [6], namely (7.83), and the diffusion coefficient we have found here, (7.97), comparable. One finds that they are equivalent up to a prefactor which depends on the adopted model for blobs. Given the fact that we find the same dependence on blob size L_b, electron density n_e and electron density fluctuation level δn_e means that the simple physical ideas in the Tsironis paper are reproduced by the more complete scattering theory used in the framework of this thesis if the same physical assumptions are employed.

7. Results for tokamak plasmas

The validity of the above-discussed assumption of a diffusion limit, however, is not granted a priori and must be verified for the physical problem under consideration. Hence, the remaining part of this section is dedicated to the question of whether the diffusion limit is appropriate.

Numerical schemes for the solution of the transport equation and the diffusion equation are compared. In the numerics section 4.2, a scattering scheme for the unapproximated wave kinetic equation was presented: Given the scattering cross section (7.92), the number of scattering events is generated by a Poisson distribution with intensity (4.25b)

$$\Sigma = \int \tilde{\sigma}(x, \phi_N, \phi'_N) \mathrm{d}\phi'_N \approx \frac{\sqrt{2\pi}}{2} \kappa^2 \frac{\omega_p^4}{\omega^4} \frac{\delta n_e^2}{n_e^2} L_\perp, \tag{7.98}$$

where, again, the assumption of small angle scattering is made and the integration over an interval of 2π around ϕ_N is replaced by an integration on $\mathbb{R}$, taking into account also the tails of the exponential in $\tilde{\sigma}(x, \phi_N, \phi'_N)$, cf. (7.92), which, however, are negligible.

In case the propagation distance l is large so that $\Sigma l \gg 1$, the mean number of scattering events reads

$$\langle n_S \rangle = \Sigma l \tag{7.99}$$

with a small relative statistical uncertainty, thanks to the general properties of Poisson distributions. For each scattering kick, the variance of the ϕ_N distribution of the electric field squared $\tilde{w}(x, \phi_N)$ is increased by (7.92)

$$V_S = \kappa^{-2} L_\perp^{-2}. \tag{7.100}$$

In total, the variance increases by

$$V = \Sigma V_S l = \frac{\sqrt{2\pi}}{2} \frac{\omega_p^4}{\omega^4} \frac{\delta n_e^2}{n_e^2} \frac{1}{L_\perp}. \tag{7.101}$$

For the diffusion equation, a numerical solution scheme is presented in [24]: After steps with step size Δl through the fluctuating medium, a Gaussian kick with variance

$$\Delta V_D = 2 D_{\phi_N} \Delta l \tag{7.102}$$

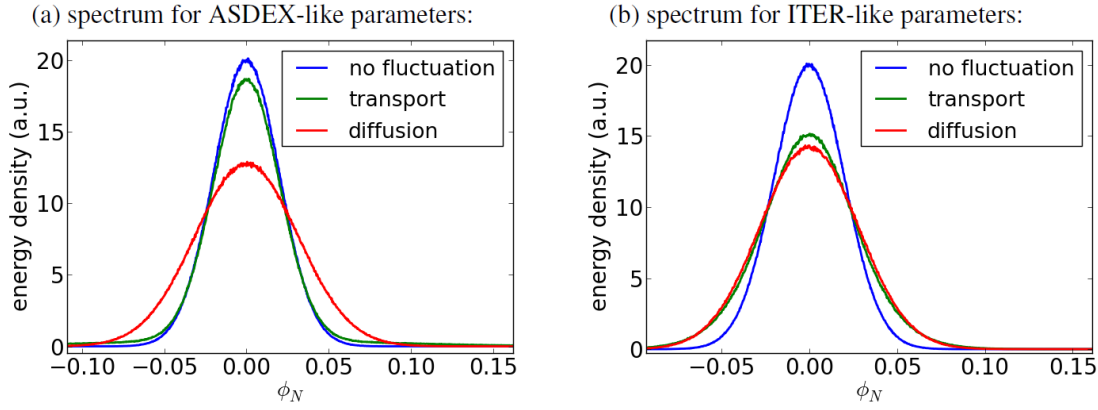(a) spectrum for ASDEX-like parameters: (b) spectrum for ITER-like parameters:

Figure 7.5.: Results of the numerical scattering scheme and the diffusive scheme. Initial spectrum is Gaussian shaped with width $\Delta\phi_{\text{init}} = 2 \cdot 10^{-2}$. Plasma frequency is $\omega_p = 50\,\text{GHz}$, beam frequency $\omega = 150\,\text{GHz}$, approximately valid for the tokamaks AUG and ITER. For the fluctuations, in physical units typical values for (a) AUG: $\delta n_e/n_e = 0.1$, $L_\perp = 0.4\,\text{cm}$, $l = 3\,\text{cm}$ and (b) ITER: $\delta n_e/n_e = 0.1$, $L_\perp = 2\,\text{cm}$, $l = 10\,\text{cm}$ are chosen, cf. section 7.5.2. Here l is identified with the width of the turbulence layer crossed by the beam.

is applied. After the propagation distance l this amounts in an increase of the variance of

$$V = 2D_{\phi_N}l = \frac{\sqrt{2\pi}}{2}\frac{\omega_p^4}{\omega^4}\frac{\delta n_e^2}{n_e^2}\frac{1}{L_\perp}. \tag{7.103}$$

It is seen that, indeed, the variances (7.101) and (7.103) are the same. Hence, the diffusion limit is appropriate in case $\Sigma l \gg 1$. On top of that the assumption of small angle scattering was made, i.e. the limit $\kappa L_\perp \gg 1$ is considered. (It is worth recalling that all lengths are normalized to the common reference scale length L.

Numerical schemes for both, the general equation and the diffusion limit, are implemented. The results are shown in figure 7.5. Typical numbers for the edge fluctuations in (a) AUG and (b) ITER are chosen, yielding $\Sigma l \approx 0.4 < 1$ and $\kappa L \perp \approx 12.6 \gg 1$ for AUG and $\Sigma l \approx 2.1$ and $\kappa L_\perp = 63 \gg 1$ for ITER. In the figure, indeed, it can be seen that for ASDEX Upgrade (a), there is a significant difference between the solution obtained simulating the general transport theory which shows broad tails, discussed in the next section, and the diffusive limit, overestimating the effect of fluctuations. Instead for typical ITER parameters (b), which is also the considered situation in [6], still a difference can be made out, but the diffusive solution constitutes a good

approximation. The difference for AUG and ITER is due to the larger propagation distance l (simulating a broader fluctuation layer) and the larger value of $L_\perp$ in ITER, which makes $\Sigma l \gg 1$ a reasonable assumption for ITER, but not for ASDEX Upgrade.

7.5.2. Absorption profiles

As mentioned in the first chapter, an important application of electron-cyclotron waves in tokamak plasmas is for heating and current drive. The latter, in particular, has been proposed as a tool to control magneto-hydrodynamic instabilities in fusion-grade plasmas. For this aim, it is important to deposit the beam power in a well-specified region. Particle and energy transport on magnetic surfaces, not affected by magnetic forces, is large. Instead, it is highly suppressed by Lorentz force in the direction perpendicular to the magnetic surfaces. Therefore, energy deposited at any point $x \in M_\rho$ on a magnetic surface M_ρ labeled by the normalized minor radius coordinate ρ, cf. coordinates introduced in figure 7.1, will equilibrate fast on the set M_ρ. Thus, people are interested rather in the magnetic surface M_ρ where the energy gets absorbed than in the point x itself. The physical wave energy flux is

$$F_{\text{phys}}(r) = \frac{c}{4\pi} F(x), \;\; x = r/L, \tag{7.104}$$

where $F(x)$ is the normalized flux defined in equation (3.80). It is worth noting that, in our convention, F has the dimensions of a squared electric field. The transport of the wave energy density then reads

$$\nabla \cdot F_{\text{phys}} = \frac{c}{4\pi L} \nabla_x \cdot F = -\frac{c}{4\pi L} \gamma \mathcal{E}, \tag{7.105}$$

where equation (3.82) has been accounted for. At last, inserting the definition of κ, (2.17), yields

$$\nabla \cdot F_{\text{phys}} = -\frac{\omega}{4\pi} \left(\gamma/\kappa \right) \mathcal{E}. \tag{7.106}$$

In magnetically confined plasmas the absorption coefficient is usually negligible away from resonances, but it is large where the beam frequency matches one of the plasma resonances; for electron-cyclotron waves, those are the Larmor frequency of the electrons (Doppler-shifted if $N_\parallel \neq 0$) and higher harmonics. For resonant absorption, the condition of weak dissipation, cf.

section 3.2, is not strictly satisfied. Since a semiclassical solution of the wave equation with strong absorption is still an open problem, a workaround is usually adopted: The physical absorption coefficient is used directly in the weakly dissipative theory. This formally corresponds to the rescaling

$$\gamma \to \kappa\gamma, \tag{7.107}$$

where γ is computed as described in section 7.4.6. At last, we have the transport equation

$$\nabla \cdot F_{\mathrm{phys}} = -\frac{\omega}{4\pi}\gamma\mathcal{E}. \tag{7.108}$$

The power injected by the beam through a magnetic surface M_ρ is by definition

$$P(\rho) = \int_{M_\rho} F_{\mathrm{phys}} \cdot \mathrm{d}S. \tag{7.109}$$

The quantity in which we are interested is the power ΔP deposited between two magnetic surfaces M_ρ and $M_{\rho+\Delta\rho}$ with $\Delta\rho$ sufficiently small. One defines the power deposition profile (or alternatively absorption profile) as the derivative

$$\frac{\mathrm{d}P(\rho)}{\mathrm{d}\rho} \approx \frac{\Delta P}{\Delta\rho} = \frac{1}{\Delta\rho}\left[\int_{M_{\rho+\Delta\rho}} F_{\mathrm{phys}} \cdot \mathrm{d}S - \int_{M_\rho} F_{\mathrm{phys}} \cdot \mathrm{d}S\right], \tag{7.110}$$

where we have assumed that the beam propagates from the outer surface inwards. Then, labeling the volume between the flux surfaces M_ρ and $M_{\rho+\Delta\rho}$ with ΔV_ρ, one has

$$\frac{\mathrm{d}P(\rho)}{\mathrm{d}\rho} \approx -\frac{1}{\Delta\rho}\int_{\Delta V_\rho} \nabla \cdot F_{\mathrm{phys}}\mathrm{d}V = \frac{\omega}{4\pi\Delta\rho}\int_{\Delta V_\rho} \gamma\mathcal{E}\mathrm{d}V = \frac{\omega L^3}{4\pi\Delta\rho}\langle 2\gamma\rangle_{\Omega_\rho}, \tag{7.111}$$

where $\mathrm{d}V = L^3\mathrm{d}x$, and Ω_ρ is the volume in normalized phase space given by

$$\Omega_\rho := \{(x, N) : x = r/L, r \in \Delta V_\rho\}. \tag{7.112}$$

The WKBeam code is able to provide the information required on the r.h.s., more specifically the expectation value $\langle 2\gamma\rangle_{\Omega_\rho}$. In order to extract it from the rays, for the binning code, a one-dimensional grid of bins (5.16) is used with $T_1(x, N) \equiv \rho$ as resolved coordinate. The bin areas

then are

$$\Omega_\nu = \left\{ (x, N) \in \mathbb{R}^6 : \nu\Delta\rho + \rho^{\min} \leq \rho < (\nu + 1)\Delta\rho + \rho^{\min} \right\} \qquad (7.113)$$

with $\Delta\rho$ the edge length of the bins, $\rho^{\min}$ the lower boundary of the grid of bins and ν an integer label. As a weight, $A(x, N) = 2\gamma(x, N)$ would be the appropriate quantity. However, we note that in practice, the expectation value of this observable can be computed more easily in terms of equation (5.15).

The absorption profile (7.111) basically provides the information on which magnetic surface the power is deposited and how narrow the absorption region is. However, it is more convenient to normalize the derivative:

$$\frac{\mathrm{d}P}{\mathrm{d}V}(\rho) = \frac{\frac{\mathrm{d}P}{\mathrm{d}\rho}(\rho)}{\frac{\mathrm{d}V}{\mathrm{d}\rho}(\rho)}, \qquad (7.114)$$

where $V \equiv V(\rho)$ is the volume enclosed by the magnetic surface ρ. In practice, this volume is computed in terms of an integral in the cylindrical tokamak coordinates introduced in figure 7.1, namely

$$V(\rho) = \int_{\{\rho(\mathrm{R},\mathrm{z}) \leq \rho\}} \mathrm{R} \, \mathrm{d}\mathrm{R}\mathrm{d}\mathrm{z}\mathrm{d}\varphi = 2\pi \int_{\{\rho' \leq \rho\}} \mathrm{R}(\rho', \theta) \left| \frac{\partial(\mathrm{R}, \mathrm{z})}{\partial(\rho', \theta)} \right| \mathrm{d}\rho' \mathrm{d}\theta. \qquad (7.115)$$

Here, the rotational invariance of the tokamak allows us to immediately compute the φ-integration and a substitution to the coordinates (ρ, θ) in the poloidal plane is performed. In the code, the Jacobian determinant $\left| \frac{\partial(\mathrm{R},\mathrm{z})}{\partial(\rho,\theta)} \right|$ is known from the magnetic field interpolation, so that the derivative

$$\frac{\mathrm{d}V}{\mathrm{d}\rho}(\rho) = 2\pi \int_0^{2\pi} \mathrm{R}(\rho, \theta) \left| \frac{\partial(\mathrm{R}, \mathrm{z})}{\partial(\rho, \theta)} \right| \mathrm{d}\theta, \qquad (7.116)$$

which is present in (7.114), can be computed numerically as a one-dimensional integral. Function (7.114) is considered the final result of WKBeam for heating and current drive applications. Physically, $\frac{\mathrm{d}P}{\mathrm{d}V}(\rho)$ gives a statement on the volume density of the absorbed power around a given magnetic surface ρ.

We shall note here that for the determination of absorption profiles, the normalization used for the electric field in appendix D, namely a central value of $A = 1$, is not reasonable. Instead, the

quantity which can be controlled experimentally is the total input beam power, which can be computed in terms of the flux propagating through the antenna plane, i.e. in physical units

$$P_a = \frac{cL^2}{4\pi} \int 4N_{a\perp} w(\mathrm{x} = 0, \mathrm{y}, N) \mathrm{dy} \mathrm{d}N \tag{7.117}$$

with Hamiltonian (7.35) for free space and $N_{a\perp}$ the refractive index component perpendicular to the antenna plane. The Wigner function (D.11) with the dimensionality $m = 3$ is substituted into integral (7.117) and the total beam power is obtained as

$$P_a = \frac{cL^2}{4\pi} \mathcal{P} |A|^2, \tag{7.118}$$

where we have defined the dimensionless constant involving an integral to be computed numerically

$$\mathcal{P} := 4 \left(\frac{2\pi}{\kappa} \right)^m \left[\left(D_1^2 + S_1^2 \right) \left(D_2^2 + S_2^2 \right) \right]^{-1/2}$$
$$\times \int \sqrt{1 - N_a^2} e^{-\kappa \frac{D_1}{D_1^2 + S_1^2} (N_1 - N_{1,0})^2 - \kappa \frac{D_2}{D_2^2 + S_2^2} (N_2 - N_{2,0})^2} \mathrm{d}^2 N_{\mathrm{y}}. \tag{7.119}$$

Here, $N_a = (N_{a1}, N_{a2})$ denotes the refractive index aligned to the antenna plane and $N_{a,0} = (N_{a1,0}, N_{a2,0})$ the central value for this refractive index. For the convention on the beam parameters D and S (not to be confused with the cold-plasma parameters defined in section 7.4.1), the reader may refer to appendix D. Furthermore, in this appendix, the amplitude A was dropped. Now, instead, it is needed and explicitly written out again in the Wigner function.

Equation (7.118) can be solved for the prefactor $|A|^2$ for the Wigner function, with the result

$$|A|^2 = \frac{4\pi}{cL^2} \frac{P_a}{\mathcal{P}}. \tag{7.120}$$

This determines $|A|^2$ given the input power P_a of the beam. On the level of dimensions, we have

$$\left[|A|^2 \right] = \frac{[\text{power}] \cdot [\text{time}]}{[\text{length}]^3} = \frac{[\text{energy}]}{[\text{length}]^3}, \tag{7.121}$$

i.e. the dimension of an energy density, which is, in cgs-units, correct for an electric field squared.
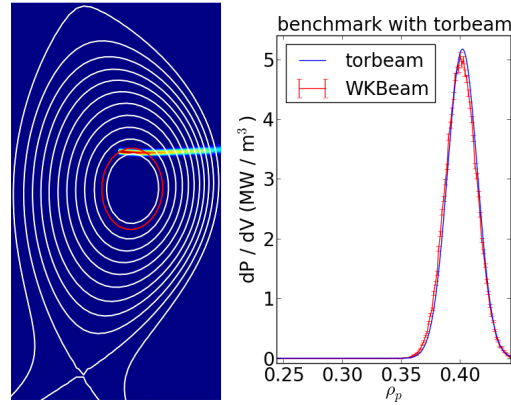
Figure 7.6.: Left: Projection of the beam on a poloidal plane on top of the magnetic surfaces of AUG. The surface where the maximum absorption takes place is drawn in red. Right: Absorption profiles obtained from torbeam and from WKBeam for the same beam parameters. The errorbars indicate the statistical uncertainty of the Monte-Carlo estimator. The plasma profiles of AUG #25485, cf. appendix G, are used, as beam the following parameters are chosen: X-mode, frequency $f = 140\,\mathrm{GHz}$, initial beam width $w = 3.5\,\mathrm{cm}$, initial curvature radius $R = 100\,\mathrm{cm}$, beam center launched at $(\mathrm{x}, \mathrm{y}, \mathrm{z}) = (236\,\mathrm{cm}, 0, 32\,\mathrm{cm})$ with a poloidal antenna orientation of $5°$ and no tilt in toroidal direction (AUG angle convention, cf. section 7.2). For the ray tracing, 50000 rays are considered.

In this section, as input power $P_a = 1\,\mathrm{MW}$ is considered. Thanks to the linearity of the problem, a different input power will just rescale the computed absorbed power. Hence, the results presented here may be understood as the absorbed power per $1\,\mathrm{MW}$ of input power.

In the following, let us discuss the outcome of the code, i.e. the power deposition profile (7.114). In case no fluctuations are present, the same function can also be determined using the TORBEAM code. Hence, as a benchmark, both results may be compared. For one set of beam parameters, such a comparison is shown in figure 7.6. It can be seen in the figure that there is a good agreement between the TORBEAM and the WKBeam solution. The solution obtained from the Monte-Carlo estimator in the wave kinetic code is the result of a random process and therefore subject to statistical uncertainties. To obtain a better resolution, more rays could be used, lengthening the runtime of the code, which for typical runs shown in this section is around $1.5\,\mathrm{h}$ on 16 cores.

In addition to diffractive effects, already described by TORBEAM, the new WKBeam code is able to take into account the effect of fluctuations. As parameters in the model presented in

section 7.4.5, the maximum relative strength of the electron density fluctuations $\delta n_e/n_e$, the width of the fluctuation layer $\Delta\rho_F$ and the parallel and perpendicular correlation lengths $L_\parallel$ and $L_\perp$ can be chosen. In the following, the fluctuation parameters are varied for a beam in ASDEX Upgrade shot #25485 (cf. appendix G) and the effects on the absorption profiles are discussed. The parallel correlation length is set to $L_\parallel = 1\,\mathrm{m}$ for all simulations. This is a reasonable number and, being much larger then the typical scale of the beam, in practice describes the limit of an infinite parallel correlation length. Therefore, varying this value does not affect the solution. For the other parameters, we consider realistic values as width of the fluctuation layer $\Delta\rho_F = 0.025$, just covering the region of steep rise, called pedestal, in the electron density profile. A typical value for the fluctuation level is $\delta n_e/n_e = 0.1$. For the perpendicular fluctuation correlation length, $L_\perp \approx 10\rho_S$ with ρ_S the ion gyroradius is usually considered [6]. For ASDEX Upgrade, this is $L_\perp = 0.4\,\mathrm{cm}$.

The basic physical effects when varying these numbers can be understood in the simple physical limit of purely perpendicular propagation of the rays, presented in section 7.5.1. The expression for the total scattering cross section Σ (7.98) integrated along a ray trajectory gives us the mean number of scattering events $\langle n_S \rangle$ for this ray, whereas the width of the differential scattering cross section σ (7.92) provides the typical order of magnitude of the deflection angle $\Delta\phi_N$ in case a scattering event happens, i.e.

$$\langle n_S \rangle = \frac{\sqrt{2\pi}}{2}\kappa^2 \int_{\mathrm{ray}} \frac{\omega_p^4(x(\tau))}{\omega^4} \frac{\delta n_e^2}{n_e^2}(x(\tau)) L_\perp(x(\tau))\mathrm{d}\tau, \tag{7.122a}$$

$$\Delta\phi_N \approx (\kappa N_\perp L_\perp)^{-1}. \tag{7.122b}$$

In order to investigate the effect of the fluctuation parameters $\Delta\rho_F$, $\delta n_e/n_e$ and $L_\perp$, in figure 7.7 two of them are held constant at the reference value introduced above, whereas the remaining parameter is changed. All absorption profiles in this figure with fluctuation turned on show a reduced absorption peak as compared to the no-fluctuation solution at the maximum position of $\rho = 0.4$. The fluctuations are seen to lead to the formation of extended tails in the power deposition profile, except for the run with $L_\perp = 2\,\mathrm{cm}$ in panel (c) of the figure. There, no tails are visible, but a broadened absorption peak is present. As also intuition would suggest, the portion of energy getting transported to the tails increases with the width of the fluctuation layer $\Delta\rho_F$ and with the electron density fluctuation level $\delta n_e/n_e$, confirmed in panels (a) and (b) of the

(a) scan on width $\Delta\rho_F$, $\delta n_e/n_e = 0.1$, $L_\perp = 0.4\,\mathrm{cm}$:
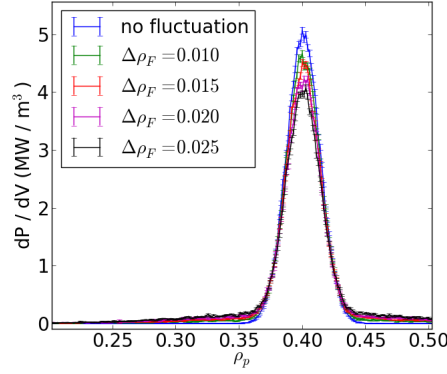
(b) scan on fluctuation level $\delta n_e/n_e$, $\Delta\rho_F = 0.025$, $L_\perp = 0.4\,\mathrm{cm}$:
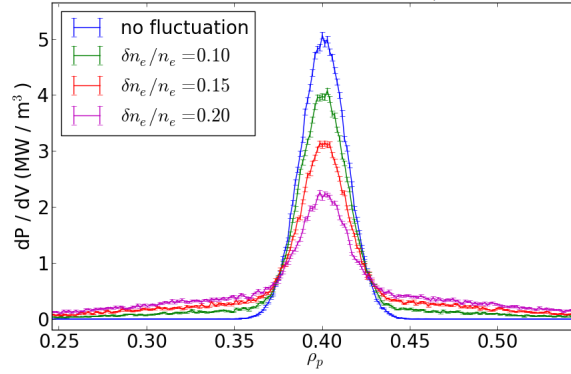
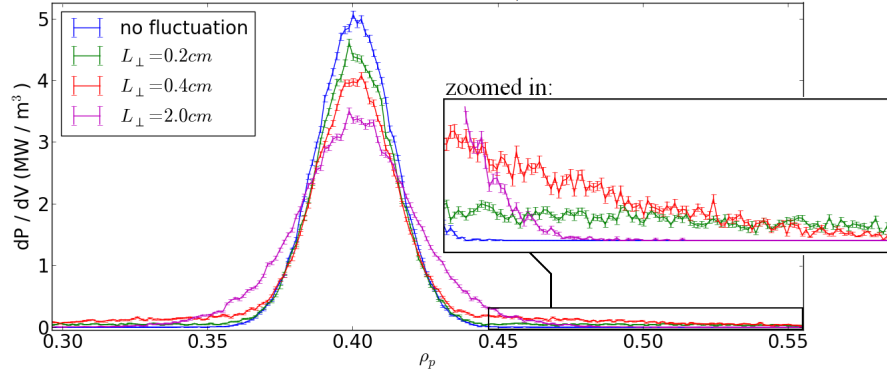(c) scan on correlation length $L_\perp$, $\delta n_e/n_e = 0.1$, $\Delta\rho_F = 0.025$:

Figure 7.7.: Absorption profiles for ASDEX Upgrade shot #25485 (cf. appendix G) with the beam parameters of figure 7.6. For the fluctuation, various parameters of (a) the width of the fluctuation layer $\Delta\rho_F$, (b) the maximum strength of electron density fluctuation $\delta n_e/n_e$, (c) the perpendicular correlation length $L_\perp$ are shown.

figure, respectively. In the limit of perpendicular propagation this can easily be understood, the mean number of scattering events being proportional to $(\delta n_e/n_e)^2$ and to the propagation length

$\Delta\tau$, deflecting a higher fraction of the rays for larger values of the electron density fluctuations and for broader fluctuation layers. Instead, changing the perpendicular correlation length $L_\perp$, cf. panel (c) of the figure, changes not only the fraction of energy found in the central peak and in the tails, but it also crucially influences the shape of the absorption profile. This effect, as well as the shape of the absorption profiles for $L_\perp = 0.4\,\text{cm}$, cf. figure 7.7 (a) and (b), is more easily discussed by means of the spectra of the beam just before reaching the fluctuation layer and just after propagating through the fluctuation layer, shown in figure 7.8. These spectra are computed using as a weight for the binning $A \equiv 1$ and binning areas

$$\Omega_k^{\phi_N} = \left\{ (x, N) \in \mathbb{R}^6 : \rho^{\min} < \rho(x, N) < \rho^{\max}, \right.$$
$$\left. 0 < \phi_N(x, N) - \phi_N^{\min,k} < \Delta\phi_N \right\} \tag{7.123a}$$

to resolve ϕ_N in a magnetic surface shell specified by the boundaries $\rho^{\min}$ and $\rho^{\max}$ and the subdivision into bins

$$\phi_N^{\min,k} = \phi_N^{\min} + k\Delta\phi_N, \tag{7.123b}$$

that resolves the angular spectrum of the wave field, with the angel ϕ_N defined in (7.10). Here, k labels the bins and $\Delta\phi_N$ is the corresponding bin resolution. In order to compute the spectrum just before the beam has reached the fluctuation layer centered at $\rho = 1$, the boundaries $\rho^{\min} = 1.03$ and $\rho^{\max} = 1.05$ are chosen. Instead, the spectrum just inside is obtained with $\rho^{\min} = 0.95$ and $\rho^{\max} = 0.97$.

In panel (b) of figure 7.8, uniquely the contribution of scattered rays to the spectrum just after propagation through the fluctuation layer is shown. The fact that smaller values of $L_\perp$ lead to a broader distribution of the propagation angle ϕ_N, predicted by (7.122b), is confirmed. A Gaussian fit in this figure provides the widths $\Delta\phi_N^{\text{fluctuation}} = 0.22,\ 0.11,\ 0.035$ for $L_\perp = 0.2\,\text{cm},\ 0.4\,\text{cm},\ 2\,\text{cm}$, respectively. Instead, the spectrum with no fluctuations present has a width of $\Delta\phi_N = 0.022$, measured by means of a Gaussian fit in figure 7.8 (c). Obviously, $\Delta\phi_N^{\text{fluctuation}} \gg \Delta\phi_N$ for the parameters $L_\perp = 0.2\,\text{cm},\ 0.4\,\text{cm}$. In the composed spectrum after propagation through fluctuation, panel (c) of the figure, this leads to a background intensity caused by the scattered rays which is much broader than the sharp contribution of unscattered

(a) spectrum outside fluctuation layer:

(b) spectrum inside fluctuation layer, contribution of scattered rays only:

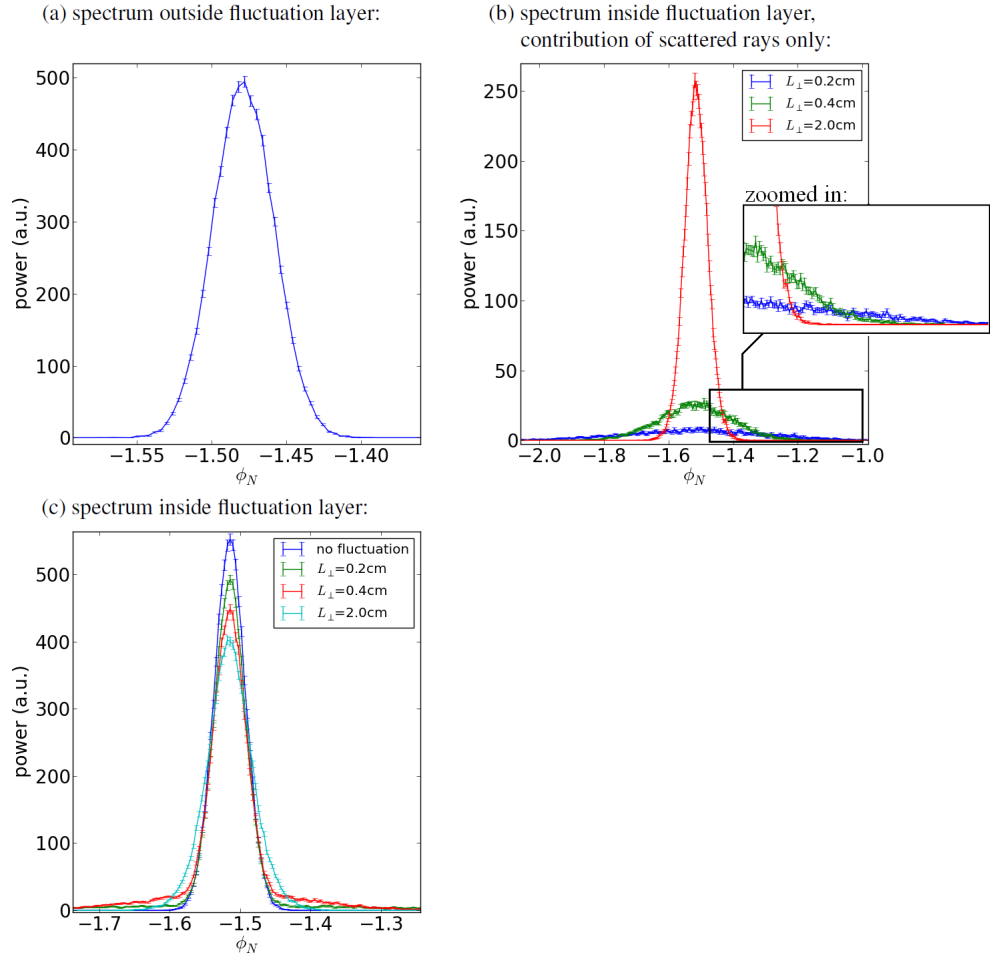(c) spectrum inside fluctuation layer:

Figure 7.8.: Spectra of the beams in AUG. (a) the spectrum just before the beam reaches the fluctuation layer for $\rho \in [1.03, 1.05)$, (b) the contribution of scattered rays to the spectrum just after the beam has propagated through the fluctuation layer for $\rho \in [0.95, 0.97)$ and (c) the spectrum of the beam after propagation through the fluctuation. The beam parameters are chosen as in figure 7.6 and for fluctuation $\Delta\rho_F = 0.025$ and $\delta n_e/n_e = 0.1$ are used.

rays, providing a tail structure in the spectrum. Instead, for $L_\perp = 2\,\mathrm{cm}$, the standard deviation of scattered rays $\Delta\phi_N^{\text{fluctuation}} = 0.035$ is of the same order as the width of the distribution of the unscattered rays $\Delta\phi_N = 0.022$. Therefore, the spectrum after propagation through the fluctuation layer does not show broad tails, but it rather is still Gaussian shaped with an increased standard deviation.

However, the maximum value of the spectrum at $\phi_N = -1.48$ is affected more by larger values of $L_\perp$. This is explained by the mean number of scattering events, estimated in terms of the integral of the total scattering cross section Σ along the central ray, yielding $\langle n_S \rangle = 0.13,\ 0.26,\ 1.31$ for the run shown in figure 7.8 with $L_\perp = 0.2\,\text{cm},\ 0.4\,\text{cm},\ 2\,\text{cm}$, respectively. This is in agreement with the dependence $\langle n_S \rangle \propto L_\perp$, predicted for the simple physical limit of perpendicular propagation, cf. (7.122a). The actual number of scattering events for the single rays being Poisson distributed, the probability of getting scattered at least once is

$$P_{\text{scattered}}(\langle n_S \rangle) = 1 - e^{-\langle n_S \rangle}, \tag{7.124}$$

leading to $P_{\text{scattered}} = 12\%,\ 23\%,\ 73\%$ for $L_\perp = 0.2\,\text{cm},\ 0.4\,\text{cm},\ 2\,\text{cm}$, respectively. This shows that in the $L_\perp = 0.2\,\text{cm},\ 0.4\,\text{cm}$ runs only a minority of the rays gets scattered, leading to the broad tails, but not carrying away from the center too much energy, whereas 73% of the rays are affected by scattering for $L_\perp = 2\,\text{cm}$, broadening the spectrum and hence crucially affecting the shape of the power absorption profile. As mentioned in section 7.5.1, the limit of rays being scattered several times is called diffusive regime, in contrast to the advection regime for which only few rays are scattered.

Broad tails in the spectrum just after the fluctuation layer physically are interpreted in terms of a contribution of energy propagating in a direction far from the central direction, leading to broad tails of the beam itself after some propagation distance. This effect is directly translated into broad tails in the absorption profile for $L_\perp = 0.2\,\text{cm},\ 0.4\,\text{cm}$ as well, see 7.7 (c), whereas the broadened peak in the spectrum for $L_\perp = 2\,\text{cm}$ makes the corresponding absorption profile become broad.

The absorption profile computed for realistic parameters in ASDEX Upgrade, $\Delta\rho_F = 0.025$, $\delta n_e/n_e = 0.1$, $L_\perp = 0.4\,\text{cm}$, is not far from the profile with fluctuations turned off, see for example figure 7.7 (a), and could still be in agreement with simultaneous measurements of absorption profiles. It is interesting to see what the simulation predicts for the absorption profiles in ITER, where, given the fact that the tokamak is not already built, no measurements exist, but precisely aimed and collimated electron-cyclotron beams are supposed to be used for the stabilization of magneto-hydrodynamic instabilities (such as neoclassical tearing modes), requiring sharp absorption profiles [44]. As for ASDEX Upgrade, the pedestal region is covered
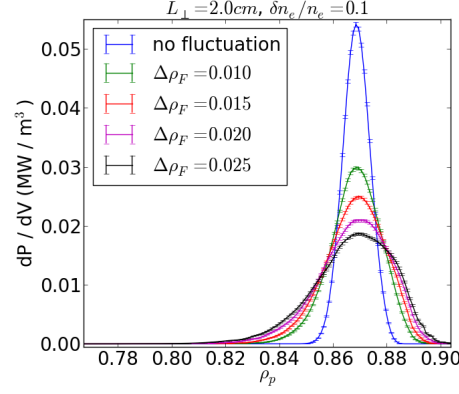
Figure 7.9.: Absorption profiles for ITER equilibrium, cf. appendix G, with the following beam parameters: O-mode, frequency $f = 170\,\text{GHz}$, initial beam width $w = 5.047\,\text{cm}$, initial curvature radius $R = 318.6\,\text{cm}$, beam center launched at $(\text{x}, \text{y}, \text{z}) = (699.871\,\text{cm}, 0, 441.441\,\text{cm})$ with a poloidal antenna orientation of $47°$ and a toroidal antenna orientation of $20°$ (ITER angle convention, cf. section 7.2). For the ray tracing, 50000 rays are considered.

with $\Delta\rho_F = 0.025$ and $\delta n_e/n_e = 0.1$ is a reasonable number for the electron density fluctuation level. Due to the increased temperature, the gyroradius in ITER is larger. This makes the choice of $L_\perp = 10\rho_S \approx 2\,\text{cm}$ appropriate [41]. The results are shown in figure 7.9, where a scan on the width $\Delta\rho_F$ is presented. It can be seen that for the reference value of $\Delta\rho_F = 0.025$, the absorption profile is dramatically broadened and the effect of fluctuation is more pronounced as in AUG with the same parameters, see figure 7.7 (c). This is due to a rescaling of the tokamak: In ITER, the minor radius will be $r_{\text{ITER}} = 201\,\text{cm}$, whereas in AUG it is $r_{\text{AUG}} = 65\,\text{cm}$. Therefore, a width of the fluctuation layer of $\Delta\rho_F = 0.025$ corresponds to a physical thickness of $\Delta F \approx 2r_{\text{ITER}}\Delta\rho_F \approx 10\,\text{cm}$ in ITER whereas it is only $\Delta F \approx 3\,\text{cm}$ in ASDEX Upgrade, leading to a larger number of rays getting scattered. The mean number of scattering events evaluated on the central ray yields $\langle n_S \rangle = 11.6$, so that most rays get scattered even several times. Another important effect of rescaling is due to propagation after the fluctuation layer: The further the beam propagates until it gets absorbed, the more its width is enlarged by a broad spectrum of the beam. For the AUG run, the distance of the central ray from the $\rho = 1$ surface where fluctuations are centered to the absorption region at $\rho = 0.4$ is found to be $\Delta l \approx 50\,\text{cm}$, whereas for ITER, even if absorption takes place around $\rho = 0.87$, the distance with $\Delta l \approx 100\,\text{cm}$ is twice as large. For test purposes, the absorption region can be shifted towards the fluctuation layer. This is achieved
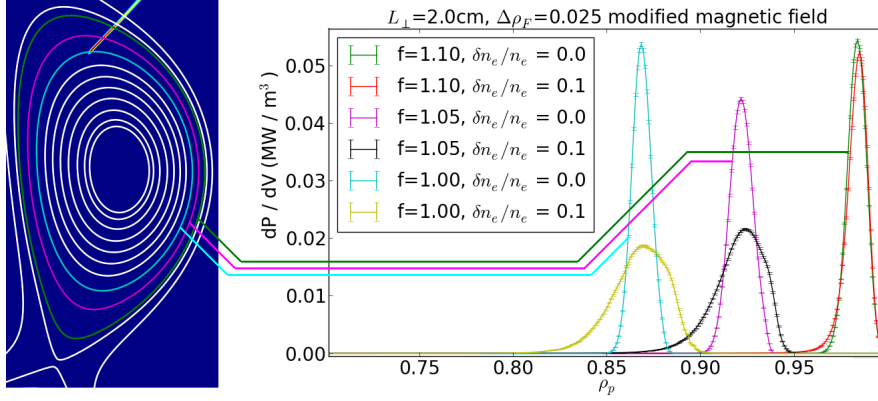
Figure 7.10.: Absorption profiles for ITER equilibrium, cf. appendix G, the beam parameters copied from figure 7.9 and fluctuation parameters $\Delta \rho_F = 0.025$, $\delta n_e/n_e = 0.1$, $L_\perp = 2\,\mathrm{cm}$. The magnetic field strength is multiplied with the factor f to shift the absorption region for test purposes.

by multiplying the magnetic field in the tokamak with some factor close to one, modifying the position R of the cyclotron resonance, cf. section 7.1. For the ITER run, this is presented in figure 7.10. Whereas absorption around $\rho = 0.87$ shows the dramatic broadening effect. When the absorption lacation is shifted outwards, the effect decreases. Absorption at $\rho = 0.98$ is almost not affected by fluctuations.

In summary this section has shown the importance of a proper estimation of the effect of fluctuations in the tokamak ITER, where absorption profiles get crucially affected by scattering.

7.5.3. Reflectometry applications

A second interesting application for the WKBeam code is the simulation of reflectometry beams. As it was presented in the benchmarks section 6.3 of a linear layer, using WKBeam, meaningful results can be produced even near the cut-off layer, if the spatial average over a domain which is large enough is considered. Reflectometry runs usually stay away from resonances and, hence, do not involve absorption, justifying the use of the cold-plasma approximation for the dielectric operator. This assumption simplifies wave equation (2.20) to a partial differential equation which, in principle, can be solved by a partial differential equation solver. However, considering the fully three dimensional geometry of the tokamak and high frequency waves, this is numerically expensive and the wave kinetic code is still more efficient if a solution in the semiclassical limit is

(a) fluctuation turned off, projection on Rz-plane:

(b) fluctuation turned off, projection on Ry-plane:

(c) fluctuation turned on, projection on Rz-plane:

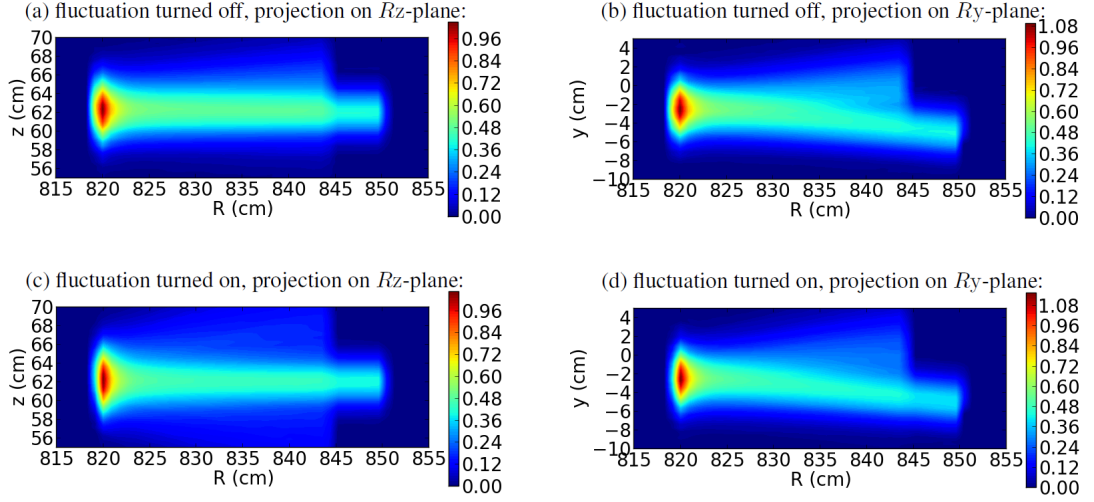(d) fluctuation turned on, projection on Ry-plane:

Figure 7.11.: Reflectometry run for ITER equilibrium, cf. appendix G. Projections of the electric field amplitude of the beam in arbitrary units on the Rz-plane (a), (c) and on the Ry-plane (b), (d). The projections are obtained as square roots of the field energy density integrated on y and z, respectively. No fluctuations are considered for (a), (b), whereas the fluctuation parameters $\Delta\rho_F = 0.025$, $\delta n_e/n_e = 0.1$, $L_\perp = 2\,\text{cm}$, $L_\parallel = 100\,\text{cm}$ are chosen for (c), (d). The beam parameters are: O-mode, frequency $f = 70\,\text{GHz}$, initial beam width $w = 2.412\,\text{cm}$, initial curvature radius $R = 1000000\,\text{cm}$, beam center launched at $(x, y, z) = (849.78\,\text{cm}, -5\,\text{cm}, 62\,\text{cm})$ with a toroidal antenna orientation of $5°$ and no tilt in poloidal direction (ITER angle convention, cf. section 7.2). For the ray tracing, 20000 rays are considered.

sufficient. We tune the beam such that it is most sensitive to fluctuations. In (7.122b), an estimate for the order of magnitude of the deflection angle $\Delta\phi_N$ in case of scattering of a ray is given and it can be seen that $\Delta\phi_N \propto N_\perp^{-1}$. Hence, the largest change of angle is achieved by beams which just reach their cut-off layer $N_\perp = 0$ in the fluctuation region, even leading to isotropic scattering in the perpendicular plane.

As an example, a reflectometry run is shown in figure 7.11. For this run, the turning point of the central ray is located at $\rho \approx 0.994$, lying near the center of the fluctuation layer. The projections of the beam onto both the Rz-plane (a,c) and the Ry-plane (b,d) are shown with and without fluctuations. The magnetic field being oriented basically in y-direction, the beam is only affected a little by the long scale parallel fluctuations, cf. panels (b) and (d) of the figure. Instead, the projection on the poloidal plane shows a broadened reflected contribution of the beam in
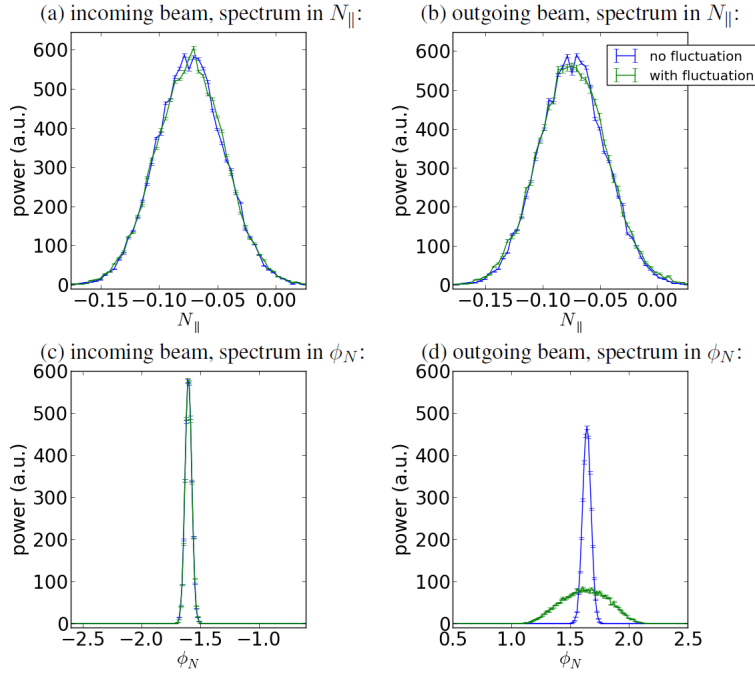
Figure 7.12.: Spectra of a reflected beam for ITER equilibrium, cf. appendix G, in the shell $\rho \in [1.03, 1.05)$. The beam parameters and fluctuation parameters are the same as in figure 7.11.

panel (c) on top of the incoming beam launched from $R \approx 850\,\mathrm{cm}$. The corresponding reflected contribution in the non-fluctuating plasma (a) is narrower and points a little upwards.

Mainly the same physical results are observed in a more quantitative way considering the spectrum of the beam when propagating towards the cutoff and backward, cf. figure 7.12. The spectra shown in this figure are obtained from binning with weight $A \equiv 1$. In order to resolve the spectrum in $N_\parallel$, the bins are

$$\Omega_k^{N_\parallel, \pm} = \Big\{ (x, N) \in \mathbb{R}^6 : \rho^{\min} < \rho(x, N) < \rho^{\max}, \ \pm \phi_N(x, N) \in [0, \pi),$$

$$0 < N_\parallel(x, N) - N_\parallel^{\min, k} < \Delta N_\parallel \Big\}. \tag{7.125a}$$

With the definition of ϕ_N (7.10) and the magnetic field mainly in y-direction, the superscript "+" selects the rays propagating outward (in positive R-direction) and "-" the ones entering the plasma, i.e. in negative R-direction, as confirmed in the spectra 7.11 (c,d).

7. Results for tokamak plasmas

The bin boundaries are $\rho^{\text{min}} = 1.03$ and $\rho^{\text{max}} = 1.05$ to select a magnetic surface shell outside the fluctuation layer and the subdivision in $N_\parallel$-direction is

$$N_\parallel^{\text{min},k} = N_\parallel^{\text{min}} + k\Delta N_\parallel. \tag{7.125b}$$

In analogy, the spectrum in ϕ_N is constructed: A bin

$$\Omega_k^{\phi_N} = \left\{ (x, N) \in \mathbb{R}^6 : \rho^{\text{min}} < \rho(x, N) < \rho^{\text{max}}, \right.$$
$$\left. 0 < \phi_N(x, N) - \phi_N^{\text{min},k} < \Delta\phi_N \right\}, \tag{7.126a}$$

subdivided in ϕ_N-direction according to the grid

$$\phi_N^{\text{min},k} = \phi_N^{\text{min}} + k\Delta\phi_N, \tag{7.126b}$$

is used. The spectra in the parallel refractive index component $N_\parallel$ and the angle of the refractive index in the poloidal plane ϕ_N are not affected by fluctuations for the incoming beam, confirmed by panels (a) and (c) of figure 7.12. Furthermore, given the fact that the parallel fluctuation correlation length is large, again, the parallel refractive index component of the reflected beam (b) is not influenced by fluctuations. Instead, the spectrum of the propagation angle ϕ_N for the reflected beam becomes broader if fluctuations are turned on, cf. panel (d).

8

Conclusions and outlook

In the framework of this thesis, a new simulation code for high frequency waves in fluctuating media has been developed. Based on Wigner-Weyl symbol calculus, a phase space description of the beam, formulated in terms of the Wigner function of the wave field, was obtained. Such description allows us to deal with projection singularities (caustics) which are present e.g. in the standard ray tracing method. The evolution of the Wigner function is described by the wave kinetic equation, derived in the semiclassical limit. This approach retains the diffraction effects, while neglecting higher order wave effects in the semiclassical expansion. It was shown how even short scale fluctuations can be taken into account in the description in a mathematically consistent way. The unfolding of caustics allows us to produce accurate results even near turning points, albeit neglecting in the semiclassical limit fine structured interference effects. In addition, the phase space description makes a natural derivation of spectra possible.

With tokamak applications in mind, in particular the effect of electron density fluctuations on electron-cyclotron waves was studied for the tokamaks ASDEX Upgrade and ITER with the aim

of addressing the possible broadening of the power deposition profile induced by turbulence in electron-cyclotron current drive experiments. Therefore, the realistic tokamak geometry as well as realistic plasma profiles have been used and fluctuations are described by an analytic model.

A new code, WKBeam, has been developed on the basis of a Monte-Carlo scheme adaptedd to the solution of the relevant boundary value problem for the wave kinetic equation. The code has been written in python, a modern and widely available high-level language, with cython modules for performance and mpi4py for the parallelization. Extensive benchmarks of the new code have been carried out. A comparison shows a good agreement between the new code and the reference solutions employed for benchmark and, for a non-fluctuating tokamak plasma, with the well-tested code TORBEAM. In presence of fluctuations instead, the concerns of previous works that larger machines will be affected more by fluctuations due to larger propagation distances was confirmed. In addition, an important influence of the fluctuation correlation length on the results was found. Previous works considering diffusive approximations which are invalid in case this correlation length is small, cf. ASDEX Upgrade parameters, could not study this effect which, however, makes a dramatic difference between ASDEX Upgrade and ITER results depending on the turbulence parameters. In the thesis also a reflectometry run is shown, including the effect of fluctuations. Such runs might be interesting for diagnostics applications.

With a view to the work we have left over for future, additional benchmarks should be performed: Even if benchmarks with simplified models show a good agreement, there might be simple errors in the expressions specific to tokamak applications, which could be found by direct comparison to other codes. Moreover, regarding the importance of the effect for ITER, an independent confirmation of correctness would be welcome. The full wave solver used for the simplified fluctuation case might be generalized to a simple, analytical tokamak geometry, which would allow such benchmarks. In addition, a more refined model for fluctuations could be employed [45].

A

Technical derivations for symbols and Weyl symbols

A.1. Relation between left symbols and Weyl symbols

We shall establish a relation between L-symbols and Weyl symbols. Following [8], the kernel $a(x, x')$ of an operator A can be expressed in terms of the corresponding L-symbol $a(x, N)$ using the quantization rule (2.31), i.e.

$$a(x, x') = \left(\frac{\kappa}{2\pi} \right)^m \int e^{i\kappa(x-x')\cdot N} a(x, N) \mathrm{d}N. \tag{A.1}$$

Starting from this kernel, the Weyl symbol map (2.33) provides the Weyl symbol:

$$A(x, N) = \left(\frac{\kappa}{2\pi} \right)^m \int e^{i\kappa s \cdot (N'-N)} a\left(x + \frac{s}{2}, N' \right) \mathrm{d}s \mathrm{d}N'. \tag{A.2}$$

A. Technical derivations for symbols and Weyl symbols

Both, s and N' appear in the exponential as well as in the arguments of the symbol a. Therefore, the integrals are not trivial to compute. Given the fact that symbols are assumed to be smooth functions, a Taylor expansion around x is appropriate. With a multi-index α, this yields

$$A(x, N) = \left(\frac{\kappa}{2\pi}\right)^m \int e^{i\kappa s \cdot (N'-N)} \sum_{|\alpha|=0}^{\infty} \frac{\frac{s^\alpha}{2} \partial_x^\alpha}{\alpha!} a\left(x, N'\right) \mathrm{d}s\mathrm{d}N'. \tag{A.3}$$

Formally, the powers of s can be replaced with $\frac{i}{\kappa}\partial_N$ acting on the exponential, because, every time such a differentiation is applied, a prefactor of $-i\kappa s$ is produced. Then, the Taylor expansion (A.3) reads

$$A(x, N) = \left(\frac{\kappa}{2\pi}\right)^m \int e^{i\kappa s \cdot (N'-N)} \sum_{|\alpha|=0}^{\infty} \frac{\left(\frac{i}{2\kappa}\right)^{|\alpha|} \overleftarrow{\partial_N^\alpha} \overrightarrow{\partial_x^\alpha}}{\alpha!} a\left(x, N'\right) \mathrm{d}s\mathrm{d}N'. \tag{A.4}$$

Here, the arrows on the partial differential operators indicate the direction in which they act. The sum in the last equation has the form of the Taylor series of an exponential with partial differentiation operators as an argument. Therefore, formally, we write

$$A(x, N) = \left(\frac{\kappa}{2\pi}\right)^m \int e^{i\kappa s \cdot (N'-N)} e^{\frac{i}{2\kappa} \overleftarrow{\partial_N} \cdot \overrightarrow{\partial_x}} a\left(x, N'\right) \mathrm{d}s\mathrm{d}N' \tag{A.5}$$

and remember that the partial differential operators in the exponential make sense when the exponential is Taylor expanded. Now, the s-integration can be performed analytically. The result yields a $\delta(N' - N)$ which also immediately allows the computation of the N'-integration:

$$A(x, N) = e^{\frac{i}{2\kappa} \overrightarrow{\partial_N} \cdot \overrightarrow{\partial_x}} a\left(x, N\right). \tag{A.6}$$

Equation (A.6) provides the relation (2.37) between L-symbols and Weyl symbols given in the body of this thesis. The inverse transformation

$$a(x, N) = e^{-\frac{i}{2\kappa} \overrightarrow{\partial_N} \cdot \overrightarrow{\partial_x}} A\left(x, N\right) \tag{A.7}$$

also holds true.

A.2. Product formula for Weyl symbols

The aim of this section is to provide a formula which, given the Weyl symbols $A(x, N)$ and $B(x, N)$ of two pseudo-differential operators A and B, respectively, gives the Weyl symbol $C(x, N)$ of the composition operator

$$C = A \circ B. \tag{A.8}$$

First, the relation is established for L-symbols instead of Weyl symbols. Then, with the relations between symbols and Weyl symbols (A.6) and (A.7), it is translated in terms of Weyl symbols.

The kernel of the operator product C is given by

$$c(x, y) = \int a(x, x')b(x', y)\mathrm{d}x', \tag{A.9}$$

with $a(x, x')$ and $b(x', y)$ the kernels of A and B, respectively. The symbol map (2.29) is used in order to express the symbol $c(x, N)$ in terms of the corresponding kernel $c(x, y)$, i.e.

$$c(x, N) = \int e^{-i\kappa N \cdot s} a(x, x')b(x', x - s)\mathrm{d}x'\mathrm{d}s. \tag{A.10}$$

In addition, the kernels $a(x, x')$ and $b(x', y)$ are given in terms of the L-symbols by equation (2.31):

$$a(x, x') = \int e^{i\kappa(x-x')\cdot N'} a(x, N')\mathrm{d}N', \tag{A.11a}$$

$$b(x', x - s) = \int e^{i\kappa(x'-x+s)\cdot N''} b(x', N'')\mathrm{d}N''. \tag{A.11b}$$

The kernels (A.11) substituted into (A.10) yields

$$c(x, N) = \left(\frac{\kappa}{2\pi}\right)^{2m} \int e^{i\kappa[s\cdot(N''-N)+(x-x')\cdot(N'-N'')]} a(x, N')b(x', N'')\mathrm{d}N'\mathrm{d}N''\mathrm{d}x'\mathrm{d}s. \tag{A.12}$$

Integration on s and then on N'' can be performed immediately. The result is

$$c(x, N) = \left(\frac{\kappa}{2\pi}\right)^{m} \int e^{i\kappa[(x-x')\cdot(N'-N)]} a(x, N')b(x', N)\mathrm{d}N'\mathrm{d}x'. \tag{A.13}$$

165

A. Technical derivations for symbols and Weyl symbols

If the x'-dependence is removed from b, the x'-integration can be performed. As done in section A.1, $b(x', N)$ is Taylor expanded around x. The result reads

$$c(x, N) = \left(\frac{\kappa}{2\pi} \right)^m \int e^{i\kappa[(x-x') \cdot (N'-N)]} a(x, N') \sum_{|\alpha|=0}^{\infty} \frac{\left(-\frac{i}{\kappa} \right)^{|\alpha|} \overleftarrow{\partial_N^\alpha} \overrightarrow{\partial_x^\alpha}}{\alpha!} b(x, N) \mathrm{d}N' \mathrm{d}x'.$$

(A.14)

Again, $x - x'$ is replaced with the derivative $-\frac{i}{\kappa} \partial_N$ acting on the exponential. The integral on x' and next on N' then can be performed and as a result, we obtain

$$c(x, N) = a(x, N) \sum_{|\alpha|=0}^{\infty} \frac{\left(-\frac{i}{\kappa} \right)^{|\alpha|} \overleftarrow{\partial_N^\alpha} \overrightarrow{\partial_x^\alpha}}{\alpha!} b(x, N)$$

(A.15)

The Taylor series of an exponential is identified, hence

$$c(x, N) = a(x, N) e^{-\frac{i}{\kappa} \overleftarrow{\partial_N} \cdot \overrightarrow{\partial_x}} b(x, N).$$

(A.16)

When Weyl symbols are involved, the corresponding L-symbols are expressed using formulas (A.6) and (A.7). Those transformations plugged into (A.16) yields

$$C(x, N) = e^{\frac{i}{2\kappa} \overrightarrow{\partial_N} \cdot \overrightarrow{\partial_x}} \left[\left(e^{-\frac{i}{2\kappa} \overrightarrow{\partial_N} \cdot \overrightarrow{\partial_x}} A(x, N) \right) e^{-\frac{i}{\kappa} \overleftarrow{\partial_N} \cdot \overrightarrow{\partial_x}} \left(e^{-\frac{i}{2\kappa} \overrightarrow{\partial_N} \cdot \overrightarrow{\partial_x}} B(x, N) \right) \right] \quad \text{(A.17)}$$

The exponential in front of the squared brackets is written out in terms of a Taylor series and Leibnitz rule is applied. In the sum, then, the terms of exponentials are identified and the result is

$$C(x, N) = A(x, N) e^{-\frac{i}{2\kappa} \overleftarrow{\partial_N} \cdot \overleftarrow{\partial_x}} e^{\frac{i}{2\kappa} \left(\overleftarrow{\partial_N} + \overrightarrow{\partial_N} \right) \cdot \left(\overleftarrow{\partial_x} + \overrightarrow{\partial_x} \right)} e^{-\frac{i}{\kappa} \overleftarrow{\partial_N} \cdot \overrightarrow{\partial_x}} e^{-\frac{i}{2\kappa} \overrightarrow{\partial_N} \cdot \overrightarrow{\partial_x}} B(x, N). \quad \text{(A.18)}$$

Given the fact that the partial differential operators in the exponentials commute, they can be put in one exponential. Then, equation (A.18) simplifies to

$$C(x, N) = A(x, N) e^{\frac{i}{2\kappa} \left[\overleftarrow{\partial_x} \cdot \overrightarrow{\partial_N} - \overleftarrow{\partial_N} \cdot \overrightarrow{\partial_x} \right]} B(x, N).$$

(A.19)

This is the product rule for Weyl symbols, cf. equation (2.40) in the body of this work. It is also referred to as the Moyal-Weyl product denoted with a "$\star$":

$$C(x, N) = A(x, N) \star B(x, N). \tag{A.20}$$

Particularly, the first two orders in the Moyal-Weyl product give

$$C(x, N) = A(x, N)B(x, N) - \frac{i}{2\kappa} \{A, B\} (x, N) + \mathcal{O}(\kappa^{-2}) \tag{A.21}$$

thus, recovering the Poisson brackets.

B

Differentiation of distributions

In the framework of this thesis, it is dealt with generalized functions such as Dirac's δ. In section 3.4, this has been worked out. To be mathematically precise such objects are not functions, but they must be considered as distributions. Only in this sense, they as well as their derivatives are properly defined. In this appendix, the basics of distribution calculus are recalled. More details on this topic can be found in [46].

A distribution f, in general, takes a function ϕ and reduces it to a single number $f(\phi)$:

$$f : \phi \mapsto f(\phi). \tag{B.1}$$

A typical example with special interest for this work is Dirac's δ-distribution:

$$\delta : \phi \mapsto \phi(0). \tag{B.2}$$

It reduces the test function ϕ to its value evaluated at point 0.

B. Differentiation of distributions

Considering a function $\tilde{f}$, a distribution f is given in terms of the integral representation

$$f : \phi \mapsto f(\phi) = \int \phi(x)\tilde{f}(x)\mathrm{d}x. \tag{B.3}$$

The function $\tilde{f}$ then is referred to as generating function of the distribution f. Such a representation can be found for any regular distribution.

The δ-distribution is not regular and no integral representation in the sense of (B.3) exists. Anyway, a function $\tilde{\delta}_\epsilon(x)$ can be given which is used in the integral (B.3) instead of the generating function, so that this integral depends on ϵ and converges to the δ-distribution in the limit $\epsilon \to 0$. We consider e.g.

$$\tilde{\delta}_\epsilon(x) = \frac{2}{\sqrt{2\pi\epsilon}}e^{-\frac{1}{2}\frac{x^2}{\epsilon^2}}. \tag{B.4}$$

This function itself is divergent for $\epsilon \to 0$. If the limit is considered after integration, the result converges to the expected result for the δ-distribution:

$$\int \phi(x)\tilde{\delta}_\epsilon(x)\mathrm{d}x \to \phi(0) \tag{B.5}$$

for $\epsilon \to 0$.

Nevertheless, in this thesis, also for the distributions f without generating function, we write

$$\int \phi(x)f(x)\mathrm{d}x = f(\phi). \tag{B.6}$$

Here, the integral notation on the l.h.s. should not be interpreted as an integral in ordinary sense. It rather is a formal way of writing, which means that the distribution f is applied on the test function ϕ, yielding $f(\phi)$. The notation is inspired by the integral representation (B.3). If and only if the distribution under investigation has a generating function $\tilde{f}(x)$, the integral may be considered as an integral in the proper sense.

For this work, also the derivative of the δ-distribution is needed. Hence, the definition of derivatives of distributions is briefly reviewed here. It is motivated by distributions which can be written in terms of generating functions. The derivative f' of distribution f is obtained by using the derivative of the generating function $\tilde{f}'(x)$ instead of $\tilde{f}(x)$ in the integral representation (B.3):

This is for the distribution applied on test function ϕ

$$f'(\phi) = \int \phi(x)\tilde{f}'(x)\mathrm{d}x. \tag{B.7}$$

Here, the prime denotes derivatives. Integration by parts for $\phi(x)$, which vanish at the integration boundaries, yields

$$f'(\phi) = -\int \phi'(x)\tilde{f}(x)\mathrm{d}x = -f(\phi'). \tag{B.8}$$

Higher-order derivatives are defined analogously. This result is generalized to distributions without generating function like for example Dirac's δ, i.e.

$$\delta'(\phi) = -\delta(\phi') = -\phi'(0), \tag{B.9}$$

even if no interpretation in terms of the integral representation is possible.

C

Hamilton's equations of motion and Poisson brackets

Hamilton's equations of motion play an important role in this work, as they present a sort of "wave trajectory" as described with reference to geometrical optics, section 2.3, and also the numerical scheme, chapter 4. In this appendix, phase space is introduced and more details are given about Hamilton's equations of motion, the evolution of phase space quantities and the connection to the Hamilton-Jacobi equation.

In the framework of high frequency wave propagation, the position-refractive index space is referred to as phase space (x, N). A smooth function $H(x, N)$ is considered as Hamiltonian and Hamilton's equations of motion in canonical form are given by

$$\frac{\mathrm{d}x}{\mathrm{d}\tau} = \partial_N H(x, N), \tag{C.1a}$$

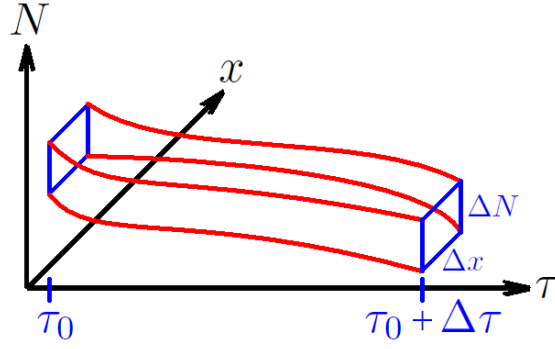$$\frac{\mathrm{d}N}{\mathrm{d}\tau} = -\partial_x H(x, N). \tag{C.1b}$$

Figure C.1.: Neighbouring Hamiltonian orbits shifted by $\Delta x \equiv \Delta x(\tau)$ and $\Delta N \equiv \Delta N(\tau)$ at time τ.

Here, the parameter τ plays the role of time. Hamilton's equations of motion are ordinary differential equations and therefore relatively straight forward to integrate, given initial conditions. Given a solution $(x(\tau), N(\tau))$ of (C.1), called orbit in phase space, its projection onto the configuration space $\{x = x(\tau)\}$ defines a curve called ray in the framework of geometrical optics, cf. section 2.3.

It can be shown [47] that neighbouring Hamiltonian orbits as shown in figure C.1 conserve the enclosed volume $\Delta V = \Delta x \Delta N$. This is called Liouville's theorem. Crossing orbits would lead to $\Delta V = 0$ at the crossing point. This would be against volume conservation. Therefore, Hamiltonian orbits do not cross in a finite $\Delta \tau$.

As a special case, Hamiltonians independent of x, i.e. $H(x, N) \equiv H(N)$, conserve the refractive index, i.e. $N \equiv$ const. As a consequence, also the derivative $\partial_N H(N)$ is conserved. Hence, straight rays trajectories are obtained. As an example, the Hamiltonian for free space (6.3) has such a structure.

For the purpose of this work, cf. chapter 3, Poisson brackets $\{H, A\}$ need to be defined, with $A(\tau, x, N)$ any phase space function depending possibly on τ. Specifically, Poisson brackets describe the change of A along a Hamiltonian orbit $(x(\tau), N(\tau))$, namely,

$$
\frac{\mathrm{d}A}{\mathrm{d}\tau}(\tau, x(\tau), N(\tau)) = \frac{\partial A}{\partial \tau}(\tau, x(\tau), N(\tau)) + \partial_x A(\tau, x(\tau), N(\tau)) \frac{\mathrm{d}x}{\mathrm{d}\tau}
$$
$$
+ \partial_N A(\tau, x(\tau), N(\tau)) \frac{\mathrm{d}N}{\mathrm{d}\tau}, \qquad \text{(C.2)}
$$

and using Hamilton's equations (C.1) one finds

$$\frac{\mathrm{d}A}{\mathrm{d}\tau}\left(\tau, x(\tau), N(\tau)\right) = \frac{\partial A}{\partial \tau}A\left(\tau, x(\tau), N(\tau)\right) + \partial_x A\left(\tau, x(\tau), N(\tau)\right)\partial_N H\left(x(\tau), N(\tau)\right)$$
$$- \partial_N A\left(\tau, x(\tau), N(\tau)\right)\partial_x H\left(x(\tau), N(\tau)\right) \tag{C.3}$$

The Poisson brackets, defined by

$$\{H, A\} := \partial_N H \partial_x A - \partial_x H \partial_N A, \tag{C.4}$$

appear naturally in equation (C.3):

$$\frac{\mathrm{d}A}{\mathrm{d}\tau}\left(\tau, x(\tau), N(\tau)\right) = \frac{\partial A}{\partial \tau}\left(\tau, x(\tau), N(\tau)\right) + \{H, A\}\left(\tau, x(\tau), N(\tau)\right). \tag{C.5}$$

Equation (C.5) simplifies to

$$\frac{\mathrm{d}A}{\mathrm{d}\tau}\left(x(\tau), N(\tau)\right) = \{H, A\}\left(x(\tau), N(\tau)\right), \tag{C.6}$$

when $A \equiv A\left(x(\tau), N(\tau)\right)$ is not explicitly dependent on τ.

Poisson brackets (C.4) have the following properties [47]:

- They are anti-symmetric when arguments are exchanged,

$$\{A, B\} = -\{B, A\}. \tag{C.7a}$$

- Leibnitz rule applies when one argument is the product of two functions,

$$\{AB, C\} = A\{B, C\} + \{A, C\}B, \tag{C.7b}$$

- The Jacobi identity holds true,

$$\{A, \{B, C\}\} + \{B, \{C, A\}\} + \{C, \{A, B\}\} = 0. \tag{C.7c}$$
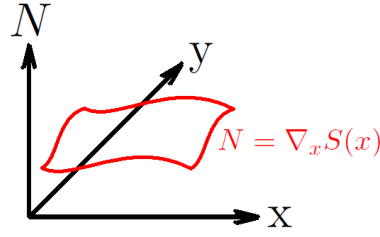
Figure C.2.: Two dimensional configuration space $x = (\mathrm{x}, \mathrm{y}) \in \mathbb{R}^2$ extended with $N \in \mathbb{R}^2$ to phase space. Shown in red is the Hypersurface defined by $N = \nabla_x S(x)$.

In particular, it follows from anti-symmetry (C.7a) that $\{H, H\}$ vanishes identically and hence, due to (C.6), the Hamiltonian itself is conserved along Hamilton orbits.

An important point for the ray tracing method as presented in section 2.3 is the relation between Hamilton's equations of motion (C.1) and the Hamilton-Jacobi equation. This relationship allows to move from a Hamilton-Jacobi type of equation (2.50a) derived from electromagnetic wave theory to a ray tracing strategy using Hamilton's equations of motion. The reader might find more details in the standard textbook [47]. The geometrical interpretation of the relationship is given in the following. Hamilton-Jacobi equation is

$$H\left(x, \nabla_x S(x)\right) = 0, \tag{C.8}$$

which, in general, is a non-linear partial differential equation for the function $S \equiv S(x)$. The solution S of this equation defines a hypersurface in phase space $(x, N = \nabla_x S(x))$ as shown in figure C.2. Here, to each configuration space point x, one single value of $N \equiv N(x)$ is attached.

A vector linking two points on this solution hypersurface is given by

$$\begin{pmatrix} v_x(x) \\ v_N(x) \end{pmatrix} = \frac{1}{\epsilon} \left[\begin{pmatrix} x + v_x(x)\epsilon \\ \nabla_x S(x + v_x(x)\epsilon) \end{pmatrix} - \begin{pmatrix} x \\ \nabla_x S(x) \end{pmatrix} \right] \rightarrow \begin{pmatrix} v_x \\ (\mathcal{D}S(x)v_x) \end{pmatrix}. \tag{C.9}$$

Here, the first components v_x describe the projection onto configuration space whereas the last components v_N give the shift in refractive index direction. The Cartesian unit vectors are denoted with e^i. Einstein's convention is used and the limit $\epsilon \rightarrow 0$ is considered. Furthermore, $\mathcal{D}S = (\partial_{x^i} \partial_{x^j} S(x))_{ij}$ denotes the Hessian of S. The first line does not contain any information, leaving the velocity projection on configuration space v_x arbitrary. Instead, the second line

determines the velocity projection on refractive index vector space v_N in terms of v_x. Formulating equation (C.9), a general tangent vector was considered. This shows that vectors tangent to the solution hypersurface have the velocity projection on refractive index vector space v_N defined by the second line of (C.9), whereas the projection on configuration space v_x is arbitrary.

On the other hand, taking the gradient of Hamilton-Jacobi equation (C.8) yields

$$[\partial_x H(x, N) + \mathcal{D}S(x)\partial_N H(x, N)]_{N=\nabla_x S(x)} = 0. \tag{C.10}$$

We choose

$$v_x = \partial_N H(x, N(x)) \tag{C.11}$$

in (C.9) and substitute equation (C.10) into the r.h.s. of the second line. As a result we find that the vector

$$\begin{pmatrix} v_x \\ v_N \end{pmatrix} = \begin{pmatrix} \partial_N H\left(x, N(x)\right) \\ -\partial_x H\left(x, N(x)\right) \end{pmatrix} \tag{C.12}$$

is compatible with (C.9) and hence tangent to the solution hypersurface of Hamilton-Jacobi equation. This proves that Hamiltonian orbits, given by Hamilton's equations of motion (C.1), are lying in the surface defined by the solution of the Hamilton-Jacobi equation. Vice versa, the solution hypersurface can be constructed as a congruence of Hamiltonian orbits. This is the basis of the ray tracing technique outlined in section 2.3.

D

Gaussian beam profiles

In this appendix, the Wigner function of a beam with given Gaussian profile is computed. It is needed as a boundary condition in the code, cf. section 5.1.1. The electric field around the antenna plane x = 0 is

$$E(\mathrm{x}, \mathrm{y}) = A e^{i\kappa \mathrm{y} \cdot N_{\mathrm{y},0} + i\kappa \mathrm{x} N_{\mathrm{x},0} + \frac{i}{2}\kappa \mathrm{y} \cdot S \mathrm{y} - \frac{1}{2}\kappa \mathrm{y} \cdot \Phi \mathrm{y}} \tag{D.1}$$

with a central amplitude A. For simplicity, $A = 1$ is considered here as well as in the benchmark tests in chapter 6. When physical results are discussed, section 7.5.2, this normalization might not be appropriate. Then, correct values are obtained when the Wigner function is multiplied with $|A|^2$. This is clear from the construction of the Wigner function (D.2).

As presented in figure 3.2, for an m-dimensional space we consider $\mathrm{x} \in \mathbb{R}$ and $\mathrm{y} \in \mathbb{R}^{m-1}$. For physical electric fields, the dimensionality must be set to $m = 3$. The dimensionality is not specified here anyway because for some tests it might also be interesting to consider two-dimensional geometries. One input parameter is the central value for the refractive index

D. Gaussian beam profiles

$(N_{\mathrm{x},0}, N_{\mathrm{y},0})$ where $N_{\mathrm{x},0} \in \mathbb{R}$ and $N_{\mathrm{y},0} \in \mathbb{R}^{m-1}$. It is supposed to fulfil the dispersion relation on the antenna plane. The symmetric matrix Φ in (D.1) describes the beam width on the antenna plane and the symmetric matrix S gives the curvature of the phase front of the beam, namely focusing or defocusing. A more detailed discussion on the physical meaning of Φ and S is given at the end of this appendix. With the Wigner transformation (2.61), the Wigner function reads

$$
w(\mathrm{x} = 0, \mathrm{y}, N_{\mathrm{x}}, N_{\mathrm{y}}) = \int e^{-i\kappa(N_{\mathrm{x}}s_{\mathrm{x}} + N_{\mathrm{y}} \cdot s_{\mathrm{y}})} E\left(\frac{s_{\mathrm{x}}}{2}, \mathrm{y} + \frac{s_{\mathrm{y}}}{2}\right) E^*\left(-\frac{s_{\mathrm{x}}}{2}, \mathrm{y} - \frac{s_{\mathrm{y}}}{2}\right) \mathrm{d}s_{\mathrm{x}} \mathrm{d}s_{\mathrm{y}}.
$$
(D.2)

We substitute the electric field (D.1) in this Wigner transform and perform the s_{x}-integration. This leads to a δ-function for the perpendicular refractive index component:

$$
w(\mathrm{x} = 0, \mathrm{y}, N_{\mathrm{x}}, N_{\mathrm{y}}) = 2\pi e^{-\kappa \mathrm{y} \cdot \Phi \mathrm{y}} \int e^{i\kappa(N_{\mathrm{y},0} - N_{\mathrm{y}}) \cdot s_{\mathrm{y}} + i\kappa \mathrm{y} \cdot S s_{\mathrm{y}} - \frac{1}{4}\kappa s_{\mathrm{y}} \cdot \Phi s_{\mathrm{y}}} \delta(N_{\mathrm{x}} - N_{\mathrm{x},0}) \mathrm{d}s_{\mathrm{y}}.
$$
(D.3)

As the matrix Φ is symmetric, it can be diagonalized with an orthogonal matrix U,

$$
\Phi = U^T D U,
$$
(D.4)

where D is the corresponding diagonal matrix with the eigenvalues D_i of Φ on its diagonal. If in (D.3), the integration variable is substituted,

$$
s_{\mathrm{y}} \to \tilde{s}_{\mathrm{y}} := U s_{\mathrm{y}}
$$
(D.5)

and the tilde is dropped, integral (D.3) yields

$$
w(\mathrm{x} = 0, \mathrm{y}, N_{\mathrm{x}}, N_{\mathrm{y}}) = e^{-\kappa \mathrm{y} \cdot \Phi \mathrm{y}} \int e^{i\kappa(N_{\mathrm{y},0} - N_{\mathrm{y}}) \cdot U^T s_{\mathrm{y}} + i\kappa \mathrm{y} \cdot S U^T s_{\mathrm{y}} - \frac{1}{4}\kappa s_{\mathrm{y}} \cdot D s_{\mathrm{y}}} \delta(N_{\mathrm{x}} - N_{\mathrm{x},0}) \mathrm{d}s_{\mathrm{y}}.
$$
(D.6)

The abbreviation

$$
\nu^T := \kappa \left[(N_{\mathrm{y},0} - N_{\mathrm{y}})^T + \mathrm{y}^T S\right] U^T
$$
(D.7)

is introduced in order to simplify equation (D.6):

$$w(\mathrm{x}=0,\mathrm{y},N_\mathrm{x},N_\mathrm{y}) = 2\pi e^{-\kappa \mathrm{y}\cdot\Phi \mathrm{y}}\int e^{i\nu\cdot s_\mathrm{y}-\frac{1}{4}\kappa s_\mathrm{y}\cdot D s_\mathrm{y}}\delta(N_\mathrm{x}-N_{\mathrm{x},0})\mathrm{d}s_\mathrm{y}$$

$$= 2\pi e^{-\kappa \mathrm{y}\cdot\Phi \mathrm{y}}\delta(N_\mathrm{x}-N_{\mathrm{x},0})\prod_{k=1}^{m-1}\int e^{i\nu_k s_k-\frac{1}{4}\kappa D_k s_k^2}\mathrm{d}s_k. \tag{D.8}$$

Here, the vector $s_\mathrm{y}=(s_1,\ldots,s_{m-1})$ is written out in terms of its components. Next, the integral under the product symbol must be evaluated. This requires standard complex analysis and the result is

$$\int e^{i\nu_k s_k-\frac{1}{4}\kappa D_k s_k^2}\mathrm{d}s_k = 2\sqrt{\frac{\pi}{\kappa D_k}}e^{-\frac{\nu_k^2}{\kappa D_k}}. \tag{D.9}$$

The result is substituted in (D.8) and the Wigner function reads

$$w(\mathrm{x}=0,\mathrm{y},N_\mathrm{x},N_\mathrm{y}) = \frac{2^m \pi^{(m+1)/2}}{\kappa^{(m-1)/2}\sqrt{\det\Phi}}e^{-\kappa \mathrm{y}\cdot\Phi \mathrm{y}}e^{-\sum_{=1}^{m-1}\frac{\nu_k^2}{\kappa D_k}}\delta(N_\mathrm{x}-N_{\mathrm{x},0}). \tag{D.10}$$

Upon accounting for definition (D.7) and that $\det\left(\Phi^{-1}\right)=(\det\Phi)^{-1}$, the final result is

$$w(\mathrm{x}=0,\mathrm{y},N_\mathrm{x},N_\mathrm{y}) = \frac{2^m \pi^{(m+1)/2}}{\kappa^{(m-1)/2}\sqrt{\det\Phi}}e^{-\kappa \mathrm{y}\cdot\Phi \mathrm{y}-\kappa[(N_{\mathrm{y},0}-N_\mathrm{y})+S\mathrm{y}]\cdot\Phi^{-1}[(N_{\mathrm{y},0}-N_\mathrm{y})+S\mathrm{y}]}\delta(N_\mathrm{x}-N_{\mathrm{x},0}).$$

$$\tag{D.11}$$

In equation (3.65), a regularized Wigner function is presented. This is obtained when the singularity is split up. Hence we define

$$\tilde{w}(\mathrm{x}=0,\mathrm{y},N_\mathrm{y}) := \frac{2^m \pi^{(m+1)/2}}{\kappa^{(m-1)/2}\sqrt{\det\Phi}}e^{-\kappa \mathrm{y}\cdot\Phi \mathrm{y}-\kappa[(N_{\mathrm{y},0}-N_\mathrm{y})+S\mathrm{y}]\cdot\Phi^{-1}[(N_{\mathrm{y},0}-N_\mathrm{y})+S\mathrm{y}]}\left|\frac{\partial H(x,N)}{\partial N_\mathrm{x}}\right|,$$

$$\tag{D.12}$$

which is in agreement with (3.65).

For physical applications, it is assumed that the matrices Φ and S are diagonal in the same reference frame. This means that the principal coordinate systems for both, beam width as well as curvature, are the same on the antenna plane. In general, they could be rotated one with respect to the other and, introducing as a parameter the rotational angle, one could describe this effect. However, for the purpose of this thesis, such effects are not further investigated. Then,
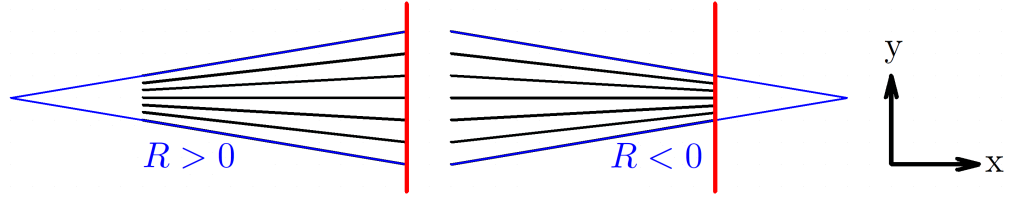
D. Gaussian beam profiles

Figure D.1.: Effect of different curvature radii on the beam. Geometrical optics rays launched on the antenna plane (red) are shown. In blue, the curvature radii are displayed. Left: positive curvature radius $R > 0$ is considered. Right: the curvature radius $R < 0$ is assumed to be negative.

considering the electric field (D.1), it is clear that the eigenvalues D_k of Φ are related to the beam width on the antenna plane w_k. Furthermore, the eigenvalues S_k of S are related to the initial curvature radius R_k of the wave front:

$$D_k = \frac{2}{\kappa w_k^2},$$ (D.13a)

$$S_k = -\frac{1}{R_k}.$$ (D.13b)

Considering Wigner function (D.11), it can be seen that the refractive index yielding the largest contribution for a given point y is

$$N_y = N_{y,0} + Sy.$$ (D.14)

As a convention, in this work, the curvature radius is considered positive, if the center of curvature is lying in direction of beam propagation (on the left in figure D.1, focused beam), whereas it is considered negative, if it is beyond the antenna plane as shown on the right in figure D.1, defocused beam. This is consistent with the sign in definition (D.13b).

E

User guide for WKBeam

In the following two sections, small user guides for the ray tracing and the binning part of WKBeam are presented. Note that in general, the code is implemented considering physical coordinates, which are not normalized by any typical length scale L, unlike the theoretical description presented throughout this thesis.

E.1. Ray tracing code

The ray tracing part of WKBeam requires as input an ascii text file with the following syntax: Every content appearing in a line after a "#"-character is ignored and the command

$$[VARIABLENAME] = [VALUE] \, ,$$

sets the variable *[VARIABLENAME]* to the value *[VALUE]*. Leading blanks are ignored. Table E.1 presents all possible parameters with a brief explanation of the meaning.

The code is run with the command

mpirun -np [NMBR CORES] python ray_trace.py [INPUT],

where *[NMBR CORES]* specifies the requested number of cores and *[INPUT]* gives a link to the file containing the input parameters. The file "ray_trace.py" is the main file of the code.

As a further input for tokamak applications, the code is looking for input files in the folder specified among the input parameters: "topfile" should provide the magnetic field and the files "ne.dat" and "Te.dat" contain information on the electron density profile and the electron temperature profile, respectively. The format of these files is compatible with the TORBEAM code [40].

The WKBeam ray tracing code produces as an output one binary file per master core, denoted by *[output_filename]_file[C].hdf5*, where *[output_filename]* is defined as input parameter and *[C]* is a number specific to the core writing the file. The file format is the standard hdf5-format. The entries maintained in this file are listed in table E.2.

Table E.1.: Input parameters for the ray tracing code, their datatype and a brief description.

variable name	datatype	description
zeroelectrondensity	boolean	if set, a simplified model or free space is used
linearlayer	boolean	if set, use linear layer as simplified model
valley	boolean	if set, use lens-like medium as simplified model
analmodel	boolean	if set and zeroelectrondensity is not set, use analytical model for the plasma profiles
neanal	float	central electron density for analytical model
deltarhopedestal	float	pedestal width for the analytical plasma model
input_dir	string	path to the input files for the plasma profiles
output_dir	string	path, where the output files are written
output_filename	string	name of the output file, "_fileC.hdf5" is added, where "C=0,1,2,..." labels the core writing the file

variable name	datatype	description
takecentralrayfirst	boolean	if set, the first ray in the output file "C=0" is the central, non-scattered ray
storeNxNyNz	boolean	if set, the refractive index components in Cartesian components are stored
storeNparallelphiN	boolean	if set, the refractive index components in coordinates aligned to the magnetic field are stored
storeGroupVelocity	boolean	if set, the group velocity is stored
storeCorrectionFactor	boolean	if set, the correction factor ξ is stored
storePsi	boolean	if set, the flux $\psi \equiv \psi(x, y, z)$ through the magnetic surface the point (x, y, z) is lying on is stored
ControlOutput	boolean	if set, information on the progress is displayed
rmaj	float	major radius of the tokamak
rmin	float	minor radius of the tokamak
twodim	boolean	if set, a two-dimensional beam in (x, z) coordinates is assumed; otherwise, a three-dimensional beam is considered
freq	float	beam frequency in GHz
sigma	float	wave mode, "+1" for O-mode, "-1" for X-mode
beamwidth1, 2	float	beamwidth in both directions
curvatureradius1, 2	float	curvature radius in both directions
rayStartX, Y, Z	float	Cartesian coordinates of the beam center on the antenna
antennatordeg	float	toroidal angle of the antenna plane in degree
antennapoldeg	float	poloidal angle of the antenna plane in degree
anglespecification	string	if set to "ITER", ITER angle convention is used, if set to "AUG", AUG angle convention is used
centraleta1, 2	float	central value for the refractive index
npt	integer	number of points per ray
timestep	float	standard timestep $\Delta\tau$ between two ray points

variable name	datatype	description
epsilonRegS	float	regularization parameter for S inversion
integratormax nmbrsteps	integer	maximal number of subdivisions for one integration step
integratorreltol	float	maximal integrator tolerance (relative)
integratorabstol	float	maximal integrator tolerance (absolute)
nmbrRays	integer	number of rays to trace
nmbrMetrHast BoundaryInit	integer	number of preliminary generated random numbers for MC-Hastings algorithm to ensure convergence
absorption	boolean	if set, absorption is turned on
absorptionModule	integer	if absorption is turned on, absorption routine is chosen: 0: Westerhof, 1: Farina routine
absorptionLayerX	float	if absorption is turned on in simplified model, absorption layer is considered for X < this parameter
absorptionStartEarlier ThenCentralRay	float	put 0 if absorption shall be computed along the whole ray, otherwise: abs. is computed starting $\Delta\tau$ earlier then it was recognized on the central ray, with $\Delta\tau$ this parameter
absorptionConsiderAs NonZeroTreshhold	float	treshold for absorption coefficient, absorption above this value is considered non-negligible, used to determine when absorption on central ray starts
absorptionSmaller TimestepsFactor	float	when absorption is computed, choose timesteps smaller by this factor
absorptionWfct Treshhold	float	treshold, when ray tracing is stopped due to negligible ray power, relative to the initial value
reflektometrie	boolean	if set, reflectometry case is considered

variable name	datatype	description
reflektometrierho Treshhold	float	if reflectometry case is considered, the ray tracing is stopped when the ray leaves the shell with this value for ρ
scattering	boolean	if set, scattering of the rays is taken into account
scatteringAmplitude	float	fluctuation strength for simplified model scattering
scatteringLengthscaleX, Z	float	correlation lengths for simplified model scattering
scatteringXmin, max	float	boundaries for x when scattering is turned on
scatteringLengthPerp	float	perpendicular correlation length in tokamak fluctuation model
scatteringLengthParallel	float	parallel correlation length in tokamak fluctuation model
scatteringDelta	float	width of the fluctuation layer in normalized minor radius units
scatteringrhocentral	float	center of fluctuation layer in normalized minor radius units
scatteringDeltaneOverne	float	$\sqrt{\langle \delta n_e^2 / n_e^2 \rangle}$ at the center of the fluctuation layer
scatteringMaxProb GuessFactor	float	factor to enlarge guess for the scattering probability so that an upper limit is obtained
scatteringintegration boundaryfactor	float	factor the guess for the boundaries of the relevant range for the numerical integration of the scattering cross section is multiplied with
nmbrinitialisation MetropolisHastings Scattering	integer	number of initialisations for MC-Hastings algorithm to ensure convergence

Table E.2.: Entries in the output file of the ray tracing code, their datatype and a brief description. Entries which are put in brackets may not be present for a special choice of parameters.

name of entry	datatype	description
Traces[a,b,c]	float	$b = 3$: value of fraction F for ray a at timestep c, $b = 0, 1, 2, c > 0$: value for x, y, z for ray a at timestep c
(TracesNparallelphiN[a,b,c])	float	$b = 0, 1, 2, c > 0$: value for N_x, N_y, N_z for ray a at timestep c
(TracesNparallelphiN[a,b,c])	float	$b = 0, 1, c > 0$: value for $N_\parallel$, ϕ_N for ray a at timestep c
(TracesGroupVelocity[a,b,c])	float	$b = 0, c > 0$: value for the group velocity $\partial_N H(x, N)$ for ray a at timestep c
(TracesCorrectionFactor[a,b,c])	float	$b = 0, c > 0$: correction factor ξ for ray a at timestep c
(TracesPsi[a,c])	float	$c > 0$: value of the magnetic flux $\psi = \psi(x, y, z)$ for ray a at timestep c
TracesTime[a,c]	float	$c > 0$: value of time parameter τ_c along ray a after timestep c
Mode	float	+1: O-mode propagation, -1: X-mode propagation
FreqGHz	float	beam frequency in GHz
antennapolangle	float	poloidal antenna angle in radian
antennatorangle	float	toroidal antenna angle in radian
nmbrRays	integer	number of rays contained in this file

name of entry	datatype	description
rayStartX, Y, Z	float	central beam point on the antenna plane in (x, y, z) coordinates
beamwidth1, 2	float	beamwidth on the antenna plane
curvatureradius1, 2	float	curvature radius on the antenna plane
centraleta1, 2	float	central value of the refractive index on the antenna plane
fileindex	integer	label 0, 1, 2, ... identifying the master-core which has written the file
inputfile	string	copy of the input file with all included comments

E.2. Binning code

The data produced by the ray tracing code needs to be post-processed with the aid of the binning code. This can be called once the output from ray tracing is available, with the command

python call_binning.py [INPUT].

Again, *[INPUT]* links to an input file, with a syntax identical to the ray tracing code, cf. section E.1. Possible entries with a short description are presented in table E.3. The output of the binning code essentially is a table containing the values of the Monte-Carlo estimator (4.50) for the binning areas Ω_α labeled with an up to four dimensional multi-index α. Together with additional information, this is stored in a hdf5-file, with entries summarized in table E.4.

Table E.3.: Input parameters for the ray tracing code, their datatype and a brief description.

variable name	datatype	description
input_directory	string	path to the input files written by the ray tracing code

variable name	datatype	description
inputfilename	list of strings	labels of one or several runs of the ray tracing code the input files for which are obtained by adding "_file[C].hdf5", where [C]=0,1,...,N-1, with N the number of files for one specific case
nmbrFiles	integer	number of files N for one specific case
outputdirectory	string	path to the directory where the output files are written
outputfilename	list of strings	if defined, the output files for the specific cases are named with those filenames plus ".hdf5", otherwise the standard output file names "[inputfilename]_binned.hdf5" are used
WhatToResolve	list of strings	μ strings (up to four) labeling what quantity is resolved in the order of this list, possible entries are: "X", "Y", "Z", "Nx", "Ny", "Nz", "Nparallel", "phiN", "Psi", "rho", "R"
min (max)	list of floats	minimum (maximum) boundaries for the considered grid in the up to four dimensions defined in [WhatToResolve]
nmbr	list of integers	number of bins in the considered grid for all dimensions
InputPower	float	if not defined: normalization is such that the central electric field on the antenna plane is 1, otherwise: specifies the total beam power
storeWfct	boolean	if set, the integral weighted with 1 is stored
storeVelocityField	boolean	if set, the integral weighted with the group velocity is stored
VelocityComponents ToStore	list of strings	which velocity components to store, possible entries are: "Nx", "Ny", "Nz"
storeAbsorption	boolean	if set, the integral weighted with the absorption coefficient is computed

variable name	datatype	description
computeAmplitude	boolean	if set, the integrals are computed taking into account scattered as well as unscattered rays
computeAmplitude Unscattered	boolean	if set, the integrals are computed taking into account only unscattered rays
computeScatteringEffect	boolean	if set, the difference between also scattered and purely unscattered integrals is computed
computeScattered Contribution	boolean	if set, the contribution of scattered rays in amplitude is computed
correctionfactor	boolean	if set, the correction factor ξ is properly taken into account, otherwise it is set to $\xi \equiv 1$

Table E.4.: Entries in the output file of the binning code, their datatype and a brief description. Entries which are put in brackets may not be present for a special choice of parameters.

name of entry	datatype	description
(BinnedTraces[a,b])	array of floats	$b = 0$: value for binning with weight 1, bin labelled with a μ-dimensional multi-index a (see dimensionality of [WhatToResolve]) $b = 1$: corresponding statistical uncertainty
(VelocityField[a,c,b])	array of floats	analogous to [BinnedTraces], where as a weight the refractive index component indicated in the c-th entry of [VelocityComponentsToStore] is used
(Absorption[a,b])	array of floats	analogous to [BinnedTraces], where as a weight the absorption coefficient is used
(BinnedTracesUnscattered[a,b])	array of floats	see [BinnedTraces], only unscattered rays are taken into account

name of entry	datatype	description
(VelocityFieldUnscattered[a,b])	array of floats	see [VelocityField], only unscattered rays are taken into account
(AbsorptionUnscattered[a,b])	array of floats	see [Absorption], only unscattered rays are taken into account
(BinnedTraces ScatteringEffect[a,b])	array of floats	difference of [BinnedTraces] and [BinnedTracesUnscattered], statistical uncertainty is computed taking into account that the unscattered rays are the same in both cases
(VelocityField ScatteringEffect[a,b])	array of floats	difference of [VelocityField] and [VelocityFieldUnscattered], statistical uncertainty is computed taking into account that the unscattered rays are the same in both cases
(Absorption ScatteringEffect[a,b])	array of floats	difference of [Absorption] and [AbsorptionUnscattered], statistical uncertainty is computed taking into account that the unscattered rays are the same in both cases
(BinnedTracesScattered Contribution[a,b])	array of floats	contribution of scattered rays in [BinnedTraces]
(VelocityFieldScattered Contribution[a,c,b])	array of floats	contribution of scattered rays in [VelocityField]
(AbsorptionScattered Contribution[a,b])	array of floats	contribution of scattered rays in [Absorption]
(Xmin)	float	lower boundary of the grid covered by bins in x-direction if resolved, analogue entries may be found for Y, Z, Nx, Ny, Nz, Nparallel, phiN, Psi, rho, R
(Xmax)	float	upper boundary of the grid covered by bins ins x-direction if resolved, see [Xmin] for more information

name of entry	datatype	description
(nmbrX)	integer	number of bins in x-direction if resolved, see [Xmin] for more information
nmbrRays	integer	number of scattered and unscattered rays taken into account
nmbrRaysUnscattered	integer	number of unscattered rays taken into account
nmbrRaysScattered	integer	number of scattered rays taken into account
Mode	float	+1: O-mode propagation rays were used, -1: X-mode propagation rays were used
FreqGHz	float	beam frequency in GHz
antennapolangle	float	poloidal angle of the antenna plane
antennatorangle	float	toroidal angle of the antenna plane
rayStartX, Y, Z	float	central beam launching x, y, z position in cm
beamwidth1, 2	float	beam width on the antenna plane in the two orthogonal principal axis in cm
curvatureradius1, 2	float	curvature radius on the antenna plane in the principal axis system in cm
centraleta1, 2	float	central value of the perpendicular refractive index in the beam center on the antenna plane

F

Metropolis-Hastings algorithm

Metropolis-Hastings algorithm can be employed to generate random numbers following any, even complicated probability distribution. In this thesis, at different points it is used, cf. the generation of initial conditions, section 5.1.1, and the scattering scheme, section 5.1.2. The reader may find a description in the textbook [48], summarized in this appendix.

Say that we are looking for a random number z_{i+1} with probability distribution $p(z_{i+1})$ needs to be generated. Let z_i be a guess for a number distributed with $p(z_i)$ as a probability density, also referred to as stationary probability in the framework of Metropolis-Hastings algorithm. Then z_{i+1} may be drawn with the following strategy:

i. Choose a candidate z: Let the so-called proposal distribution $q(z|z_i)$ be the conditional probability density function of z given z_i.

ii. Define the acceptance probability

$$a(z, z_i) := \min \left\{ 1, \, \frac{p(z)q(z_i|z)}{p(z_i)q(z|z_i)} \right\}. \qquad \text{(F.1)}$$

This may be computed even if the probability distributions involved are not normalized. The candidate z is accepted, i.e. $z_{i+1} = z$, with probability $a(z, z_i)$. If it is not accepted, the previous value is copied, i.e. $z_{i+1} = z_i$. In order to decide whether or not to accept the candidate z, an event with probability $a(z, z_i)$ must be simulated. This is most easily done by generating a uniformly distributed number f within the interval $[0, 1)$ and accept the candidate if the condition

$$f < a(z, z_i) \tag{F.2}$$

is fulfilled.

The new value z_{i+1} obtained from this algorithm is distributed according to the stationary probability distribution $p(z_{i+1})$.

Note that for the purpose of this thesis, as initial value z_0, the most likely value $z : p(z) = \sup p(z)$ is chosen and the probability distribution of z_{i+1} converges to the stationary probability after performing steps (i) and (ii) several times, where convergence is improved the closer the proposal probability distribution $q(z|z_i)$ is to $p(z)$. Let us point out that in this thesis, the special case of a non-conditioned proposal distribution, independent of the previous value z_i is considered, i.e. $q(z|z_i) = q(z)$.

G

Plasma profiles

In this appndix, plasma profiles considered in this thesis, namely for the tests of the Hamiltonian, cf. section 7.4.4, and the results, presented in section 7.5, are presented. These equilibria are AUG #25485 in figure G.1 and a simulated ITER equilibrium in figure G.2. It is difficult to profide the entire information on the magnetic field on paper, given the fact that it is a function on the two coordinates R and z. Hence, z is treated as a parameter when the toroidal magnetic field component is shown. The fact that this parameter has only a small impact on the toroidal field component B_t (cf. figures G.1 (c) and G.2 (c)) confirms that the magnetic field is basically a function on R.

(a) electron density profile:

(b) electron temperature profile:

(c) toroidal component of the magnetic field:
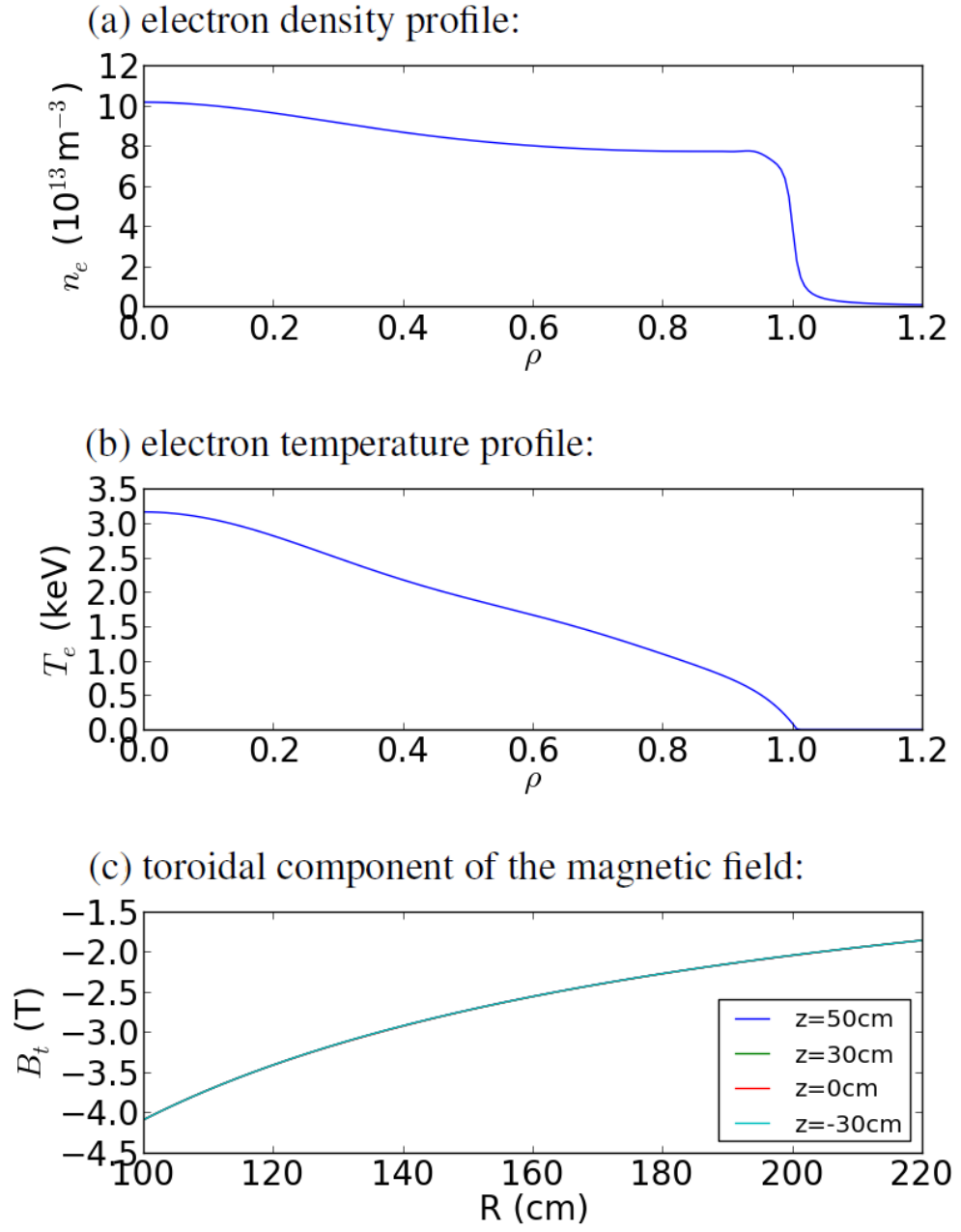
Figure G.1.: Equilibrium of ASDEX Upgrade #25485. (a) electron density profile, (b) temperatur profile and (c) toroidal component of the magnetic field.

Figure G.2.: Simulated ITER equilibrium. (a) electron density profile, (b) temperature profile and (c) toroidal component of the magnetic field.

List of Figures

Bibliography

[1] R. A. Gross. *Fusion Energy*. Wiley, New York, 1984.

[2] F. Jenko. Plasmaphysik ii - anwendungen. lecture script, university of Ulm, 2010.

[3] I. B. Bernstein. Geometric optics in space- and time-varying plasmas. *Physics of Fluids*, **18**, 320, 1975.

[4] M. Bornatici, R. Cano, O de Barbieri, et al. Electron cyclotron emission and absorption in fusion plasmas. *Nucl. Fusion*, **23**, 1153, 1983.

[5] Yu. A. Kravtsov. The geometrical optics approximation in the general case of inhomogeneous and nonstationary media with frequency and spatial dispersion. *Sov. Phys. JETP*, **28**, 769, 1969.

[6] C. Tsironis, A. G. Peeters, and H. Isliker. Electron-cyclotron wave scattering by edge density fluctuations in iter. *Physics of Plasmas*, **16**, 112510, 2009.

[7] K. Hizanidis, A. K. Ram, Y. Kominis, et al. Fokker-planck description of the scattering of radio frequency waves at the plasma edge. *Physics of Plasmas*, **17**, 022505, 2010.

[8] S. W. McDonald. Phase-space representations of wave equations with applications to the eikonal approximation for short-wavelength waves. *Physics Reports*, **158**, 337, 1988.

[9] S. W. McDonald. Wave kinetic equation in a fluctuating medium. *Physical Review A*, **43**, 4484, 1991.

[10] J. D. Jackson. *Classical Electrodynamics*. Wiley, New York, 1998.

Bibliography

[11] D. B. Melrose and R. C. McPhedran. *Electromagnetic processes in dispersive media.* Cambridge University Press, Camebridge, 1991.

[12] T. H. Stix. *The Theory of Plasma Waves*. McGraw-Hill Book Company, New York, 1962.

[13] M. Brambilla. *Kinetic Theory of Plasma Waves.* Oxford Science Publications, Oxford, 2008.

[14] A. Martinez. *An Introduction to Semuclassical and Microlocal Analysis.* Springer-Verlag, New York, 2002.

[15] O. Maj. *Asymptotic Solutions of Pseudodifferential Wave Equations.* dissertation, University of Milan, Italy, 2003.

[16] M. Wilkens. Quantenmechanik i - das eikonal. lecture script, university of Potsdam, 2012.

[17] Yu. A. Kravtsov and Yu. I. Orlov. *Geometrical Optics in Inhomogeneous Media.* Springer-Verlag, Berlin, 1990.

[18] J. J. Duistermaat. *Fourier Integral Operators.* Birkhäuser, Boston, 1996.

[19] S. W. McDonald and A. N. Kaufman. Weyl representation for electromagnetic waves: The wave kinetic equation. *Physical Review A*, **32**, 1708, 1985.

[20] F. Karal and J. B. Keller. Elastic, electromagnetic and other waves in a random media. *Journal of Mathematical Physics*, **5**, 537, 1964.

[21] O. Maj. private communication, 2013.

[22] L. Friedland and A. N. Kaufman. Congruent reduction in geometric optics and mode conversion. *Physics of Fluids*, **30**, 3050, 1987.

[23] W. Greiner and J. Reinhart. *Quantum Electrodynamics.* Springer-Verlag, Berlin, 2003.

[24] B. Lapeyre, E. Pardoux, and R. Sentis. *Introduction to MC methods for transport and diffusion Equation.* Oxford University Press, Oxford, 2003.

[25] M. A. Henderson, F. Albajar, S. Alberti, et al. An overview of the iter ec h&cd system and functional capabilities. 23rd IAEA Fusion Energy Conference, Daejon, Republic of Korea,

2010.

[26] E. Hairer, C. Lubich, and G. Wanner. *Geometric Numerical Integration: Structure-Preserving Algorithms for Ordinary Differential Equations*. Springer-Verlag, Heidelberg, 2006.

[27] G. v. Rossum. Python reference manual. CWI Report CS-R9525; http://www.python.org, 1995.

[28] E. Jones, T. Oliphant, P. Peterson, et al. Scipy: Open source scientific tools for python. http://www.scipy.org, 2001.

[29] Message-passing interface forum. http://www.mpi-forum.org, 2013.

[30] L. Dalcín, R. Paz, and M. Storti. Mpi for python. *Journal of Parallel and Distributed Computing*, **65**, 1108, 2005.

[31] S. Behnel, R. W. Bradshaw, and D. S. Seljebotn. Cython tutorial. Proceedings of the 8th Python in Science Conference, Pasadena, 2009.

[32] Introduction to the computer facilities of the rzg. homepage Rechenzentrum Garching; http://www.rzg.mpg.de/services/computing/hardware, 2013.

[33] W. Greiner. *Quantum mechanics: an introduction*. Springer-Verlag, Heidelberg, 2001.

[34] M. Bornatici and O. Maj. Wave beam propagation in a weakly inhomogeneous isotropic medium: paraxial approximation and beyond. *Plasma Physics and Controlled Fusion*, **45**, 707, 2003.

[35] O. Maj, G. V. Pereverzev, and E. Poli. Validation of the paraxial beam-tracing method in critical cases. *Physics of Plasmas*, **16**, 062105, 2009.

[36] M. Abramowitz and I. A. Stegun. *Handbook of Mathematical Functions With Formulas, Graphs and Mathematical Tables*. National Bureau of Standards, Washington D. C., 1972.

[37] J. Wesson. *Tokamaks*. Oxford University Press, Oxford, 2011.

[38] E. Poli. private communication, 2013.

Bibliography

[39] R. Prater, D. Farina, Yu. Gribov, et al. Benchmarking of codes for electron cyclotron heating and electron cyclotron current drive under iter conditions. *Nuclear Fusion*, **48**, 2008, 035006.

[40] E. Poli, A. G. Peeters, and G.V. Pereverzev. Torbeam, a beam tracing code for electron-cyclotron waves in tokamak plasmas. *Computer Physics Communications*, **136**, 90, 2001.

[41] Y. Peysson, J. Decker, L. Morini, et al. Rf current drive and plasma fluctuations. *Plasma Physics and Controlled Fusion*, **53**, 124028, 2011.

[42] E. Westerhof. Kinetic theory of plasma waves - part ii: Homogeneous plasma. *Fusion Science and Technology*, **57**, 92, 2010.

[43] E. Westerhof. Implementation of toray at jet. Rijnhuizen Report 89-183, 1989.

[44] G. Ramponi, D. Farina, M. A. Henderson, et al. Physics analysis of the iter ecw system for optimized performance. *Nuclear Fusion*, **48**, 054012, 2008.

[45] M. W. Shafer, R. J. Fonck, G. R. McKee, et al. 2d properties of core turbulence on diii-d and comparison to gyrokinetic simulations. *Physics of Plasmas*, **19**, 032504, 2012.

[46] W. Rudin. *Functional Analysis*. McGraw-Hill Book Company, New York, 1973.

[47] L. D. Landau and E. M. Lifshitz. *Course of Theoretical Physics, Mechanics*. Pergamon Presse, Oxford, 1969.

[48] C. Lemieux. *Monte Carlo and Quasi-Monte Carlo Sampling*. Springer Science+Business Media, New York, 2009.

Name: Hannes Weber   Matrikelnummer: 671464

Erklärung

Ich erkläre, dass ich die Arbeit selbstständig verfasst und keine anderen als die angegebenen
Quellen und Hilfsmittel verwendet habe.

Ulm, den . . . .

<div align="right">Hannes Weber</div>